

Cooling and Self-Excitation of a One-Electron Oscillator

A thesis presented

by

Brian Richard D'Urso

to

The Department of Physics

in partial fulfillment of the requirements

for the degree of

Doctor of Philosophy

in the subject of

Physics

Harvard University

Cambridge, Massachusetts

May 2003

©2003 - Brian Richard D'Urso

All rights reserved.

Thesis advisor

Gerald Gabrielse

Author

Brian Richard D'Urso

Cooling and Self-Excitation of a One-Electron Oscillator

Abstract

With a superposition of static electric and magnetic fields, a Penning trap can confine a single electron indefinitely. A weak coupling of the electron to its environment makes the system ideal for precision measurements but renders detection of the electron's motion difficult. In order to measure fundamental properties of an electron, we employ a Penning trap cooled by a dilution refrigerator. This experimental setup requires extremely low-noise and low-power cryogenic amplifiers for detection of the electron's axial motion. We design and demonstrate new amplifiers, resulting in a significant decrease of the axial temperature and in an improved signal to noise ratio. We use feedback to cool the axial motion and to self-excite the axial motion for continuous monitoring of the axial frequency. These techniques for cooling and measuring the axial frequency may contribute to an improved measurement of the electron g factor, a more stringent CPT test in leptons, and a more precise measurement of the proton-electron mass ratio.

Contents

Title Page	i
Abstract	iii
Table of Contents	iv
List of Figures	vii
List of Tables	xiii
Acknowledgments	xiv
1 Introduction	1
1.1 $g - 2$ Measurement	2
1.1.1 QED	3
1.1.2 Fine Structure Constant	3
1.2 Penning Trap	4
1.2.1 Basic Particle Motions	5
1.2.2 Experimental Frequencies	8
2 Apparatus and Basic Detection	10
2.1 Apparatus	11
2.1.1 Closed Endcap Cylindrical Trap	11
2.1.2 Ultra-cold Temperatures	13
2.1.3 Quantum Jump Spectroscopy	13
2.1.4 Microwave Source	15
2.2 Axial Motion and Detection	17
2.2.1 Anharmonicity	17
2.2.2 Damping and Detection	21
2.2.3 Comparison of Axial Frequency Monitoring Techniques	27
2.3 DC Trap Biasing	31
2.3.1 Ring Voltage Supply	31
2.3.2 Loading and Dumping	34
2.3.3 Changing the Axial Frequency	35

3	Cyclotron and Anomaly Lineshapes	39
3.1	Overview of Calculations	40
3.2	Cyclotron and Anomaly Lineshapes	41
3.3	Weak Drive Quantum Jump Spectroscopy	45
3.4	Simplified Model	47
3.4.1	Lineshapes with Discrete Axial States	53
3.4.2	Analytical Solution for Continuous Axial States	56
3.4.3	Comparison of Methods	60
3.5	Lineshapes with Weak Axial Coupling	64
3.5.1	Lineshape with Driven Axial Motion	65
3.6	Correlated Cyclotron and Anomaly Measurement	66
3.6.1	Calculation	67
3.6.2	Numerical Results	68
4	Low-Power Detection	71
4.1	Amplifier Challenges	72
4.1.1	Power Dissipation	72
4.1.2	Heat Sinking	74
4.1.3	Feedback and Stability	75
4.2	Single-Gate HEMT Amplifier Design	77
4.2.1	Cryogenic HEMT Performance	78
4.2.2	Feedback and Stability	83
4.3	Single-Gate HEMT Amplifiers	88
4.3.1	Cryogenic Surface Mount Components	88
4.3.2	Common Amplifier Circuit Features	89
4.3.3	64 MHz First Stage	92
4.3.4	64 MHz Second Stage	100
4.3.5	200 MHz First Stage	105
4.3.6	200 MHz Second Stage	110
4.4	SiGe Bipolar Transistors	112
4.5	Future and Limits	114
5	Axial Feedback Cooling	116
5.1	Damping and Feedback Cooling	117
5.1.1	Detection Signal to Noise Ratio	122
5.1.2	Comparison to Cooling a Resistor	123
5.2	Experimental Realization	125
5.3	Experimental Results	127
5.4	Amplifier Feedback	132
5.5	Fundamental Limits of Feedback Cooling	133

6	Self-Excited Axial Oscillator	135
6.1	The Self-Excited Anharmonic Oscillator	136
6.2	Direct Self-Excitation and Instability	138
6.3	Limiting the Self-Excited Oscillator	142
6.3.1	Geometric Limiting	142
6.3.2	Dither	144
6.3.3	Electronic Limiting	144
6.4	Comparator Limited Self-Excitation	147
6.4.1	Noiseless Analysis	148
6.4.2	The Effects of Noise	149
6.4.3	Experimental Results	152
6.5	DSP Limited Self-Excitation	172
6.5.1	DSP Algorithms	174
6.5.2	Analysis	176
6.5.3	Experimental Results	177
6.6	Frequency Stability with Limiting	182
6.7	Other Observations with Self-Excitation	185
6.7.1	Self-Excitation of Multiple Electrons	185
6.7.2	Magnetron Sideband Cooling and Self-Excitation	186
6.7.3	Parametrically Driven Self-Excitation	188
7	Towards $g - 2$	189
7.1	Axial Sideband Cooling	189
7.1.1	Coupling by the Drive Geometry	190
7.1.2	Coupling by the Magnetic Bottle	192
7.1.3	Comparison of Cooling Methods	192
7.2	$g - 2$ Measurement	193
7.2.1	Anomaly Transition	193
7.2.2	Magnetic Field Stability	194
7.3	Other Applications	195
7.3.1	Quantum Computing	195
7.4	Conclusions	198
A	Field Emission Point Etching	200
B	High Frequency Feedthrough	202
C	DSP Program	205
	Bibliography	223

List of Figures

1.1	Difference of measurements of the fine structure constant α from the 1998 CODATA value.	4
1.2	Penning trap fields and resulting motions.	5
1.3	Energy levels of one electron in a Penning trap.	6
1.4	Motions of a single electron in a Penning trap.	8
2.1	Three-dimensional (left) and two-dimensional (right) representations of trap.	11
2.2	Dilution refrigerator apparatus with expanded view of trap.	14
2.3	Glass (left) and sapphire (right) microwave window.	16
2.4	Simplified axial detection schematic.	21
2.5	Amplifier noise resonance.	23
2.6	Equivalent particle and detector circuit near the axial frequency.	24
2.7	Driven axial response of a single electron showing both the absorptive (left) and dispersive (right) responses.	25
2.8	Parametrically driven axial response with the drive sweeping down in frequency.	26
2.9	Simplified detection schematic diagram for tracking the zero crossing of the dispersive axial response.	28
2.10	Simplified multiple drive detection schematic diagram.	29
2.11	Details of trap wiring. Values without units are resistances in ohms.	32
2.12	Simplified schematic diagram of the ring voltage supply.	33
2.13	Normalized power required to drive the anomaly transition as a function of axial frequency.	37
3.1	States used in simplified model of cyclotron and spin states.	48
3.2	Cyclotron or anomaly transition lineshapes as calculated with discrete axial states for $\bar{n}_z = 10$, $\gamma_c = 0$. The axial states are truncated at $n_{max} = 400$	57

3.3	Cyclotron or anomaly transition lineshapes as calculated with continuous axial states for $\bar{n}_z = 10$, $\gamma_c = 0$. The series is truncated at $N_{terms} = 100$ near the Lorentzian limit, or up to $N_{terms} = 200$ near exponential limit.	61
3.4	Comparison of discrete lineshapes (solid lines) and continuous lineshapes (dashed lines) with $\bar{n}_z = 10$	62
3.5	Correlated transition lineshapes as calculated with discrete axial states for $\bar{n}_z = 10$, $\gamma_c/\delta_a = 10$. The axial states are truncated at $n_{max} = 200$. The cyclotron damping was set artificially high for the cyclotron transition, $\gamma_c/\delta_a = 0.25$ to prevent the discrete peaks of the cyclotron transition from getting impractically narrow.	69
4.1	Fujitsu FHX13LG HEMT with the ceramic cover removed. The gate lead is at the bottom, the drain is at the top, and the side leads are both connected to the source. Carriers in the channel are conducted in the vertical direction.	79
4.2	DC characteristic curves (top) of a Fujitsu FHX13LG HEMT at 300 K (left) or 4 K (right). The transconductance (bottom) is found from the slope of the characteristic curves.	80
4.3	DC characteristic curves (top) of a Fujitsu FHX13LG HEMT at 300 K (left) or 4 K (right). The output resistance (bottom) is found from the slope of the characteristic curves.	82
4.4	Single-gate model HEMT with feedback (a), model HEMT with drain load (b), and model HEMT with gate load (c). Components inside the dashed circle are modeled as being internal to the device.	83
4.5	Photographs of the 64 MHz amplifiers (top) and 200 MHz amplifiers (bottom), with the first stage amplifiers (left) and second stage amplifiers (right).	90
4.6	First stage 64 MHz amplifier schematic. Values without units are resistances in ohms.	93
4.7	First stage 64 MHz amplifier board layout. Values without units are resistances in ohms.	93
4.8	First stage 64 MHz amplifier noise resonance connected to a test capacitor with $V_D = 0.2$ V, $I_D = 60$ μ A (left), and with $V_D = 1.0$ V, $I_D = 120$ μ A (right).	95
4.9	Reflection off the 64 MHz first stage amplifier output with $V_D = 0.2$ V, $I_D = 60$ μ A (left), and with $V_D = 1.0$ V, $I_D = 90$ μ A (right).	95
4.10	Cyclotron resonances with the the cryogenic amplifiers on (top) or off (bottom). The measured axial temperatures are also shown. The dashed lines show the expected 68% confidence region for the data.	97

4.11	Temperature of the first stage amplifier heat sink after the amplifier was turned off (open circles) or after a heater on the heat sink was turned off (closed circles). When on, each was dissipating about $10 \mu\text{W}$.	99
4.12	Equivalent electrical model for the FET cooling analysis.	99
4.13	Second stage 64 MHz amplifier schematic. Values without units are resistances in ohms	102
4.14	Second stage 64 MHz amplifier board layout. Values without units are resistances in ohms	102
4.15	Response of the 64 MHz second stage amplifier: forward gain (a), reverse gain (b), forward reflection (c), and reverse reflection (d). The amplifier was biased to $V_D = 1.0 \text{ V}$ and $I_D = 130 \mu\text{A}$	103
4.16	Forward gain of the 64 MHz second stage amplifier.	104
4.17	First stage 200 MHz amplifier schematic. Values without units are resistances in ohms.	107
4.18	First stage 200 MHz amplifier board layout. Values without units are resistances in ohms.	107
4.19	First stage 200 MHz amplifier noise resonance with $V_D = 0.15 \text{ V}$, $I_D = 80 \mu\text{A}$ (left), and with $V_D = 1.0 \text{ V}$, $I_D = 200 \mu\text{A}$ (right).	108
4.20	Reflection of the 200 MHz amplifier output with $V_D = 0.15 \text{ V}$ and $I_D = 80 \mu\text{A}$ (left), and a narrower frequency span to show the input tuned circuit in the output reflection (right).	109
4.21	Second stage 200 MHz amplifier schematic. The trim capacitor is an open coaxial stub used to tune the input network. Values without units are resistances in ohms.	111
4.22	Second stage 200 MHz amplifier board layout. Unitless values are resistances in ohms.	111
4.23	Response of the 200 MHz second stage amplifier: forward gain (a), reverse gain (b), forward reflection (c), and reverse reflection (d). The amplifier was biased to $V_D = 0.5 \text{ V}$ and $I_D = 529 \mu\text{A}$	112
4.24	Forward gain of the 200 MHz second stage amplifier.	113
4.25	DC characteristics of a SiGe bipolar transistor (Infineon BFP620) at room temperature (left) and at 4 K (right).	114
5.1	Effective circuit for damping and detecting the electron without (a) or with (b) feedback. Circuit (c) is an equivalent circuit to (a) for the electron.	118
5.2	Diagram of system used for feedback cooling. The components inside of the dashed box are at cryogenic temperatures.	126
5.3	One electron noise dips with no feedback (top left), feedback to increase damping (top center, right), or feedback to decrease damping (bottom center). The bottom (left and right) show the effect of a slightly incorrect phase when decreasing the damping.	128

5.4	One electron noise dips with several feedback gains showing the narrowing of the dip with increasing feedback.	129
5.5	Cyclotron resonances taken at several different feedback amplitudes which show the decrease in linewidth associated with the cooling. The dashed lines show the expected 68% confidence region for the data.	130
5.6	Axial temperature obtained as the feedback amplitude is varied (top), the axial damping rate obtained as the feedback amplitude is varied (middle), and the ratio of the temperature and damping rate (bottom).	131
6.1	Amplifier noise resonance with a single electron self-excited by direct feedback.	140
6.2	Cyclotron response with direct axial self-excitation. The large shift of ~ 85 MHz is due to the large axial amplitude. The dashed lines show the expected 68% confidence region for the data.	142
6.3	Comparator amplitude response for a signal without noise or combined with noise with the given signal to noise amplitude ratio.	150
6.4	Change in gain $\delta_G(A)$ with a comparator for a signal without noise or combined with noise with the given signal to noise amplitude ratio.	151
6.5	Diagram of the system used for hard limited self-excited oscillator characterization. The components inside of the dashed box are at cryogenic temperatures. The active crystal filter, cryogenic amplifiers, and comparator are detailed separately.	152
6.6	Schematic diagram of the active crystal filter used for comparator limited self-excitation.	153
6.7	Hard limited self-excited oscillator response with a 150 Hz filter (left) and a 50 Hz filter (right), averaged over 80 s.	154
6.8	Comparison of periodogram (left) and ARMA (right) power spectrum estimation of the hard limited self-excited oscillator, taken near the harmonic amplitude (top) or in a highly anharmonic region (bottom).	156
6.9	Cyclotron resonances at different feedback amplitudes and compensation potential settings. The dashed lines show the expected 68% confidence region for the data.	157
6.10	Absolute amplitude measured from a cyclotron spectrum plotted against the electrical signal measured. The fit gives an absolute calibration relating the signal size to the amplitude of the oscillation.	158
6.11	Axial temperature as measured from the cyclotron resonance at different axial amplitudes. The zero amplitude point had no feedback.	159
6.12	Axial frequency measured as a function of axial amplitude by varying the feedback gain while holding the feedback phase constant. This process is repeated at many compensation potential settings to map out the variation in anharmonicity.	161

6.13	The change in axial frequency as the trapping potential is varied (upper left), used to find C_2 . The change in axial frequency as the compensation potential is varied (upper right), used to find D_2 . The variation in C_4 as measured from the anharmonic axial response at different compensation potential settings (lower left), gives a measure of D_4 . The variation in C_6 as measured from the anharmonic axial response at different compensation potential settings (lower right), gives a measure of D_6	163
6.14	Maps of the hard limited self-excited oscillator response over different feedback phase and gain. The contours, calculated from the noiseless hard limited feedback theory, are at equal steps in frequency (upper left) or amplitude ² (all others). In the frequency plot (upper left), the contours are only drawn in the region above the excitation threshold and the scale clips the extreme high and low frequencies of the region below threshold.	165
6.15	Transient response of the self-excited oscillator response at different pre-comparator filter widths. In each case the feedback was turned on at time = 0.	168
6.16	Frequency scatter measured at each compensation potential from the frequency standard deviation (open circles) or the FWHM of the ARMA peak (filled circles). These show what compensation voltage range should be chosen to get maximum axial frequency stability.	170
6.17	Frequency stability of self-excited axial oscillator based detection with a 150 Hz pre-comparator filter (circles) or 50 Hz pre-comparator filter (squares). In each case the frequencies are determined from the peak of the periodogram (open) or ARMA analysis (filled).	171
6.18	Quantum jumps of the cyclotron motion driven by a weak μ -wave drive as detected by monitoring the frequency of the hard limited self-excited axial oscillator.	171
6.19	Schematic diagram for DSP limited self-excitation.	173
6.20	Comparison of the FFT of the detected self-excited oscillator signal with the amplitude tuned to the harmonic region (left) or with the amplitude mistuned (right). Each was taken with a 1 second square window with 100 spectra averaged.	177
6.21	FFT of the detected self-excited oscillator axial signal with an 8 second square window.	178
6.22	Cyclotron resonances at different feedback amplitudes and compensation potential settings with DSP limited self-excitation. The dashed lines show the expected 68% confidence region for the data.	179
6.23	Axial temperatures measured from cyclotron spectra with different DSP limited self-excited oscillator amplitudes.	180

6.24	Frequency instability measured for different dwell times for the DSP limited self-excited oscillator.	181
6.25	Quantum jumps as detected with the DSP limited self-excited oscillator.	181
6.26	Large amplitude direct self-excitation of one electron (left) and two electrons (right).	186
6.27	Self-excited axial oscillator response with a strong sideband cooling drive near resonance. In each plot, the detuning of the cooling drive from $\nu_z + \nu_m$ is indicated.	187
7.1	Axial-cyclotron sideband cooling (top) and heating (bottom) response. The direct cyclotron response is also shown (middle). The dashed lines show the expected 68% confidence region for the data.	191
B.1	Assembly of the high frequency amplifier feedthrough and trap.	203

List of Tables

1.1	Trapped electron frequencies and damping rates.	9
2.1	Fixed trap parameters for the gold plated copper electrode trap. . . .	12
4.1	Amplifier input impedance Z_{in} due to feedback for several drain loads. The input impedance is also expressed as parallel resistance R_p and parallel capacitance C_p	85
4.2	Amplifier output impedance Z_{out} due to feedback for several gate loads. The output impedance is also expressed as parallel resistance R_p and parallel capacitance C_p	87
5.1	Axial temperatures obtained under several conditions. The feedback reported as optimal is associated with the lowest axial temperature measured.	129
6.1	Calculated and measured trap parameters. The uncertainties in the calculated values are estimated using 0.0005 inch variations in z_0 , ρ_0 , and Δz_c due to machining tolerance and thermal contraction.	162

Acknowledgments

I would like to thank Professor Gerald Gabrielse for giving me the freedom to do the research I wanted, but also providing the resistance necessary to keep me objectively analyzing the approach.

I have had the pleasure of interacting with graduate students Steve Peil, Carla Levy, Peter Yesley, John Estrada, Paul Oxley, Nathaniel Bowden, Tanya Zelevinsky, Andrew Speck, and Dan Farkas, and also with postdocs Timothy Roach, Joseph Tan, and Cody Storry. I would like to thank Brian Odom for running the experiment with me, particularly through the dilution refrigerator problems. I would also like to thank David Hanneke who will be continuing the experiment and who helped with the high frequency amplifier feedthrough. I also owe particular thanks to Ramon van Handel and his enthusiasm for the self-excited oscillator.

I am grateful to Jan Ragusa for help with the inevitable paperwork, and to Stan Cotreau for teaching me to machine metal. I am particularly grateful to Jim MacArthur, who revolutionized our electronics capabilities and was always willing to give helpful advice.

I would like to thank my parents and family for their unending support. I am most thankful to Victoria D'Urso, who makes it all worthwhile.

My graduate education and research was generously supported by the Fannie and John Hertz Foundation. This experiment was funded by the National Science Foundation.

Chapter 1

Introduction

A Penning trap, which consists of a superposition of static magnetic and electric fields, can hold a single electron indefinitely. The stability of those fields and the weak coupling of the electron to its environment make the system ideal for precision measurements. With one electron, the electron g factor can be measured. By trapping a positron instead, a comparison of the electron and positron g factors can be made to test CPT symmetry. Finally, by adding a proton, the proton to electron mass ratio can be measured.

For precision measurements on electrons or positrons, only the axial motion of the particle is directly detected. Since the cyclotron and spin frequencies are too high to be measured directly, they are instead coupled into the axial motion. However, even with very weak coupling, noise from the detector drives the axial motion and may interfere with the precision measurement. To minimize this effect, we cool the axial motion with a dilution refrigerator or with feedback. We examine the effects of the finite axial motion in Chapter 3. In Chapter 4, we demonstrate new amplifiers

to improve detection of the axial signal while reducing the axial temperature. In Chapters 5 and 6, we consider the use of feedback to cool the particle or to self-excite the particle for improved detection.

1.1 $g - 2$ Measurement

Our present goal is to measure the electron g factor, which is a constant that gives the strength of the electron magnetic moment $\vec{\mu}$ in terms of the spin \vec{S} as

$$\vec{\mu} = \frac{g}{2} \left(\frac{e}{m} \right) \vec{S}. \quad (1.1)$$

The magnitude of the magnetic moment μ can be written as

$$\mu = \frac{g}{2} \left(\frac{e\hbar}{2m} \right) = \frac{g}{2} \mu_B, \quad (1.2)$$

where μ_B is the Bohr magneton and g is the electron g factor. The electron g factor is related to the electron gyromagnetic ratio γ_e , which is

$$\gamma_e = \frac{g\mu_B}{\hbar}. \quad (1.3)$$

Since g is equal to 2 to within about one part in 10^3 , it is convenient to instead work with $g - 2$. The electron anomaly a is defined by

$$a \equiv \frac{g - 2}{2}. \quad (1.4)$$

The choice to work with a instead of g is more than just a mathematical decision.

The most precise measurement of g measures a directly [1]. The measured value is

$$a = 1.159\,652\,188\,4(43) \times 10^{-3}. \quad (1.5)$$

We also take the approach of measuring a . The experimental reasons for this choice are discussed in Section 1.2.1.

1.1.1 QED

Quantum electrodynamics (QED) predicts that the electron anomaly is given by a series expansion in the fine structure constant α ,

$$a = C_1 \left(\frac{\alpha}{\pi}\right) + C_2 \left(\frac{\alpha}{\pi}\right)^2 + C_3 \left(\frac{\alpha}{\pi}\right)^3 + C_4 \left(\frac{\alpha}{\pi}\right)^4 + \dots, \quad (1.6)$$

where the coefficients C_1, C_2, C_3, \dots are predicted by QED. The first three coefficients can be calculated analytically, but the calculation of C_4 requires 891 four-loop Feynman diagrams [2]. Progress on this calculation has been made with the aid of computers, but a recent correction [3] gave a significant shift to the previous calculation of the C_4 term. This expansion is important because it can provide a means of determining α from a measurement of a , or it provides a test of QED by using a measurement of a and an independent measurement of α from another experiment.

1.1.2 Fine Structure Constant

The fine structure constant α is a unitless combination of fundamental constants,

$$\alpha = \frac{\mu_0 c e^2}{2h}, \quad (1.7)$$

where μ_0 is the permeability of free space, c is the speed of light, and h is Planck's constant. The electron g factor measurement combined with QED compares favorably to other measurements of α [4]. Figure 1.1 shows a comparison of several measurements of α . Presently, the most precise determination of α is from the electron $g - 2$ measurement [1], which we seek to improve upon. The precision of the helium fine structure constant experiment [5] is limited by theory [6]. The measurement based on the cesium recoil shift and mass ratios is preliminary [7]. Other measurements

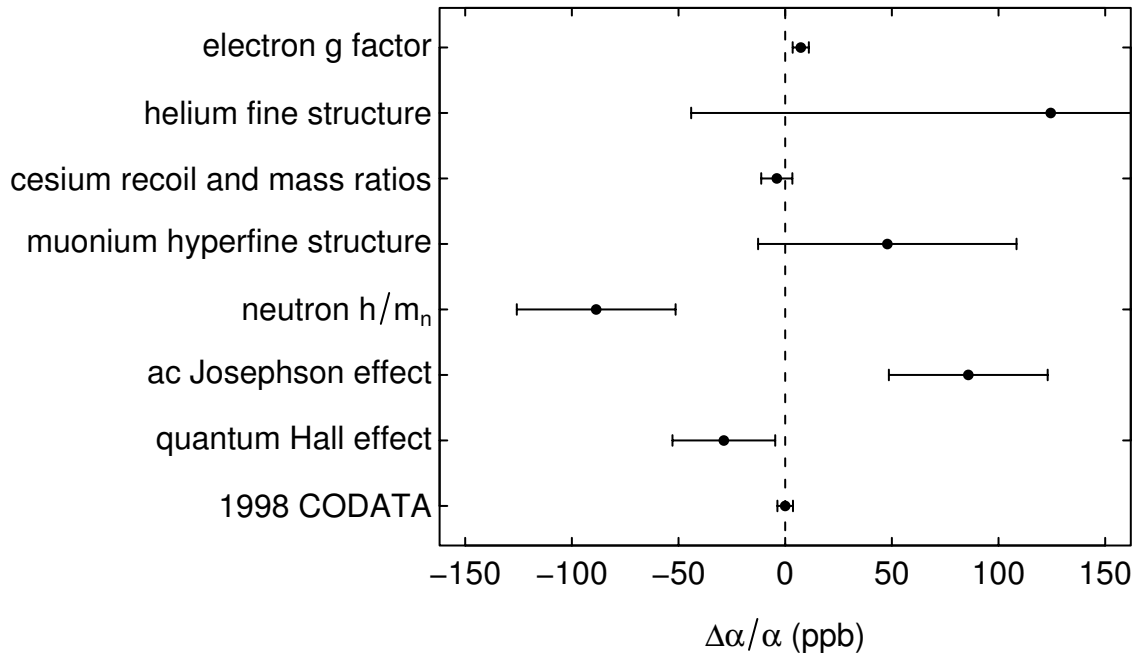


Figure 1.1: Difference of measurements of the fine structure constant α from the 1998 CODATA value.

of α are from the muonium hyperfine structure [8], the neutron h/m_n [9], the ac Josephson effect [10], and the quantum Hall effect [11]. Several of these measurements were combined in the 1998 CODATA [10] value of α , with the electron g factor result weighted most heavily. Since then, the correction [3] of an error in the QED expansion has shifted the electron g factor result.

1.2 Penning Trap

We give a brief introduction to Penning traps. For a more thorough treatment, see [12, 13]. A Penning trap consists of a strong, static, homogeneous magnetic field and a weak electrostatic quadrupole field. The fields and resulting motions are illustrated in Figure 1.2. The strong (5.2 Tesla) magnetic field provides confinement

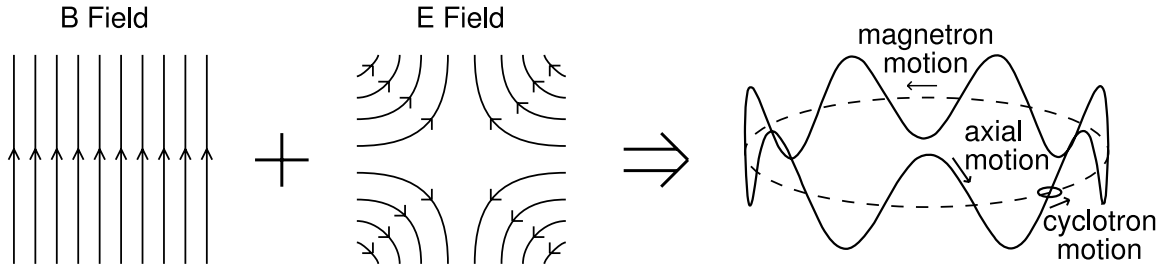


Figure 1.2: Penning trap fields and resulting motions.

in the horizontal direction, perpendicular to the magnetic field, while the electric field provides confinement in the axial direction.

1.2.1 Basic Particle Motions

There are three spatial motions of a single electron in a Penning trap: cyclotron, axial, and magnetron. In addition to the spatial degrees of freedom, there is the electron spin. Quantum mechanically, the result is the energy level structure shown in Figure 1.3. We give a description of the motion which uses the free space values of the cyclotron and spin frequencies and ignores higher order corrections, but is accurate enough for experimental purposes here. For a complete description suitable for precision measurement calculations, see [12].

Cyclotron and Spin States

The cyclotron motion is a tight circular orbit of the electron in the magnetic field. The cyclotron frequency ν_c and angular frequency ω_c are given by

$$\omega_c = 2\pi\nu_c = \frac{eB}{m}. \quad (1.8)$$

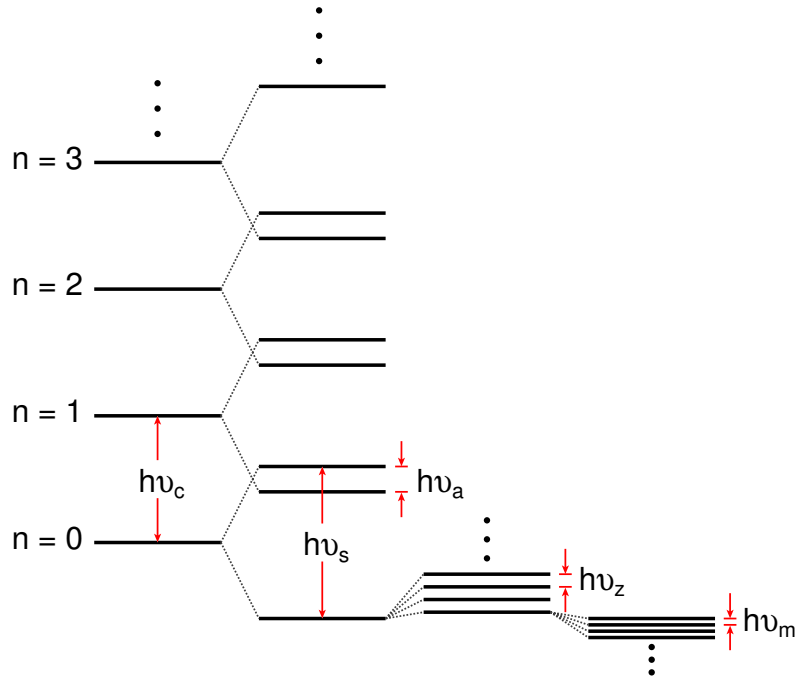


Figure 1.3: Energy levels of one electron in a Penning trap.

Neglecting the small shifts due to special relativity, the cyclotron states form an infinite ladder of states separated by equal energy steps $h\nu_c$.

In the strong magnetic field, the spin may have one of two states, spin up $|\uparrow\rangle$ or spin down $|\downarrow\rangle$. The states are separated by energy $h\nu_s$, where ν_s is given by

$$\nu_s = \frac{g}{2}\nu_c, \quad (1.9)$$

or as an angular frequency $\omega_s = 2\pi\nu_s$.

Instead of measuring ν_c and ν_s to find the electron g factor, we measure the anomaly frequency ν_a given by the difference between the spin and cyclotron frequencies,

$$\nu_a = \nu_s - \nu_c = a\nu_c. \quad (1.10)$$

We may also write the angular frequency $\omega_a = 2\pi\nu_a$. In practice, the anomaly

transition is easier to drive than the very weakly coupled spin transition, and the anomaly frequency is directly proportional to $g - 2$ or to the electron anomaly a . By directly measuring a , it is not necessary to take the difference between measurements of the cyclotron and spin frequencies, which are large and nearly equal frequencies.

Axial Motion

The axial motion is the oscillation parallel to the magnetic field in the \hat{z} direction. Its frequency ν_z and angular frequency ω_z are determined by the electric field alone,

$$\omega_z = 2\pi\nu_z = \sqrt{\frac{eV_0}{md^2}} (1 + C_2), \quad (1.11)$$

where V_0 is the electrostatic trapping potential, d gives the size of the trap, and C_2 is a constant which describes the trap geometry. All detection and monitoring of a single trapped electron is done through the axial motion. See Chapter 2 for more information on the axial motion and detection.

Magnetron Motion

The final spatial degree of freedom is the magnetron motion, which is a result of the $\vec{E} \times \vec{B}$ drift. The magnetron frequency ν_m and angular frequency ω_m are given by

$$\omega_m = 2\pi\nu_m = \frac{\nu_z^2}{2\nu_c}. \quad (1.12)$$

The magnetron frequency is independent of both the particle properties e and m , being determined by the electric and magnetic fields alone.

Unlike the other spatial motions, the magnetron motion is only metastable. Any damping of this motion would cause the magnetron orbit to grow until the electron

collides with an electrode. In practice, the radiative damping rate for the magnetron motion is less than $(10^5 \text{ years})^{-1}$, since the radiative damping rate scales as ω^2 . Additionally, the magnetron motion can be “cooled” into a higher energy and smaller radius orbit with magnetron-axial sideband cooling [12]. With the assistance of sideband cooling, the magnetron motion can be controlled and a single particle can remain trapped indefinitely.

1.2.2 Experimental Frequencies

Experimentally, the frequencies of the spatial degrees of freedom (see Figure 1.4) of

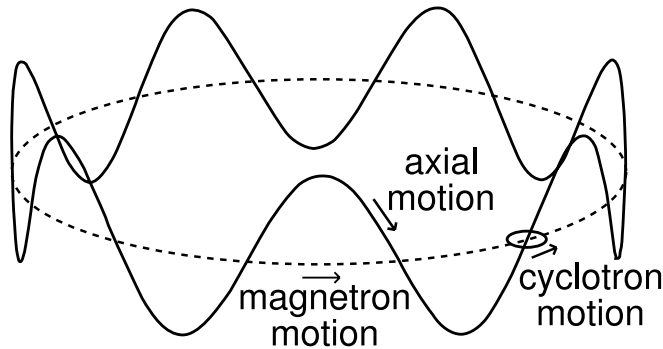


Figure 1.4: Motions of a single electron in a Penning trap.

a single trapped electron are well separated. Some sample oscillation frequencies and damping rates are shown in Table 1.1 for a trapping potential V_0 near 10 V. Only the cyclotron motion has significant natural damping, and this damping is suppressed by more than a factor of 100 by the high Q microwave cavity formed by the trap electrodes [14, 15]. The axial motion is damped by the tuned circuit used for its detection.

By expressing the transition energies in temperature units, it is clear that with a

transition:	frequency:	$h\nu/k_b$:	damping:
Magnetron	$\nu_m = 11.85$ kHz	$\frac{h\nu_m}{k_b} = 0.57$ μ K	$\frac{\gamma_m}{2\pi} \approx 10^{-15}$ Hz
Axial	$\nu_z = 64.42$ MHz	$\frac{h\nu_z}{k_b} = 3.1$ mK	$\frac{\gamma_z}{2\pi} \approx 5$ Hz
Cyclotron	$\nu_c = 146.8$ GHz	$\frac{h\nu_c}{k_b} = 7.0$ K	$\frac{\gamma_c}{2\pi} \approx 0.02$ Hz
Spin	$\nu_s = 147.0$ GHz	$\frac{h\nu_s}{k_b} = 7.0$ K	$\frac{\gamma_s}{2\pi} \approx 10^{-12}$ Hz

Table 1.1: Trapped electron frequencies and damping rates.

dilution refrigerator with a base temperature of 100 mK, the cyclotron motion will damp into its ground state. The other degrees of freedom are either not significantly damped or will be in an excited thermal state.

In later experiments, we use an axial frequency ν_z near 200 MHz by increasing the trapping potential V_0 to ~ 100 V, which also causes the magnetron frequency to increase significantly and modifies the axial damping. See Chapter 2 for more discussion of the effects of changing the axial frequency.

Chapter 2

Apparatus and Basic Detection

The electric field which partially defines a Penning trap is created by static voltages applied to carefully machined trap electrodes. The details of these electrodes are important in determining the shape of the electric field and thus the anharmonicity of the axial and magnetron motions. At the same time, the electrode surfaces may form a microwave cavity which can affect the frequency and damping of the cyclotron motion [16, 17]. So, the choice of trap electrode geometry and properties is critical for the $g - 2$ measurement.

Here we discuss some details of the experimental apparatus and their consequences for the particle motions. We also introduce detection techniques for directly monitoring the axial motion of the electron and indirectly monitoring the cyclotron and spin states.

2.1 Apparatus

At the heart of the experimental apparatus is the trap itself. The trap is enclosed in an ultra-high vacuum can and secured to the base temperature region of a dilution refrigerator. The vacuum obtained in such a cryogenic enclosure can be better than 5×10^{-17} Torr [18], which eliminates collisions between the trapped electron and background gas atoms seen in some experiments [19].

2.1.1 Closed Endcap Cylindrical Trap

We use a closed endcap cylindrical trap geometry [20], as shown in Figure 2.1. The

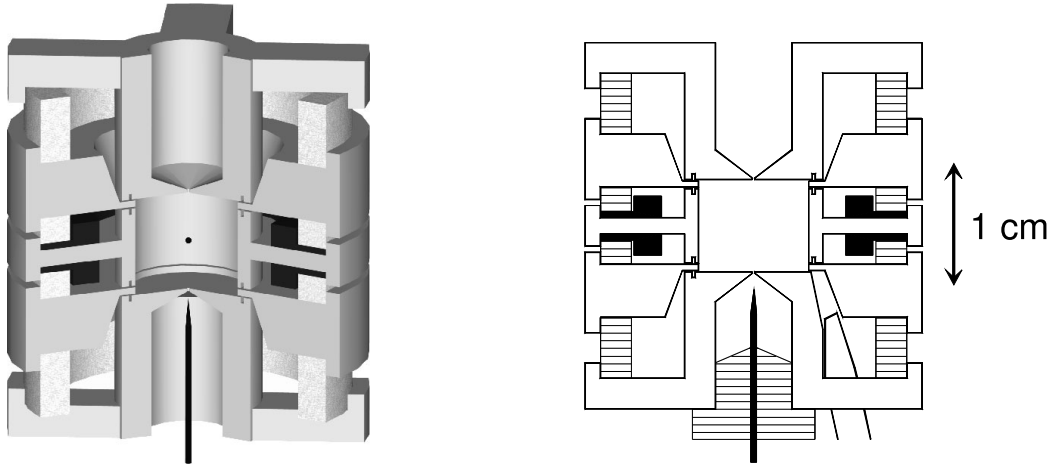


Figure 2.1: Three-dimensional (left) and two-dimensional (right) representations of trap.

tight fitting electrodes form a high Q microwave cavity which suppresses spontaneous emission of the cyclotron motion [16, 17]. We have observed a cyclotron excited state lifetime of up to 15 seconds [14], far longer than the 94 ms lifetime in free space, or the 0.27 s lifetime which signaled the first observation of inhibited spontaneous emission in a cavity [21].

For almost all the data presented here we used the gold plated copper electrodes that were also used to first observe quantum structure in the cyclotron motion [14, 15], although the grease sealed vacuum can enclosing the trap was replaced with a more reliable indium sealed can [22]. The fixed parameters of the trap are shown in Table 2.1. See [20] for a complete discussion of the electrostatics of compensated cylindrical Penning traps. The self-excited oscillator data with $\nu_z = 200$ MHz was taken in a

parameter:	value:
B	5.24 T
ρ_0	0.1797 in (0.4564 cm)
z_0	0.1513 in (0.3842 cm)
Δz	0.0274 in (0.0696 cm)
d	0.14 in (0.35 cm)
κ	0.79

Table 2.1: Fixed trap parameters for the gold plated copper electrode trap.

new trap with gold plated silver electrodes designed to improve the magnetic field stability [22].

Cavity Shifts

One of the primary reasons for choosing a cylindrical trap is to gain control over the shifts in the cyclotron frequency caused by the modification of the microwave field by the cavity formed by the trap electrodes.

The complex geometry of hyperbolic electrodes makes calculation of the cavity effects [23] and the machining of the electrodes difficult. With a cylindrical trap, the machining is more straightforward, the mode structure of the trap is easily calculated [16, 17], and the coupling of the cyclotron motion with the radiation field can be

dramatically decreased by creating a high Q microwave cavity.

2.1.2 Ultra-cold Temperatures

In order to reduce the thermal motion of the trapped electron, the trap is cooled to 100 mK with an Oxford Kelvinox 300 dilution refrigerator. The assembly of the refrigerator, magnet, and trap are shown in Figure 2.2. The ultra-cold temperature produced by the dilution refrigerator allows the cyclotron motion to be cooled to the ground quantum state, and reduces the thermal axial motion. However, even with a dilution refrigerator, cooling the axial motion to ultra-cold temperatures while using it for detection is difficult, because the amplifier needed for detection can heat the axial motion (see Chapter 4).

2.1.3 Quantum Jump Spectroscopy

A one quantum change in cyclotron energy is clearly resolved [14]. In order to measure the cyclotron and spin states, a weak quadratic gradient is added to the magnetic field. The gradient is produced by a pair of nickel rings stacked between the trap electrodes. The magnetization of the nickel is saturated in the strong magnetic field.

The quadratic magnetic field gradient makes the axial frequency depend on the total magnetic moment of the particle, which in turn depends on the cyclotron and spin state [24, 25]. The coupling performs a QND measurement on the cyclotron and spin states, so a continuous series of measurements give the same quantum state as a result. However, the coupling does broaden and/or shift the cyclotron and anomaly

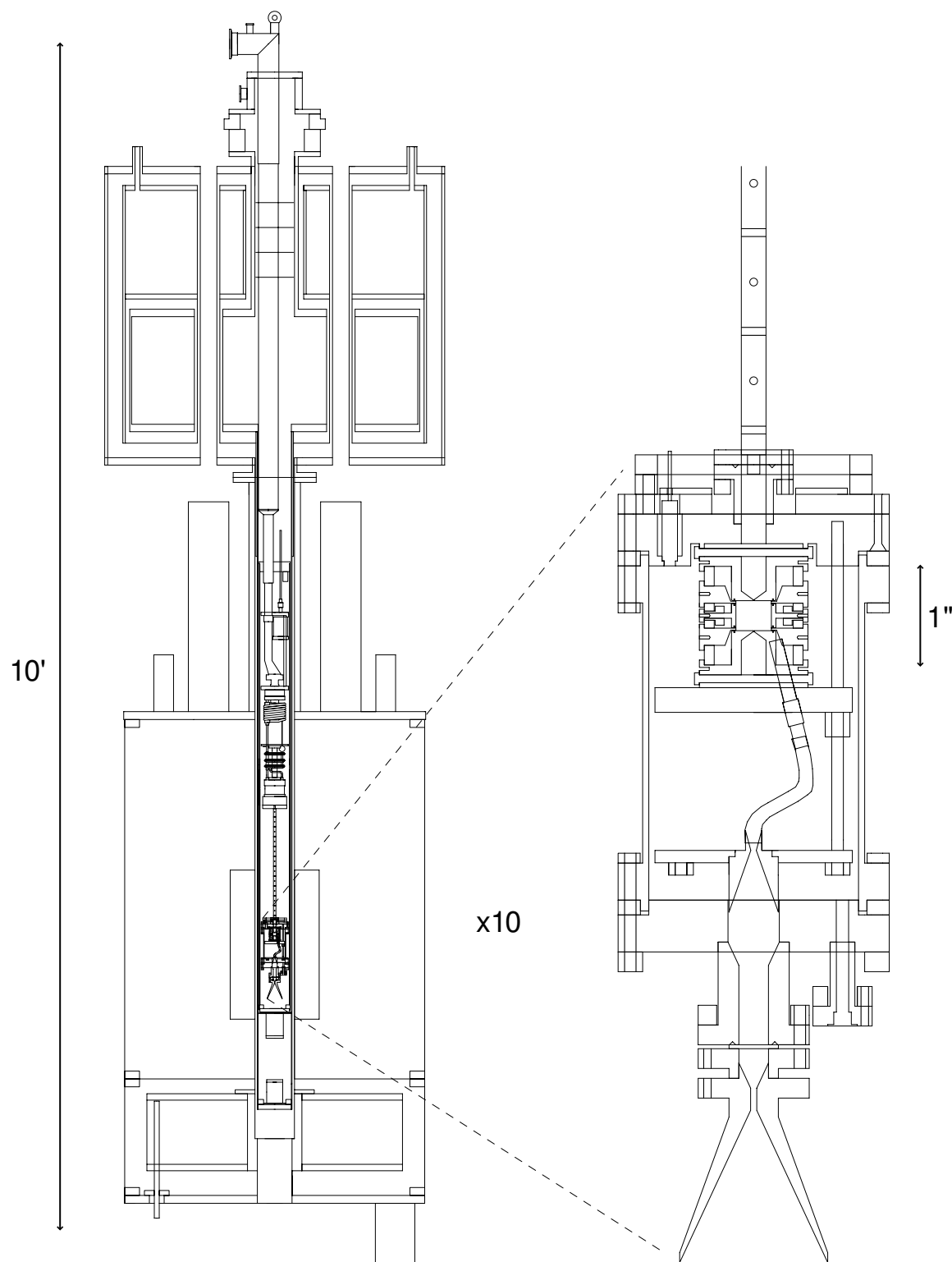


Figure 2.2: Dilution refrigerator apparatus with expanded view of trap.

resonances due to the finite axial thermal motion. Analysis of the measurement and the transition lineshapes is done in Chapter 3. We use a dilution refrigerator or feedback to cool the axial motion and decrease the broadening and shift of the cyclotron and anomaly lineshapes.

The combination of a long excited cyclotron state lifetime and cooling to the ground cyclotron state with a dilution refrigerator make it possible to measure the cyclotron frequency with quantum jump spectroscopy [14, 15], where the cyclotron frequency response is mapped out by driving transitions from the ground cyclotron state to the first excited cyclotron state. Utilizing only the lowest transition eliminates shifts due to special relativity at higher cyclotron states.

2.1.4 Microwave Source

In order to drive the cyclotron transition, we require a microwave source at the cyclotron frequency, 146 GHz (sometimes called millimeterwaves). We use a system designed to pull the cyclotron excitation to very high amplitudes, which requires ultra-low phase noise. Our phase noise requirements are likely much less stringent. The source starts with RF synthesizers and multiplies them up to the final frequency [26]. The last step in the chain multiplies the frequency by 13 with a GaAs Schottky-barrier diode and launches the microwaves out of a horn antenna.

Microwave Window

The microwaves are produced at room temperature and guided through a series of Teflon lenses into a collection horn at the bottom of the cryogenic trap vacuum

enclosure [15]. The microwaves are then guided into the trap by a waveguide. In order to get the microwaves into the innermost vacuum enclosure, a glass to metal seal was used. We recently replaced this seal with a sapphire window as shown in Figure 2.3. The thickness of the window was chosen to maximize microwave transmission at the

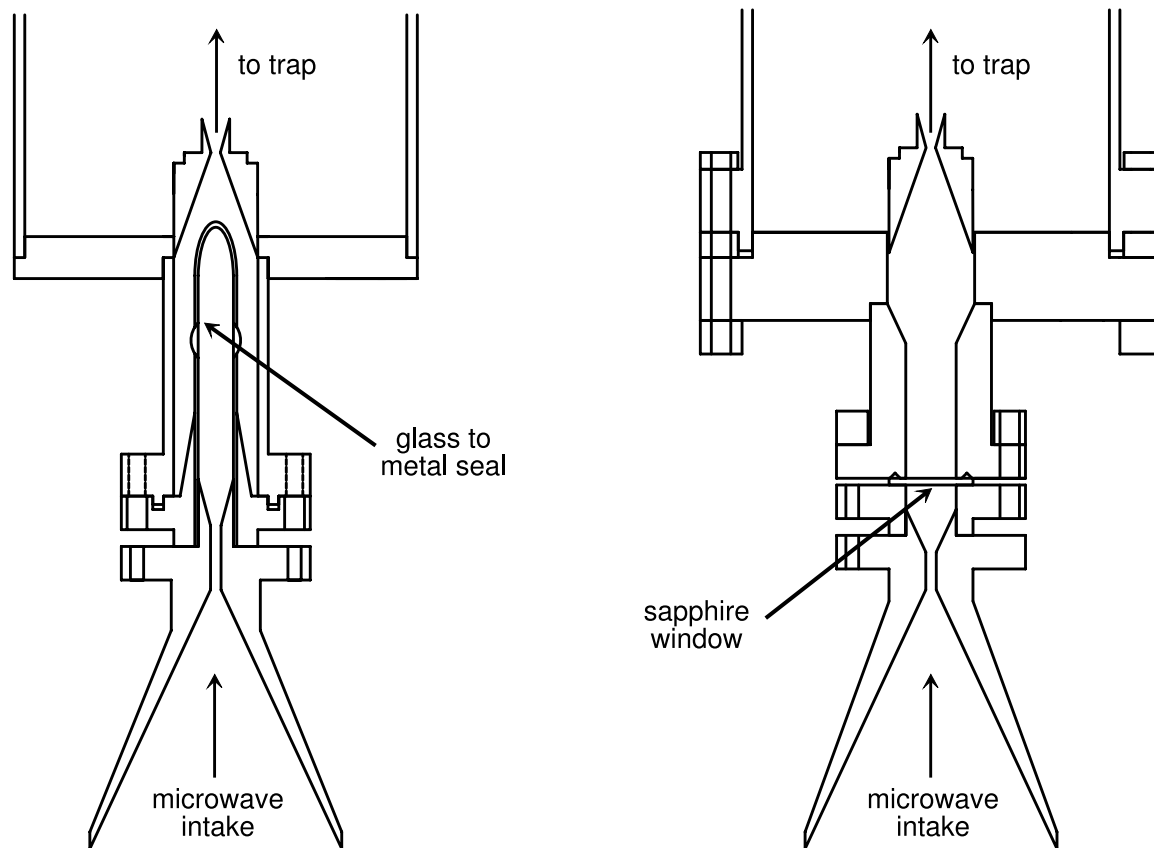


Figure 2.3: Glass (left) and sapphire (right) microwave window.

cyclotron frequency.

The new window is much wider and more smoothly integrated into the waveguide than the glass to metal seal, so more power is transmitted through into the trap. We estimate that there was a 10 dB increase in microwave power available in the trap due to this improvement. Unfortunately, it appears that the coupling is also good

enough to allow thermal radiation in from higher temperatures to reach the trapped electron, resulting in thermal cyclotron jumps around once per hour. We will likely have to add cold attenuation back in to decrease the rate of thermal jumps. A cold attenuator which can be moved in or out of the microwave path on demand could allow higher microwave power for axial-cyclotron sideband cooling while producing a tolerable thermal jump rate.

2.2 Axial Motion and Detection

The axial motion of the electron is the only motion of the electron that we can detect directly. All information about the cyclotron and spin states is coupled into the axial motion as shifts in the axial frequency. Thus, it is crucial to have a thorough understanding of the axial motion, the detection process, and the techniques for quickly measuring the axial frequency.

2.2.1 Anharmonicity

In a perfectly harmonic trap, the electron could be driven to an arbitrarily large amplitude (until it collides with an electrode) and the resulting electrical signal would be so large that it could be easily detected. However, in real traps the axial frequency depends on the oscillation amplitude. Even in hyperbolic electrode traps, the electrostatic potential well is not perfectly harmonic due to the truncation of the electrodes and imperfections in the electrodes. Thus, compensation electrodes are added which can be biased to tune out some of the anharmonicity [27, 20].

The equation of motion for a forced, damped harmonic oscillator is given by

$$m \left[\frac{d^2}{dt^2} + \gamma_z \frac{d}{dt} \right] z + q \frac{dV}{dz} = F_d(t), \quad (2.1)$$

where $F_d(t)$ is a driving force and $V(\vec{r})$ is the static potential in a Penning trap, commonly expressed as

$$V(\vec{r}) = \frac{V_0}{2d^2}(z^2 - \rho^2/2) + \frac{V_0}{2} \sum_k C_k \left(\frac{r}{d} \right)^k P_k(\cos \theta), \quad (2.2)$$

where ρ is the radial coordinate, d is a measurement of the size of the trap, and θ is the polar angle. We will take this to provide the definition of the coefficients C_k which describe the potential. In practice, there are two potentials applied to the trap: the trapping potential V_0 , and the compensation voltage V_c . Thus, a full expression for $V(\vec{r})$ is

$$V(\vec{r}) = \frac{V_0}{2d^2}(z^2 - \rho^2/2) + \frac{1}{2} \sum_k \left(V_0 C_k^{(0)} + V_c D_k \right) \left(\frac{r}{d} \right)^k P_k(\cos \theta) \quad (2.3)$$

where $C_k^{(0)}$ and D_k are properties of the geometry of the trap, and do not depend on the potentials applied. Comparing Eqs. (2.2) and (2.3) we can see the following relationship holds between these trap parameters:

$$C_k = C_k^{(0)} + \frac{V_c}{V_0} D_k. \quad (2.4)$$

We assume that the electron's magnetron radius is cooled to a value that is small and constant enough that we can take $\rho = 0$. Then we have

$$V(\rho=0) = \frac{V_0}{2} \left(\frac{z}{d} \right)^2 + \frac{V_0}{2} \sum_k C_k \left(\frac{z}{d} \right)^k. \quad (2.5)$$

We next assume the trap is symmetric under $z \rightarrow -z$, so that all uneven powers are discarded. We can now express the axial force as

$$\begin{aligned}
 -q \frac{dV}{dz} &= -q \left. \frac{\partial V}{\partial z} \right|_{\rho=0} \\
 &= \frac{qV_0}{d^2} \left[1 + \sum_{k \text{ even}} \frac{kC_k}{2} \left(\frac{z}{d} \right)^{k-2} \right] z \\
 &= \frac{qV_0}{d^2} \left[1 + C_2 + 2C_4 \left(\frac{z}{d} \right)^2 + 3C_6 \left(\frac{z}{d} \right)^4 + \dots \right] z \\
 &= m\omega_z^2 \left[1 + \frac{2C_4}{1+C_2} \left(\frac{z}{d} \right)^2 + \frac{3C_6}{1+C_2} \left(\frac{z}{d} \right)^4 + \dots \right] z, \tag{2.6}
 \end{aligned}$$

where

$$\omega_z^2 = \frac{qV_0}{md^2} (1 + C_2). \tag{2.7}$$

The equation for the axial motion of a driven electron in a Penning trap is then given by

$$m \left\{ \frac{d^2}{dt^2} + \gamma_z \frac{d}{dt} + \omega_z^2 \left[1 + \frac{2C_4}{1+C_2} \left(\frac{z}{d} \right)^2 + \frac{3C_6}{1+C_2} \left(\frac{z}{d} \right)^4 + \dots \right] \right\} z = F_d(t). \tag{2.8}$$

Since the potential is anharmonic, the particle's motion will in general involve many overtones of the fundamental motion. However, since the anharmonicities are typically small and any overtones would not be significant in detection or feedback, we will neglect them.

We seek a steady state solution which is a simple harmonic oscillation with some frequency ω and phase ψ ,

$$z(t) = A \cos(\omega t + \psi). \tag{2.9}$$

The equation of motion contains terms proportional to z^3 and z^5 . By neglecting the overtones, these can be expressed linearly in z and only nonlinearly in the amplitude

of oscillation A ,

$$z^3 = A^3 \cos(\omega t + \psi) \cos^2(\omega t + \psi) = A^3 \cos(\omega t + \psi) \left[\frac{1}{2} + \frac{1}{2} \cos(2\omega t + 2\psi) \right] \quad (2.10)$$

$$= \frac{A^2}{2} z + \frac{A^3}{4} [\cos(\omega t + \psi) + \cos(3\omega t + 3\psi)] = \frac{3}{4} A^2 z + \text{overtone}, \quad (2.11)$$

and similarly

$$z^5 = z^3 z^2 = \frac{3}{4} A^2 z^3 + \frac{A^5}{4} \cos(3\omega t + 3\psi) \left[\frac{1}{2} + \frac{1}{2} \cos(2\omega t + 2\psi) \right] = \frac{5}{8} A^4 z + \text{overtones}. \quad (2.12)$$

Neglecting higher order anharmonicities, we have approximately

$$m \left\{ \frac{d^2}{dt^2} + \gamma_z \frac{d}{dt} + \omega_z^2 \left[1 + \frac{3C_4}{2(1+C_2)} \left(\frac{A}{d} \right)^2 + \frac{15C_6}{8(1+C_2)} \left(\frac{A}{d} \right)^4 \right] \right\} z = F_d(t). \quad (2.13)$$

The equation of motion is thus simply a harmonic oscillator, with the amplitude-dependent frequency

$$\bar{\omega}_z(A) = \omega_z \sqrt{1 + \frac{3C_4}{2(1+C_2)} \left(\frac{A}{d} \right)^2 + \frac{15C_6}{8(1+C_2)} \left(\frac{A}{d} \right)^4}. \quad (2.14)$$

Typically $|C_6/(1+C_2)| < 1$ and the trap is tuned so that $|C_4/(1+C_2)| \ll 1$, while $A/d \ll 1$. That is, the electron has an amplitude which is small compared to the trap size. Thus we may perform a Taylor expansion on the square root,

$$\bar{\omega}_z(A) = \omega_z \left[1 + \frac{3C_4}{4(1+C_2)} \left(\frac{A}{d} \right)^2 + \frac{15C_6}{16(1+C_2)} \left(\frac{A}{d} \right)^4 \right]. \quad (2.15)$$

From now on we will refer to the amplitude dependent frequency $\bar{\omega}_z(A)$ as simply $\omega_z(A)$.

Inserting the amplitude dependent frequency into the axial equation of motion, Eq. (2.1), we get the anharmonic axial equation of motion which will be our starting point for many calculations,

$$\frac{d^2 z}{dt^2} + \gamma_z \frac{dz}{dt} + [\omega_z(A)]^2 z = \frac{1}{m} F_d(t). \quad (2.16)$$

2.2.2 Damping and Detection

The axial motion of the electron induces a current in nearby electrodes due to the image charge in the electrodes. This current is the source of the axial signal used for detection, and the axial damping rate γ_z is a consequence of the current passing through some resistance for detection. This method can be used to continuously detect the axial oscillation of a single electron [19].

The tuned circuit amplifier for detection and damping of the axial motion is shown in Figure 2.4. An inductor is placed in parallel with the trap to tune out the parasitic

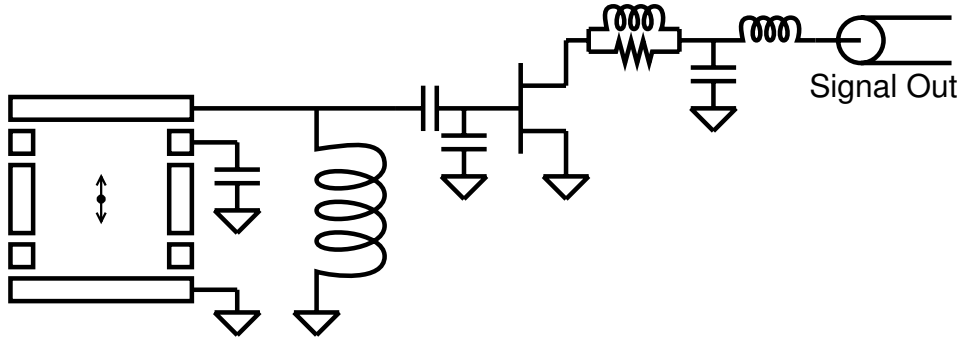


Figure 2.4: Simplified axial detection schematic.

capacitance of the trap electrodes and amplifier. This tuned circuit behaves as a high resistive impedance on resonance. The voltage from the detected current passing through this resistor is amplified by the cryogenic amplifier to become the detected signal.

The current I from the axial motion of the electron is given by

$$I = \frac{e\kappa}{2z_0} \dot{z}, \quad (2.17)$$

where \dot{z} is the instantaneous axial velocity of the electron, z_0 is half of the distance

between the endcap electrodes in the \hat{z} direction and κ is a constant of order one that characterizes the trap [12]. In our trap $\kappa = 0.79$.

For detection, the current is passed through an effective resistance R which extracts energy from the axial motion, resulting in an axial damping rate γ_z , given by

$$\gamma_z = \left(\frac{e\kappa}{2z_0} \right)^2 \frac{R}{m}. \quad (2.18)$$

Typically, the damping rate $\gamma_z/2\pi$ is 2 to 8 Hz for a single electron in our trap, depending on the the value of the damping resistance R . While we generally try to maximize the damping by maximizing R , the value obtained depends upon the axial frequency chosen for detection.

Equivalent Circuit Description

The tuned circuit used for detection of the axial motion can be modeled as a capacitor C , and inductor L and a resistance R in parallel. Without a trapped electron, the thermal Johnson noise from the resistor R drives the tuned circuit and results in a detected “noise resonance” of the amplifier, as shown in Figure 2.5. The tuned circuit is characterized by its Q which can be easily measured from the width of the noise resonance. The parallel resistance R of the tuned circuit can be determined from the Q and trap capacitance with the relationship

$$R = \frac{Q}{\omega_z C}. \quad (2.19)$$

The resistance R is important because it determines the axial damping rate and the magnitude of the detected signal. The tuned circuit Q is generally made as high as possible to maximize the damping rate and the detected signal amplitude.

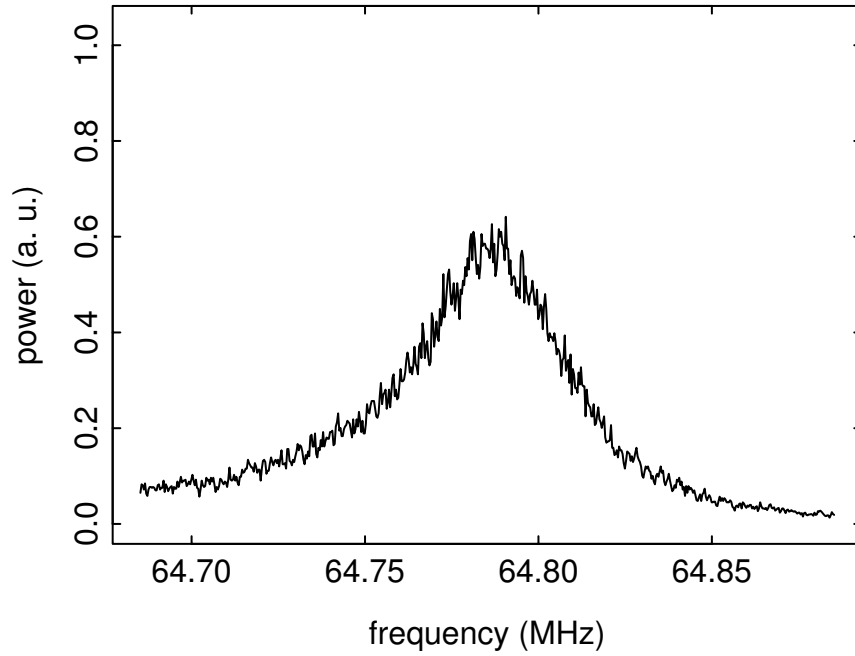


Figure 2.5: Amplifier noise resonance.

The one electron axial oscillator can be represented electrically by an equivalent series LC circuit [19, 28] with capacitance c and inductance l given by

$$l = m \left(\frac{2z_0}{e\kappa} \right)^2 \approx 3360 \text{ H} \quad (2.20)$$

$$c = \frac{1}{l\omega_z^2} \approx 1.8 \times 10^{-21} \text{ F}, \quad (2.21)$$

where the values are typical for our trap with $\nu_z = 64$ MHz. With the axial frequency ω_z adjusted to be near the center of the amplifier tuned circuit, the particle and amplifier can be represented by a simple equivalent circuit near the axial frequency, as shown in Figure 2.6. The remaining details of the tuned circuit can be neglected because the single electron axial resonance is much narrower than that of the detection tuned circuit.

With the help of the series LC equivalent circuit description, it is easy to see

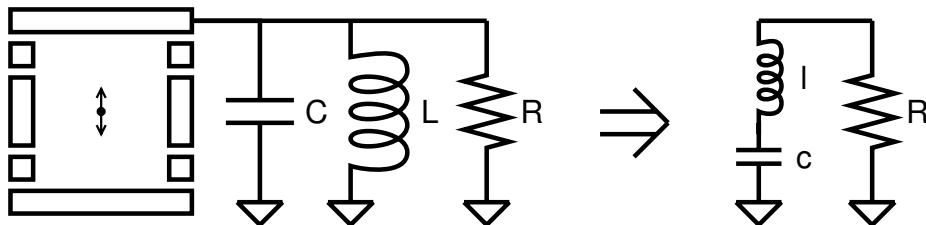


Figure 2.6: Equivalent particle and detector circuit near the axial frequency.

the origin of the “dip” visible in the amplifier noise resonance at the particle axial frequency: the particle series LC shorts out the noise on resonance. The FWHM of the dip in the noise power spectrum is γ_z [28]. This gives a simple way to measure the axial damping rate, which we use in Chapter 5.

Eliminating Feedthrough

Since the axial motion of the trapped electron acts like a simple harmonic oscillator at low amplitudes, it can be driven to get a larger signal for detection. Experimentally, the particle is driven by applying an oscillating potential to one of the trap electrodes. Unfortunately, the drive also capacitively couples directly to the amplifier, resulting in “feedthrough” of the drive which may completely overwhelm the signal from the particle response.

One solution is to drive the particle at two frequencies [19], typically 5 MHz and near $\nu - 5$ MHz, where ν is near ν_z . The particle mixes the two drives together and the response is amplified. By keeping track of the phase, the response can be separated out into two components as shown in Figure 2.7. For final detection, the signal is filtered and mixed with the $\nu - 5$ MHz drive used as a local oscillator (LO), and the resulting 5 MHz signal is filtered again. The signal then may be mixed down

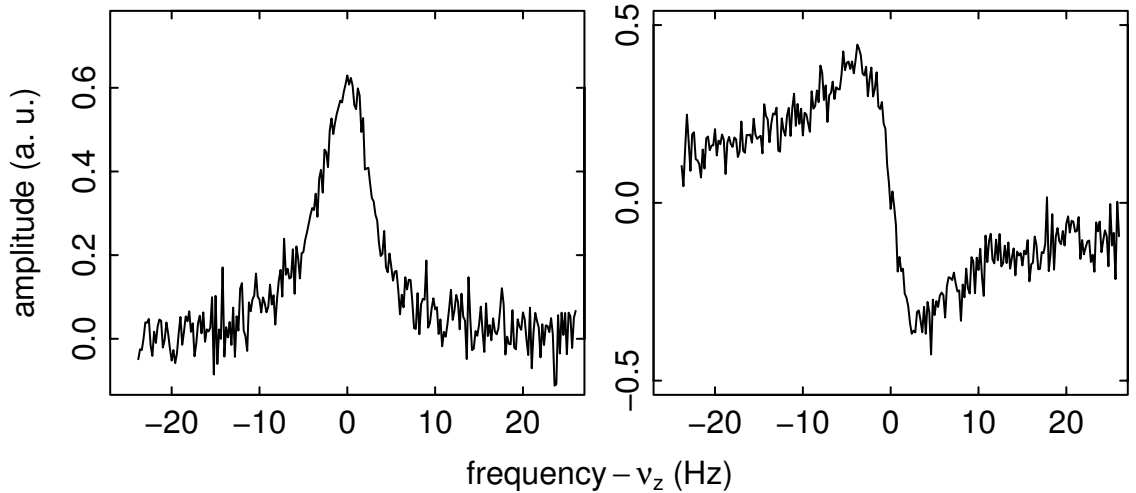


Figure 2.7: Driven axial response of a single electron showing both the absorptive (left) and dispersive (right) responses.

again or measured with a lock-in amplifier. The drive feedthrough is typically much less than with a direct drive at ν , but nonlinearities in the amplifier may result in some residual feedthrough.

Another approach to eliminating feedthrough is to add a second drive at the same frequency as the direct drive which also couples into the amplifier and (optionally) the particle. Then the phase and amplitude of the second drive can be adjusted to cancel out the coupling to the amplifier [19]. As long as the second drive is in a different location from the first drive, the drives will typically not cancel out from the point of view of the electron. We use this approach to eliminate feedthrough in feedback cooling in Chapter 5 and in self-excitation in Chapter 6.

Parametric Excitation

A different excitation method which completely avoids the problems with feedthrough is parametric excitation, where a drive near $2\nu_z$ modulates the trapping

potential to excite the axial oscillation [19]. However, the response of the particle is quite different than with simple resonant excitation, as shown in Figure 2.8. Despite

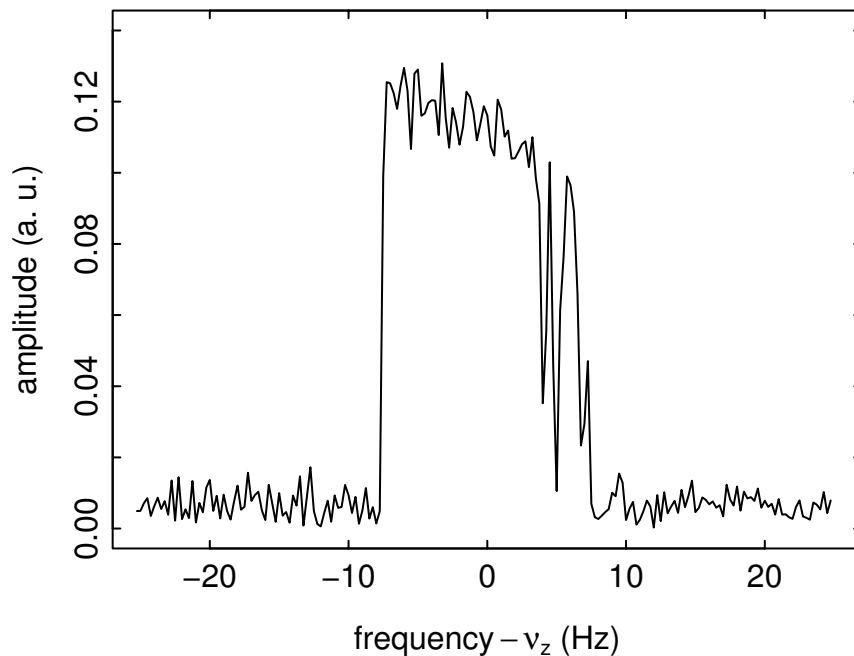


Figure 2.8: Parametrically driven axial response with the drive sweeping down in frequency.

the unusual response, parametric excitation can be used for detection in some forms. One technique involves using the hysteresis in the parametric excitation as a one bit parametric memory [29].

We choose not to use parametric excitation because for our purpose we need a sharp, reproducible feature in the response. We focus on measuring small shifts in the axial frequency which indicate cyclotron or spin state changes, so direct axial excitation is more appropriate.

2.2.3 Comparison of Axial Frequency Monitoring Techniques

Since detection of the cyclotron and spin states is done by measuring the axial frequency, it is important to have a robust method for monitoring that frequency. If there were no time constraint, the axial frequency could be determined by scanning a drive across the axial resonance and measuring the result as in Figure 2.7.

In practice, we only have about 1 second to determine the axial frequency, but we need about 1 second to get the amplitude and phase of the response at a single frequency. There is not nearly enough time to complete a scan over the resonance. The anharmonicity of the axial motion limits the amplitude that the oscillation can be driven to with a fixed drive frequency and also adds hysteresis to the response, further complicating detection.

The axial drives must be turned off when attempting to excite the cyclotron or anomaly transition and then turned on again to detect the result, since a large axial excitation would shift and broaden the cyclotron and anomaly lineshapes. It must be possible to repeat this process many times, monitoring the axial frequency for many hours without losing track of it. In addition to detecting jumps in the axial frequency due to state transitions, the signal is used to detect small changes in the frequency in order to make corrections to the trapping potential needed to maintain a constant axial frequency in the absence of cyclotron or spin state changes.

Since the magnetic bottle that couples the cyclotron and spin state to the axial frequency also broadens the cyclotron and anomaly transitions, it is beneficial to the $g-2$ measurement to minimize the size of the magnetic bottle. However, this decreases the size of the axial frequency shifts and makes determining the axial frequency

accurately enough to detect jumps even more difficult.

Locking the Axial Frequency

One method of finding the axial frequency is to track the zero crossing of the dispersive driven response and lock it to a known frequency by adjusting the trapping potential. A simple schematic diagram for the detection system is shown in Figure 2.9. The voltage needed to keep the axial frequency constant is recorded and analyzed

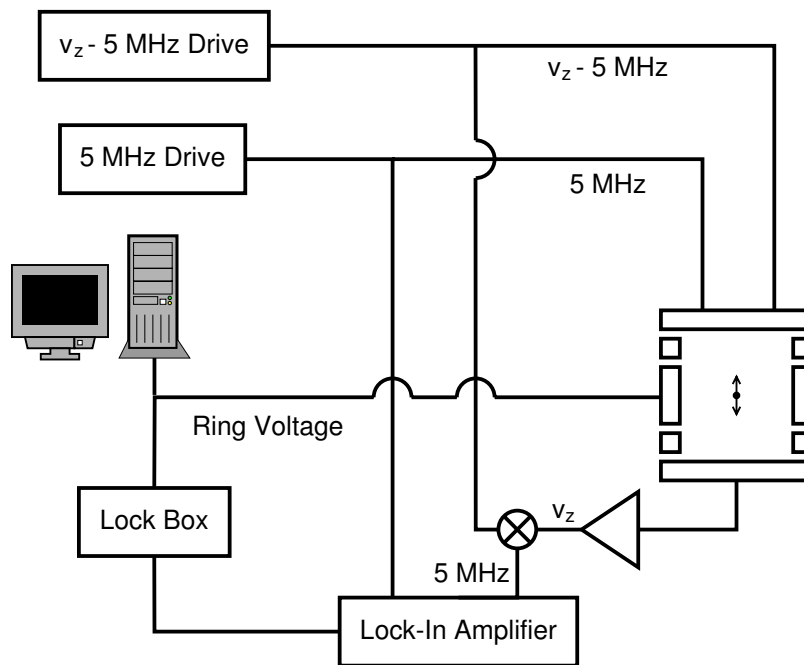


Figure 2.9: Simplified detection schematic diagram for tracking the zero crossing of the dispersive axial response.

for jumps. This method was used for the first quantum jump spectroscopy of the cyclotron motion [14, 15], but it has several problems. The locking method works well when the axial frequency is changing slowly or not at all, but it is inadequate when there is a large jump in the axial frequency. The response time can be improved

by increasing the gain in the lock, but if the lock is too aggressive there is a risk of losing it the lock by pushing the axial frequency too far away.

Three Drive Detection

A more rapid technique requires the application of three axial drives to the particle simultaneously, as illustrated in Figure 2.10. The drive frequencies are chosen to align

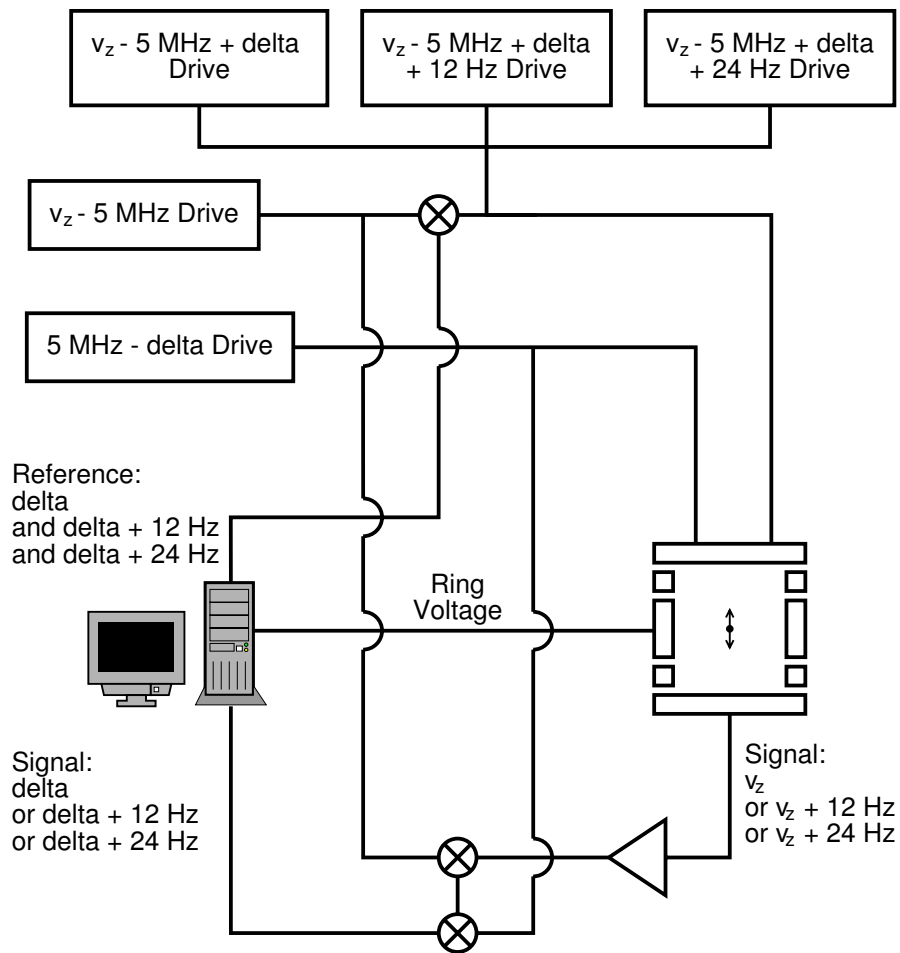


Figure 2.10: Simplified multiple drive detection schematic diagram.

with the center of the axial response in three different cyclotron or spin states. The

phase sensitive response of the particle at each of the three drive frequencies is used to measure the state of the particle and to determine whether the trapping potential should be adjusted.

We had great success with this method, particularly when detecting large frequency jumps with a large magnetic bottle. However, there is a problem with trying to scale it down to detect jumps when using a smaller bottle. The problem is that the axial anharmonicity causes a nonlinear response if the drives are too close in frequency. The particle interacts with all three drives, but does not respond as if there are three separate drives. Instead, the responses mix together making it difficult to determine the center axial frequency.

Self-Excited Oscillator

If the detected axial signal is fed back to the particle as an axial drive with the correct amplitude and phase, then the particle should drive itself into oscillation. This technique has several advantages. The self-excited oscillator tracks frequency changes almost instantaneously, limited only by the bandwidth of the feedback loop. The normally metastable anharmonic response is stabilized by self-excitation. As the oscillation amplitude increases, the anharmonicity causes the oscillation frequency to shift, but the frequency of the oscillation-produced drive shifts with it.

However, it is not clear that self-excitation is practical in a system where there is so much noise. Even more problematic is the difficulty of controlling the amplitude of self-excitation, which grows or shrinks exponentially in time if the gain of the feedback is not exactly right. We will study the use of self-excitation to measure the

axial frequency in Chapter 6.

2.3 DC Trap Biasing

The wiring of DC voltages for the trap and amplifiers is carefully designed to avoid grounding and noise problems that could blur out the narrow single electron axial resonance. A schematic of the trap and amplifier wiring is shown in Figure 2.11. A twisted wire pair is run for each DC voltage required with the low wire connecting to a point (the pinbase) defined to be ground at the trap. All voltage supplies for the trap and amplifiers are floating. This insures that all supplies are referenced to the same ground, the pinbase, and that currents from one supply do not shift the voltage that another supply produces on the trap.

Each DC line, high and low, is filtered though LC low-pass filters to eliminate high frequency noise which could heat up the axial motion. Additional RC filters are placed on lines which do not draw considerable current. The ring voltage, the most critical voltage for axial frequency stability, is handled specially.

2.3.1 Ring Voltage Supply

In an orthogonalized Penning trap, the axial frequency depends weakly on the compensation electrode voltage, but it depends strongly on the ring to endcap electrode potential difference. Typically we operate the experiment with the endcap electrodes grounded, so that the only non-zero critical voltage is the one on the ring electrode.

In order to avoid blurring out the axial response, the ring electrode voltage must

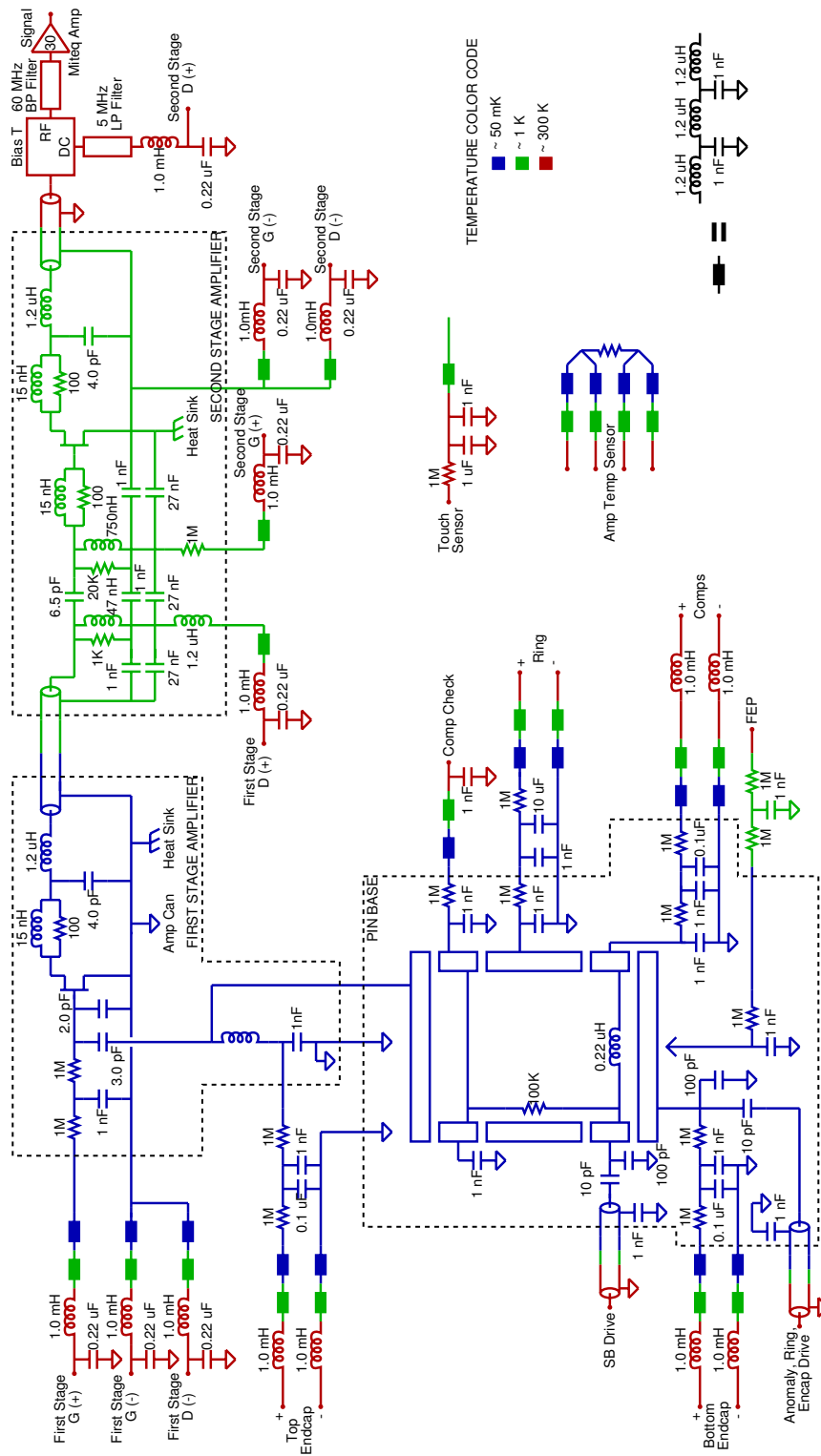


Figure 2.11: Details of trap wiring. Values without units are resistances in ohms.

be very stable. With $\nu_z \approx 64$ MHz, the axial response is about 5 Hz wide, so the ring voltage must be stable to $\sim 1 \mu\text{V}$ out of ~ 10 V. With $\nu_z \approx 200$ MHz the requirement is even more stringent: it must be stable to $\sim 1 \mu\text{V}$ out of ~ 100 V since the axial response is less than 2 Hz wide.

Previous Penning trap experiments used a battery of temperature regulated standard cells or a slowly discharging capacitor [14, 15] to produce the ring voltage. However, these have disadvantages in flexibility or stability.

We produce a stable voltage with a Fluke 5720A voltage calibrator which is heavily filtered as in Figure 2.12. The $101 \text{ M}\Omega$ resistance and $10 \mu\text{F}$ capacitor form a low pass

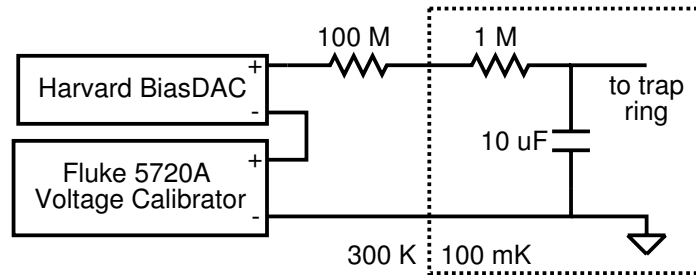


Figure 2.12: Simplified schematic diagram of the ring voltage supply.

filter with a time constant longer than 15 minutes. The $100 \text{ M}\Omega$ resistor is at room temperature and can be bypassed for the initial charging of the capacitor or if a large voltage change is desired. All electronics closer to the trap than the $100 \text{ M}\Omega$ must have very low leakage resistance to ground to avoid the formation of a voltage divider. The cryogenic environment stabilizes the $10 \mu\text{F}$ capacitor and greatly improves its leakage resistance.

While the long time constant of the RC filter makes the short term stability of the ring voltage dependent on the capacitor, the long term stability depends on the

Fluke voltage calibrator. Since its stability is not adequate, the voltage must be regularly corrected to hold the axial frequency constant. The corrections take place in two steps. First, the BiasDAC stacked on the Fluke supply (which usually produces 0 V) produces a voltage pulse 50 ms long with variable amplitude to push a pulse of charge through the 100 M Ω resistor, changing the voltage on the capacitor. Second, the Fluke voltage supply is updated to match the new voltage on the capacitor. In this way, quick but small voltage corrections can be made which leave the system in equilibrium. In practice, a voltage correction is made after each observation of the cyclotron and spin state, about once per second, in order to hold the axial frequency constant.

2.3.2 Loading and Dumping

Rather than inverting the voltage on the 10 μ F capacitor to dump particles out of the trap, we leave the ring voltage stable and raise the endcap electrode potentials to clear the trap. Then, they can just be grounded again to return to a stable trapping configuration before the field emission point is fired to load one or more electrons. This dumping and loading procedure results in a more stable ring potential and more consistent axial potential because it avoids the hysteresis in the capacitor when discharging and recharging. Capacitors may have significant hysteresis at the voltage level we are concerned with due to a phenomenon often called “dielectric absorption” or “dielectric soakage”.

2.3.3 Changing the Axial Frequency

While traditionally a trapping potential around 10 V and an axial frequency of about 64 MHz have been used in our experiment, this choice of frequency was based more on convenience than merit for the $g - 2$ measurement. With the flexible ring voltage supply we have developed, we are not restricted to voltages that are accessible with a small number of standard cells. Instead, we can optimize the choice of axial frequency for the $g - 2$ measurement. Here we examine the scaling of several relevant quantities with respect to the axial frequency.

The axial frequency shift δ_c due to a cyclotron transition is (see Eq. (3.18))

$$\delta_c = \frac{e\hbar}{m\omega_z} B_2 \propto \frac{1}{\omega_z}. \quad (2.22)$$

That is, the effective bottle coupling gets weaker as the axial frequency is increased. By itself, this makes cyclotron and spin transitions more difficult to detect.

To find the cyclotron linewidth $\Delta\omega_c$, we need the average axial state $\bar{n}_z \sim \frac{kT_z}{\hbar\omega_z}$ to find

$$\Delta\omega_c \sim \bar{n}_z \delta_c \propto \frac{1}{\omega_z^2} \quad (2.23)$$

(See Chapter 3 for more information). That is, the lineshapes get narrower with increasing axial frequency. A comparison of Eqs. (2.22) and (2.23) shows the advantage of increasing the axial frequency. The bottle coupling gets weaker but the cyclotron lineshape narrows more than it would by directly decreasing the coupling with a smaller magnetic bottle. Simply making the bottle smaller would give the same proportional decrease in δ_c and $\Delta\omega_c$.

Although the above results look promising, we still must be able to detect the axial motion. With a higher axial frequency, the stray capacitance of the trap presents a

lower impedance to the tiny current from the electron's axial oscillation, which could make detection more difficult at higher frequencies. The magnitude of the voltage signal produced by the axial motion of the particle V_z is

$$V_z = IR = \frac{e\kappa Q}{2z_0 C} \frac{\dot{z}}{\omega_z} \propto \text{constant}, \quad (2.24)$$

where we assume that the trap capacitance C and the amplifier Q are constant with respect to axial frequency. The trap capacitance C is independent of frequency, but the attainable Q may vary due to practical limitations of the amplifier, and must be determined experimentally.

In order to detect axial frequency shifts, the axial damping rate γ_z is also relevant. It is given by

$$\gamma_z = \left(\frac{e\kappa}{2z_0} \right)^2 \frac{R}{m} \propto \frac{1}{\omega_z}, \quad (2.25)$$

again assuming constant C and Q . So, as the axial frequency is increased, the axial signal strength should stay about the same but the axial linewidth should decrease, which makes detecting small frequency jumps easier. At the same time, the anharmonicity remains fractionally the same relative to the axial frequency. Combined with the decreasing linewidth with increasing axial frequency, the anharmonicity becomes much more severe with a higher axial frequency. This could make detection at higher axial frequencies more difficult.

The one remaining issue is how much power it takes to drive an anomaly transition, and how much this depends on the axial frequency. The anomaly transition can be driven by forcing the electron axially in the magnetic field gradient produced by the magnetic bottle at the transition frequency $\nu_a \approx 170$ MHz. If the axial frequency is near the anomaly frequency, it is much easier to drive the anomaly transition. Using

[15] Eq. (4.12) we see that the power required to drive a transition compared to the power required to drive a transition at $\nu_z = 0$ is

$$\frac{P(\omega_z)}{P(\omega_z = 0)} = \frac{(\omega_a^2 - \omega_z^2)^2 + \omega_a^2 \gamma_z^2}{\omega_a^4 + \omega_a^2 \gamma_z^2} \approx \left(1 - \frac{\omega_z^2}{\omega_a^2}\right)^2, \quad (2.26)$$

where the approximate result is valid as long as ω_z is not very close to ω_a . As expected, it is easier to drive the anomaly transition when the axial and anomaly transitions are close together. The power needed to drive the transition is plotted in Figure 2.13. The

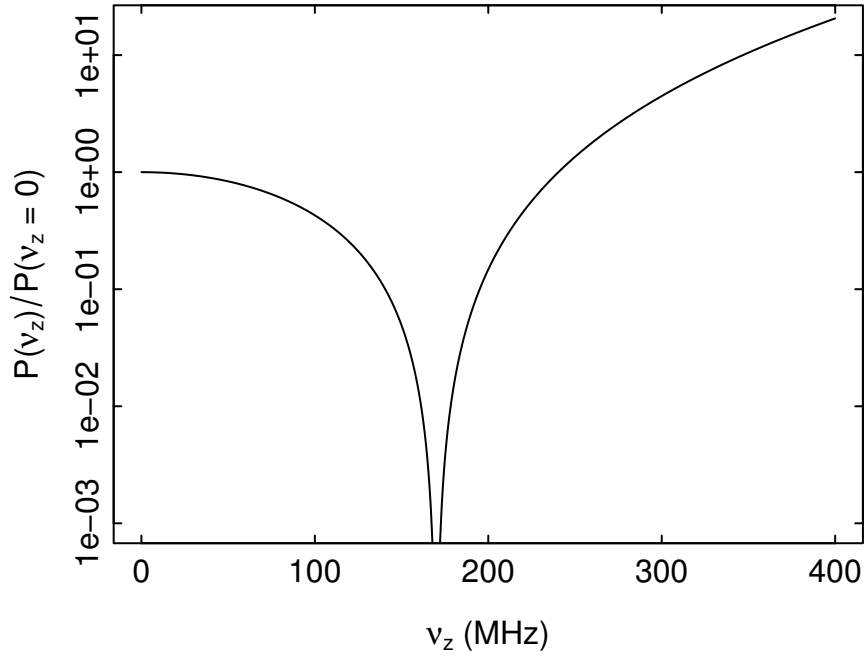


Figure 2.13: Normalized power required to drive the anomaly transition as a function of axial frequency.

power required to drive the anomaly transition is important because at high power there may be significant systematic error introduced into the $g - 2$ measurement. However, if the axial frequency is too close to the anomaly frequency, thermal axial motion or simply driving the axial motion for detection may cause accidental anomaly transitions.

When all scalings are considered, it appears that the optimal axial frequency is as high as possible to minimize the cyclotron linewidth without being so high as to make driving the anomaly transition excessively difficult. With the axial frequency above the anomaly frequency, there is a trade-off between anomaly power and cyclotron linewidth. We chose 200 MHz as our new axial frequency. It is expected to give a ~ 10 times narrower cyclotron linewidth while requiring 5 times less drive power to make an anomaly transition than at $\nu_z = 64$ MHz. We discuss the difficulties this presents for the cryogenic axial signal amplifiers in Chapter 4.

Chapter 3

Cyclotron and Anomaly

Lineshapes

In order to measure the cyclotron and spin state of an electron in our Penning trap, we use a magnetic “bottle” to shift the axial frequency depending on the magnetic moment of the particle [1]. The bottle field is a small quadratic variation in the axial magnetic field which is introduced with a nickel ring, so the total field $B(z)$ on the central axis of the trap is

$$B(z) = B + B_2 z^2, \quad (3.1)$$

where B is the magnitude of the homogeneous field and B_2 is the strength of the bottle. The interaction of the total magnetic moment of the particle and the bottle field causes a change in the restoring force of the axial oscillator, which is detected as a change in the axial oscillation frequency ω_z . Unfortunately, the thermal axial motion in the magnetic field gradient broadens and/or shifts the cyclotron and anomaly transition lineshapes.

This is an example of a quantum non-demolition (QND) measurement [30, 14] because the measurement Hamiltonian commutes with the cyclotron and spin Hamiltonians, which means that two measurements separated in time will yield the same result in the absence of other interactions. We calculate the lineshapes of the cyclotron and anomaly transitions treating the cyclotron, spin, and axial motions with quantum mechanics. The results qualitatively agree with those derived by Brown in a calculation treating the axial motion classically [31].

An understanding of the transition lineshapes requires calculation of the decay of coherences in the cyclotron and spin degrees of freedom, which also relates to the measurement time. Estimates of the measurement time of this system under some conditions have been made [24, 25, 32]. A more complete understanding of the lineshapes and the measurement process may allow more accurate measurement of the properties of the electron. In particular, we consider a correlated technique for determining the cyclotron and anomaly frequencies for a $g - 2$ measurement.

3.1 Overview of Calculations

We begin the calculation in Section 3.2, with the cyclotron motion as a harmonic oscillator, the spin as a two level system, and the axial motion as a harmonic oscillator. We write down the interaction Hamiltonian and write the time evolution of the system with the density matrix formalism.

Before proceeding with the calculation of the lineshape, we first examine the behavior of a simple two-level system in Section 3.3. A calculation shows that the lineshape in the weak drive limit is the real part of the Fourier transform of the

off-diagonal element of the density matrix.

Next, in Section 3.4, we simplify the cyclotron and spin states to a three level system. We retain only the off-diagonal element of the density matrix, and reduce the problem of finding the time evolution of the matrix element to finding the eigenvectors and eigenvalues of a matrix. We plot the lineshape that results in several specific cases by numerically diagonalizing the matrix with a truncated set of axial states.

In Section 3.4.2, we find a series solution for the lineshapes by taking the axial states to be a continuous rather than a discrete set. The solution we find is nearly identical to that of Brown [31]. We compare the results of the numerical solution with discrete axial states and the series solution with continuous axial states to illustrate when the approximation is valid.

Finally, in Section 3.5 and Section 3.6, we discuss a few other special cases where the lineshapes are of interest. We propose a correlated measurement technique which may have advantages in a high-precision $g - 2$ measurement.

3.2 Cyclotron and Anomaly Lineshapes

We begin with the axial and cyclotron states represented by independent harmonic oscillators and the spin in a magnetic field as a two level system. The eigenstates of the axial motion are labeled with quantum number $n_z = 0, 1, 2, \dots$ while the cyclotron levels are labeled by $n_c = 0, 1, 2, \dots$ and the spin levels are labeled \uparrow and \downarrow . The axial, cyclotron, and spin transition frequencies are ω_z , ω_c , and ω_s , respectively. We ignore anharmonicities in the axial and cyclotron motions. We will also ignore the small shifts that a trap makes to some of these frequencies.

The axial motion is coupled to a tuned circuit amplifier which detects, damps, and also heats the axial motion. Without any drives, the axial motion damps with rate γ_z and comes into equilibrium in a thermal state at temperature T_z . The cyclotron motion is damped at rate γ_c to equilibrium in the ground state.

We introduce a_z^\dagger , a_c^\dagger , a_s^\dagger , creation operators for the axial, cyclotron, and spin states and a_z , a_c , a_s , annihilation operators for the axial, cyclotron, and spin states respectively,

$$a_{z,c}^\dagger = \sum_{n_{z,c}=0}^{\infty} \sqrt{n_{z,c} + 1} |n_{z,c} + 1\rangle \langle n_{z,c}| \quad (3.2)$$

$$a_{z,c} = \sum_{n_{z,c}=0}^{\infty} \sqrt{n_{z,c} + 1} |n_{z,c}\rangle \langle n_{z,c} + 1| \quad (3.3)$$

$$a_s^\dagger = |\uparrow\rangle \langle \downarrow| \quad (3.4)$$

$$a_s = |\downarrow\rangle \langle \uparrow|. \quad (3.5)$$

Note that a_z^\dagger , a_z and a_c^\dagger , a_c , follow the familiar harmonic oscillator commutation relations but a_s^\dagger and a_s do not. We then have the usual Hamiltonian for each degree of freedom,

$$H_z = \hbar\omega_z \left(a_z^\dagger a_z + \frac{1}{2} \right) \quad (3.6)$$

$$H_c = \hbar\omega_c \left(a_c^\dagger a_c + \frac{1}{2} \right) \quad (3.7)$$

$$\begin{aligned} H_s &= \frac{1}{2} \hbar\omega_s (|\uparrow\rangle \langle \uparrow| - |\downarrow\rangle \langle \downarrow|) \\ &= \frac{1}{2} \hbar\omega_s (a_s^\dagger a_s - a_s a_s^\dagger) = \hbar\omega_s \left(a_s^\dagger a_s - \frac{1}{2} \right). \end{aligned} \quad (3.8)$$

The total Hamiltonian is

$$H = H_z + H_c + H_s + H_I, \quad (3.9)$$

where H_I is the interaction Hamiltonian that describes the effect of the magnetic bottle. The bottle creates a magnetic field gradient described by Eq. (3.1). The impact on the electron is that the measured cyclotron transition frequency ω'_c and spin flip frequency ω'_s depend on the spatial position z as

$$\omega'_c(z) = \omega_c + \beta_c z^2 \quad (3.10)$$

$$\omega'_s(z) = \omega_s + \beta_s z^2, \quad (3.11)$$

where $\beta_c = \frac{e}{m} B_2$ and $\beta_s = \frac{e}{m} \frac{g}{2} B_2$ are constants determined by the bottle strength. The interaction Hamiltonian is the change in $H_c + H_s$ when we replace ω_c with $\omega'_c(z)$ and ω_s with $\omega'_s(z)$,

$$H_I = \hbar z^2 \left[\beta_c \left(a_c^\dagger a_c + \frac{1}{2} \right) + \beta_s \left(a_s^\dagger a_s - \frac{1}{2} \right) \right]. \quad (3.12)$$

We next expand the operator z in creation and annihilation operators to get

$$z^2 = \frac{\hbar}{2m\omega_z} (a_z a_z + a_z^\dagger a_z^\dagger + 2a_z^\dagger a_z + 1). \quad (3.13)$$

We switch to the interaction picture to define new creation and annihilation operators,

$$\mathcal{A}_{z,c,s}^\dagger = a_{z,c,s}^\dagger e^{i\omega_{z,c,s}t} \quad (3.14)$$

$$\mathcal{A}_{z,c,s} = a_{z,c,s} e^{-i\omega_{z,c,s}t}. \quad (3.15)$$

Dropping rotating terms to get the Hamiltonian in the interaction picture,

$$\mathcal{H} = \left[\mathcal{A}_z^\dagger \mathcal{A}_z + \frac{1}{2} \right] \left[\hbar \delta_c \left(\mathcal{A}_c^\dagger \mathcal{A}_c + \frac{1}{2} \right) + \hbar \delta_s \left(\mathcal{A}_s^\dagger \mathcal{A}_s - \frac{1}{2} \right) \right], \quad (3.16)$$

where $\delta_c \equiv \frac{\hbar \beta_c}{m\omega_z}$, and $\delta_s \equiv \frac{\hbar \beta_s}{m\omega_z}$. In terms of the bottle strength B_2 , we have

$$\delta_c = \frac{e\hbar}{m\omega_z} B_2 \quad (3.17)$$

$$\delta_s = \frac{e\hbar}{m\omega_z} \frac{g}{2} B_2. \quad (3.18)$$

The δ_c and δ_s are nearly equal, and can be measured experimentally. The frequency δ_c is the magnitude of the shift in axial frequency due to a single cyclotron transition, while δ_s is the magnitude of the shift in axial frequency due to a single spin flip. With $\nu_z = 64$ MHz, we have $\delta_c = 2\pi(12 \text{ Hz})$, and with $\nu_z = 200$ MHz, we have $\delta_c = 2\pi(4 \text{ Hz})$.

Note that the measurement Hamiltonian H_I commutes with H_c and H_s , which is the formal requirement for a quantum non-demolition (QND) measurement. In a QND measurement, a series of measurements over time give the same result if there are no other interactions. Therefore, continuous measurement of the cyclotron and spin states is possible without changing the state in the process.

To study the time evolution of the system, we work with the density matrix ρ of the system, with the usual damping terms [33] added to represent the coupling of the axial motion to an amplifier for measuring the axial excitation and the coupling of the cyclotron motion to lossy cavity modes. The axial motion starts in a thermal state with a Boltzmann distribution which has reduced density matrix (that is, a trace over the reservoir states have been done),

$$\rho_z = \left(1 - e^{-\frac{\hbar\omega_z}{k_B T}}\right) \sum_{n=0}^{\infty} e^{-n\frac{\hbar\omega_z}{k_B T}} |n\rangle \langle n|. \quad (3.19)$$

We define $\bar{n}_z \equiv \left[\exp\left(\frac{\hbar\omega_z}{k_B T_z}\right) - 1\right]^{-1}$ as the average excitation of the axial motion at temperature T_z . The cyclotron motion also begins in a thermal state, but since $\hbar\omega_c \gg kT$, the cyclotron motion is in the ground state. Thus, we ignore the effects of finite temperature on the cyclotron motion. The time evolution of the density matrix is given by a master equation [33]

$$\begin{aligned}
\frac{d\rho}{dt} = & -\frac{i}{\hbar} [\mathcal{H}, \rho] - \frac{\gamma_z}{2} \bar{n}_z (\mathcal{A}_z \mathcal{A}_z^\dagger \rho - 2\mathcal{A}_z^\dagger \rho \mathcal{A}_z + \rho \mathcal{A}_z \mathcal{A}_z^\dagger) \\
& - \frac{\gamma_z}{2} (\bar{n}_z + 1) (\mathcal{A}_z^\dagger \mathcal{A}_z \rho - 2\mathcal{A}_z \rho \mathcal{A}_z^\dagger + \rho \mathcal{A}_z^\dagger \mathcal{A}_z) \\
& - \frac{\gamma_c}{2} (\mathcal{A}_c^\dagger \mathcal{A}_c \rho - 2\mathcal{A}_c \rho \mathcal{A}_c^\dagger + \rho \mathcal{A}_c^\dagger \mathcal{A}_c), \tag{3.20}
\end{aligned}$$

where γ_z is the classical damping rate of the axial oscillator by the resistor, and γ_c is the damping rate of the cyclotron motion into the cavity modes. Note that the damping terms for the cyclotron motion are simpler than those for the axial motion because the equilibrium cyclotron state $\bar{n}_c = 0$.

3.3 Weak Drive Quantum Jump Spectroscopy

Experimentally, we determine the lineshape by measuring the probability of a transition due to a drive at each of many frequencies. We need to connect this measurement with the time evolution of the density matrix. Instead of trying to handle the full system immediately, we first look at the driven response of a model two level system, driven for a long time by a very weak drive. The drive time must be long compared to the inverse linewidth, but the transition probability in the end must be small. With this model, we can treat the drive as a perturbation, so it does not need to be explicitly included in the calculation from the start.

Consider a two level system with ground state $|a\rangle$ and excited state $|b\rangle$. The drive Hamiltonian H_D is

$$H_D = \hbar A (|a\rangle \langle b| e^{i\omega t} + |b\rangle \langle a| e^{-i\omega t}), \tag{3.21}$$

where the rotating wave approximation has already been taken for the drive. The

density matrix ρ is given by

$$\rho = \begin{pmatrix} \rho_{aa} & \rho_{ab} \\ \rho_{ba} & \rho_{bb} \end{pmatrix}. \quad (3.22)$$

We take the usual time evolution of the density matrix for the drive and add damping phenomenological terms with rate γ to account for spontaneous decay. The parameter $\lambda = -\gamma' + i\omega_0$, where the energy separation between states $|a\rangle$ and $|b\rangle$ is $\hbar\omega_0$, and γ' is another damping rate. The γ' includes the damping from spontaneous decay γ , and possibly additional decoherence which we will require later. So, without the drive $\rho_{ba}(t) = \rho_{ba}(0)e^{\lambda t}$. We then have the following equation for the time evolution of the whole density matrix:

$$\frac{d\rho}{dt} = -\frac{i}{\hbar}[H_D, \rho] + \begin{pmatrix} \gamma\rho_{bb} & \lambda^*\rho_{ab} \\ \lambda\rho_{ba} & -\gamma\rho_{bb} \end{pmatrix}. \quad (3.23)$$

This gives an equation for each element of the density matrix,

$$\dot{\rho}_{aa} = iA(\rho_{ba}e^{i\omega t} - \rho_{ab}e^{-i\omega t}) + \gamma\rho_{bb} \quad (3.24)$$

$$\dot{\rho}_{ab} = iA(\rho_{bb} - \rho_{aa})e^{i\omega t} + \lambda^*\rho_{ab} \quad (3.25)$$

$$\dot{\rho}_{ba} = iA(\rho_{aa} - \rho_{bb})e^{-i\omega t} + \lambda\rho_{ba} \quad (3.26)$$

$$\dot{\rho}_{bb} = iA(\rho_{ab}e^{-i\omega t} - \rho_{ba}e^{i\omega t}) - \gamma\rho_{bb}, \quad (3.27)$$

where the dot represents a time derivative. We assume the drive is weak but applied for a long time, so ρ_{aa} does not change significantly and ρ_{bb} is always small. Then, we only need to retain two equations because $\rho_{ab} = \rho_{ba}^*$ and we can take $\rho_{bb} = 0$,

$$\dot{\rho}_{ba} = iA\rho_{aa}e^{-i\omega t} + \lambda\rho_{ba} \quad (3.28)$$

$$\dot{\rho}_{bb} = -2A \text{Im}(\rho_{ba}e^{i\omega t}), \quad (3.29)$$

So, the damping γ is not important with a small transition probability, although this damping must still be reflected in the constant λ . We look for an equilibrium solution, $\rho_{ba} = p_{ba}e^{-i\omega t}$, with p_{ba} constant, assuming that ρ_{ab} comes into equilibrium in a time short compared to the drive time so the transient is not important. Then

$$-i\omega p_{ba} = iA\rho_{aa} + \lambda p_{ba} \quad (3.30)$$

$$\dot{\rho}_{bb} = -2A \operatorname{Im}(p_{ba}), \quad (3.31)$$

which can be solved to give the steady state

$$p_{ba} = \frac{iA\rho_{aa}}{\lambda - i\omega} \quad (3.32)$$

With this solution for ρ_{ba} , it is straightforward to find the transition rate to the excited state,

$$\dot{\rho}_{bb} = 2A^2 \operatorname{Re} \left(\frac{-\rho_{aa}}{\lambda - i\omega} \right) = \frac{2A^2 \rho_{aa} \gamma'}{\gamma'^2 + (\omega - \omega_0)^2}, \quad (3.33)$$

This is a Lorentzian response in frequency as expected, with center frequency and width determined by λ . We could have obtained this result by taking the Fourier transform of the off-diagonal element of the density matrix (or more generally the Fourier transform of the first order temporal coherence function [34]), a result known as the linear response approximation. We used an extended derivation to demonstrate the origin of the quantum jump spectroscopy lineshape. We will return to this result to find the lineshapes for the cyclotron and anomaly transitions.

3.4 Simplified Model

In practice, the system we have presented thus far is more complex than necessary. Experimentally, the cyclotron frequency spectrum can be measured using only

transitions between the ground state ($n_c = 0$) and first excited state ($n_c = 1$). So, we can make a significant simplification and only include the $n_c = 0$ and $n_c = 1$ states in the calculation. This truncation is made even more reasonable by the fact that the cyclotron motion is slightly anharmonic. There is a relativistic shift that causes the transition frequency to change approximately 1 part per billion for each increment of n_c . The anharmonicity may make the higher cyclotron states even less relevant experimentally.

With this restricted set of states, we can write down the density matrix in a simplified form. First, we relabel the cyclotron and spin states as

$$|0, \downarrow\rangle \rightarrow |a\rangle \quad (3.34)$$

$$|1, \downarrow\rangle \rightarrow |b\rangle \quad (3.35)$$

$$|0, \uparrow\rangle \rightarrow |c\rangle. \quad (3.36)$$

The relabeling of states is also illustrated in Figure 3.1.

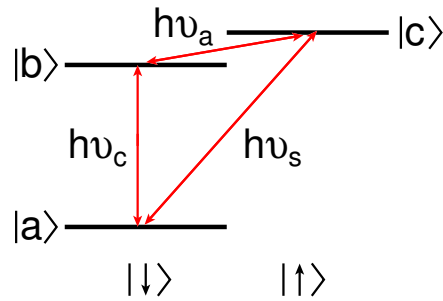


Figure 3.1: States used in simplified model of cyclotron and spin states.

We then can write the density matrix as

$$\rho = \begin{pmatrix} \rho_{aa} & \rho_{ab} & \rho_{ac} \\ \rho_{ba} & \rho_{bb} & \rho_{bc} \\ \rho_{ca} & \rho_{cb} & \rho_{cc} \end{pmatrix}, \quad (3.37)$$

where each $\rho_{ij} = \langle i | \rho | j \rangle$ is still a matrix over the axial states. The complete density matrix has dimensions $3 \times 3 \times \infty$.

In this notation we can write down some of the relevant operators in simple matrix form,

$$\mathcal{A}_c^\dagger = \begin{pmatrix} 0 & 0 & 0 \\ 1 & 0 & 0 \\ 0 & 0 & 0 \end{pmatrix} \quad \mathcal{A}_c = \begin{pmatrix} 0 & 1 & 0 \\ 0 & 0 & 0 \\ 0 & 0 & 0 \end{pmatrix} \quad \mathcal{A}_c^\dagger \mathcal{A}_c = \begin{pmatrix} 0 & 0 & 0 \\ 0 & 1 & 0 \\ 0 & 0 & 0 \end{pmatrix} \quad (3.38)$$

and

$$\mathcal{A}_s^\dagger = \begin{pmatrix} 0 & 0 & 0 \\ 0 & 0 & 0 \\ 1 & 0 & 0 \end{pmatrix} \quad \mathcal{A}_s = \begin{pmatrix} 0 & 0 & 1 \\ 0 & 0 & 0 \\ 0 & 0 & 0 \end{pmatrix} \quad \mathcal{A}_s^\dagger \mathcal{A}_s = \begin{pmatrix} 0 & 0 & 0 \\ 0 & 0 & 0 \\ 0 & 0 & 1 \end{pmatrix}. \quad (3.39)$$

We next rewrite Eq. (3.16) by breaking up the Hamiltonian into several pieces,

$$\mathcal{H} = \mathcal{H}_z (\mathcal{H}_c + \mathcal{H}_s) \quad (3.40)$$

$$\mathcal{H}_z \equiv \mathcal{A}_z^\dagger \mathcal{A}_z + \frac{1}{2} \quad (3.41)$$

$$\mathcal{H}_c \equiv \hbar \delta_c \left(\mathcal{A}_c^\dagger \mathcal{A}_c + \frac{1}{2} \right) \quad (3.42)$$

$$\mathcal{H}_s \equiv \hbar \delta_s \left(\mathcal{A}_s^\dagger \mathcal{A}_s - \frac{1}{2} \right). \quad (3.43)$$

This representation makes it easier to evaluate the time evolution of the density matrix as in Eq. (3.20), by expanding

$$\begin{aligned}
[\mathcal{H}, \rho] &= \mathcal{H}_z[\mathcal{H}_c + \mathcal{H}_s, \rho] + [\mathcal{H}_z, \rho(\mathcal{H}_c + \mathcal{H}_s)] \\
&= \hbar \mathcal{H}_z \begin{pmatrix} 0 & -\delta_c \rho_{ab} & -\delta_s \rho_{ac} \\ \delta_c \rho_{ba} & 0 & -(\delta_s - \delta_c) \rho_{bc} \\ \delta_s \rho_{ca} & (\delta_s - \delta_c) \rho_{cb} & 0 \end{pmatrix} \\
&\quad + \frac{1}{2} \hbar \left[\mathcal{H}_z, \begin{pmatrix} (\delta_c - \delta_s) \rho_{aa} & (3\delta_c - \delta_s) \rho_{ab} & (\delta_c + \delta_s) \rho_{ac} \\ (\delta_c - \delta_s) \rho_{ba} & (3\delta_c - \delta_s) \rho_{bb} & (\delta_c + \delta_s) \rho_{bc} \\ (\delta_c - \delta_s) \rho_{ca} & (3\delta_c - \delta_s) \rho_{cb} & (\delta_c + \delta_s) \rho_{cc} \end{pmatrix} \right] \quad (3.44)
\end{aligned}$$

and

$$\mathcal{A}_c^\dagger \mathcal{A}_c \rho = \begin{pmatrix} 0 & 0 & 0 \\ \rho_{ba} & \rho_{bb} & \rho_{bc} \\ 0 & 0 & 0 \end{pmatrix} \quad (3.45)$$

$$\mathcal{A}_c \rho \mathcal{A}_c^\dagger = \begin{pmatrix} \rho_{bb} & 0 & 0 \\ 0 & 0 & 0 \\ 0 & 0 & 0 \end{pmatrix} \quad (3.46)$$

$$\rho \mathcal{A}_c^\dagger \mathcal{A}_c = \begin{pmatrix} 0 & \rho_{ab} & 0 \\ 0 & \rho_{bb} & 0 \\ 0 & \rho_{cb} & 0 \end{pmatrix}. \quad (3.47)$$

The important result of this is that since we are only interested in the the time evolution of ρ_{ba} and ρ_{cb} to get the lineshapes, we can ignore all the other parts of the density matrix since they are independent. We next relabel the two portions of the

density matrix that we are interested in: $\rho_{ba} \rightarrow \rho_c$ and $\rho_{cb} \rightarrow \rho_a$. We can then extract two useful independent equations:

$$\begin{aligned} \dot{\rho}_c &= \left(-i\delta_c \mathcal{H}_z - \frac{\gamma_c}{2} \right) \rho_c + \frac{i}{2} (3\delta_c - \delta_s) [\mathcal{H}_z, \rho_c] \\ &\quad - \frac{\gamma_z}{2} \bar{n}_z (\mathcal{A}_z \mathcal{A}_z^\dagger \rho_c - 2\mathcal{A}_z^\dagger \rho_c \mathcal{A}_z + \rho_c \mathcal{A}_z \mathcal{A}_z^\dagger) \\ &\quad - \frac{\gamma_z}{2} (\bar{n}_z + 1) (\mathcal{A}_z^\dagger \mathcal{A}_z \rho_c - 2\mathcal{A}_z \rho_c \mathcal{A}_z^\dagger + \rho_c \mathcal{A}_z^\dagger \mathcal{A}_z) \end{aligned} \quad (3.48)$$

$$\begin{aligned} \dot{\rho}_a &= \left(-i(\delta_s - \delta_c) \mathcal{H}_z - \frac{\gamma_c}{2} \right) \rho_a + \frac{i}{2} (\delta_c + \delta_s) [\mathcal{H}_z, \rho_a] \\ &\quad - \frac{\gamma_z}{2} \bar{n}_z (\mathcal{A}_z \mathcal{A}_z^\dagger \rho_a - 2\mathcal{A}_z^\dagger \rho_a \mathcal{A}_z + \rho_a \mathcal{A}_z \mathcal{A}_z^\dagger) \\ &\quad - \frac{\gamma_z}{2} (\bar{n}_z + 1) (\mathcal{A}_z^\dagger \mathcal{A}_z \rho_a - 2\mathcal{A}_z \rho_a \mathcal{A}_z^\dagger + \rho_a \mathcal{A}_z^\dagger \mathcal{A}_z). \end{aligned} \quad (3.49)$$

Clearly, these equations are not yet in a suitable format. We still need to expand the axial creation and annihilation operators. Here we are interested in finding the time dependence of all diagonal entries in the z density matrix since we will ultimately need to trace over them. Fortunately, we find that the time dependence of the diagonal entries only couples to other diagonal entries. We can expand all remaining operators with

$$\langle n | \mathcal{A}_z^\dagger \mathcal{A}_z \rho_{c,a} | n \rangle = n \langle n | \rho_{c,a} | n \rangle \quad (3.50)$$

$$\langle n | \rho_{c,a} \mathcal{A}_z^\dagger \mathcal{A}_z | n \rangle = n \langle n | \rho_{c,a} | n \rangle \quad (3.51)$$

$$\langle n | \mathcal{A}_z \mathcal{A}_z^\dagger \rho_{c,a} | n \rangle = \langle n | (\mathcal{A}_z^\dagger \mathcal{A}_z + 1) \rho_{c,a} | n \rangle = (n + 1) \langle n | \rho_{c,a} | n \rangle \quad (3.52)$$

$$\langle n | \rho_{c,a} \mathcal{A}_z \mathcal{A}_z^\dagger | n \rangle = \langle n | \rho_{c,a} (\mathcal{A}_z^\dagger \mathcal{A}_z + 1) | n \rangle = (n + 1) \langle n | \rho_{c,a} | n \rangle \quad (3.53)$$

$$\langle n | \mathcal{A}_z^\dagger \rho_{c,a} \mathcal{A}_z | n \rangle = n \langle n - 1 | \rho_{c,a} | n - 1 \rangle \quad (3.54)$$

$$\langle n | \mathcal{A}_z \rho_{c,a} \mathcal{A}_z^\dagger | n \rangle = (n + 1) \langle n + 1 | \rho_{c,a} | n + 1 \rangle. \quad (3.55)$$

Finally, this allows us to write usable equations of motion for the relevant density

matrix entries,

$$\begin{aligned} \frac{d}{dt} \langle n | \rho_c | n \rangle &= \left[-i\delta_c \left(n + \frac{1}{2} \right) - \frac{\gamma_c}{2} - \gamma_z(2\bar{n}_z + 1)n - \gamma_z\bar{n}_z \right] \langle n | \rho_c | n \rangle \\ &+ \gamma_z\bar{n}_zn \langle n-1 | \rho_c | n-1 \rangle + \gamma_z(\bar{n}_z + 1)(n+1) \langle n+1 | \rho_c | n+1 \rangle \end{aligned} \quad (3.56)$$

and

$$\begin{aligned} \frac{d}{dt} \langle n | \rho_a | n \rangle &= \left[-i\delta_a \left(n + \frac{1}{2} \right) - \frac{\gamma_c}{2} - \gamma_z(2\bar{n}_z + 1)n - \gamma_z\bar{n}_z \right] \langle n | \rho_a | n \rangle \\ &+ \gamma_z\bar{n}_zn \langle n-1 | \rho_a | n-1 \rangle + \gamma_z(\bar{n}_z + 1)(n+1) \langle n+1 | \rho_a | n+1 \rangle, \end{aligned} \quad (3.57)$$

where we define the frequency $\delta_a \equiv \delta_s - \delta_c$ as the magnitude of the shift in the axial frequency due to an anomaly transition. In practice δ_a is usually too small to be measured directly. However, it is easy to calculate δ_a since $\delta_a = \frac{1}{2}(g-2)\delta_c$ and δ_c can be measured.

At this point, notice that the formulae are the same for the cyclotron (Eq. (3.56)) and anomaly (Eq. (3.57)) transitions as long as the appropriate δ is chosen. So, we let either $\rho_n = \langle n | \rho_c | n \rangle$ and $\delta = \delta_c$ or $\rho_n = \langle n | \rho_a | n \rangle$ and $\delta = \delta_a$. We will also write ω_0 for ω_c or ω_a , in order to write down completely generic equations. From here on, we only need to work with one set of equations, as long as we remember to put in the appropriate values for the transition. This is not a trivial result since it was not clear from the beginning that γ_c would affect both the cyclotron and anomaly transition in the same way.

So, we can finally write the generic result

$$\begin{aligned} \dot{\rho}_n &= \left[-i\delta \left(n + \frac{1}{2} \right) - \frac{\gamma_c}{2} - \gamma_z(2\bar{n}_z + 1)n - \gamma_z\bar{n}_z \right] \rho_n \\ &+ \gamma_z\bar{n}_zn\rho_{n-1} + \gamma_z(\bar{n}_z + 1)(n+1)\rho_{n+1}. \end{aligned} \quad (3.58)$$

This equation is the starting point for all of our transition lineshape calculations.

3.4.1 Lineshapes with Discrete Axial States

We restate the problem in matrix notation to make it more convenient to solve. Ultimately, the solution will require diagonalizing a truncated version of the density matrix numerically. We start by defining the vector

$$\vec{r}(t) \equiv \begin{pmatrix} \rho_0(t) \\ \rho_1(t) \\ \rho_2(t) \\ \vdots \end{pmatrix}. \quad (3.59)$$

So we can write the matrix equivalent of Eq. (3.58),

$$\frac{d}{dt}\vec{r}(t) = \mathcal{R} \cdot \vec{r}(t), \quad (3.60)$$

where the matrix \mathcal{R} dictates the time evolution and is given by

$$\mathcal{R} = \begin{pmatrix} -\frac{i}{2}\delta - \bar{n}_z\gamma_z - \frac{1}{2}\gamma_c & (\bar{n}_z + 1)\gamma_z & 0 & & \\ \bar{n}_z\gamma_z & -\frac{3i}{2}\delta - (3\bar{n}_z + 1)\gamma_z - \frac{1}{2}\gamma_c & 2(\bar{n}_z + 1)\gamma_z & \cdots & \\ 0 & 2\bar{n}_z\gamma_z & -\frac{5i}{2}\delta - (5\bar{n}_z + 2)\gamma_z - \frac{1}{2}\gamma_c & & \\ & \vdots & & & \end{pmatrix} \quad (3.61)$$

We now denote the eigenvectors of \mathcal{R} , \vec{e}_n and the eigenvalues of \mathcal{R} , λ_n . Since \mathcal{R} is not generally hermitian, each λ_n is in general complex. We choose each eigenvector to be normalized so that its elements sum to 1. Next, we express the initial condition $\vec{r}(0)$ as written in Eq. (3.19) as a sum of \vec{e}_n ,

$$\vec{r}(t) = \sum_{n=0}^{\infty} b_n(t) \vec{e}_n. \quad (3.62)$$

We can easily find the value of each $b_n(0)$ by inverting

$$\vec{r}(0) = \mathcal{E} \cdot \vec{b}(0), \quad (3.63)$$

where \mathcal{E} is the matrix of eigenvectors,

$$\mathcal{E} \equiv \begin{pmatrix} \vec{e}_0 & \vec{e}_1 & \vec{e}_2 & \cdots \end{pmatrix} \quad \text{and} \quad \vec{b}(t) \equiv \begin{pmatrix} b_0(t) \\ b_1(t) \\ b_2(t) \\ \vdots \end{pmatrix}. \quad (3.64)$$

Each of the eigenvectors naturally has very simple differential equation for its time dependence,

$$\frac{d}{dt} [b_n(t) \vec{e}_n] = b_n(t) \mathcal{R} \cdot \vec{e}_n = \lambda_n b_n(t) \vec{e}_n. \quad (3.65)$$

So, the differential equation for the time dependence of \vec{r} is

$$\frac{d}{dt} \vec{r}(t) = \frac{d}{dt} \left[\sum_{n=0}^{\infty} b_n(t) \vec{e}_n \right] = \sum_{n=0}^{\infty} \lambda_n b_n(t) \vec{e}_n. \quad (3.66)$$

While the solution is trivial, we add in the drive before completing the calculation.

Quantum Jump Spectroscopy

We now proceed to add in the cyclotron or anomaly drive in a manner analogous to the solution of the two level driven system in Eq. (3.22). We simply make the substitutions

$$\rho_{aa} \rightarrow \sum_{n=0}^{\infty} b_n(0) \vec{e}_n \quad (3.67)$$

$$\rho_{ba} \rightarrow \sum_{n=0}^{\infty} b_n(t) \vec{e}_n \quad (3.68)$$

$$\lambda \rho_{ba} \rightarrow \sum_{n=0}^{\infty} \lambda_n b_n(t) \vec{e}_n \quad (3.69)$$

in Eqs. (3.28) and (3.29) to get the time evolution with a weak drive,

$$\frac{d}{dt} \left[\sum_{n=0}^{\infty} b_n(t) \vec{e}_n \right] = -iA \left[\sum_{n=0}^{\infty} b_n(0) \vec{e}_n \right] e^{-i\omega t} - \sum_{n=0}^{\infty} \lambda_n b_n(t) \vec{e}_n \quad (3.70)$$

$$\dot{\rho}_{bb} = -2A \text{Im} \left[\sum_{n=0}^{\infty} b_n(t) e^{i\omega t} \vec{e}_n \right]. \quad (3.71)$$

We want a solution where the $b_n(t)$, are in steady state. So, we can switch to a frame rotating as $e^{i\omega t}$ and find the steady state solution by requiring equality for each eigenvector individually. The steady state result, analogous to Eq. (3.32), is

$$b_n(t) = \frac{iA b_n(0)}{\lambda_n - i\omega} e^{-i\omega t}. \quad (3.72)$$

If we use Eq. (3.71), add back in even the fastest rotation, and trace over the axial states, the transition rate is, analogous to Eq. (3.33),

$$\dot{\rho}_{bb} = 2A^2 \sum_{n=0}^{\infty} \text{Re} \left[\frac{-b_n(0)}{\lambda_n - i(\omega - \omega_0)} \right]. \quad (3.73)$$

The transition lineshape is proportional to the weak drive transition rate but with different normalization (we use the convention of Brown [12, 31]). The final anomaly or cyclotron transition lineshape with a weak drive is

$$\chi(\omega) = \frac{1}{\pi} \sum_{n=0}^{\infty} \text{Re} \left[\frac{-b_n(0)}{\lambda_n - i\Delta} \right], \quad (3.74)$$

where $\Delta = \omega - \omega_0$ is the drive detuning. Recall that the coefficients $b_n(0)$ can be found by solving Eq. (3.63).

Numerical Results

There are two calculations that must be done to determine the lineshape in any specific case. First, the eigenvalues and eigenvectors of the matrix \mathcal{R} (Eq. (3.61))

must be determined. Next, the initial condition must be expanded in the eigenvector basis as in Eq. (3.63). Finally, the lineshape can be plotted with Eq. (3.74).

The lineshapes are parameterized by three values. The first is the average axial state \bar{n}_z . The second parameter, γ_z/δ , is the axial damping rate relative to the jump size. The third parameter, γ_c/δ is the cyclotron damping rate in units of the jump size. Note that when quantum mechanics is included, a new parameter (\bar{n}_z) must be included. The cyclotron damping is typically not included in the calculations by Brown [31], leaving only one parameter in his calculations.

For numerical calculations it is necessary to truncate the number of axial states to a finite value n_{max} . For an example calculation, we choose $\bar{n}_z = 10$. By trial and error, we find that we require $n_{max} > 100$ for good convergence in the large γ_z limit with this choice of \bar{n}_z . Fewer axial states are needed with weaker axial damping. We used $n_{max} = 400$ for these calculations to ensure convergence. Results for several values of γ_z/δ are plotted in Figure 3.2. The cyclotron damping rate γ_c/δ was chosen to be 0 for these results, since it simply blurs out the lineshape. We delay discussion of the lineshapes until Section 3.4.3 where they are compared with those from other calculation methods.

3.4.2 Analytical Solution for Continuous Axial States

In order to get an approximate analytical (series) result, we take the continuous n limit of the equation of motion for the density matrix. It seems that this may be reasonable even for the coldest temperatures we are interested in, which have $\bar{n} \sim 10$. In practice we will see when the results match those of the discrete axial

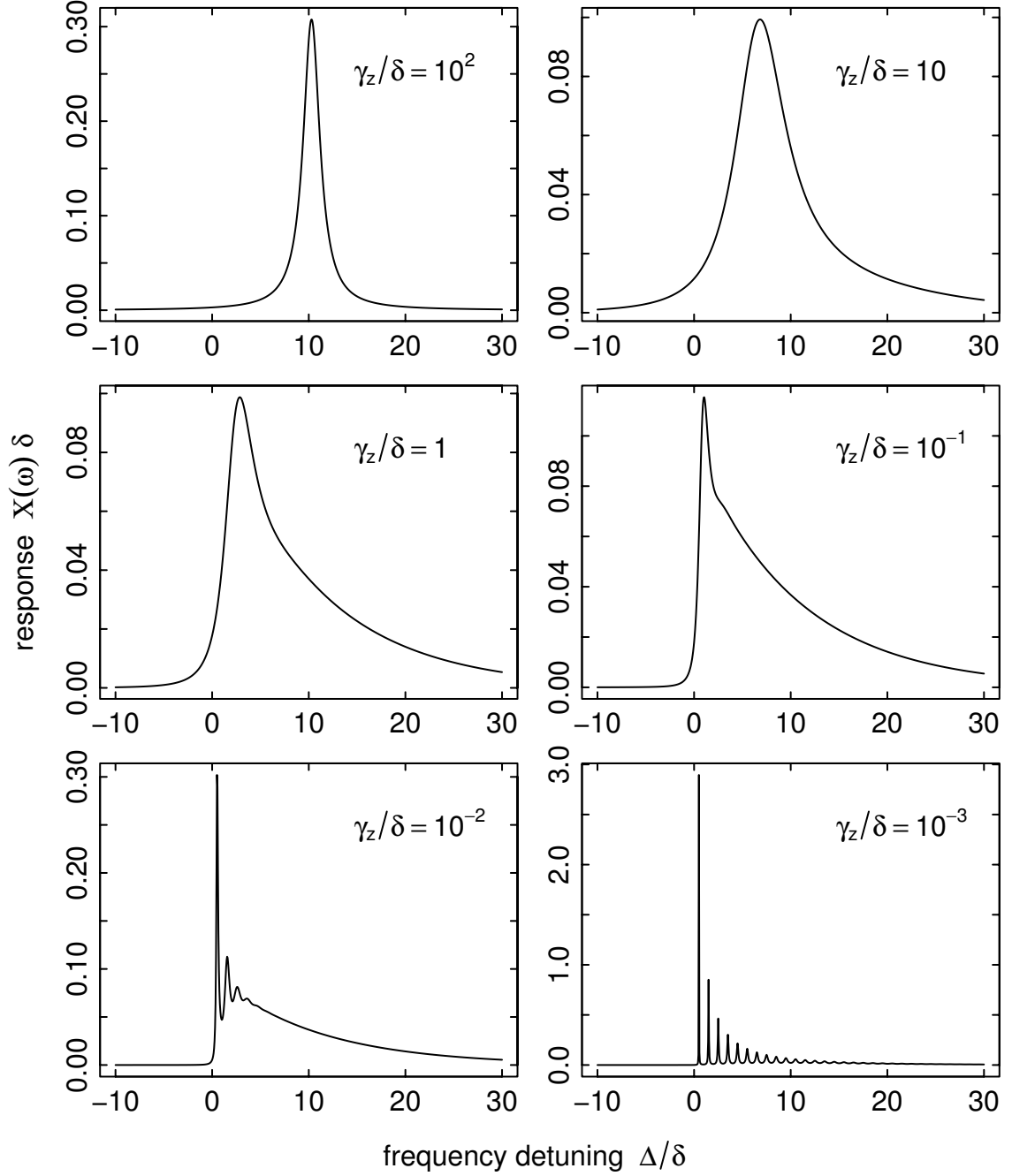


Figure 3.2: Cyclotron or anomaly transition lineshapes as calculated with discrete axial states for $\bar{n}_z = 10$, $\gamma_c = 0$. The axial states are truncated at $n_{max} = 400$.

state calculation. For simplicity, we will take $\gamma_c = 0$.

First we must write a partial differential equation for the time evolution of the off-diagonal element of the density matrix. Regrouping the terms of Eq. (3.58) into a more suggestive form, we get

$$\begin{aligned} \frac{d\rho_n}{dt} = & -\frac{i}{2}\delta(2n+1)\rho_n + \gamma_z \bar{n}_z (\rho_{n+1} - \rho_n) \\ & + \gamma_z n (\rho_{n+1} - \rho_n) + \gamma_z \rho_{n+1} \\ & + \gamma_z \bar{n}_z n (\rho_{n-1} - 2\rho_n + \rho_{n+1}). \end{aligned} \quad (3.75)$$

Taking n to be a continuous variable, changing differences into derivatives, and taking $\bar{n}_z \gg 1$, we arrive at a partial differential equation for $\rho(n, t)$,

$$\frac{\partial \rho}{\partial t} = -i\delta \left(n + \frac{1}{2} \right) \rho + \gamma_z \left(1 + n \frac{\partial}{\partial n} \right) \left(1 + \bar{n}_z \frac{\partial}{\partial n} \right) \rho. \quad (3.76)$$

To solve this equation we first change to a rotating frame with $\rho = p e^{-it\delta/2}$, and take the Laplace transform of Eq. (3.76) to get the much simplified first order partial differential equation,

$$\frac{\partial L}{\partial t} = -\gamma_z \bar{n}_z s L - [\gamma_z s (1 + \bar{n}_z s) - i\delta] \frac{\partial L}{\partial s}, \quad (3.77)$$

where L is the Laplace transform of p ,

$$L(s, t) \equiv \int_0^\infty e^{-sn} p(n, t) dn. \quad (3.78)$$

We seek a solution which begins in a thermal state,

$$\rho(n, 0) \propto \exp(-n/\bar{n}_n) \quad (3.79)$$

or

$$L(s, 0) \propto \frac{1}{\bar{n}_z^{-1} + s}. \quad (3.80)$$

Fortunately, Eq. (3.77) can be solved by elementary (but tedious) methods. After much work, we arrive at a solution for $L(s, t)$, which is too complex to be presented here. However, we are only interested in the trace over the density matrix ρ , which is given by $e^{-it\delta/2}L(0, t)$. Conveniently, there is no need to invert the Laplace transform. The trace over the density matrix with rotation added back in is

$$U(t) \equiv \int_0^\infty \rho(n, t) dn = e^{-it\delta/2}L(0, t), \quad (3.81)$$

which, plugging in our solution, is

$$U(t) = \frac{4\gamma_z\gamma'e^{\frac{1}{2}(-i\delta+\gamma_z+\gamma')t}}{-(\gamma_z-\gamma')^2+(\gamma_z+\gamma')^2e^{t\gamma'}}, \quad (3.82)$$

where $\gamma' \equiv \sqrt{\gamma_z^2 + 4i\gamma_z\bar{n}_z\delta}$.

Finally, we wish to calculate the lineshape, which we will take to be the real part of the Fourier transform of the off-diagonal density matrix element, as a generalization of the quantum mechanical derivation earlier. Still working in a frame rotating at the cyclotron or anomaly frequency ω_0 , we transform $\tilde{\chi}(t)$ into Fourier space to get the lineshape $\chi(\omega)$, with normalization chosen to match [12, 31], as

$$\chi(\omega) = \frac{4}{\pi} \operatorname{Re} \left[\int_0^\infty \frac{\gamma_z\gamma'e^{i(\omega-\omega-\frac{1}{2}\delta)t+\frac{1}{2}(\gamma_z+\gamma')t}}{-(\gamma_z-\gamma')^2+(\gamma_z+\gamma')^2e^{t\gamma'}} dt \right], \quad (3.83)$$

This can be evaluated by changing variables to $u = e^{t\gamma'}$, where u follows an outward spiraling path in the complex u plane, starting at $u = 1$. Since all poles occur for $|u| < 1$, the contour can be distorted to a path along the real axis from 0 to $+\infty$.

The integral can then be evaluated to

$$\chi(\omega) = \frac{4}{\pi} \operatorname{Re} \left[\frac{\gamma_z {}_2F_1 \left[1, -K, 1 - K, \frac{(\gamma_z-\gamma')^2}{(\gamma_z+\gamma')^2} \right]}{K (\gamma_z + \gamma')^2} \right], \quad (3.84)$$

where ${}_2F_1$ is a hypergeometric function, and

$$K = \frac{2i \left(\Delta - \frac{1}{2}\delta \right) + \gamma_z - \gamma'}{2\gamma'}, \quad (3.85)$$

where $\Delta = \omega - \omega_0$ is the drive detuning. Alternatively, the lineshape can be expanded in a series,

$$\chi(\omega) = \frac{4}{\pi} \operatorname{Re} \left[\frac{\gamma'\gamma}{(\gamma' + \gamma)^2} \sum_{n=0}^{\infty} \frac{(\gamma' - \gamma)^{2n} (\gamma' + \gamma)^{-2n}}{\left(n + \frac{1}{2} \right) \gamma' - \frac{1}{2}\gamma - i \left(\Delta - \frac{1}{2}\delta \right)} \right]. \quad (3.86)$$

The formula for the lineshape is nearly identical to that derived by Brown [12, 31], except for a frequency shift of $\delta/2$ from the zero point energy of the axial motion which originates from the Hamiltonian, Eq. (3.16). However, the approximations taken in this derivation make the accuracy of the exact lineshape doubtful on the frequency scale of δ .

Numerical Results

We plot lineshapes using Eq. (3.86) with the same parameters as with discrete axial states, and the results are shown in Figure 3.3. We delay discussion of the lineshapes until Section 3.4.3 where they are compared with those from other calculation methods.

3.4.3 Comparison of Methods

The lineshapes for discrete and continuous axial states are plotted together for comparison in Figure 3.4, with the same parameters as before. There are three ranges for the parameter γ_z/δ relative to \bar{n}_z that have simple lineshapes. The three limits

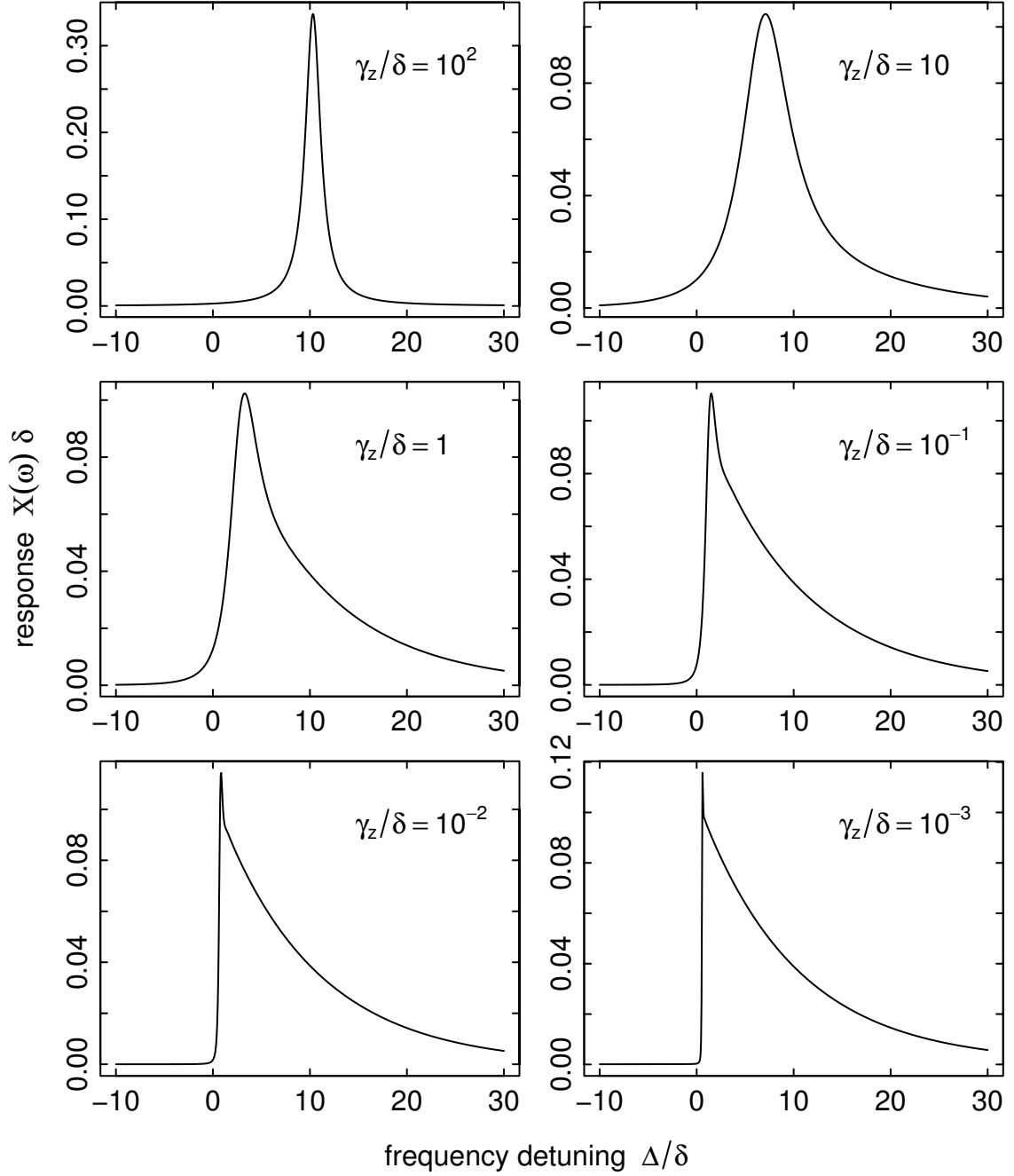


Figure 3.3: Cyclotron or anomaly transition lineshapes as calculated with continuous axial states for $\bar{n}_z = 10$, $\gamma_c = 0$. The series is truncated at $N_{terms} = 100$ near the Lorentzian limit, or up to $N_{terms} = 200$ near exponential limit.

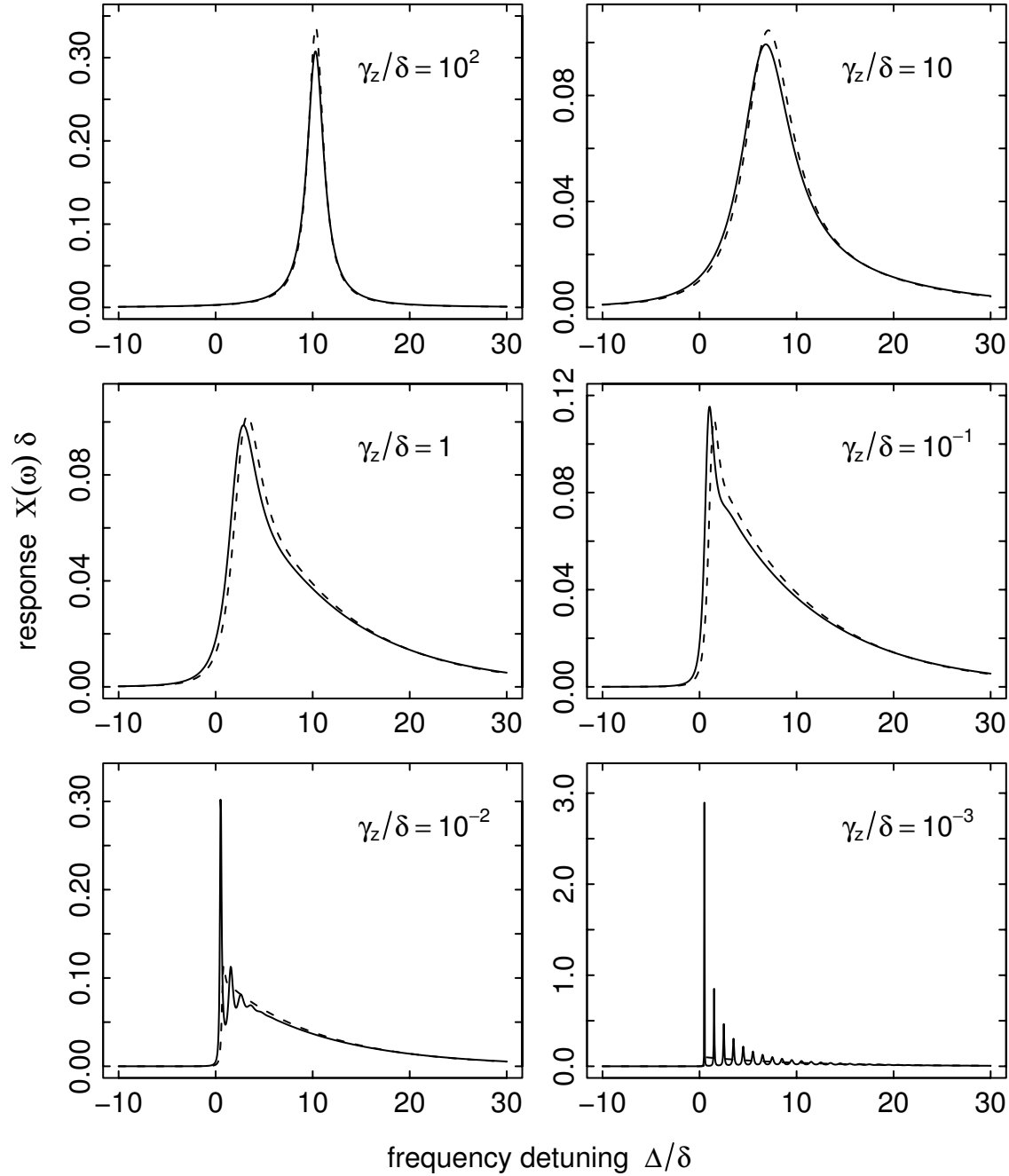


Figure 3.4: Comparison of discrete lineshapes (solid lines) and continuous lineshapes (dashed lines) with $\bar{n}_z = 10$.

and corresponding lineshapes are:

$$\frac{\gamma_z}{\delta} \gg \bar{n}_z \Rightarrow \text{Lorentzian lineshape} \quad (3.87)$$

$$\frac{1}{\bar{n}_z} \ll \frac{\gamma_z}{\delta} \ll \bar{n}_z \Rightarrow \text{continuous exponential lineshape} \quad (3.88)$$

$$\frac{\gamma_z}{\delta} \ll \frac{1}{\bar{n}_z} \Rightarrow \text{discrete exponential lineshape.} \quad (3.89)$$

As is visible in the figure, the two calculation methods produce very similar lineshapes in the Lorentzian limit (strong axial damping). As the axial damping is decreased, the agreement diminishes. However, they are still very similar in the exponential limit, as long as the axial damping is strong enough to blur out the quantum structure. In the weak axial damping limit, the lineshape breaks up into a series of peaks due to the discrete axial states in quantum mechanics. The continuous axial state model blurs the states and the lineshape out.

Not surprisingly, the continuous model series converges quickly in the Lorentzian limit, slowly in the continuous exponential limit, and is incorrect in the discrete exponential limit. The discrete model converges in all limits, but in practice far more axial states must be included in the calculation in the strong axial damping (Lorentzian) limit than in the weak axial damping (exponential) limit.

In this example, with $\bar{n}_z = 10$, there is only a small region of parameter space with a continuous exponential lineshape and good agreement between the two calculations. While $\bar{n}_z \approx 10$ at $\nu_z = 200$ MHz and $T_z = 100$ mK, \bar{n}_z is much larger under many experimental conditions. This may greatly expand the usability of the continuous calculation. It is not clear whether the zero point shift of the lineshape which we have included is important. It is probably preferable to use the exact model if accuracy on that scale is required.

In addition to the extra parameters needed for the quantum calculation, the parameterization used by Brown [12, 31] is different. His choice of parameter is less convenient with quantum mechanics, and the choice of parameterization here is usually easier to connect to experiments.

While these results are very useful for aiding in understanding of the lineshapes, it may be necessary to do more complete calculations to match experimental data for a precision measurement. Often the drive is not weak enough in an experiment to keep the transition probability small, so saturation effects become important. It may also not be desirable to keep the drive on for much longer than the coherence time to make the data collection faster. In these cases, it would be best to include a strong drive of finite duration in the calculations. Such calculations can be performed with numerical techniques similar to those used here, but they have been omitted because there is little new physical insight to be gained from them.

3.5 Lineshapes with Weak Axial Coupling

In the range of axial damping where a continuous exponential lineshape is usually obtained,

$$\frac{1}{\bar{n}_z} \ll \frac{\gamma_z}{\delta} \ll \bar{n}_z, \quad (3.90)$$

it is useful to generalize the result.

We therefore state without proof that if the probability of the axial motion having

energy between E and $E + dE$ is $P_E(E)dE$, then the lineshape $\chi(\omega)$ is

$$\chi(\omega) = \begin{cases} 0 & \text{if } \omega < \omega_0 \\ \frac{\hbar\omega_z}{\delta} P_E \left[\frac{\hbar\omega_z}{\delta} (\omega - \omega_0) \right] & \text{if } \omega \geq \omega_0 \end{cases}. \quad (3.91)$$

For further discussion and proof, see [12].

3.5.1 Lineshape with Driven Axial Motion

We next use Eq. (3.91) to find a cyclotron or anomaly lineshape when the axial motion is driven and damped, instead of being in a thermal state. This derivation is largely thanks to R. van Handel [35] and a similar derivation is done by Brown [12].

In general, the energy E_z of the axial motion oscillating with amplitude A is

$$E_z = \frac{1}{2} m \omega_z^2 A^2. \quad (3.92)$$

We split this energy into a portion due to a single frequency drive E_D which alone would give amplitude A_D and another due to thermal noise E_N which alone would give amplitude A_N . These amplitudes are given by

$$A_D = \sqrt{\frac{2E_D}{m\omega_z^2}} \quad (3.93)$$

$$A_N = \sqrt{\frac{2E_N}{m\omega_z^2}}. \quad (3.94)$$

The probability distribution due to the thermal noise is

$$P_E(E_N) = \frac{1}{kT} \exp\left(\frac{-E_N}{kT}\right) dE. \quad (3.95)$$

The total energy of the axial oscillator is

$$E_z = \frac{1}{2} m \omega_z^2 |A_D + A_N|^2. \quad (3.96)$$

The two amplitudes must be added as vectors with a random angle between them since the phase of the thermal noise relative to the drive is random.

To get the total probability distribution, we integrate over all phases between the drive and noise,

$$\begin{aligned}
P_E(E_z) &= \frac{dE}{kT} \int_0^{2\pi} \frac{d\phi}{2\pi} \exp\left(-\frac{m\omega_z^2}{2kT}|A_D + A_N|^2\right) \\
&= \frac{dE}{kT} \exp\left(-\frac{E_D + E_N}{kT}\right) \int_0^{2\pi} \frac{d\phi}{2\pi} \exp\left(-\frac{2\sqrt{E_DE_N}}{kT} \cos\phi\right) \\
&= \frac{dE}{kT} \exp\left(-\frac{E_D + E_N}{kT}\right) I_0\left(\frac{2\sqrt{E_DE_N}}{kT}\right). \tag{3.97}
\end{aligned}$$

Taking the average axial state \bar{n}_z to be

$$\bar{n}_z \approx \frac{kT}{\hbar\omega_z}, \tag{3.98}$$

we arrive at a lineshape,

$$\chi(\omega) = \begin{cases} 0 & \text{if } \omega < \omega_0 \\ \frac{1}{\bar{n}_z\delta} \exp\left(-\frac{\omega-\omega_0}{\bar{n}_z\delta}\right) \exp\left(-\frac{\Delta\omega_D}{\bar{n}_z\delta}\right) I_0\left(\frac{2\sqrt{(\omega-\omega_0)\Delta\omega_D}}{\bar{n}_z\delta}\right) & \text{if } \omega \geq \omega_0 \end{cases}, \tag{3.99}$$

where

$$\Delta\omega_D = \frac{m\omega_z\delta}{2\hbar} A_D^2. \tag{3.100}$$

3.6 Correlated Cyclotron and Anomaly Measurement

It is possible to measure both the cyclotron and anomaly frequencies simultaneously to reduce the effects of a finite axial temperature and of magnetic field drift. Instead of measuring a cyclotron resonance lineshape and then an anomaly resonance

lineshape, we could attempt both transitions simultaneously to acquire a compound two dimensional lineshape.

The idea is to make the axial damping small, so that

$$\frac{\gamma_z}{\delta} \ll \frac{1}{\bar{n}_z}, \quad (3.101)$$

which makes the lineshape a series of discrete axial peaks, with one for each possible axial number state, as in Figure 3.2. Ideally, this condition is satisfied for both the cyclotron and anomaly transitions, so that both have the same discrete lineshape. With such weak axial damping, the axial state effectively does not change during the time that the drives are applied. With the system started in the ground cyclotron and spin state $|0, \downarrow\rangle$, both the cyclotron and anomaly drives are applied. If both are resonant, the state may end up in $|0, \uparrow\rangle$. If only the anomaly drive is resonant, then nothing can happen. If only the cyclotron drive is resonant, then the state may change to $|1, \downarrow\rangle$, but it will spontaneously decay back down to the starting point, $|0, \downarrow\rangle$.

3.6.1 Calculation

To calculate the simultaneous transition lineshape for the correlated measurement, we use discrete axial states and set up the calculation for each transition as for independent transitions. Let \mathcal{R}_c be the matrix \mathcal{R} (see Eq. (3.61)) with $\delta \rightarrow \delta_c$ and let \mathcal{R}_a be the matrix \mathcal{R} with $\delta \rightarrow \delta_a$.

We denote the eigenvectors of \mathcal{R}_c , \vec{f}_n , and the eigenvalues of \mathcal{R}_c , β_n . We also denote the eigenvectors of \mathcal{R}_a , \vec{e}_n , and the eigenvalues of \mathcal{R}_a , α_n . Each \vec{f}_n and \vec{e}_n is normalized to sum to 1.

Next, we express the initial condition $\vec{r}(0)$ as written in Eq. (3.19) as a sum of \vec{f}_n ,

$$\vec{r}(0) = \sum_{n=0}^{\infty} c_n \vec{f}_n. \quad (3.102)$$

This expansion effectively describes the cyclotron transition. To find the correlated transition rate, we expand the eigenvectors of \mathcal{R}_c in the basis of eigenvectors of \mathcal{R}_a ,

$$\vec{f}_n = \sum_{m=0}^{\infty} a_{nm} \vec{e}_m. \quad (3.103)$$

The correlated transition lineshape for a single eigenvector of \mathcal{R}_c is a product of lineshapes analogous to Eq. (3.74), weighted by the expansion coefficients:

$$\chi(\omega) = \frac{1}{\pi^2} \sum_{n=0}^{\infty} \sum_{m=0}^{\infty} \text{Re} \left[\frac{-c_n}{\beta_n - i\Delta_c} \right] \text{Re} \left[\frac{-a_{nm}}{\alpha_m - i\Delta_a} \right], \quad (3.104)$$

where Δ_c is the detuning of the cyclotron drive from the unperturbed cyclotron frequency and Δ_a is the detuning of the anomaly drive from the unperturbed anomaly frequency.

3.6.2 Numerical Results

Two dimensional lineshapes for simultaneously driving the cyclotron and anomaly transitions are shown in Figure 3.5. In the limit of very strong or very weak axial damping, the correlated transition has a potentially useful response. In these limits, a measurement of the center of the correlated response gives a measurement of $g - 2$, since both the cyclotron and anomaly responses are shifted similarly. In practice, it is difficult to reach the strong axial damping limit, so we focus on the weak axial damping limit.

In the weak axial damping limit, the resonance may be at any one of the peaks in the comb in any one trial since the axial state is not known. So, most of the time the

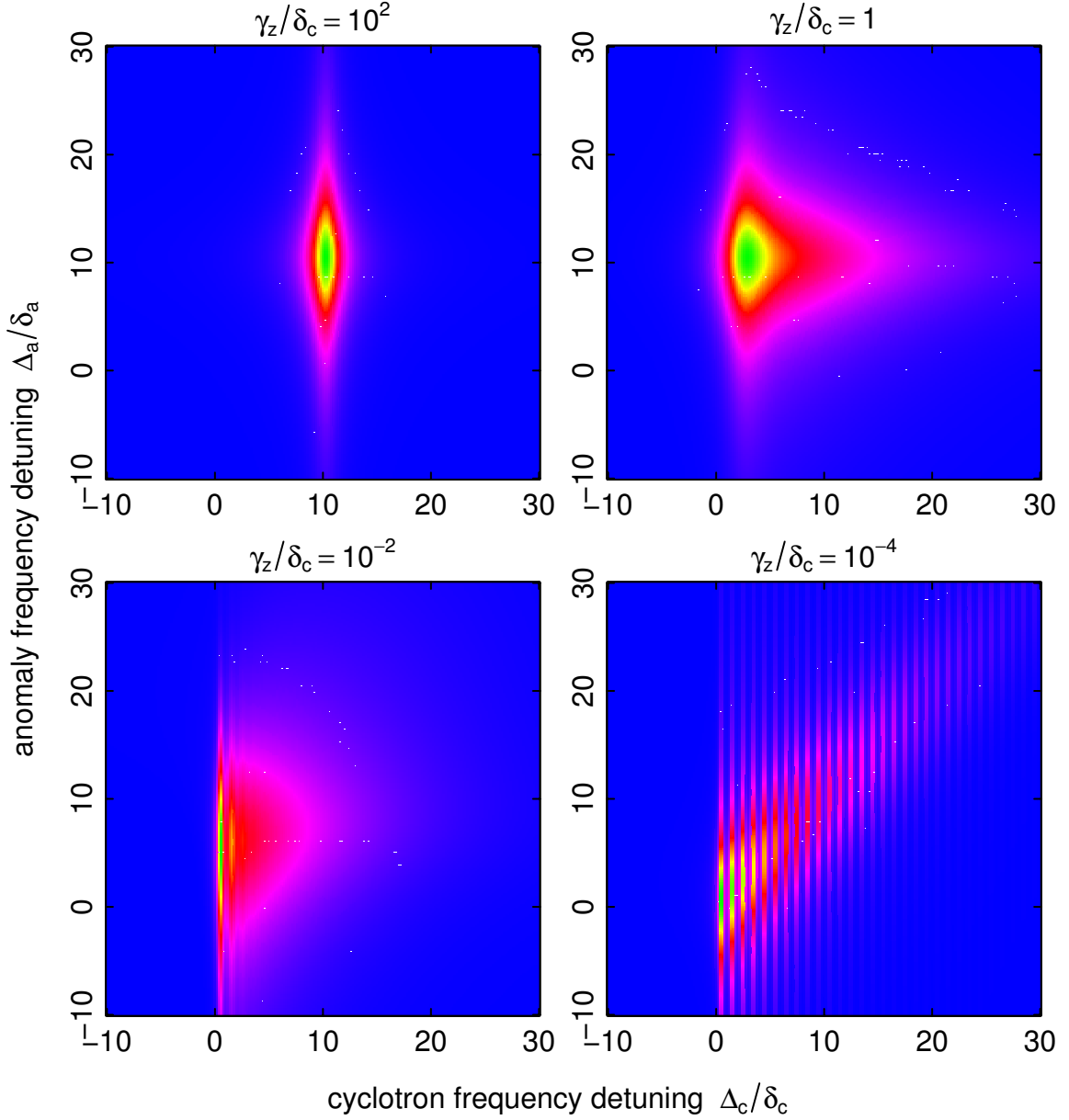


Figure 3.5: Correlated transition lineshapes as calculated with discrete axial states for $\bar{n}_z = 10$, $\gamma_c/\delta_a = 10$. The axial states are truncated at $n_{max} = 200$. The cyclotron damping was set artificially high for the cyclotron transition, $\gamma_c/\delta_a = 0.25$ to prevent the discrete peaks of the cyclotron transition from getting impractically narrow.

drives and state will not align, and no excitation will result. However, when there is an excitation, both the cyclotron and anomaly frequencies are obtained simultaneously to within the (narrow) linewidth, which is limited by the cyclotron lifetime.

The correlated measurement gives fewer excitations than the uncorrelated measurement, but each excitation gives much more valuable data. If the axial temperature increases, there will be fewer excitations, but each excitation still gives a complete measurement. Even if the magnetic field drifts, only the drift over the drive time can disturb the measurement. Otherwise, the drift only decreases the number of excitations since the appropriate frequency range to drive at may be moving around. However, if the magnetic field is too unstable or the axial temperature is too high, there may not be any excitations in an experimentally practical length of time.

We do not have a usable method for decoupling the axial motion from the tuned circuit which causes the axial damping. Possibilities for decoupling include a cryogenic switch to short out the tuned circuit, or detuning of the axial frequency from the tuned circuit resonance. While some success has been obtained by detuning the axial frequency, there may still be difficulties with this approach since the axial frequency must be reliably returned to the original frequency with an uncertainty much less than the shift which would occur due to a cyclotron or spin transition. If the axial motion is decoupled, axial-cyclotron sideband cooling may be used to cool the axial motion to the ground state before performing the correlated measurement, which could give the field drift tolerance of the correlated measurement and a high excitation rate.

Chapter 4

Low-Power Detection

The cryogenic amplifiers used to boost the signal power from the axial oscillation of a single trapped electron are at the heart of the $g - 2$ measurement. These amplifiers provide all information about the electron's motion. Despite their importance, no systematic redesign of these amplifiers using modern components has recently been attempted. The problem of initially adapting traditional cryogenic amplifier designs to the low power requirements of a dilution refrigerator was solved by Peil using a field effect transistor produced at Harvard [14, 15].

Low noise cryogenic radio frequency amplifiers are also used extensively for radio astronomy [36, 37, 38, 39] where a variety of transistor types have been considered, mostly for use at frequencies above 300 MHz. Similar amplifiers based on HEMTs are also used for a search for axions [40] where ultra low noise is of critical importance. Cryogenic amplifiers using MESFETs have been used below 1 MHz [41]. The advantages of cryogenic amplifiers, even for room temperature experiments, are reduced thermal noise, improved device performance, and reduced loss. Some experiments

also make use of superconducting components to reduce loss [42], although our magnetic field is too strong for type I superconductors and our frequencies may be too high for type II superconductors to be helpful.

The data presented in this chapter for cryogenic operation is typically taken at 4 K because that temperature can be easily achieved under controlled test conditions. We have found that the changes in device performance between 4 K and 100 mK are generally small compared to the changes between room temperature and 4 K.

4.1 Amplifier Challenges

The difficulties normally associated with cryogenic low noise amplifiers for Penning trap detection are even more significant in our dilution refrigerator based experiment. While the cylindrical trap gives us much better control of the cavity shifts of the cyclotron motion, it has a smaller harmonic region relative to Penning traps with hyperbolic electrodes. This means that the amplitude of harmonic axial oscillations is smaller, so the noise requirements of the amplifiers are even more stringent.

4.1.1 Power Dissipation

While our dilution refrigerator is capable of cooling to below 20 mK with no heat load, it has only 50 μW of cooling power at 100 mK, and much of that is used to cool wires and coaxial cables that extend down from warmer temperature regions of the experiment. In practice, the first stage cryogenic amplifier thermally connected to the mixing chamber can only dissipate about 10 μW of power if the mixing chamber is to stay below or around 100 mK. This is a significant challenge

since the traditional metal semiconductor field effect transistor (MESFET) based amplifiers used in cryogenic Penning trap experiments [15], even though operated at currents much smaller than intended, typically dissipate ~ 3 mW.

The choice of transistor is critical to the low noise and low power operation of the cryogenic amplifier. Si JFET transistors generally do not work at cryogenic temperatures because the carriers freeze out, and Si metal oxide semiconductor field effect transistors (MOSFETs) have been used [28], but now are considered too noisy [41]. Therefore, GaAs based transistors have been the choice for low noise cryogenic amplifiers. SiGe bipolar transistors have recently become popular for high frequency low noise amplification [43] and we will examine them further in Section 4.4.

In recent years, the transistor of choice for cryogenic amplifiers in our lab is the Mitsubishi MGF-1100 [26]. The MGF-1100 is a dual-gate MESFET designed for 4 V drain-source bias voltage (V_D) and a drain current (I_D) of at least 10 mA. Since such high power dissipation would lead to excessive boil-off of liquid ^4He in a 4 K experiment, the MESFET is typically “starved down” to $I_D \approx 1$ mA giving a total power dissipation of ≈ 3 mW and ≈ 10 mS transconductance. Operation at lower power leads to significantly decreased gain [15]. Since this power dissipation was unacceptable for a dilution refrigerator cooled experiment, an attempt was made to construct an inductively coupled amplifier which could allow the use of a MESFET with power dissipation of ~ 3 mW by sinking the heat to a warmer part of the dilution refrigerator [15]. However, too much heat was still dumped into the mixing chamber and the base temperature of the refrigerator was dramatically increased.

The first amplifier used to detect a single electron in a Penning trap with a dilution

refrigerator below 100 mK used a high electron mobility transistor (HEMT) produced in collaboration with the Westervelt group at Harvard University [15]. We have taken to calling this transistor an HFET, for heterojunction field effect transistor. Although normally the names HEMT and HFET are interchangeable, we will reserve the name HFET for this Harvard built device here. Unfortunately, the gain of the HFET amplifier seemed to degrade over time to the point that the noise resonance was no longer visible. The degradation probably occurred because the HFET is not hermetically sealed from atmospheric gases which could diffuse into or react with the GaAs over time, although this could likely be eliminated with an appropriate coating.

4.1.2 Heat Sinking

Despite the significant improvements in power dissipation of the cryogenic amplifiers, there is another obstacle which prevents the particle from reaching ultra cold temperatures. The amplifier can directly heat the axial motion of the trapped electron through its electrical connection to the particle. Electrical noise in the transistor of thermal or other origin (such as shot noise) can drive the axial motion into a higher temperature thermal state. Much of this noise can perhaps be eliminated by cutting off the drain current of the amplifier, but the transistor must still cool down in order for its Johnson noise to be reduced.

There were early warnings that the heat sinking in our cryogenic amplifiers was not adequate. The case of the inductively coupled amplifier reached 23 K, and even with the 10 μ W HFET amplifier the case temperature was measured to be over 1 K. Peil [15] measured the axial temperature to be 17 K with the amplifier on, but could

not locate the cyclotron resonance when turning the amplifier off during the cyclotron excitation. Later experiments with a cascode HEMT amplifier found that the axial temperature did not significantly decrease from 5 K, the axial temperature with the amplifier on, even when allowing the transistor 5 seconds to cool down before the cyclotron excitation. The temperature of the circuit board of the cascode HEMT amplifier was ~ 800 mK, much higher than the 75 mK mixing chamber temperature, and the circuit board temperature did not decrease noticeably in the few seconds that are available to let the amplifier cool. Since the amplifier must be turned off for each attempted cyclotron or anomaly excitation, it is not practical to wait longer than a few seconds for the amplifier to cool. It is then not surprising that the HEMT, which is expected to have a much higher temperature than the circuit board, does not cool down.

Solving this problem ultimately required redesigning the amplifiers around the heroic heat sinking requirement. At dilution refrigerator temperatures, the thermal conductivities of relatively pure metals decrease linearly with temperature, so a substantial thermal conduction path is required to keep the FET from getting excessively hot.

4.1.3 Feedback and Stability

Although it is not often mentioned in the literature, stable operation of FETs at cryogenic temperatures is not trivially obtained. Since the electrical conductivity of metals increases, the resistive losses in FETs decreases, and the gain of FETs increases as the temperature is decreased, a small amount of positive feedback in the

amplifier can lead to oscillation.

Two effects of positive feedback are commonly observed experimentally. A relatively small amount of positive feedback at the amplifier tuned circuit frequency typically causes regeneration. Regeneration is marked by an apparent increase in the Q of the tuned circuit which may become more severe at higher gain, an increase in the amplitude of the noise resonance, and a “peaky” noise resonance. Regeneration can be understood as the positive feedback creating an effective negative resistance which is in parallel with the tuned circuit. This negative resistance increases the Q which could improve particle detection except that it increases the electrical noise temperature of the tuned circuit as well (while the amplifier is on), so it can heat up the detected particle.

A more extreme form of feedback is oscillation. There are two forms of oscillation that are commonly observed experimentally. The first is simply a stronger form of regeneration, where the noise resonance becomes a sharp signal because the positive feedback has overcome the losses in the input circuit, rendering the amplifier useless for particle detection. The second form of oscillation is oscillation at a frequency other than the tuned circuit frequency, typically a much higher frequency. The FETs we use often have significant gain up to ~ 20 GHz so oscillation is possible at much higher frequencies than we intend the amplifiers to be used for. Experimentally, it may or may not be possible to directly detect the oscillation, but the onset of oscillation is marked by a jump in the DC characteristics of the FET. The problem of feedback will be analyzed in detail for a HEMT single gate amplifier.

4.2 Single-Gate HEMT Amplifier Design

A variety of FETs and HEMTs have been compared for cryogenic performance [36, 37, 15] and HEMTs generally outperform MESFETs in terms of noise performance at frequencies that are high enough to avoid $1/f$ noise. At low frequencies, the small gate area of most commercial HEMTs may make them excessively noisy. We were also motivated to try HEMTs by the demonstration of very good noise performance at cryogenic temperatures down to 300 MHz [38, 39].

High electron mobility transistors (HEMTs) were invented 1979 at Fujitsu Laboratories [44], but were not extensively commercially used until around 1987 when they started to replace MESFETs in satellite receivers because of their improved noise performance. Even earlier, HEMTs were used in cryogenic amplifiers for radio astronomy. While the noise performance of HEMTs is well known, their ability to run at the low power required for use with a dilution refrigerator is not since they are intended to be used with more than 10 mW power dissipation. Recently, HEMTs have been used at cryogenic temperatures and low power for scanning tunneling microscopy [45], but we learned of this well after independently finding that similar transistors are suitable for our experiment.

An apparent additional complication with HEMTs is that they are typically made with only a single gate, in contrast with the dual-gate MESFETs we traditionally use. While it is possible to connect two HEMTs in series to form a cascode circuit which behaves like a single dual-gate FET, there are reasons to consider using only one single-gate HEMT. The second FET in the cascode boosts the output impedance of the amplifier and improves the isolation of the input and output, but at the same time

adds to the power dissipation and possibly to the noise of the amplifier. In practice, the power gain cannot be fully realized since the output must always be matched to a $50\ \Omega$ transmission line. The matching network required to reach the higher output impedance would need to have a higher Q which is often not achievable.

A more critical problem with the cascode amplifier design is that heat sinking of the second FET in the cascode is very difficult. Only one of the FETs has a source lead which may be soldered to a heat sinking ground lead. Since insulators are generally excessively poor conductors at 100 mK, a direct connection may be required for heat sinking. Thermal conduction through the first transistor could cool the second, but this is also not very effective. So, if we can manage the increased input-output coupling without stability problems, the single-gate HEMT amplifier design would be far preferable.

4.2.1 Cryogenic HEMT Performance

It has been noted that room temperature performance of FETs is not a good indicator of cryogenic performance [36], so the choice of the most appropriate FET for cryogenic use is not trivial. A survey of the literature and the limitations on availability of a small order of HEMTs lead us to Fujitsu, where we initially selected the FHC40LG HEMT. The FHC40LG is a good starting point because it is the lowest frequency rated HEMT offered by Fujitsu (but it is still intended for 4 GHz operation). While this transistor was used for a short time, we soon switched to the FHX13LG after finding it had a much higher input impedance due to having a much narrower gate and channel. Although all the data and amplifiers studied here use

the FHX13LG, the FHC40LG may still be more appropriate for some applications, especially at lower frequencies where $1/f$ noise is a concern.

To get an understanding of the internal construction of the HEMT, the ceramic cover of a FHX13LG is removed. Figure 4.1 shows a photograph of the magnified



Figure 4.1: Fujitsu FHX13LG HEMT with the ceramic cover removed. The gate lead is at the bottom, the drain is at the top, and the side leads are both connected to the source. Carriers in the channel are conducted in the vertical direction.

HEMT, revealing the geometry of the internal connections. In order to minimize the effect of magneto-resistance [46], the current conduction in the channel should be parallel to the 5 T magnetic field used in our experiments. Therefore, we build all of our amplifiers such that the HEMT has the appropriate orientation in the field.

Since the Fujitsu FHX13LG HEMT is intended for such high frequencies (12 GHz), many of its characteristics at 64 or 200 MHz can be determined from its DC characteristics. In particular, the transconductance and output resistance are easy to measure at DC.

The transconductance of the FET can be determined from the change in drain current I_D while sweeping the gate voltage V_G at constant drain-source voltage V_D . The results are shown in Figure 4.2, with the HEMT at room temperature and 4 K.

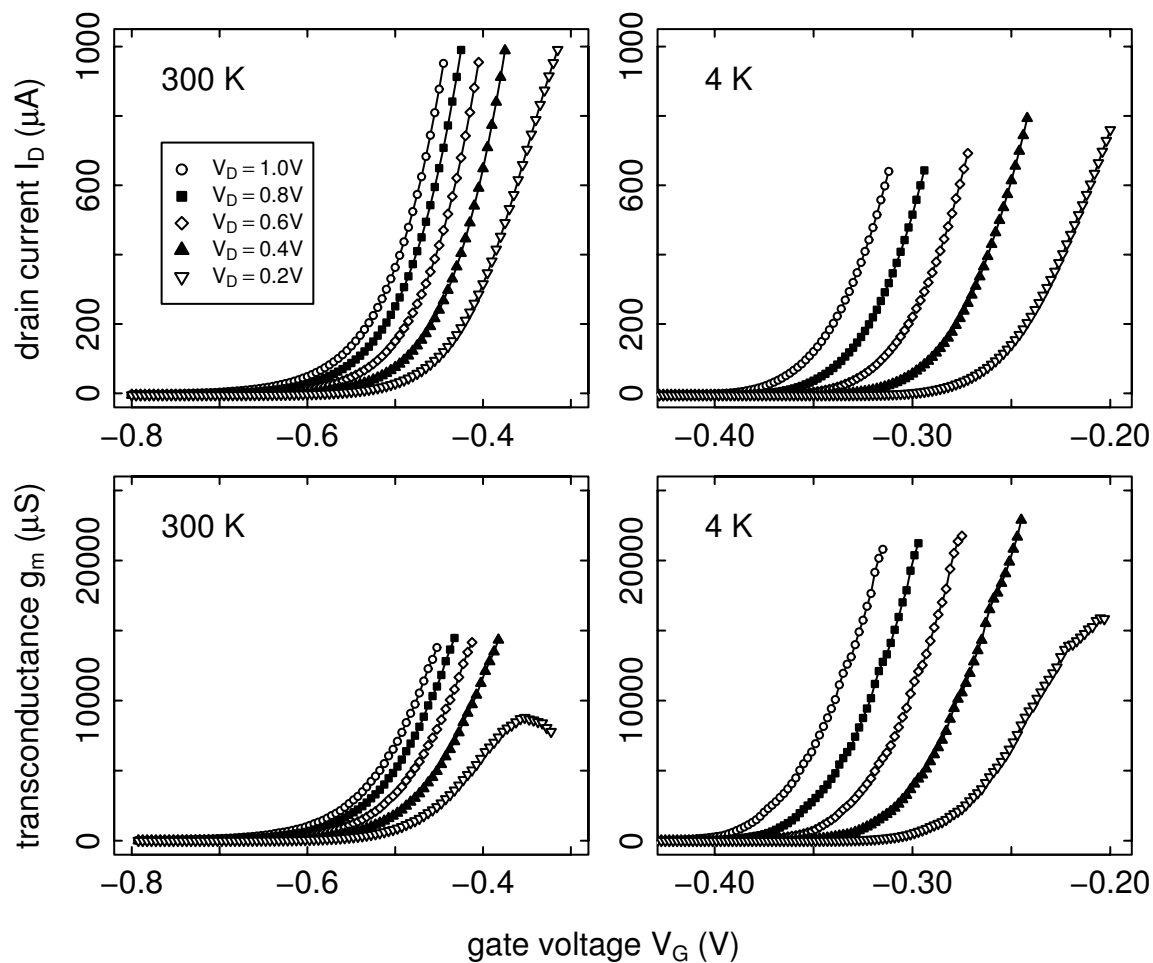


Figure 4.2: DC characteristic curves (top) of a Fujitsu FHX13LG HEMT at 300 K (left) or 4 K (right). The transconductance (bottom) is found from the slope of the characteristic curves.

The transconductance g_m is found from the slope,

$$g_m = \left. \frac{dI_D}{dV_G} \right|_{V_D}. \quad (4.1)$$

At 4 K the transconductance is about twice as large as at room temperature for the

same drain current. At 4 K, it is possible to obtain a transconductance higher than 5 mS (1 mS = 10^{-3} A/V) while only dissipating 10 μ W of power or transconductance higher than 20 mS if more power dissipation is acceptable. This low power transconductance is comparable to that of the Harvard-built HFET, but the FHX13LG will provide a much higher transconductance at the cost of higher power.

In practice, the power gain of the amplifier is more important than the transconductance. The power gain also involves the input and output resistances of the HEMT. The output resistance can be measured at DC from the drain current I_D while sweeping the drain voltage V_D at constant gate voltage V_G , as shown in Figure 4.3 with the HEMT at room temperature and 4 K. The output resistance R_D is found from the slope,

$$R_D = \left(\left. \frac{dI_D}{dV_D} \right|_{V_G} \right)^{-1}. \quad (4.2)$$

The output resistance of the HEMT is also modified at cryogenic temperatures, although the value of the output resistance can vary widely at room temperature and 4 K depending on the bias settings. On the whole, the output resistance of the single-gate HEMTs is lower than that of dual-gate MESFETs, which gives a lower power gain in principle. However, much of the power gain in a dual-gate MESFET amplifier may not be utilized because of the impedance matching difficulties.

Measurement of the input resistance of the HEMT is not as simple as measurement of the transconductance or output resistance because it cannot be determined from DC measurements. At DC, the HEMT input appears almost purely capacitive. At 64 MHz, the capacitance can be tuned out by inclusion in a tuned circuit. From the input Q of amplifiers for 64 MHz, we estimate that the parallel input resistance

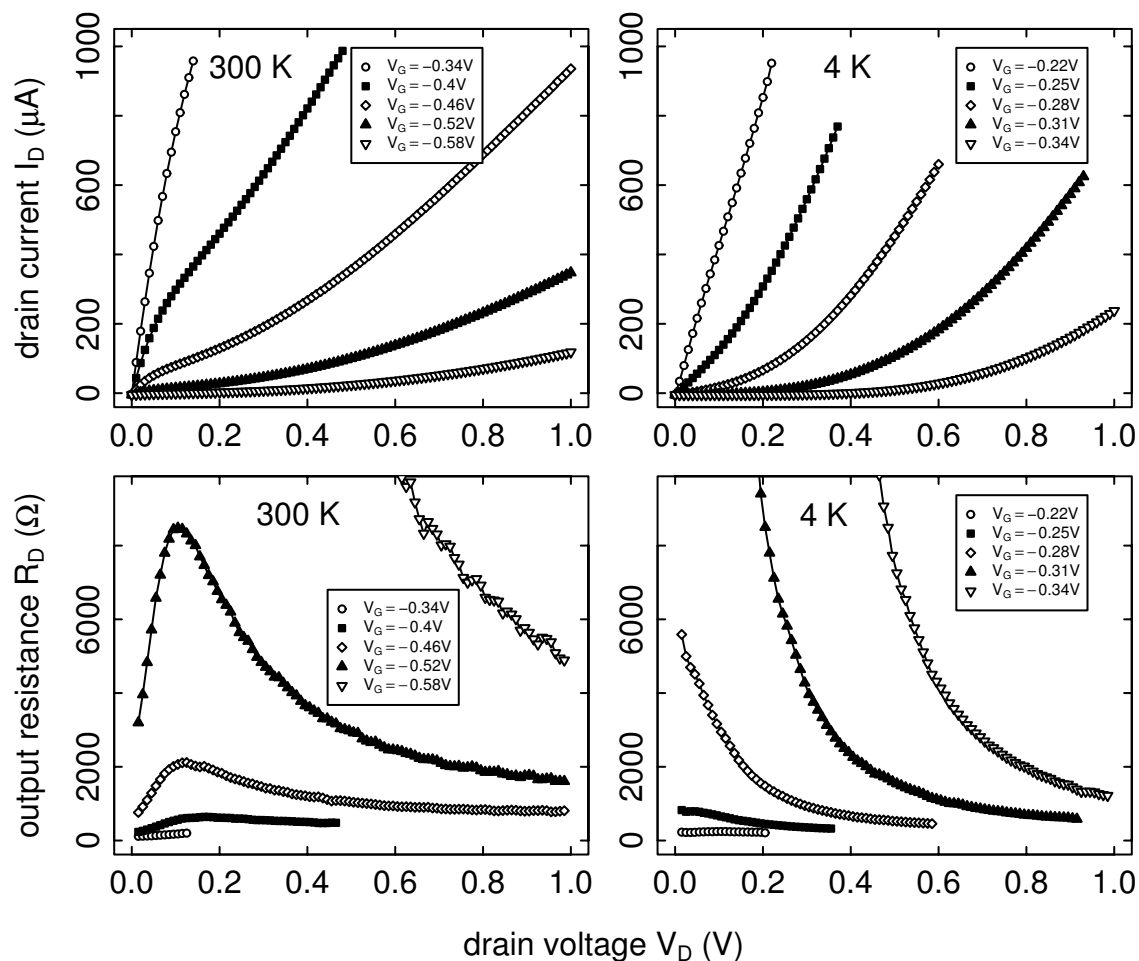


Figure 4.3: DC characteristic curves (top) of a Fujitsu FHX13LG HEMT at 300 K (left) or 4 K (right). The output resistance (bottom) is found from the slope of the characteristic curves.

of the HEMT is $100\text{ k}\Omega$ at 4 K and 64 MHz. This is much higher than the input resistance of either the Harvard made HFET or the traditional Mitsubishi MESFETs, and contributes to the higher power gain and improved signal to noise ratio we have obtained with HEMT based amplifiers.

4.2.2 Feedback and Stability

The motivation for studying the effects of feedback in a single-gate HEMT amplifier is that this simple amplifier design can give significant experimental improvements in the signal to noise ratio and heat sinking of the amplifiers. Without the second FET in a cascode circuit or the second gate of a dual-gate FET, minimization of the problems due to feedback depends heavily on the detailed design of the circuit instead of being handled actively by the circuit. However, we have not found that stability is automatic even with a dual-gate FET or cascode, so the simpler design of a single-gate amplifier may be overall easier to design and control.

Model HEMT

Our model HEMT is shown in Figure 4.4 (a), along with our labeling conventions

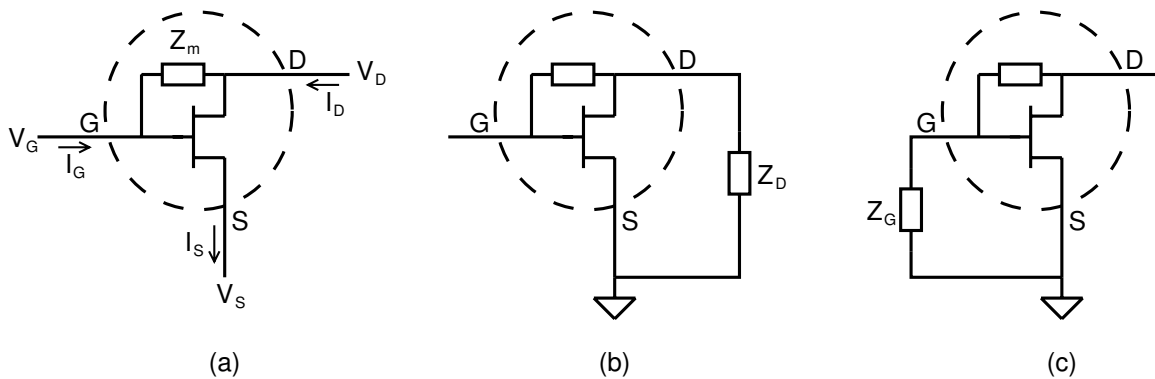


Figure 4.4: Single-gate model HEMT with feedback (a), model HEMT with drain load (b), and model HEMT with gate load (c). Components inside the dashed circle are modeled as being internal to the device.

for voltages and currents. The model HEMT is an ideal FET with infinite input and output impedances and transconductance g_m , but with finite gate-drain impedance Z_m . Often, Z_m is identified as the Miller capacitance, but we leave it more general for

now. In calculations, we include the intrinsic finite input and output impedance as part of the external load since they are typically involved in external tuned circuits.

There are three equations to describe the behavior of the model HEMT:

$$I_G + I_D - I_S = 0 \quad (4.3)$$

$$I_G = \frac{V_G - V_D}{Z_m} \quad (4.4)$$

$$I_S = g_m V_G. \quad (4.5)$$

The third equation describes the ideal FET embedded in the model HEMT. In order to get useful properties of the feedback through Z_m , we will have to add a load to the gate or drain.

Feedback from Drain Load

In order to see the effect of feedback on the amplifier input impedance, we add a load to the output by connecting the drain to the source with a finite impedance Z_D as in Figure 4.4 (b). We also ground the source as is done experimentally. This adds only one more equation to the behavior of the circuit,

$$V_D = -I_D Z_D. \quad (4.6)$$

After some algebra, we find the effective impedance ($Z_{in} = V_G/I_G$) looking into the gate of the amplifier,

$$Z_{in} = \frac{Z_D + Z_m}{1 + g_m Z_D}. \quad (4.7)$$

To get a better understanding of the behavior, we work out a few examples. At a frequency of 64 MHz, let Z_m be a 0.1 pF capacitor and the transconductance $g_m = 5$ mS. The results for several drain loads are summarized in Table 4.1.

frequency	Z_D	$Z_{in} (\Omega)$	$R_p (\Omega)$	$C_p (pF)$
64 MHz	1.0 k Ω resistor	$167 - 4144i$	$103k$	0.60
64 MHz	4.0 pF capacitor	$7431 - 2391i$	$8.2k$	0.10
64 MHz	1.2 μ H inductor	$-8625 - 3575i$	$-10k$	0.10
200 MHz	1.0 k Ω resistor	$167 - 1326i$	$11k$	0.59
200 MHz	4.0 pF capacitor	$4078 - 4100i$	$8.2k$	0.098
200 MHz	0.47 μ H inductor	$-2238 - 758i$	$-2.5k$	0.11

Table 4.1: Amplifier input impedance Z_{in} due to feedback for several drain loads. The input impedance is also expressed as parallel resistance R_p and parallel capacitance C_p .

The results for Z_{in} are complex impedances, where the real and imaginary parts represent the series resistance and reactance, respectively. The table also shows Z_{in} expressed as a resistor R_p and a capacitor C_p in parallel. With a resistive drain load, the feedback adds a primarily capacitive load to the FET input, which would shift the input resonance lower in frequency. With a capacitive drain load, the feedback puts on resistive load on the input tuned circuit, effectively lowering the Q of the amplifier. For an inductive drain load, there is a significant *negative* resistive load on the input tuned circuit. A negative resistance corresponds to positive feedback which increases the apparent Q of the input tuned circuit. If this positive feedback is strong enough, the amplifier will oscillate near the center frequency of the input tuned circuit. Note that the values used in this example calculation are extreme. They are meant to give a qualitative indication of the feedback behavior. Still, they demonstrate how much feedback could modify circuit behavior.

The lesson to take away from these examples is that an inductive drain load must be avoided to improve stability by decreasing positive feedback. Our typical output network (the π -net) presents an inductive load at frequencies below resonance, a

resistive load on resonance, and a capacitive load above resonance. The moral is that the input network should align with the middle to high frequency side of the output network resonance if regeneration and oscillation are to be avoided. Placement of the input tuned circuit resonance below the output tuned circuit resonance should be avoided. The negative feedback which results from aligning the input circuit with the high frequency side of the π -net resonance may decrease the Q , but negative feedback is much easier to control than positive feedback.

Feedback from Gate Load

In order to see the effect of feedback on the amplifier output impedance, we add connect the gate to the source with a finite impedance Z_G as in Figure 4.4 (c). Without any feedback, there is of course no current on the gate, so this load is only relevant with feedback. This adds only one more equation to the behavior of the model HEMT,

$$V_G = -I_G Z_G. \quad (4.8)$$

After some algebra, we find the effective impedance ($Z_{out} = V_D/I_D$) looking into the drain of the amplifier,

$$Z_{out} = \frac{Z_G + Z_m}{1 + g_m Z_G}. \quad (4.9)$$

To get a better understanding of the behavior, we again work out a few examples at frequency of 64 MHz, with Z_m as a 0.1 pF capacitor and transconductance $g_m = 5$ mS. The results for several gate loads are summarized in Table 4.2.

Feedback to the amplifier output due to Z_G is similar to that to the input from a drain load. The primary difference is that the gate load far from the tuned circuit

frequency	Z_D	$Z_{out} (\Omega)$	$R_p (\Omega)$	$C_p (pF)$
64 MHz	25 k Ω resistor	198 – 197 <i>i</i>	395	6.3
64 MHz	5.0 pF capacitor	8780 – 3531 <i>i</i>	10 <i>k</i>	0.1
64 MHz	1.2 μ H inductor	–8625 – 3575 <i>i</i>	–10 <i>k</i>	0.10
200 MHz	8.3 k Ω resistor	195 – 187 <i>i</i>	375	2.0
200 MHz	2.0 pF capacitor	835 – 67 <i>i</i>	840	0.076
200 MHz	0.63 μ H inductor	–3747 – 2958 <i>i</i>	–6.0 <i>k</i>	0.10

Table 4.2: Amplifier output impedance Z_{out} due to feedback for several gate loads. The output impedance is also expressed as parallel resistance R_p and parallel capacitance C_p .

resonance (such as a 5.0 pF capacitor) provides insignificant feedback since the output impedance is normally low (~ 1 k Ω) to begin with. However, the feedback is very significant near or on the input tuned circuit resonance where the gate load may be a very high impedance. In practice, we see that the output matching to a coaxial line is significantly perturbed at frequencies in the immediate vicinity of the input tuned circuit resonance.

Unfortunately, the feedback from a resistive gate load presents a capacitive drain load, effectively making the output network appear shifted lower in frequency at the input tuned circuit resonance frequency. This makes the impedance mismatch from the misalignment of the input and output desired for stability even worse. To optimize the output coupling, it may be useful to treat the HEMT output like a lower impedance than it is without feedback if the amplifier Q on an experiment is known. We make little effort to compensate for the output impedance changes due to feedback, in part because the strength of this feedback depends highly on the Q of the input circuit, which tends to be different while testing and when on an experiment. Instead, we match the output impedance to the coaxial cable near but not on the

input tuned circuit center frequency.

Feedback from Source Load

It is possible to add a finite impedance between the HEMT source and ground. This can also add positive or negative feedback. While this method of adding feedback is easily controlled and thus can be used to make an amplifier with noise temperature below the ambient temperature, we are not concerned with a detailed analysis because the source lead should be soldered directly to a grounded heat sink to cool off the HEMT as quickly as possible. Heat sinking through an inductor or capacitor would likely slow down the cooling of the HEMT.

4.3 Single-Gate HEMT Amplifiers

With the need for new transistors in our amplifiers, there was an opportunity for a more thorough review of the amplifier design. Our traditional design used mostly through-hole components arranged in a three dimensional layout with the transistor straddling across two sides of a circuit board to isolate the input and output. The inductors were hand wound, and the capacitors required bends in the leads to relieve strain for cooling down to 4 K.

4.3.1 Cryogenic Surface Mount Components

The Fujitsu HEMTs are compact, surface mount devices. So, if surface mount substitutes compatible with cryogenic temperatures are available, the entire amplifier can be built on a printed circuit board. Suitable non-magnetic surface mount induc-

tors are available from Coilcraft in a variety of sizes. COG (or NP0) capacitors are both stable enough in value to be usable and durable enough to survive the thermal cycling, although it appears that they may be likely to fail during thermal cycling if they are overheated while soldering.

For use down to 100 mK, thin (metal) film resistors should be used, since thick film (usually ruthenium oxide) resistors have such a large temperature dependence that they are used as temperature sensors for dilution refrigerators. We have found that thick film resistors cannot even reliably be used for the gate biasing resistors where the exact resistance is not crucial.

In our most recent amplifiers, SMA connectors have replaced micro-coax lines soldered directly to the board. These give a much more robust connection to the circuit board than the directly soldered micro-coax lines, which can tear pads off of the circuit board if excessively stressed.

The amplifier circuit boards are copper clad FR-4 (G-10) or Teflon with the layout defined by machining some of the copper away with a computer numerical control (CNC) mill. The copper is plated with tin before soldering on components. We have found that an electroless tin plating solution works well without damaging the board.

Photographs of several HEMT based amplifiers are shown in Figure 4.5, including first and second stage amplifiers for 64 MHz and 200 MHz axial frequencies.

4.3.2 Common Amplifier Circuit Features

Several features have become standard in all of our modern amplifier circuits. These are particularly important for heat sinking the HEMTs and controlling the

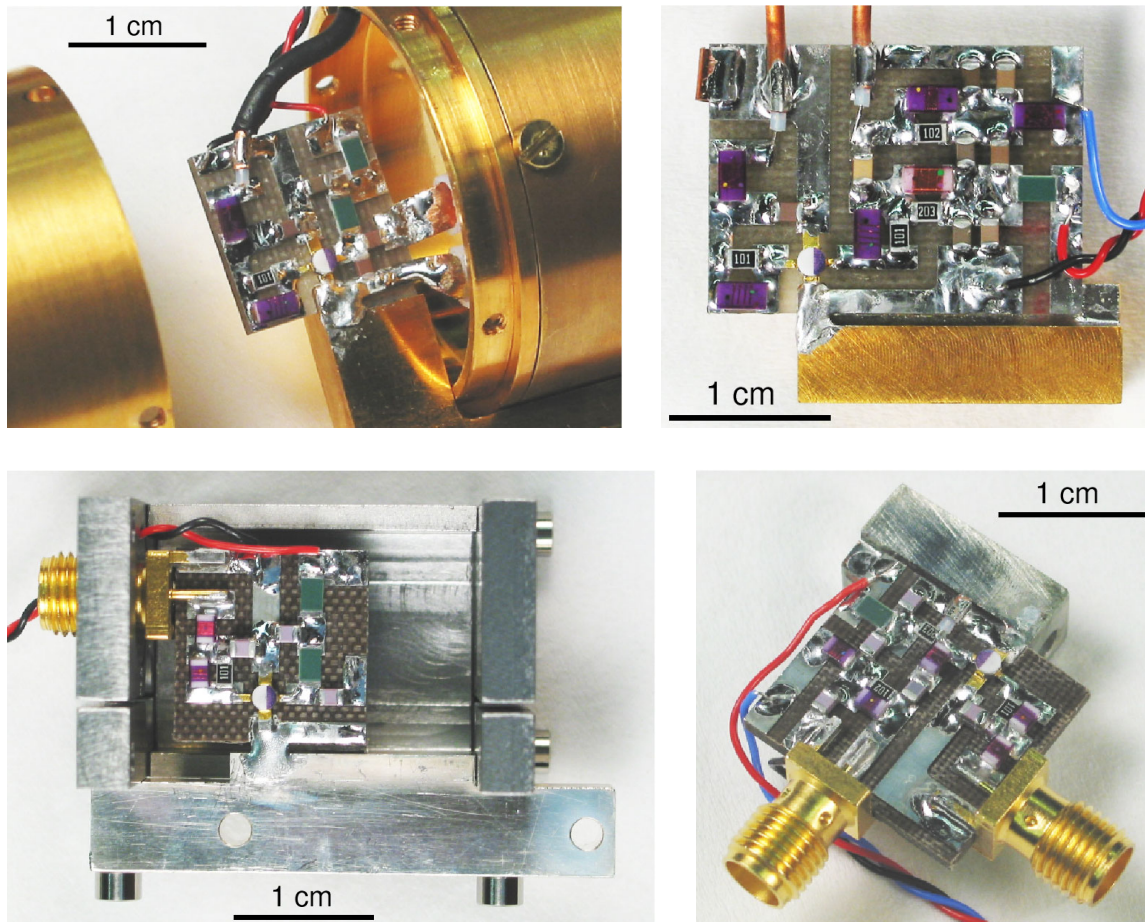


Figure 4.5: Photographs of the 64 MHz amplifiers (top) and 200 MHz amplifiers (bottom), with the first stage amplifiers (left) and second stage amplifiers (right).

coupling between the input and output circuits.

Surface mounting all components allows a natural method of heat sinking the HEMT. The amplifier circuit board is machined with a slot on one side, where a thick nub of copper or silver sticks through to act as a soldering pad for the HEMT source lead to ground. The metal nub is part of a larger piece which can be screwed directly to the tripod under the mixing chamber or other surface. However, the rated maximum storage temperature for the HEMT is 175 °C. Above this temperature the materials and dopants that define the HEMT may diffuse around excessively.

Soldering the HEMT to the heat sink nub with lead/tin solder requires so much heat ($> 191\text{ }^\circ\text{C}$) that it often degrades the performance of the HEMT, leading in particular to regeneration or oscillation at 4 K. We have found that we can instead use an indium52/tin48 eutectic solder alloy which melts at $118\text{ }^\circ\text{C}$ to make the electrical connection without damaging the HEMT.

Although the HEMT chip is mounted on an alumina (Al_2O_3) substrate, heat sinking is primarily accomplished through the source lead at 4 K. Since this means the wire bonds from the source on the chip to the source on the case are important thermal conductors, the professional packing may be a major advantage over the Harvard made HFET. The commercial HEMT has 4 short wire bonds thanks to the carefully cut chip and tightly fitting package, while our typical packaging of the HFET uses only one or two wires which are much longer.

The use of surface mount components and machined circuit boards has made it possible to obtain reproducible performance from amplifiers with the same component values. Previous amplifiers relied on careful layout of the components during assembly to control coupling. With surface mount components and carefully designed circuit boards, the layout can be planned in advance to minimize coupling.

Care is taken in all amplifier designs to minimize coupling between the input and output circuits. The HEMT has two source leads, which allows separation of the source current for the input and the source current for the output. By splitting the input and output source currents, coupling which would result from any inductance or resistance along the common path is eliminated. The circuit board traces that extend the source leads form a ground strip separating the input and output circuits.

Furthermore, the ground plane on the back of the circuit board is split so that the input and output circuits have independent ground planes which are joined together through the HEMT, so all currents in the ground planes are controlled. To cut down on any resonances that could develop as a result of this separation, the two sides are joined with a $100\ \Omega$ resistor on the back of the board. This split and rejoined ground plane detail is not visible on the individual amplifier circuit schematics or diagrams, but is recommended.

4.3.3 64 MHz First Stage

The first surface mount amplifier we built was a first stage amplifier for use at 64 MHz. The amplifier input uses an inductor placed in parallel with the trap to cancel out the 13 pF trap capacitance. Figures 4.6 and 4.7 show the circuit schematic and assembly of the amplifier.

The input tuned circuit inductor is enclosed in a gold plated copper can to form a high Q inductor resonator [47] with the trap capacitance. Since the Q of this circuit is critical in determining the signal to noise ratio for detection of the axial motion of the electron, the tuned circuit is coupled to the HEMT through a voltage divider made from two capacitors. The voltage divider decreases the loading down of the tuned circuit Q by the finite input resistance of the HEMT. In previous designs, the connection to the FET was made by “tapping down” on the inductor by connecting the FET only a few turns up the inductor to form a voltage divider. Here, a capacitive voltage divider is used instead to avoid undesirable additional resonances. With a capacitive divider, the input capacitance of the HEMT adds in parallel with one of

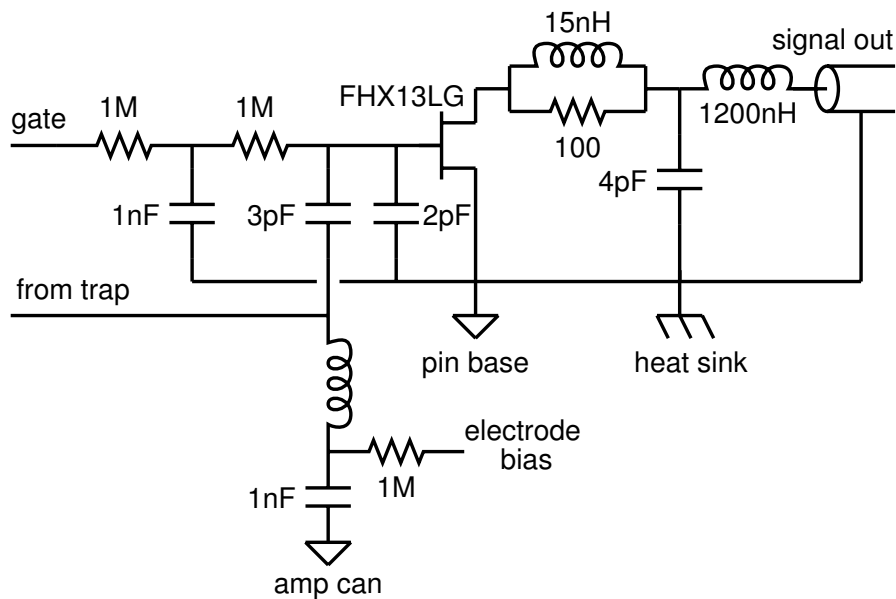


Figure 4.6: First stage 64 MHz amplifier schematic. Values without units are resistances in ohms.

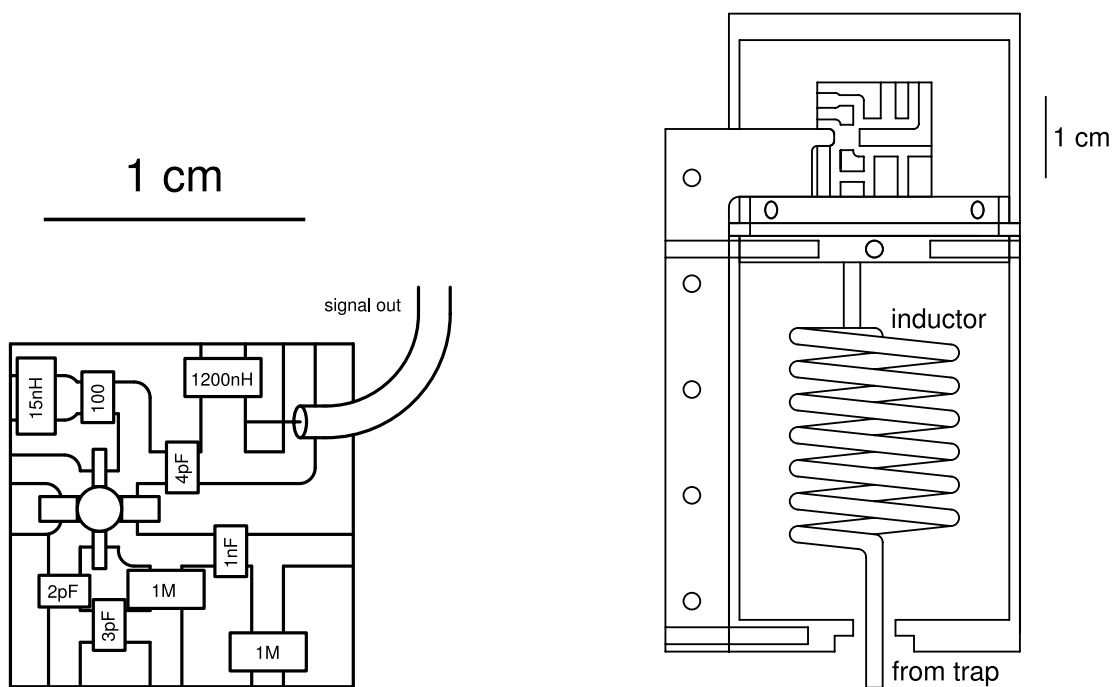


Figure 4.7: First stage 64 MHz amplifier board layout. Values without units are resistances in ohms.

the capacitors used in the voltage divider.

The output of the amplifier is coupled to the coaxial output line by a simple tuned circuit which also includes the output reactance of the HEMT. In dual-gate amplifiers, a second capacitor is usually used directly in parallel with the output coaxial cable in order to accomplish a larger impedance transformation. This matching network is commonly known as a π -net. The second capacitor is typically not needed with a single-gate HEMT amplifier because of the smaller impedance mismatch.

Between the HEMT and output network, there is a 15 nH and 100 Ω resistor in parallel. This pair of components, which has been traditionally called a “suppression circuit”, adds loss at high frequencies in order to help suppress oscillations at high frequencies. The small inductor value is chosen so that the suppression circuit has little effect at 64 MHz. Experience has shown that adding loss almost anywhere in the output circuit has a similar effect in improving stability, but adding more loss beyond this does not seem to further improve stability.

The noise resonance observed with the amplifier at 4 K is shown in Figure 4.8. The input tuned circuit Q as measured from the shape of the noise resonance is > 1200 when tested with a 13 pF capacitor to take the place of the trap. When used on the experiment with the trap in place of the capacitor, the Q typically drops to ~ 400 . We believe that this loss in Q is largely due to losses in the extended leads and feedthrough between the trap electrode and amplifier. The slight asymmetry in the tuned circuit resonance is due to the changing feedback caused by the gradual change in the drain load impedance and more importantly from the change in output coupling due to the feedback from the rapidly changing input impedance across the

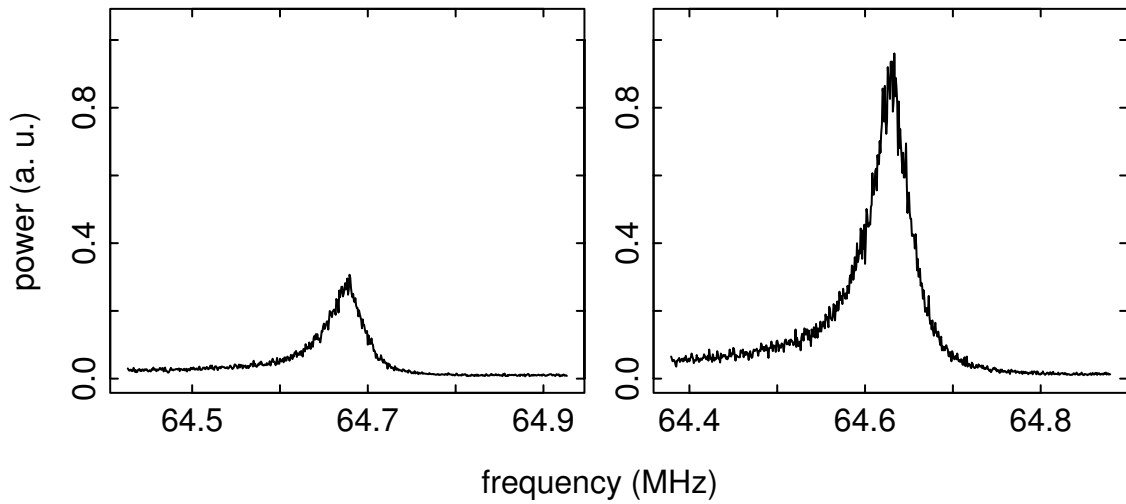


Figure 4.8: First stage 64 MHz amplifier noise resonance connected to a test capacitor with $V_D = 0.2$ V, $I_D = 60$ μ A (left), and with $V_D = 1.0$ V, $I_D = 120$ μ A (right).

tuned circuit resonance.

We can learn more about the output coupling by looking at the signal reflection off of the output of the amplifier as in Figure 4.9. This reflection can be measured

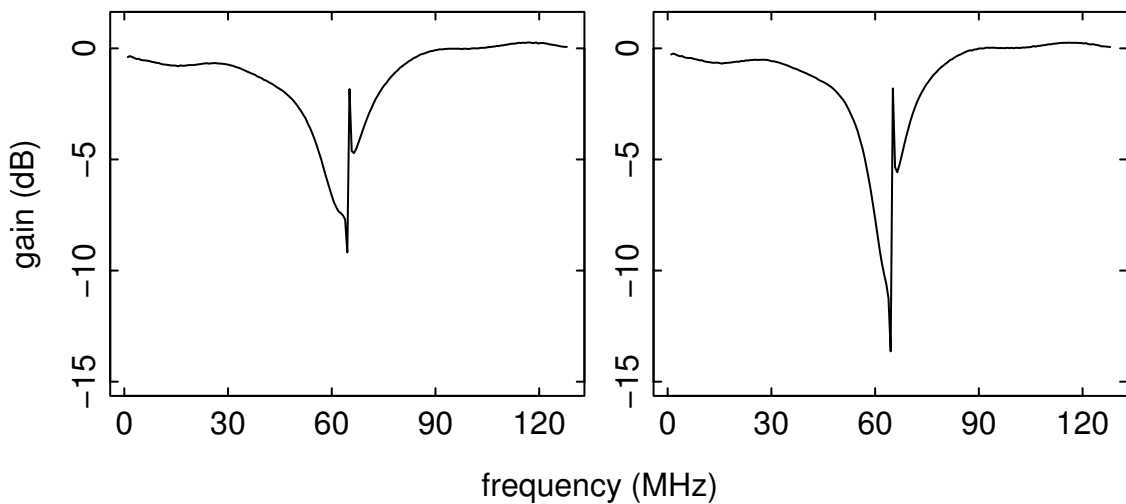


Figure 4.9: Reflection off the 64 MHz first stage amplifier output with $V_D = 0.2$ V, $I_D = 60$ μ A (left), and with $V_D = 1.0$ V, $I_D = 90$ μ A (right).

with the aid a network analyzer, which sends a test signal backward down the output

coaxial cable and measures the the reflected signal. In this case we are looking at only the magnitude of the reflected signal. The attenuation after reflecting gives a measure of how well the impedance of the amplifier output is matched to the cable. The broad dip seen in the reflection at either low or high power is the resonance of the output network of the amplifier. In this case, the dip is slightly deeper at higher power indicating slightly improved impedance matching. The sharp feature in the broad dip is caused by the change in output impedance due to the interaction of the input network with feedback. Note that it is clear from the reflection that the input tuned circuit frequency is positioned just above the output tuned circuit center frequency as desired for stability. This simple test, which requires only the amplifier to be cold, provides a strong signal and a complete characterization of the amplifier. In practice, it is often easier to locate the input tuned circuit resonance with this method than directly looking for the noise resonance when an amplifier is first constructed and the resonant frequency of the input tuned circuit is not known.

Axial Temperature Results

The most important consequence of improved amplifiers for the g factor measurement is a decrease in axial temperature due to the heroic heat sinking of the HEMT. Figure 4.10 shows the cyclotron quantum jump spectrum measured with the amplifiers on and off. With the amplifiers on, the axial temperature is determined to be ~ 5 K, similar to previous HEMT amplifiers. However, with the amplifiers off, the axial temperature drops to 320 mK. The cyclotron lineshapes are fit to exponential lineshapes as discussed in Chapter 3, and drive saturation effects are included.

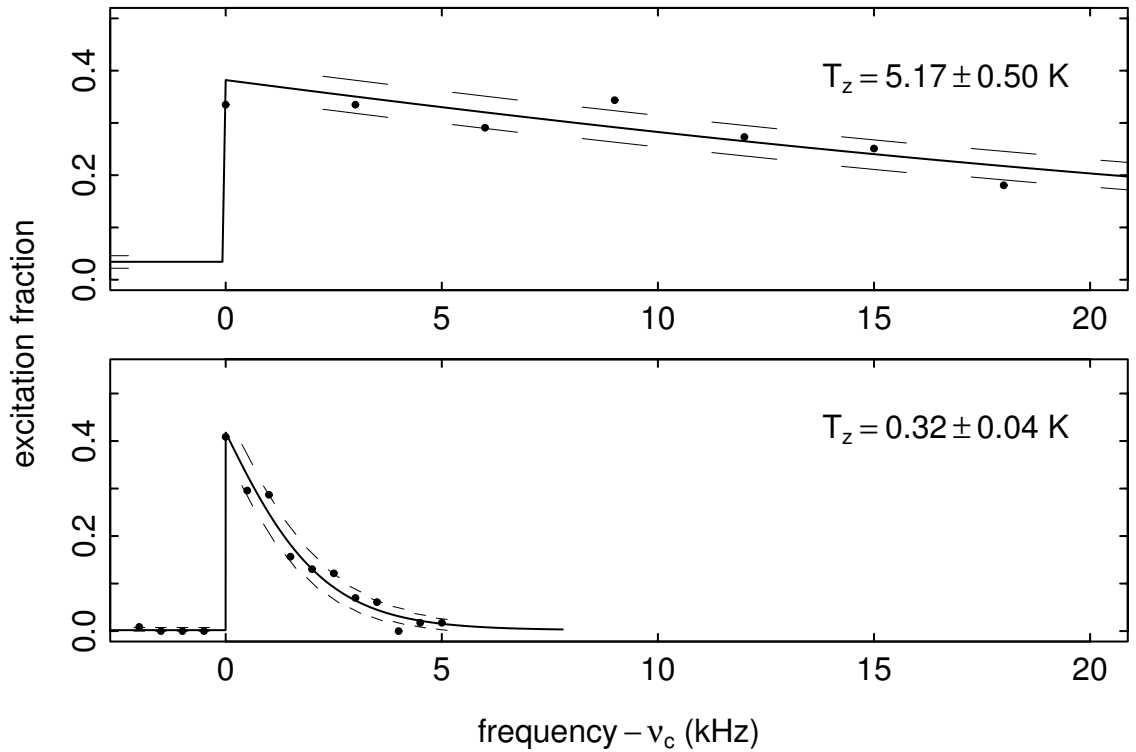


Figure 4.10: Cyclotron resonances with the the cryogenic amplifiers on (top) or off (bottom). The measured axial temperatures are also shown. The dashed lines show the expected 68% confidence region for the data.

For the coldest temperature, both the first and second stage cryogenic amplifiers are turned off. Leaving the second stage amplifier on results in a higher temperature of 680 mK. When on, the second stage amplifier produces both Johnson and shot noise which are transmitted back to the first stage amplifier. Some of this noise passes backward through the first stage amplifier and heats the particle.

Although the axial temperature did not reach the ambient temperature of 100 mK, it is a huge improvement over any previously measured axial temperature. The remaining elevation above the ambient temperature does not necessarily mean that the amplifiers have not cooled down, it may be caused by noise getting to the particle

from other sources.

Cooling Time Constant

Further information can be acquired from the change in the physical temperature of the amplifier when it is turned off. A temperature sensor mounted on the heat sink and support plate of the first stage axial amplifier shows an elevated temperature when the amplifier is on (dissipating $10 \mu\text{W}$) which decreases when the amplifier is shut off. A similar temperature change occurs when a “dummy” heater mounted to the same part of the amplifier is turned off after heating the amplifier with about the same power level as the amplifier dissipates when in operation. When on, each was allowed to come to equilibrium over many hours. Both responses are shown in Figure 4.11. A small difference in power dissipation causes the temperatures to start at slightly different values.

The cooling behavior, which is more complex than the simple exponential that might be expected, is caused by the response of the dilution refrigerator. There are two cooling steps taking place. The first is the conduction of heat from the amplifier to the support tripod and mixing chamber. The second is the cooling of the mixing chamber by the dilution refrigerator circulation with less heat load from the amplifier.

An equivalent electrical model for the cooling behavior of the amplifier is shown in Figure 4.12. The heat capacity of the amplifier is represented by C_{FET} , while the temperature of the amp is T_{FET} . The thermal resistance between the amplifier and mixing chamber is R_{FET} . C_{mc} and R_{mc} give the time scale for the mixing chamber to be cooled by the dilution refrigerator. While the time dependence of this system is in

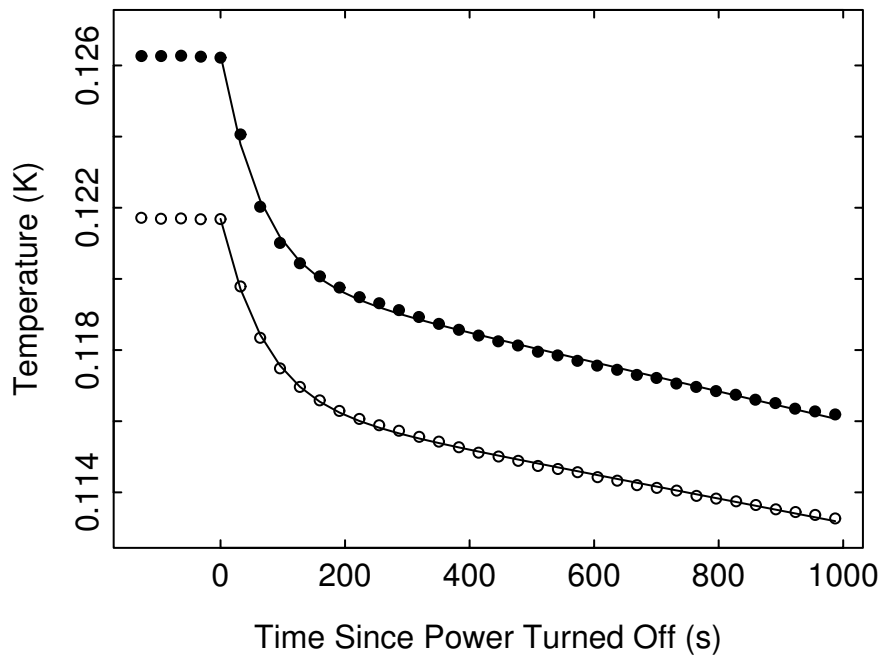


Figure 4.11: Temperature of the first stage amplifier heat sink after the amplifier was turned off (open circles) or after a heater on the heat sink was turned off (closed circles). When on, each was dissipating about $10 \mu\text{W}$.

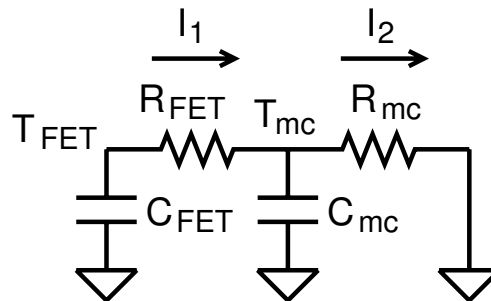


Figure 4.12: Equivalent electrical model for the FET cooling analysis.

general complex, the change in temperature of the mixing chamber is so small that we can assume that I_2 is constant, that is heat is extracted from the mixing chamber at a constant rate. Then requiring that $I_1 = I_2$ initially, the time dependence has the

form

$$T_{FET}(t) = A - Bt + Ce^{-t/\tau}, \quad (4.10)$$

where A , B , and C are constants that are not interesting for us, while τ gives the time constant for the amplifier to cool down. The linear term with coefficient B represents the cooling of the mixing chamber by the dilution refrigerator. A linear approximation of this cooling is valid because the time scale of the test is short compared to the cooling time scale of the mixing chamber. Fits to the data show that the cooling time constants are $\tau = 66 \pm 2$ s after turning off the dummy heater, $\tau = 71 \pm 2$ s after turning off the HEMT.

The mostly insignificant difference between the two time constants shows that the HEMT itself is cooling off quickly, or at least nearly as quickly as the heater resistor. Otherwise it would take much longer for the amplifier to cool off after the HEMT is turned off than after the dummy heater is turned off. So, the slow step in the cooling appears to be the coupling between the heat sink plate and the mixing chamber, not the link between the HEMT and the heat sink.

4.3.4 64 MHz Second Stage

With only a first stage cryogenic amplifier, the final detected signal has a significant noise contribution from the first stage room temperature amplifier, even though it has a noise temperature of only 70 K. The reason is that with such low power operation, the gain of the first stage amplifier combined with the attenuation in the long length of stainless steel coaxial cable from the base temperature region to room temperature produces a signal which is small compared to the Johnson noise at 70 K.

A natural solution is the addition of a second stage cryogenic amplifier at an intermediate temperature which is cold enough to get a low noise temperature, close enough to the first stage to have little attenuation in the cable, but with high enough cooling power to handle a second amplifier. The still of the dilution refrigerator is an excellent choice because it is typically at a temperature less than 1 K but it can handle 1 mW of power.

The circuit schematic and board layout of the 64 MHz second stage amplifier are shown in Figures 4.13 and 4.14. The input circuit of the second stage amplifier is responsible for matching the impedance of the 50 Ω coaxial input to the HEMT and for biasing the first stage amplifier drain through the coax. The input matching network of the amplifier is similar to a standard π -net, except the inductors and capacitors are swapped. The switch was made because the modified network is more convenient for biasing both the first stage drain and second stage gate, since it allows both biases to be applied at low impedance points in the effective high frequency circuit, which minimizes the perturbation to the circuit and allows easy low-pass filtering of the bias voltages. Additionally, the modified π -net is more effective in attenuating low frequencies, where the standard π -net on the output of the first stage amplifier is more effective at attenuating high frequencies. Together, they form a more symmetric bandpass filter which is desirable for eliminating out of band noise. All inductors have resistors in parallel with them to damp out any high frequency resonances that might cause instability. The 20 k Ω resistor on the input to the HEMT also intentionally decreases the input impedance of the HEMT to improve stability. Finally, a suppression circuit is also added as part of the input circuit to add more

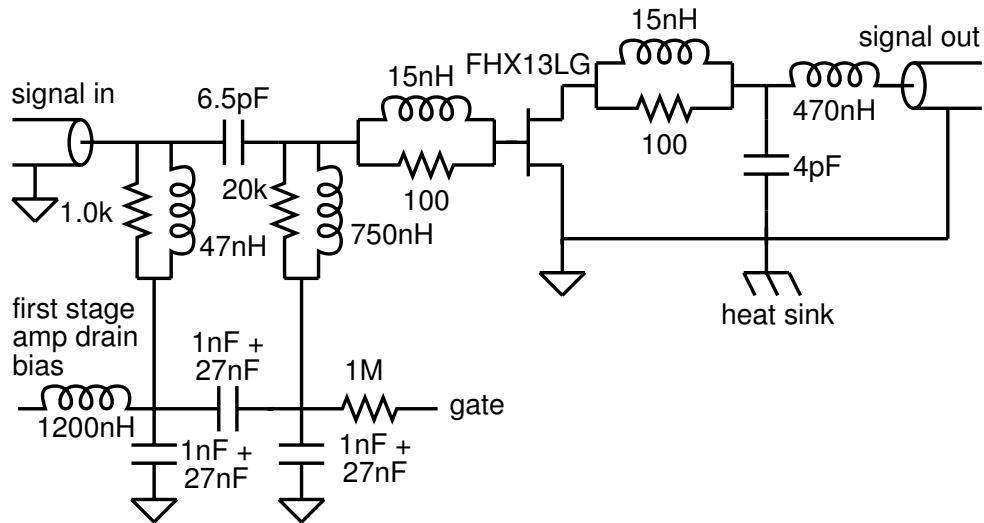


Figure 4.13: Second stage 64 MHz amplifier schematic. Values without units are resistances in ohms

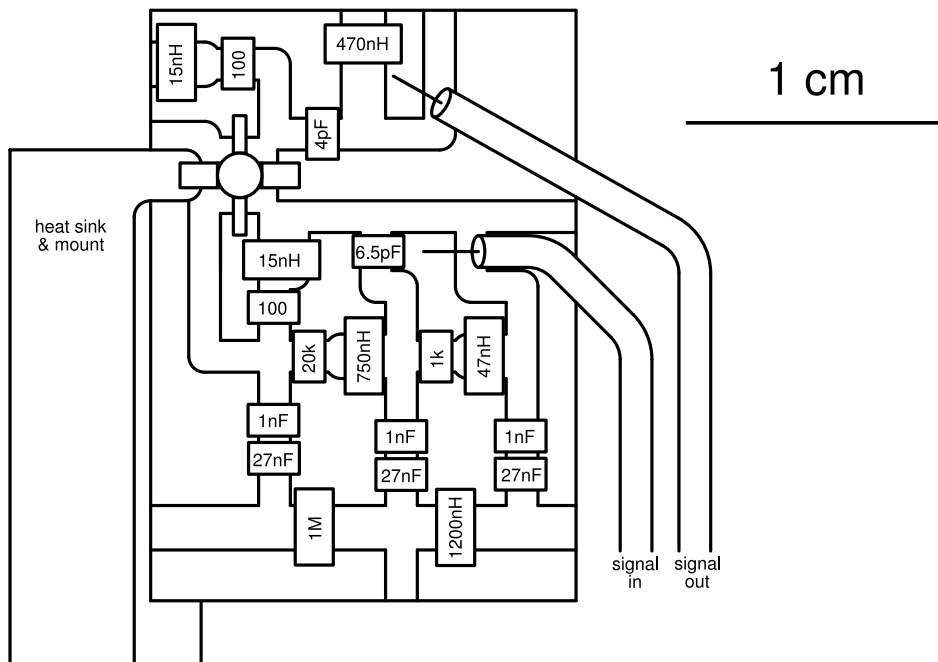


Figure 4.14: Second stage 64 MHz amplifier board layout. Values without units are resistances in ohms

loss and prevent oscillation at high frequencies.

The output network of the second stage amplifier is mistuned when compared to that of the first stage amplifier, as can be seen in the amplifier response in Figure 4.15. This mistuning, which puts the center frequency on the “wrong side” of the

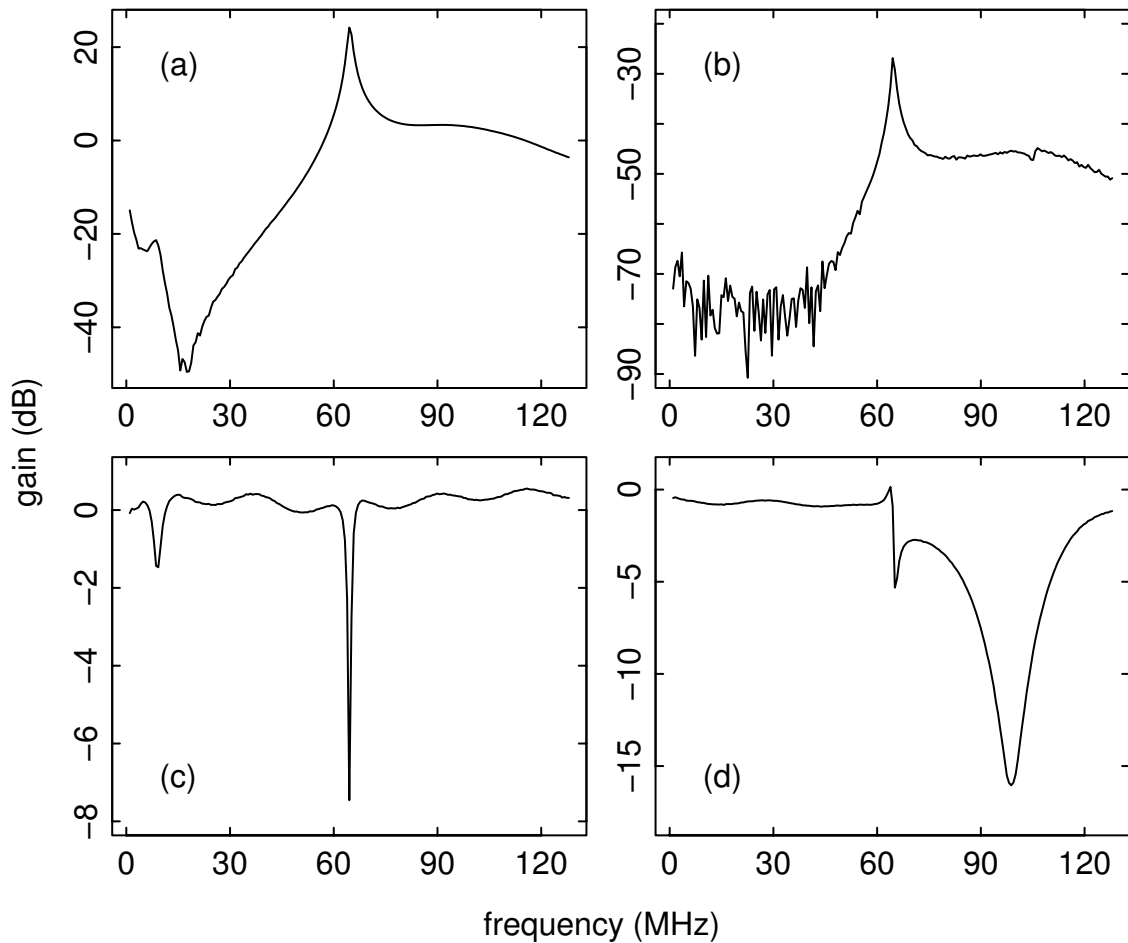


Figure 4.15: Response of the 64 MHz second stage amplifier: forward gain (a), reverse gain (b), forward reflection (c), and reverse reflection (d). The amplifier was biased to $V_D = 1.0$ V and $I_D = 130$ μ A.

π -net compensates for the modification of the output impedance by feedback due to the input impedance, so the output is matched at the center frequency. The input is also tuned for impedance matching, but the cost of this tuning is that there is

positive feedback to the input. The positive feedback increases the gain but decreases the usable bandwidth by narrowing the response. The gain over a much narrower frequency span is shown in Figure 4.16.

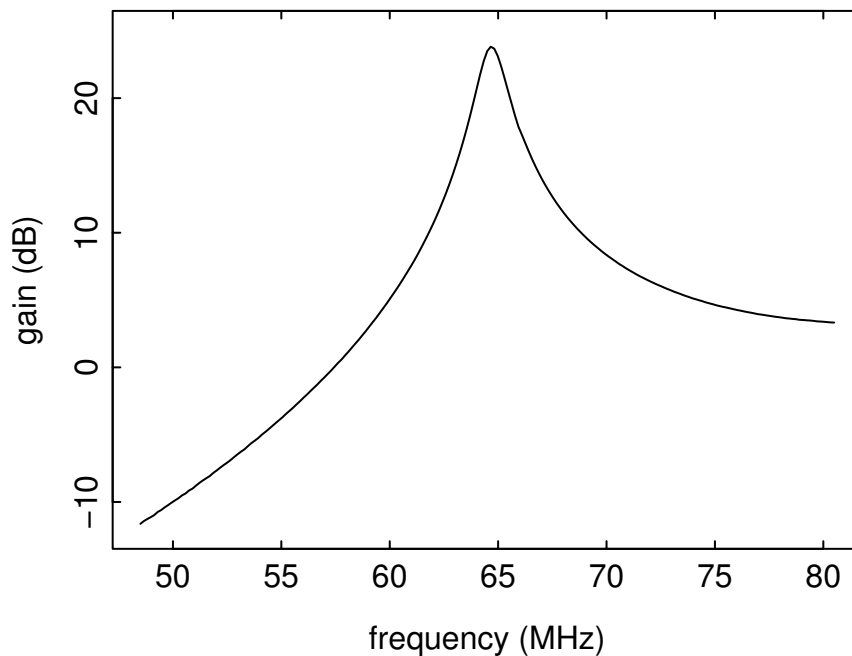


Figure 4.16: Forward gain of the 64 MHz second stage amplifier.

Positive feedback is tolerable in the second stage amplifier because the input impedance of the HEMT is intentionally made lower. In a first stage amplifier it would be far more likely to lead to instability. Even though the positive feedback is tolerable in a second stage amplifier, the bandwidth with high gain is small enough that the first stage amplifier was never well centered on the second stage. We were able to shift and broaden the response of the second stage amplifier by modifying the bias settings to those used for the data here. Despite the overall success of this design, the 200 MHz amplifier designed later is built with a negative feedback design

instead, and negative feedback is generally recommended for stable behavior.

Another function of the second stage amplifier is the attenuation of signals traveling backward down the signal line which might otherwise drive the particle and heat it up. The reverse attenuation of the second stage amplifier is also shown in Figure 4.15. The directionality of the amplifier (difference between forward gain and reverse gain) is over 50 dB.

The 64 MHz second stage amplifier has adequate gain to make the noise contribution from the following room temperature amplifiers almost negligible. The success of feedback cooling (see Chapter 5) with this amplifier as part of the feedback loop demonstrates the success of the amplifier chain.

4.3.5 200 MHz First Stage

Potential improvements in the g factor measurement from an increased axial frequency (see Section 2.3.3) prompted the consideration of moving the axial frequency up to 200 MHz. While the trapping potential modifications required to change the axial frequency are almost trivial, the detection of axial oscillations from a single electron at the increased frequency is not.

Challenges in building a higher frequency first stage amplifier come mostly from the increased importance of parasitic capacitance and inductance. Unfortunately, the construction of our trap and trap vacuum enclosure prohibit placement of the amplifier spatially close to the trap. Instead, the signal must travel a minimum of about 4 inches to get out of the vacuum enclosure and give clearance for access to the other feedthroughs. Cryogenic amplifiers which have been built for detection of the

proton cyclotron motion around 90 MHz have had significantly degraded Q, especially when the lead from the trap electrode to the amplifier is long. So, we expect even more serious problems at 200 MHz.

However, the difficulties with directly using our traditional amplifier design at 200 MHz are even more severe. While the inductor resonator used at 65 MHz has ~ 8 turns, at 200 MHz we would expect less than 3 turns. The inductance of the lead between the trap and the amplifier would reduce the number of turns even further. The result is that a lumped inductor is not usable in this application.

The solution is to use the distributed inductance and capacitance as a coaxial transmission line resonator, rather than trying to ignore or minimize them. The design and assembly of our first stage 200 MHz amplifier using a coaxial resonator is shown in Figures 4.17 and 4.18. The coaxial resonator is a tuned length of coaxial cable with the trap capacitance on one end and with the opposite end shorted. The shield of the coaxial transmission line on the trap end is connected to the top compensation electrodes, which have the most capacitance to the top endcap used for detection. The coaxial resonator serves two functions: it spatially transfers the signal from the trap to the amplifier and forms a tuned circuit with the trap capacitance. The length of the coaxial transmission line is less than $\lambda/4$ at 200 MHz so that it behaves like an inductor. The signal is picked off the transmission line near the middle of the line to be amplified by the HEMT. The HEMT is coupled to the transmission line with a 1 pF capacitor so that it minimally disturbs the transmission line characteristics.

In order to minimize losses in the transmission line tuned circuit, the diameter of the coaxial line is made large (0.23 inches inside diameter), with a silver tube as

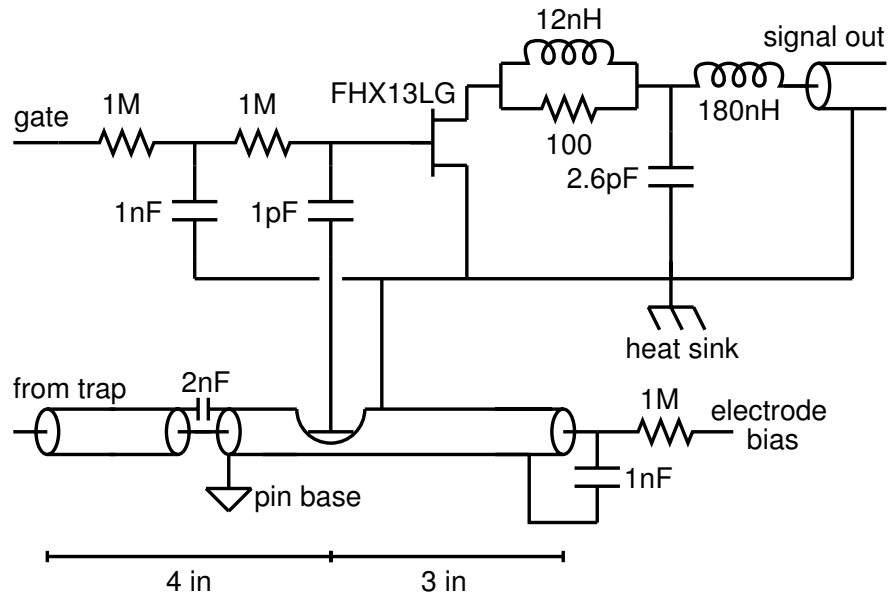


Figure 4.17: First stage 200 MHz amplifier schematic. Values without units are resistances in ohms.

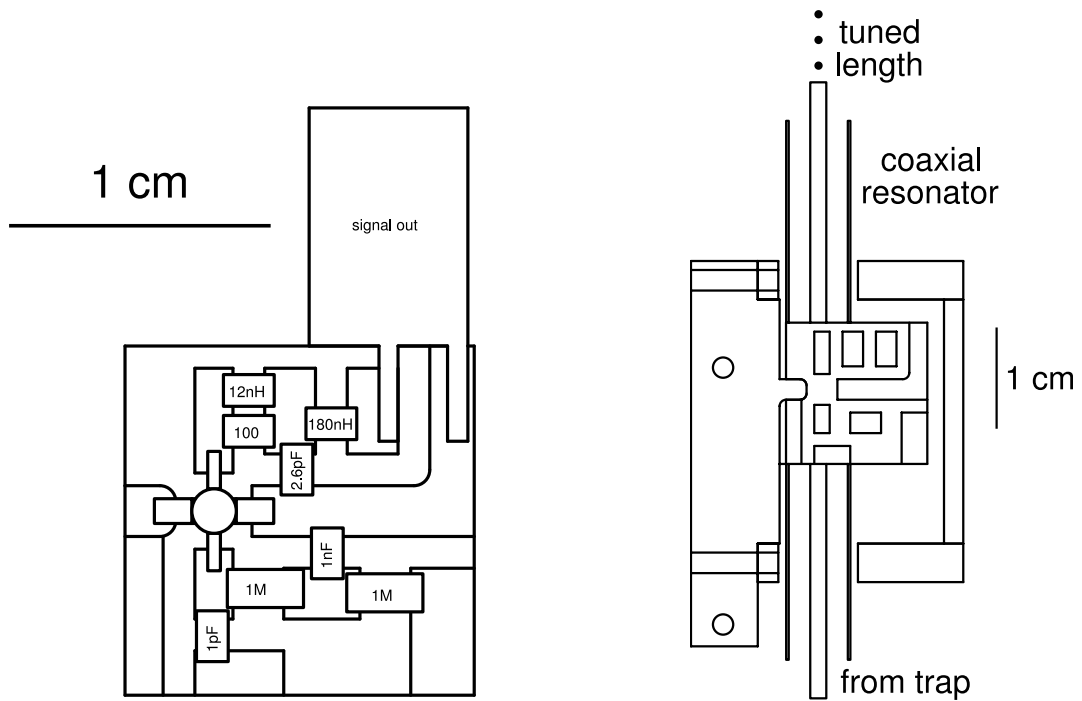


Figure 4.18: First stage 200 MHz amplifier board layout. Values without units are resistances in ohms.

the outer conductor and a silver rod (0.0625 inches diameter) as the inner conductor. The inner conductor is supported by thin Teflon spacers so that there is primarily a vacuum instead of the usual solid dielectric material. The characteristic impedance of the line is 78Ω , a trade-off between the high impedance desired for the tuned circuit, losses in the inner conductor, and the need for an inner conductor of manageable diameter.

Instead of the usual ceramic and metal feedthrough, the coaxial resonator uses a glass to metal seal from Larson Electronic Glass. This feedthrough maintains the characteristic impedance better than our usual feedthroughs. However, special care must be taken to avoid damaging the delicate glass seal, particularly while soldering. See Appendix B for details of the feedthrough assembly.

Noise resonances measured while testing the amplifier are shown in Figure 4.19. The maximum Q obtained in the test setup was 275 at 4 K, using a narrow diameter

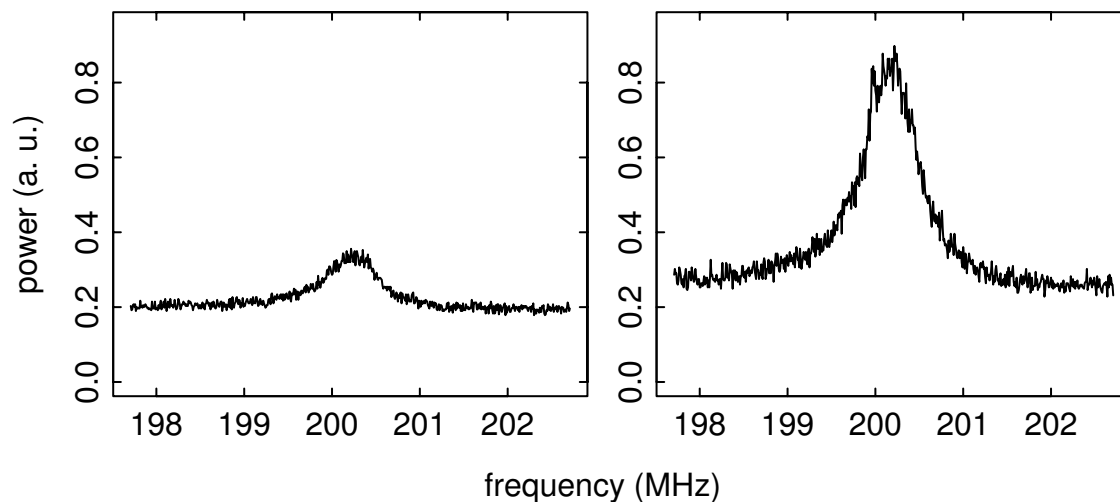


Figure 4.19: First stage 200 MHz amplifier noise resonance with $V_D = 0.15 \text{ V}$, $I_D = 80 \mu\text{A}$ (left), and with $V_D = 1.0 \text{ V}$, $I_D = 200 \mu\text{A}$ (right).

Teflon coaxial cable as the resonator. With a larger coaxial cable on the experiment, the Q is measured to be ~ 250 at 300 K. Unfortunately, no significant further improvement was seen after cooling down, although thermal changes caused the input tuned circuit frequency to shift much higher in frequency. This shift adds a lot of negative feedback, so a higher Q may be realized with more tuning.

The reflection off of the output of the amplifier (Figure 4.20) shows the same

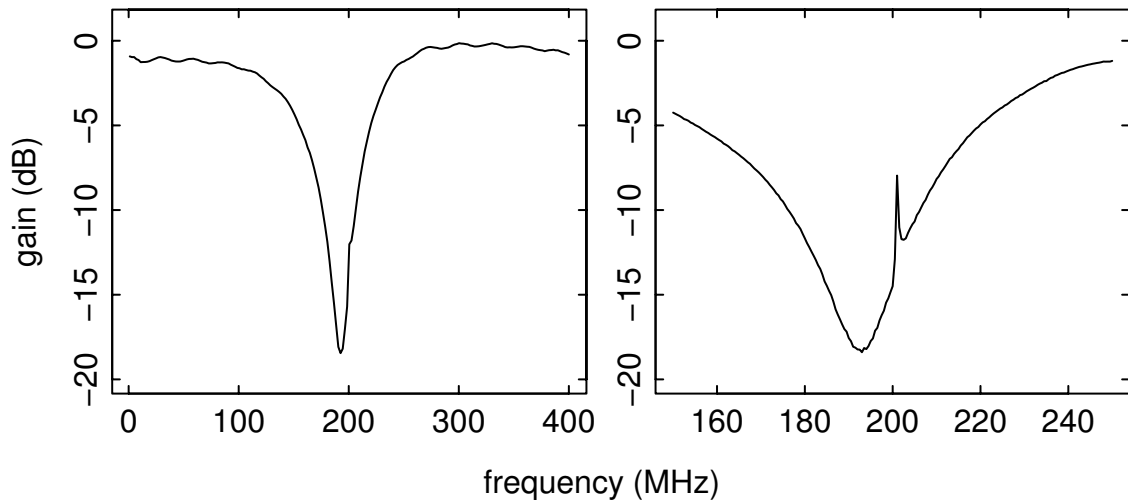


Figure 4.20: Reflection of the 200 MHz amplifier output with $V_D = 0.15$ V and $I_D = 80 \mu\text{A}$ (left), and a narrower frequency span to show the input tuned circuit in the output reflection (right).

characteristics as the 64 MHz amplifiers. The input tuned circuit resonance can be seen in the output reflection, positioned on the high frequency side of the output network to keep the amplifier stable, as described earlier.

The 200 MHz first stage amplifier circuit is analogous to that at 64 MHz, with a few changes. The capacitor from the gate to ground as part of a voltage divider on the input was eliminated because extracting the signal from the middle of the transmission line already divides down the voltage. The circuit board itself is copper

clad Teflon with glass weave instead of FR-4 in order to reduce the capacitance of traces and reduce loss, since Teflon has a lower dielectric constant and less loss. Finally, the layout of the circuit is redesigned to eliminate excess stray capacitance by reducing the size of some of the solder pads.

4.3.6 200 MHz Second Stage

A new second stage amplifier is also required at 200 MHz. At such high frequencies, the attenuation through the stainless steel coaxial cable in our experiment is even more severe than at 64 MHz, so the second stage cryogenic amplifier is even more important. Figures 4.21 and 4.22 show the circuit schematic diagram and circuit board layout for the amplifier, and Figure 4.23 shows the resulting response. The forward gain over a narrower frequency span is shown in Figure 4.24.

The input matching network is modified from that used for the 64 MHz second stage amplifier. In order to get a broader bandwidth, the capacitance at the input of the HEMT is minimized, with only a trim capacitor (a short stub of coaxial cable) to tune the input network. Most of the matching work is done by the 470 nH inductor and the HEMT gate capacitance. The suppression circuit was eliminated from the input because the stability is adequate without it.

The output network is identical to that of the first stage 200 MHz amplifier, which makes this amplifier have primarily negative feedback to the input. The result is a broad, stable gain region but poor impedance matching over much of the output range.

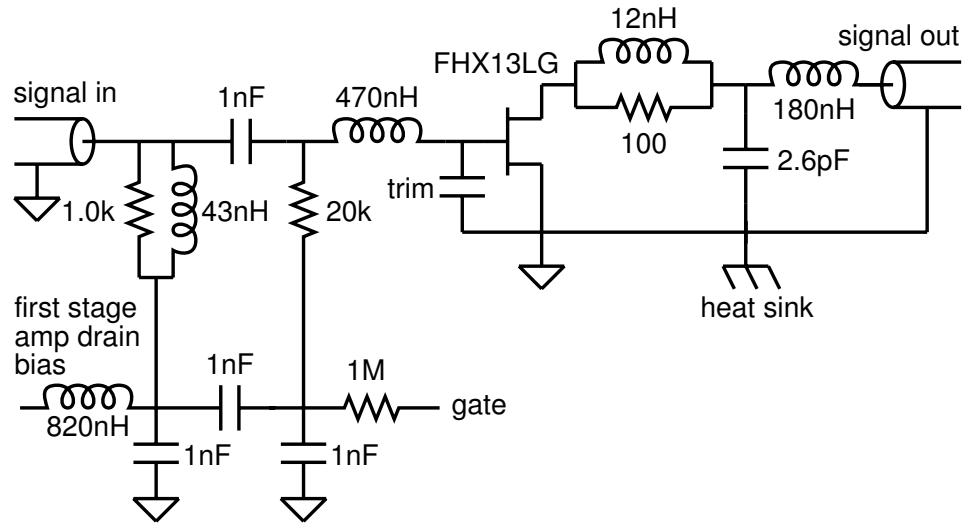


Figure 4.21: Second stage 200 MHz amplifier schematic. The trim capacitor is an open coaxial stub used to tune the input network. Values without units are resistances in ohms.

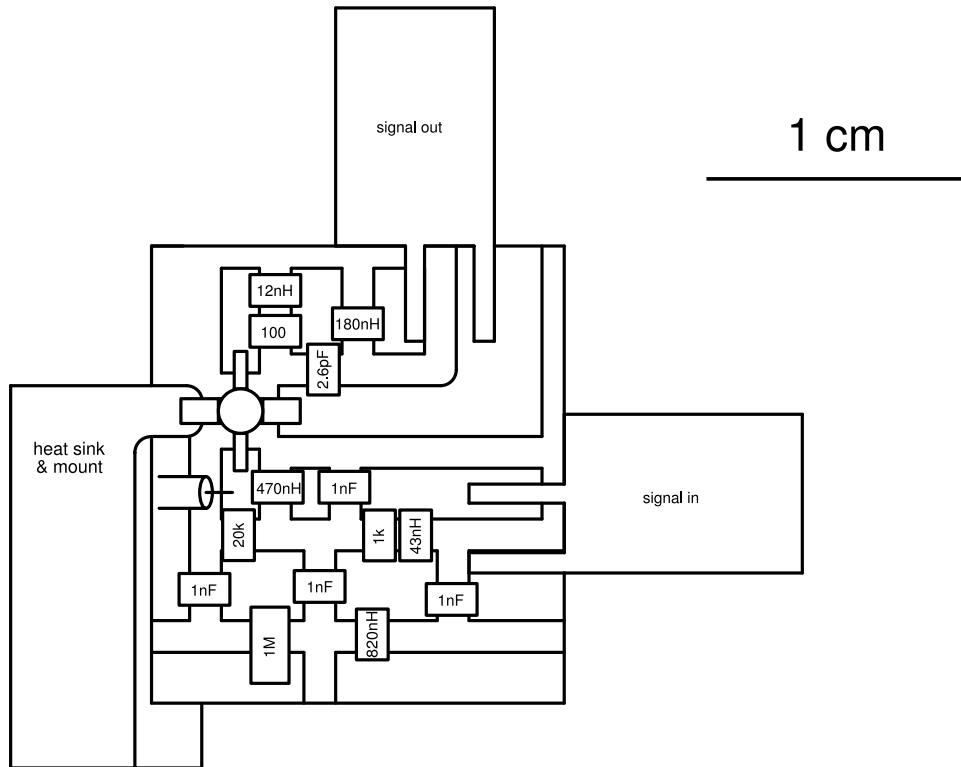


Figure 4.22: Second stage 200 MHz amplifier board layout. Unitless values are resistances in ohms.

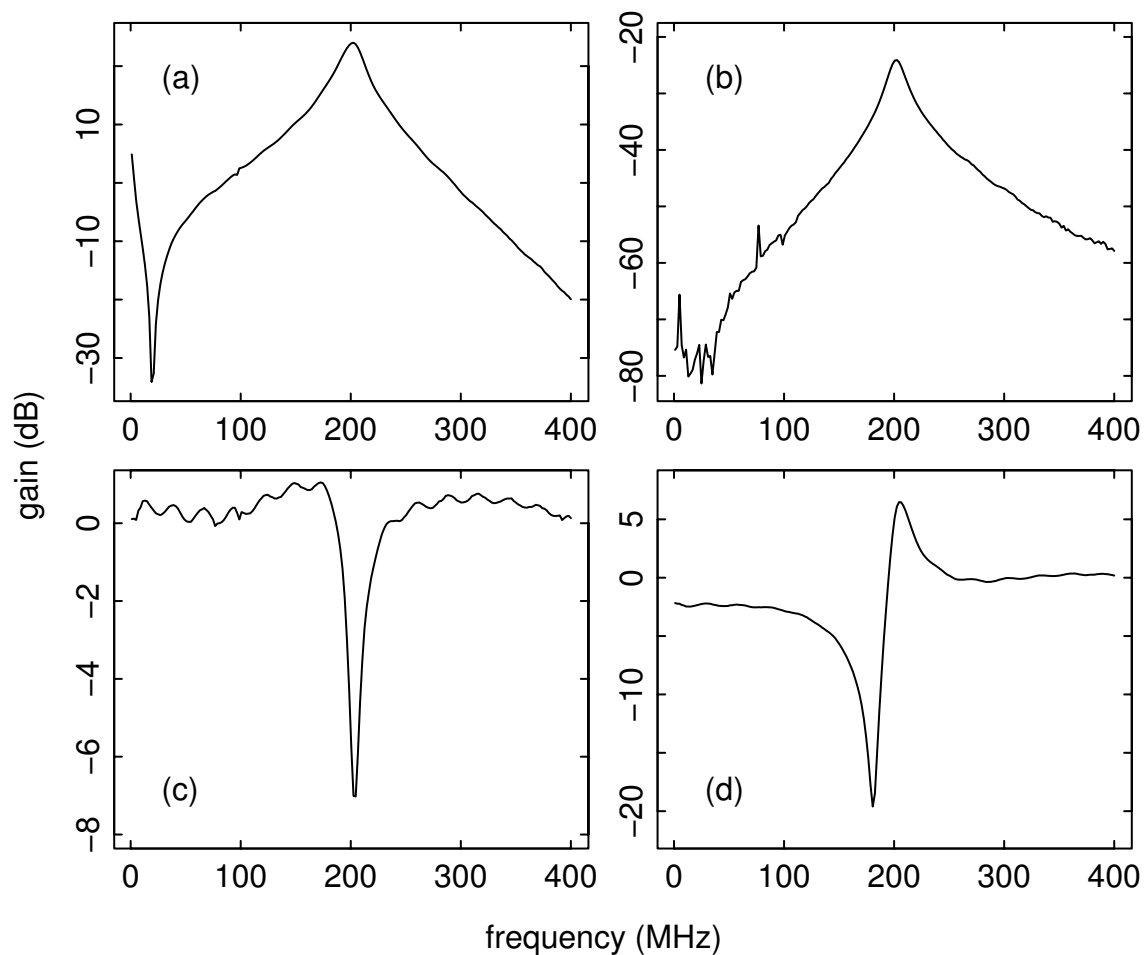


Figure 4.23: Response of the 200 MHz second stage amplifier: forward gain (a), reverse gain (b), forward reflection (c), and reverse reflection (d). The amplifier was biased to $V_D = 0.5$ V and $I_D = 529$ μ A.

4.4 SiGe Bipolar Transistors

While GaAs HEMTs have been the high frequency, low noise transistor of choice since they became commercially available, SiGe bipolar transistors have recently appeared as an alternative [43]. Using far cheaper technology, SiGe bipolar transistors are now commercially available with a transition frequency over 65 GHz. Unlike many silicon based devices, SiGe devices work at cryogenic temperatures.

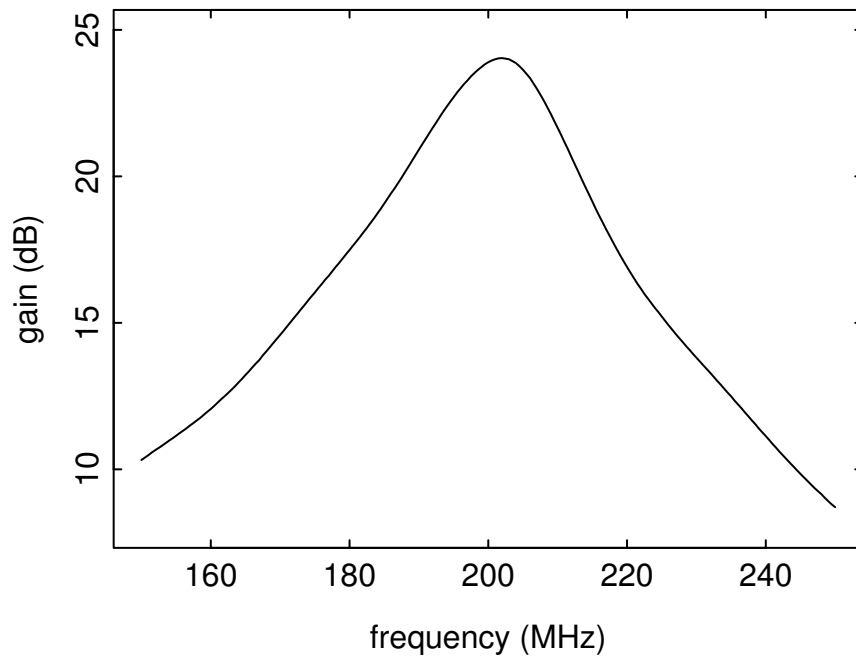


Figure 4.24: Forward gain of the 200 MHz second stage amplifier.

A comparison of the DC current gain characteristics of an Infineon BFP620 SiGe bipolar transistor at room temperature and 4 K is shown in Figure 4.25. The characteristics show a dramatic change in behavior at cryogenic temperatures, including increase of the current gain β by a factor of 4.

SiGe bipolar transistors may have advantages in high frequency cryogenic amplifiers. They may also be more durable since they do not have the fragile gate insulation layer of a HEMT. However, we do not yet know the power gain or noise performance that can be obtained with a SiGe bipolar transistor amplifier.

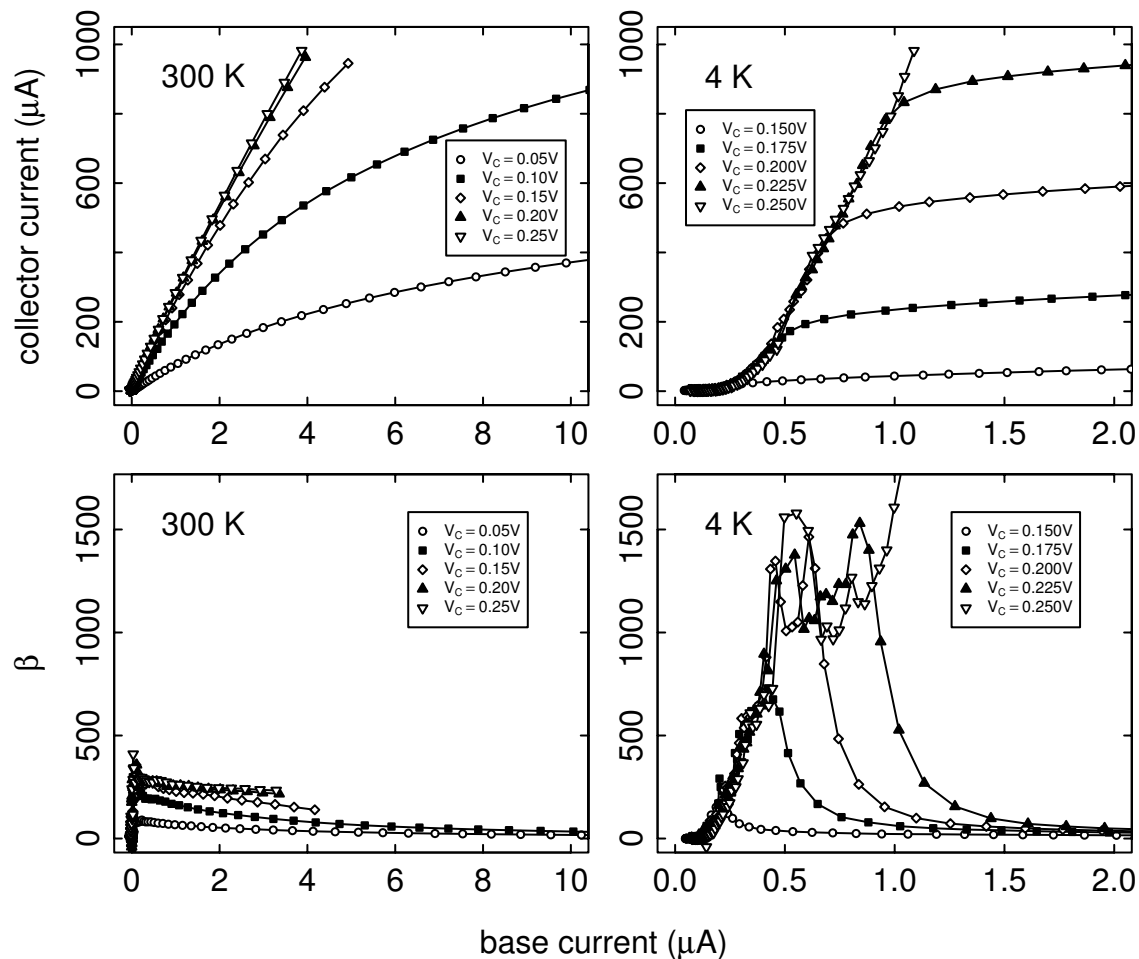


Figure 4.25: DC characteristics of a SiGe bipolar transistor (Infineon BFP620) at room temperature (left) and at 4 K (right).

4.5 Future and Limits

While the use of a single electron transistor (SET) or superconducting quantum interference device (SQUID) instead of a conventional transistor may give further signal to noise improvements over HEMT amplifiers, they do not reach quantum limited noise levels. This means, for example, that they cannot be used to cool the axial motion to very near the ground state with feedback (see Chapter 5).

The quantum mechanical limits of amplifiers have been studied [48]. Parametric

amplification has also been studied on the quantum mechanical level [49, 50] and can be used as an ideal form of amplification. Parametric amplification is particularly interesting because it may be possible to implement with a cloud of electrons in a Penning trap [29, 51].

Chapter 5

Axial Feedback Cooling

We use feedback to cool the axial motion of a single trapped electron from 5.2 K to 850 mK [52]. Since we can detect the axial motion of the electron, in principle we should be able to detect the thermal motion of the particle and send a correction drive to decrease the thermal motion. This is the principle of feedback cooling of the axial motion. In order to understand feedback cooling, it is helpful to understand the source of the thermal motion, which is Johnson (or Johnson-Nyquist) noise in the detection resistance. Thermal noise in resistors was discussed by Johnson in 1928 [53] in connection with noise in vacuum tube amplifiers and was explained with a simple thermodynamic argument by Nyquist [54].

Suppression of Johnson noise in amplifiers was studied with early vacuum tube amplifiers [55, 56]. Noiseless damping was discussed more generally by Kittel [57]. It was used to reduce thermal motion in electrometers [58] and torsion balances [59]. An improved signal to noise ratio with feedback has been seen in a rotating gravity gradiometer [60], and improved frequency stability has been observed in an electrically

cooled mechanical rotor [61]. Cooling and heating of a mirror with optical feedback has been demonstrated [62, 63]. Feedback has also been proposed as part of a method to improve detection sensitivity of impulsive forces [64].

Cooling particles in a Penning trap with feedback has been suggested and demonstrated as a way of rapidly cooling the axial motion of very hot particles to above the ambient temperature [65, 66, 67], or of cooling the radial motion [68]. Feedback cooling of charged particles in a Paul trap has been numerically simulated [69]. This cooling is very similar to the stochastic cooling used in particle accelerators [70] although there has been some confusion associated with the term “stochastic cooling” in the literature when concerning Penning traps. Improved detection sensitivity was observed with single ions in a Penning trap [71], but cooling was not observed. Stochastic cooling of trapped ions or atoms has also be discussed with optical feedback [72, 73].

Cooling with feedback should not be confused with noise squeezing techniques which can decrease thermal noise in one phase of motion at the expense of the other [74] or trade off amplitude and phase noise [75]. Squeezing can improve measurement precision or give noise reduction, and has been demonstrated in a Penning trap with a single ion [76].

5.1 Damping and Feedback Cooling

We are interested in calculating the axial temperature of a particle interacting with a tuned circuit amplifier and a feedback loop. Over the narrow range of frequencies that the electron interacts with, the tuned input circuit of the axial signal amplifier

is effectively a simple resistor with resistance R and temperature T . Separating this finite impedance, the remaining amplifier can then be modeled as having a noiseless and infinite input impedance as in Figure 5.1(a). The resistor R produces thermal

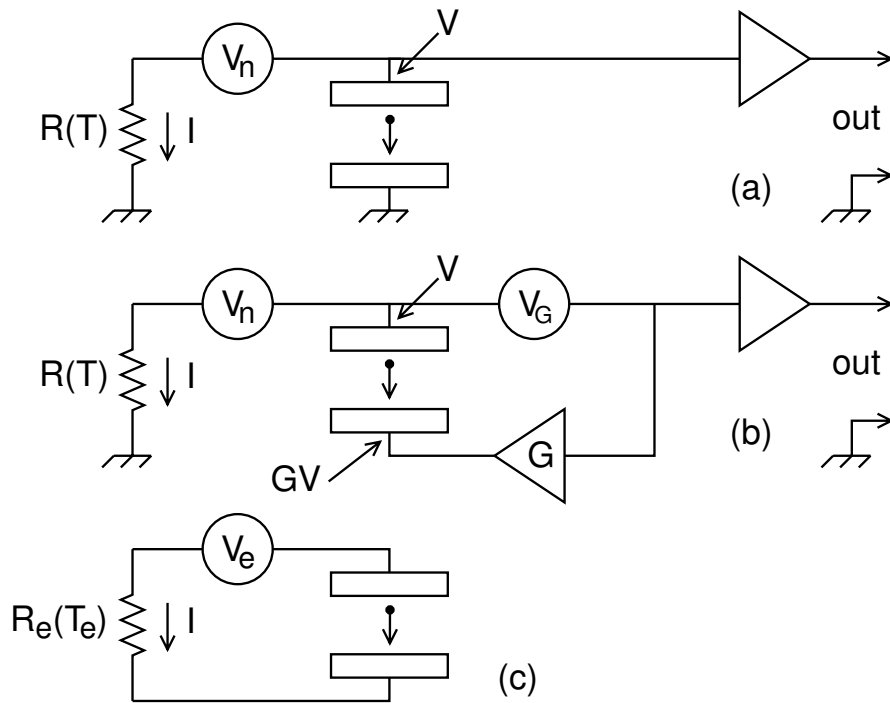


Figure 5.1: Effective circuit for damping and detecting the electron without (a) or with (b) feedback. Circuit (c) is an equivalent circuit to (a) for the electron.

noise which acts like a voltage noise source of magnitude V_n in series with the resistor. The feedback loop can be modeled as having a voltage gain G going around the loop and back to the trap. However, since the amplifiers in the feedback loop may add noise of their own due to shot noise or thermal noise in later amplification stages, we include an additional noise source V_G which represents all the additional noise seen by the particle in the feedback drive but not on the input of the amplifier (see Figure 5.1(b)). The resistor R combined with the feedback gives an effective resistance R_e and noise voltage V_e which corresponds to an effective noise temperature T_e .

Instead of calculating the dynamics of a particle interacting with the Johnson noise and feedback, it is much simpler to find the temperature of the effective damping resistance R_e and effective temperature T_e seen by the particle. In equilibrium, the particle will have the same temperature as the effective resistance it sees. We will also see how the damping of the axial motion is modified by the change in the effective resistance, which determines how long it takes for the particle to come to equilibrium with the resistance. This simplifies the analysis to that of an active cooled “artificial” resistor, which has been studied [77].

The Johnson noise voltage developed across a resistor of resistance R and temperature T measured in a bandwidth B is $V = \sqrt{4kTRB}$, where k is the Boltzmann constant. Consider resistors R and R_e at temperatures T and T_e , and noise voltages V_n and V_e , respectively. The ratio of their temperatures is given by

$$\frac{T_e}{T} = \left(\frac{V_e}{V_n}\right)^2 \left(\frac{R}{R_e}\right). \quad (5.1)$$

Thus, all we need to do is calculate the effective changes in resistance and noise voltage seen by the particle to get the equilibrium temperature change.

The damping rate γ_z of the electron is (from Chapter 2)

$$\gamma_z = \left(\frac{e\kappa}{2z_0}\right)^2 \frac{R}{m}. \quad (5.2)$$

With effective resistance R_e , the effective damping is γ_e . Then, the ratio of the damping is

$$\frac{\gamma_e}{\gamma_z} = \frac{R_e}{R}. \quad (5.3)$$

So, if we calculate the ratio of the effective resistance R_e to the initial resistance R , we know the ratio of the axial damping rate.

First we calculate the effective resistance R_e with which the particle interacts. The noise voltages V_n and V_G do not affect the damping on average since they have a random phase relative to the motion of the electron. So, we can do the calculation ignoring the noise. If the particle motion induces a current I to flow through the tuned circuit resistance R , then the voltage at the top of the resistor R is $V = IR$ and the voltage fed back to the other endcap is $V_{FB} = GIR$. Since the particle is driven by the difference in voltage across the endcaps it sees a voltage $V_p = (1-G)IR$. So, we find that the effective resistance seen by the particle R_e is

$$R_e = (1 - G)R. \quad (5.4)$$

That is, the resistance goes linearly to 0 as the feedback gain approaches unity.

If we neglect the noise V_G added by the amplifier chain, calculation of the effective noise voltage V_e is also very simple. The noise voltage on the top endcap is V_n , and the noise voltage on the bottom endcap is GV_n . Once again, the particle is only sensitive to the difference in voltage across the endcaps so

$$V_e = (1 - G)V_n. \quad (5.5)$$

By simply combining Eqs. (5.4) and (5.5) with Eq. (5.1), we find that the effective temperature decreases with increasing gain as

$$T_e = (1 - G)T. \quad (5.6)$$

Combining Eqs. (5.3) and (5.4), we obtain a similar relationship for the damping,

$$\gamma_e = (1 - G)\gamma_z. \quad (5.7)$$

Finally, we can see that the ratio of the effective temperature T_e and effective damping γ_e is constant, that is

$$\frac{T_e}{\gamma_e} = \frac{T}{\gamma_z} \quad (5.8)$$

independent of the gain G around the feedback loop. So, even with perfect noiseless amplifiers the temperature can only be decreased at the expense of damping. It is also clear that feedback can be used to increase the damping (by making $G < 0$) in order to cool hot particles [65, 66, 67] but only at the expense of an elevated axial temperature.

In our real feedback loop, the amplifiers do add noise which should not be neglected. Contributions from the noise voltages V_n and V_G add in quadrature since they are not correlated, but the thermal resistor noise V_n is partially canceled out by the feedback as in the noiseless case. In total, the particle sees a voltage across the endcaps V_e which is given by

$$V_e = \sqrt{(1 - G)^2 V_n^2 + G^2 V_G^2}. \quad (5.9)$$

We can now put this result into equation (5.1) to find the feedback cooled particle temperature T_e with noise added in the feedback loop,

$$T_e = T \left[1 - G + \frac{G^2}{1 - G} \left(\frac{V_G}{V_n} \right)^2 \right]. \quad (5.10)$$

The additional amplifier noise limits how cold the particle can be made, even though the damping will continue to decrease linearly with increasing feedback.

Although the ratio of the temperature and the damping is not invariant when noise is included, the noise can only increase the temperature. Thus, we can still

place a limit on the ratio,

$$\frac{T_e}{\gamma_e} \geq \frac{T}{\gamma_z}, \quad (5.11)$$

which is correct with or without noise and for positive (cooling) or negative (heating) feedback.

We can further simplify and understand Eq. (5.10) by introducing the feedback gain temperature T_G , defined by

$$\frac{T_G}{T} = \left(\frac{V_G}{V_n} \right)^2. \quad (5.12)$$

Substituting into Eq. (5.10), we have

$$T_e = T \left[1 - G + \frac{G^2}{1 - G} \frac{T_G}{T} \right]. \quad (5.13)$$

For $T_G \ll T$, feedback cooling can be optimized by choosing $G \approx 1 - \sqrt{T_G/T}$, and the coldest temperature obtained is $T_{min} \approx 2\sqrt{T_G T}$.

5.1.1 Detection Signal to Noise Ratio

It is natural to question whether feedback modifies the signal to noise ratio in the detected signal. Some improvement might be expected because of the reduced axial temperature. In practice, whether there is improvement in the signal to noise ratio depends primarily on what signal is desired.

The simplest measurement of the signal to noise ratio is the amplitude of the driven response compared to the amplitude of the background noise. The amplitude of the driven response is limited by anharmonicity, and does not change with feedback. The amplitude of the background noise in the detected signal is also independent of feedback. With weak feedback, the depth of the dip in the background noise caused

by the particle shorting out the noise does not change either, although with strong feedback the dip becomes shallower or disappears entirely. Thus, by this measure, the signal to noise ratio does not change.

For determination of the axial frequency, feedback may help. Since the damping decreases with increasing feedback, the noise dip or driven response becomes narrower and the center frequency can be more accurately determined. On the other hand, it takes longer for the particle to come into equilibrium with a drive or the noise, so it could take longer to get a measurement.

Therefore, feedback has a mixed effect on the detection signal to noise ratio. The analysis becomes even more complex with feedback at $G = 1$, self-excitation, as is considered in Chapter 6.

5.1.2 Comparison to Cooling a Resistor

If cooling of a physical object can be accomplished by electronic means alone, why is this technique not commonly used to cool macroscopic objects? A calculation of the cooling rate for a macroscopic resistor will illustrate the difficulties. This technique has actually been considered for cooling very small solid objects [78], but the difficulties with scaling it up to larger objects will be clear.

Consider cooling a resistor R by attaching it to another resistor R' through a transmission line of length L . The resistor R starts at temperature T while R' is maintained near $T' = 0$ K. The maximum power transfer, and thus the maximum cooling rate will occur when $R' = R$, that is we choose the cooling resistor to match the resistor we want to cool. Then the Johnson noise power emitted by R is optimally

absorbed by R' , which in turn does not produce any thermal noise above the quantum limit to heat up R .

Two equal value resistors connected by a transmission line is exactly the thought experiment used by Nyquist [54] in his derivation of the source of thermal noise in resistors. In this case, the whole problem is a simple case of one dimensional blackbody radiation, and quantum mechanical effects can easily be included [79, 80]. The power emitted by the resistor R between ω and $\omega + d\omega$ is

$$P_{d\omega} = \frac{1}{2\pi} \frac{\hbar\omega}{e^{\frac{\hbar\omega}{kT}} - 1}, \quad (5.14)$$

and the total power can be found by integrating over all frequencies,

$$P_{total} = \frac{1}{2\pi} \int_0^\infty \frac{\hbar\omega}{e^{\frac{\hbar\omega}{kT}} - 1} d\omega = \frac{k^2 T^2}{24h}, \quad (5.15)$$

where k is the Boltzmann constant. We could have estimated the value of this simply by noting that in the classical limit $kT \gg \hbar\omega$ the power emitted in a frequency span Δf is $P = kT\Delta f$ (independent of frequency). The largest value that Δf can have is if it goes from $f = 0$ to $f \sim kT/h$ where quantum mechanics causes the power to drop off, so the maximum power is

$$P_{total} \sim \frac{k^2 T^2}{h}, \quad (5.16)$$

which gives the same result up to a constant factor.

The maximum cooling power available to cool the resistor is $\dot{q} = P_{total}$ since the best that can be done is to absorb all of the power emitted by the resistor over all frequencies. Note that this is the total power radiated from the resistor, but practical amplifiers have finite bandwidth which is typically much smaller than the bandwidth

the power is radiated over. Thus, the upper bound on the cooling rate $\frac{dT}{dt}$ of the resistor is then

$$\frac{dT}{dt} = \frac{1}{c}\dot{q} = \frac{k^2}{24hc}T^2, \quad (5.17)$$

where c is the heat capacity of the resistor being cooled. Note that the cooling may not be exponential because the cooling rate is proportional to T^2 and the heat capacity will likely depend on temperature. Still, it is useful to try out some numbers. At $T = 1.6$ K the cooling power $\dot{q} = 3 \times 10^{-14}$ W. At 300 K the cooling power increases to 1×10^{-9} W. Even with this higher cooling power, it would take more than 10 years to cool down 1 gram of copper from 300 K to 299 K!

5.2 Experimental Realization

Experimentally, feedback cooling is slightly more complex. Figure 5.2 shows the experimental setup. The signal from the particle is amplified by the two HEMT based cryogenic amplifiers. The signal is gently filtered through a broad, constant impedance bandpass filter to eliminate far out of band noise and then further amplified. Part of the signal is split off for detection purposes, while the rest is passed through a variable length of cable and variable attenuators with 0.1 dB resolution. The variable length of cable is used to adjust the feedback phase, while the attenuators are used to adjust the gain.

In order to prevent the feedback signal from coupling directly to the amplifier, the signal is split into two and one branch is passed through another variable length of cable and attenuators. One drive goes to the bottom endcap, the other to a compensation electrode. The phase and attenuation are adjusted so that the coupling

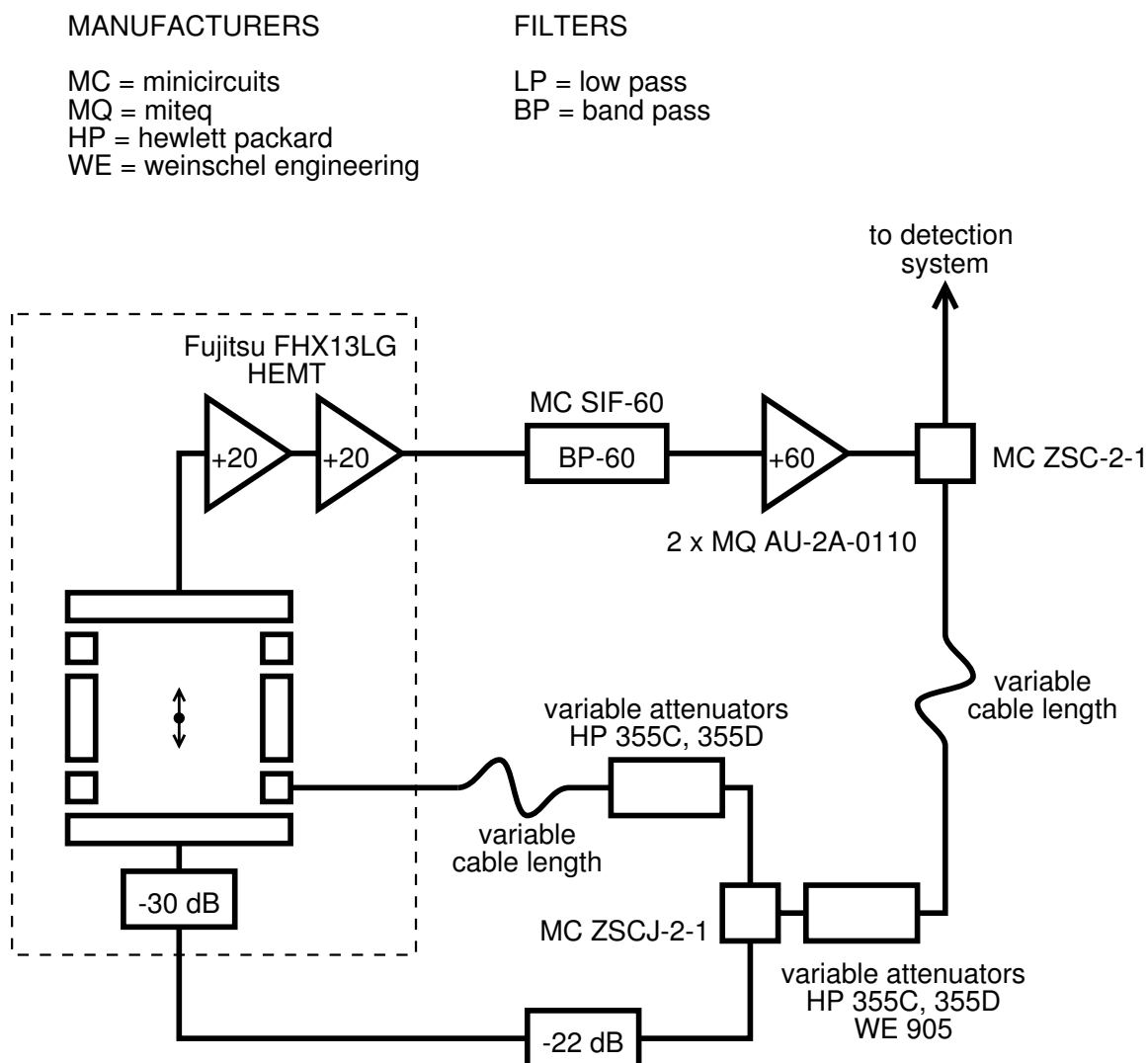


Figure 5.2: Diagram of system used for feedback cooling. The components inside of the dashed box are at cryogenic temperatures.

to the amplifier is canceled out, but the coupling to the particle is not. The adjustment is done precisely by using a strong drive (on the magnetron sideband cooling side of the axial frequency) as a test signal and with a lock in for detection amplifier. The cancellation of the direct feedthrough is complete enough so that no distortion of the amplifier response is visible even with the strongest feedback settings.

All these feedback cooling experiments were performed at an ambient temperature of 1.6 K, obtained by pumping on the ^4He in the 1 K pot, without running the dilution refrigerator. Running experiments with just the 1 K pot allows the first stage amplifier to dissipate $420 \mu\text{W}$ instead of the $12 \mu\text{W}$ typical with the dilution refrigerator running.

5.3 Experimental Results

Before feedback cooling can be attempted, the phase of the feedback must be optimized for cooling. Figure 5.3 shows the noise dip of one electron with feedback at several different phases and magnitudes. When the feedback phase is 180° off from the ideal cooling phase, the noise dip gets wider with increasing gain. If the phase is slightly off, the dip gets narrower with increasing gain but does not remain symmetrical. Thus, the shape of the dip can be used to optimize the phase of the feedback. With the phase adjusted, the noise dip width can be measured with increasing feedback from noise spectra like those in Figure 5.4.

Typically, the broadening of the cyclotron lineshape due to a finite axial temperature is a nuisance for the $g - 2$ measurement, but it can also be used to measure the axial temperature. The exponential tail of the cyclotron lineshape gives a direct measurement of the axial state distribution. Details of the lineshape are derived in Chapter 3.

A series of cyclotron spectra in order of increasing feedback are shown in Figure 5.5. Saturation of the transition probability is included in the fits to an exponential lineshape. The cyclotron spectra show that the lineshape significantly narrows as

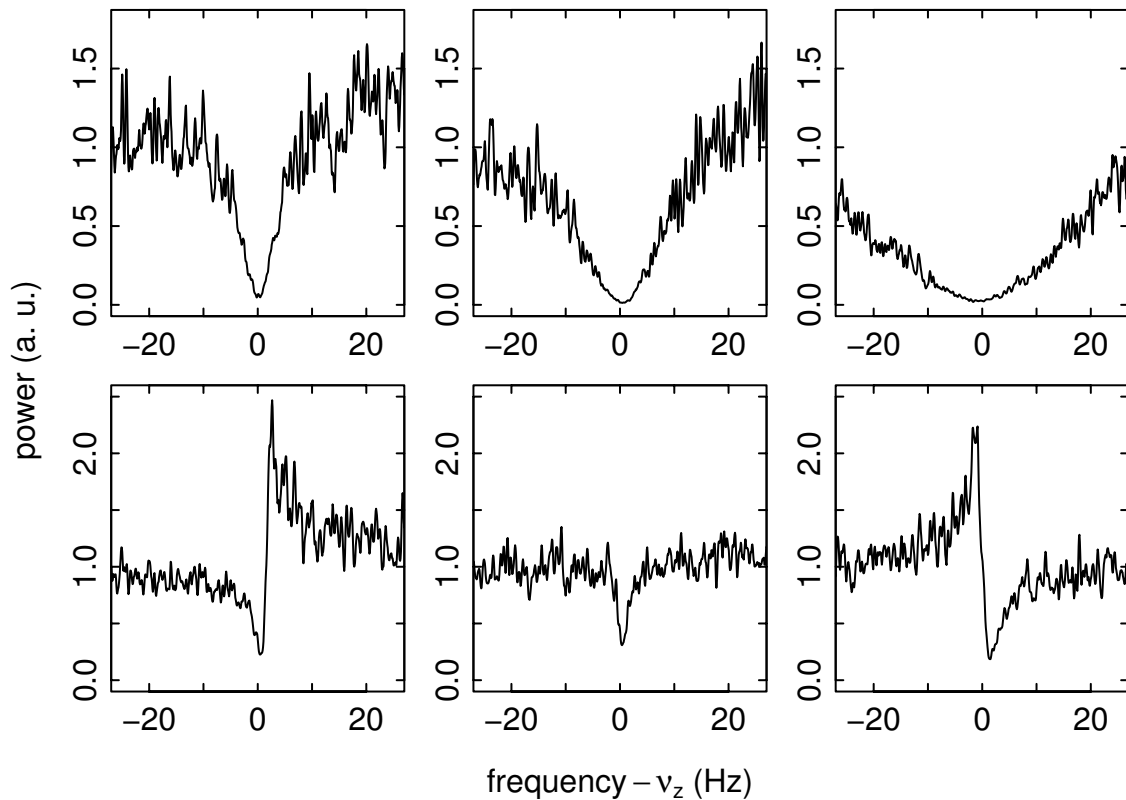


Figure 5.3: One electron noise dips with no feedback (top left), feedback to increase damping (top center, right), or feedback to decrease damping (bottom center). The bottom (left and right) show the effect of a slightly incorrect phase when decreasing the damping.

the gain is increased, but the last spectrum shows some broadening again. The axial temperature, damping, and the ratio of the two are plotted in Figure 5.6. As expected, the axial temperature first decreases linearly with increasing feedback, but then increases rapidly when the gain is near 1. The fit to Eq. (5.10) is very good including the rapid increase. When G is near 1, the residual extra noise from the amplifier chain drives the almost undamped particle to a higher temperature.

Figure 5.6 also shows the linear decrease in damping as expected. For gains near 1 there is no data on the damping because the depth of the noise dip decreases rapidly at

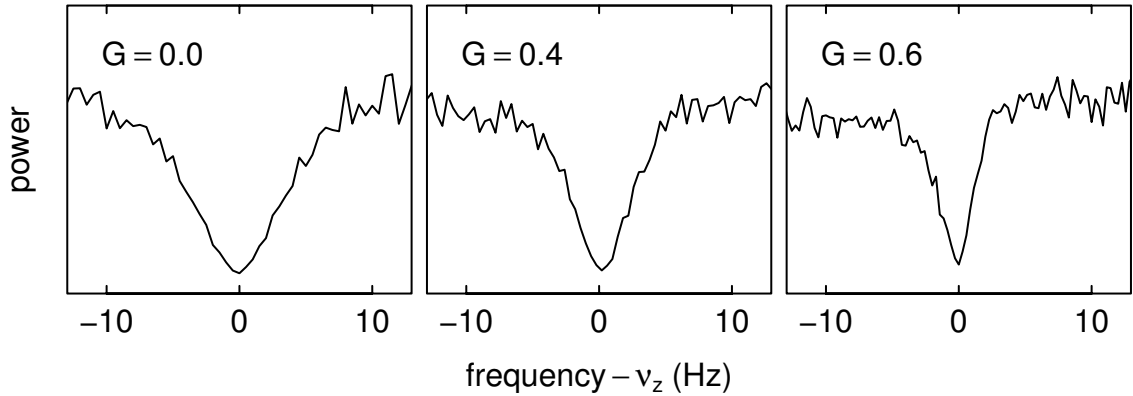


Figure 5.4: One electron noise dips with several feedback gains showing the narrowing of the dip with increasing feedback.

high gains, once again because the extra amplifier noise drives the nearly undamped particle. The ratio of the damping and temperature does not change significantly in the region where the axial temperature is decreasing linearly. This is the range where the cooling acts like noiseless feedback cooling, so the ratio is expected to be invariant.

The most important temperature results are summarized in Table 5.1. The lowest

amplifiers	feedback	temperature (K)
on	none	5.17(50)
on	optimal	0.85(13)
off	none	2.04(14)

Table 5.1: Axial temperatures obtained under several conditions. The feedback reported as optimal is associated with the lowest axial temperature measured.

temperature obtained with feedback is 850 mK, decreased by more than a factor of 5 from the 5 K temperature with no feedback, and below the ambient temperature of 1.6 K. For comparison, the lowest temperature reached by turning the amplifier off and allowing it to cool was 2 K. In the notation used earlier, the feedback gain

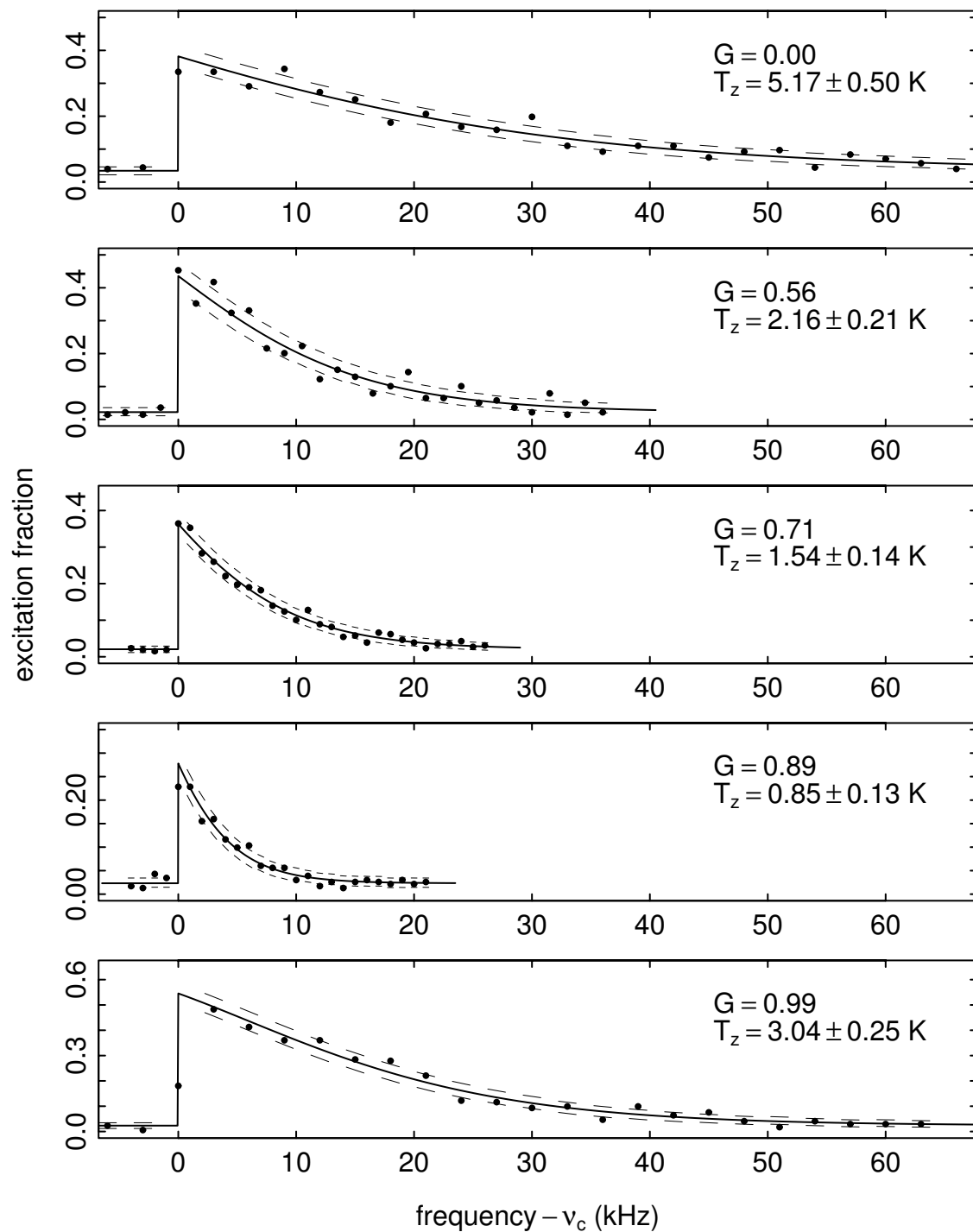


Figure 5.5: Cyclotron resonances taken at several different feedback amplitudes which show the decrease in linewidth associated with the cooling. The dashed lines show the expected 68% confidence region for the data.

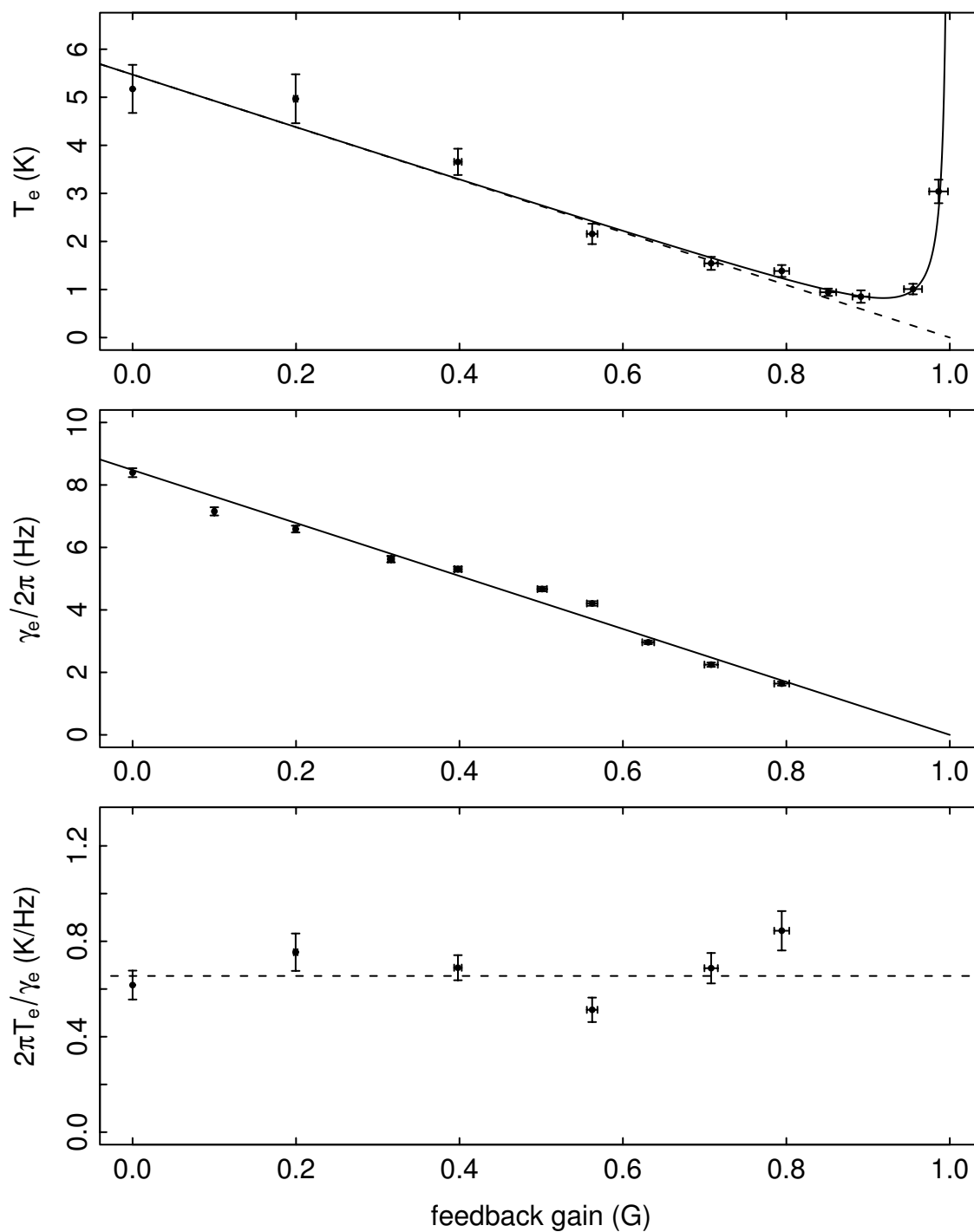


Figure 5.6: Axial temperature obtained as the feedback amplitude is varied (top), the axial damping rate obtained as the feedback amplitude is varied (middle), and the ratio of the temperature and damping rate (bottom).

temperature is $T_G \approx 40$ mK.

In summary, we demonstrate using electronic feedback to cool the axial temperature from 5.2 K to 850 mK without a dilution refrigerator. With temperatures and damping measured as frequencies, this elegant demonstration also shows the invariance of the temperature to damping ratio in the noiseless limit.

5.4 Amplifier Feedback

In the feedback cooling system we use, the direct coupling to the amplifier is carefully canceled out while the coupling to the electron is maintained. Another option is to couple feedback only directly to the amplifier, and not to the particle. Such a strategy has been used with positive feedback to increase damping [67] by making a regenerating amplifier, or with negative feedback which could give cooling [71].

We have several reasons for preferring direct feedback to the particle. First, the bandwidth of the feedback must be very large without extra phase changes in order to get positive or negative feedback over the entire amplifier response (compared to the particle response). If the feedback were not uniformly negative, it would be difficult to adjust the phase exactly. Second, there is no threshold with amplifier feedback as there is at $G = 1$ with feedback to the particle. This means that the strength of the feedback can only be calibrated with the change in the amplifier response shape, which again requires a broad bandwidth.

5.5 Fundamental Limits of Feedback Cooling

The apparatus used for this feedback cooling demonstration was optimized for detection with the first stage amplifier dissipating only $12 \mu\text{W}$ and with the dilution refrigerator running. Instead, we ran the amplifier at $420 \mu\text{W}$ and used the 1 K pot to cool the trap and amplifier. Since the signal-to-noise ratio is of critical importance for feedback cooling, it is likely that further improvements could be made by optimizing the amplifiers to run at higher power. With more cooling power available or a different apparatus, coaxial signal cables with less attenuation could be used to carry the signal out of the experiment, further improving the signal to noise ratio and the lowest temperature available with feedback cooling.

Ultimately, the performance of the HEMT may be limited by shot noise. The effect of shot noise can be decreased by running the HEMT with a larger drain current. Increasing the drain current I improves the signal-to-noise ratio as \sqrt{I} because the transconductance increases roughly proportional to I , but the shot noise increases at \sqrt{I} . In the language of Section 5.1, $T_G \propto I^{-1}$, but the minimum temperature obtained with feedback $T_{min} \propto I^{-\frac{1}{2}}$. If the output resistance of the HEMT is constant, then the power P dissipated by the HEMT goes as I^2 . Putting it all together, we estimate $T_{min} \propto P^{-\frac{1}{4}}$. With such a weak improvement with increased power, it may not be practical to improve the cooling by simply running the amplifier at higher power.

To get a dramatic improvement in feedback cooling, it may be necessary to use an amplifier based on a device other than a HEMT. SQUID based amplifiers may provide decreased noise, but the difficulties of using a SQUID in a strong magnetic field make that approach unattractive. Since we have a dilution refrigerator, feedback

cooling may not be our most effective axial cooling technique for the future.

Beyond practical limitations, quantum mechanics limits the minimum noise in an amplifier [48] and the lowest temperature that can be obtained with feedback cooling [81, 82, 83]. However, this limit is near the ground state of the motion, which, for our purposes, still gives a lot of room for improvement.

Chapter 6

Self-Excited Axial Oscillator

If the axial motion were perfectly harmonic, detecting the axial frequency would be almost trivial. A drive strong enough to force the electron to an easily detectable amplitude could be used, so the averaging time required to separate the response from the noise would be short. The only time requirement would come from the need to resolve small frequency shifts. With a completely linear response, multiple drives could be applied simultaneously and the lineshape could be quickly and completely mapped, making it easy to pick out the axial frequency.

In practice, however, the axial motion in a cylindrical Penning trap is anharmonic. Although this anharmonicity is adjustable to first order, the second order dependence of the frequency on the amplitude of excitation is significant. Self-excitation has potential advantages in detecting small shifts in the axial frequency despite the anharmonicity because it can be stable even when the driven response is metastable. Additionally, the self-excited oscillator response tracks the axial frequency almost instantaneously. Self-excitation was proposed as a means of detecting the axial fre-

quency of a single trapped particle by Dehmelt [84], but it was never demonstrated experimentally and the limiting mechanisms he proposed proved to be inadequate or impractical in our trap. Self-excitation has been used in other systems such as cantilevers where it has given improvements over other detection methods [85], in particular with a cantilever based electrometer [86]. For a more complete discussion of the advantages and disadvantages of several axial frequency monitoring techniques see Chapter 2.

6.1 The Self-Excited Anharmonic Oscillator

Many useful properties of the self-excited oscillator as a method of detection can be seen from a simple steady state analysis of the response. We first assume that the difficulties with the instability of the amplitude discussed in section 6.2 have been solved so the amplitude can be assumed to be constant and the feedback gain is exactly 1.

We begin the analysis with the anharmonic axial equation of motion, Eq. (2.16), with $\dot{z} = \frac{dz}{dt}$ and $\ddot{z} = \frac{d^2z}{dt^2}$,

$$\ddot{z} + \gamma_z \dot{z} + [\omega_z(A)]^2 z = \frac{1}{m} F_d(t). \quad (6.1)$$

Now we wish to make the force $F_d(t)$ correspond to feedback which causes stable self-excitation of the electron. The feedback force begins with a current induced on a trap endcap and amplified up. This signal is then phase shifted by being delayed by a time τ and applied to the opposite endcap, changing the voltage on that endcap

and exerting a force on the particle. Thus, we write down the force,

$$\begin{aligned} F_d(t) &= Gm\gamma_z \left. \frac{dz}{dt} \right|_{t-\tau} \\ &= -AGm\gamma_z\omega \sin(\omega t - \omega\tau + \psi), \end{aligned} \quad (6.2)$$

where G is the gain going around the feedback loop. Let $-\omega\tau = \phi$ be the phase change around the loop which is approximately constant over the narrow bandwidth of interest. Although experimentally a time delay is often used to adjust the phase, it is mathematically more convenient to represent it as a simple phase change. We can expand the phase shifted force,

$$\begin{aligned} F_d(t) &= -AGm\gamma_z\omega \sin(\omega t + \phi + \psi) \\ &= -AGm\gamma_z\omega [\sin(\omega t + \psi) \cos \phi + \cos(\omega t + \psi) \sin \phi]. \end{aligned} \quad (6.3)$$

We then plug this into the equation of motion (2.13) along with the solution (2.9) to find two equations for $A \neq 0$,

$$G \cos \phi = 1 \quad (6.4)$$

$$\omega^2 = G\omega\gamma_z \sin \phi + \omega_z(A)^2. \quad (6.5)$$

The equations have a simple interpretation: the first is the requirement that the damping be canceled out by the drive in order to reach steady state, while the second equation gives the effect of the component of the feedback which is $\pi/2$ out of phase with the damping. Notice that if the phase $\phi = 0$, then $G = 1$ gives a force which exactly cancels out the natural damping of the axial motion and results in self-excitation. These equations can be easily solved for the frequency of oscillation ω while eliminating the gain G to give

$$\omega^2 - \omega\gamma_z \tan \phi - \omega_z(A)^2 = 0, \quad (6.6)$$

which can be solved for ω to get

$$\omega = \frac{\gamma_z}{2} \tan \phi + \sqrt{\left(\frac{\gamma_z}{2} \tan \phi\right)^2 + \omega_z(A)^2}. \quad (6.7)$$

Since $\gamma_z/\omega_z \sim 10^{-6}$, the $(\gamma_z \tan \phi)^2$ term can be neglected for reasonable ϕ to give

$$\omega(A, \phi) \simeq \omega_z(A) + \frac{\gamma_z}{2} \tan \phi. \quad (6.8)$$

This approximation only fails if the phase is so far shifted that the self-excitation is occurring way out on the tail of the axial response. For practical detection the phase will be chosen to excite oscillation near the center of the response.

6.2 Direct Self-Excitation and Instability

Experimentally, the same feedback arrangement used for feedback cooling (see Figure 5.2) can also be used for self-excitation of a single electron. The detected signal from the cryogenic amplifiers is passed through a broad filter and amplified significantly. It is then phase shifted through a variable length of cable and attenuated before it is used as a drive. This drive is applied to two electrodes with phase and amplitude such that the coupling to the amplifier cancels out, but the drive the particle sees does not cancel. While this method of feedthrough prevention requires more tuning than driving at two frequencies that the particle mixes together (see Chapter 2), it requires much lower drive strengths and can be used over a wide bandwidth without any distortion of the drive.

However, there are two problems with using this simple self-excited oscillator for detection of the axial frequency. Fundamentally, both of these problems are

caused by the lack of any amplitude selection by the feedback. That is, there is no stable equilibrium amplitude even under ideal conditions; a fluctuation in amplitude of the oscillation caused for example by noise is not corrected. Furthermore, any deviation in the gain causes the amplitude to change exponentially. Without a stable amplitude, the frequency of oscillation is not stable because the motion is significantly anharmonic.

The first problem is that the gain G must be adjusted so that Eq. (6.4) is satisfied exactly. It is more convenient at this stage to ignore the anharmonicity for this analysis, so with optimal feedback phase ($\phi = 0$), the equation of motion for the self-excited harmonic oscillator with feedback gain G is

$$\ddot{z} + \gamma_z \dot{z} + \omega_z^2 z = \gamma_z G \dot{z}. \quad (6.9)$$

The solution,

$$z(t) = A_0 e^{\frac{1}{2}(G-1)\gamma_z t} \sin(\omega_z t + \phi), \quad (6.10)$$

shows that if the gain is slightly too high or low then the oscillation will exponentially grow or shrink in amplitude, respectively. Since γ_z is typically at most 8 Hz, adjusting G to within 1 part in 10^{-2} would give exponential growth or decay on a time scale of seconds, which might be slow enough to be useful if the amplitude could be consistently started at the same value. In practice, it is inconvenient to repeatedly reset and restart the excitation, and further complications could make the method completely unusable.

The second problem becomes apparent when examining the results of the feedback cooling experiments described in Chapter 5. As the feedback gain approaches 1, which is the self-excitation threshold, the axial temperature goes to $+\infty$. This happens

because the axial damping approaches 0 but there is still a finite amplitude noise drive on the particle from the non-ideal additional noise in the amplifier chain. This noise drives the particle around while there is almost no damping to oppose an increase in the oscillation amplitude. It is possible to leave the feedback gain a little low ($G < 1$) to oppose the noise drive, but this results in a noise driven response which is not very stable over time.

Experimentally, the best that can be achieved in steady state with this arrangement is a huge excitation as in Figure 6.1. Compare this to the amplifier noise resonance in Figure 2.5. The electron signal peak is obvious. Here, the exponential

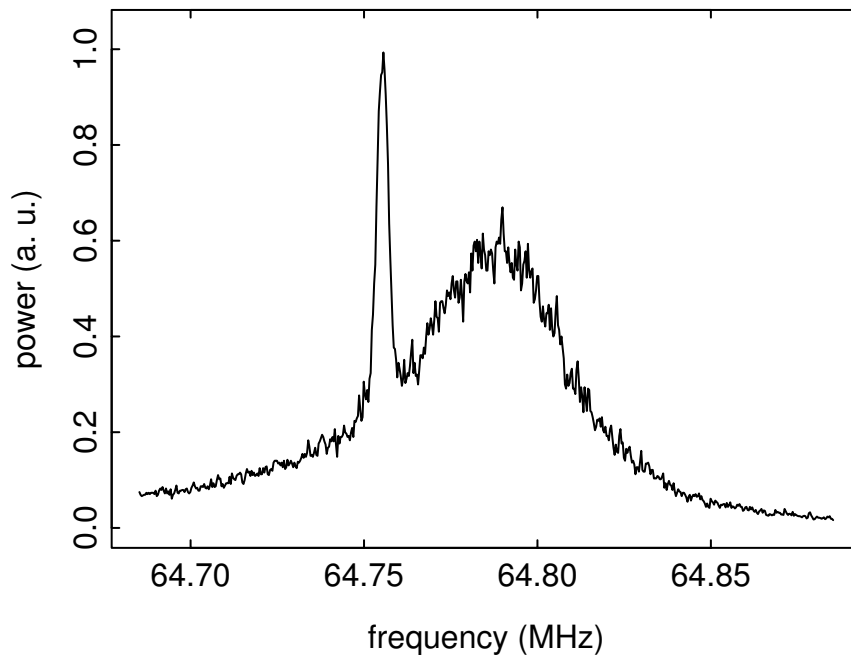


Figure 6.1: Amplifier noise resonance with a single electron self-excited by direct feedback.

amplitude growth is only stopped by the phase and gain changes as the particle shifts in frequency due to the anharmonicity. In a more harmonic trap it is likely that the

electron would collide with the trap endcaps. Although this huge excitation is an entertaining result, it gives little information about the axial frequency. The resulting peak frequency is essentially independent of small changes in the starting frequency. It is, however, useful to use this uncontrolled response to help with the loading of a single electron. It is possible to apply the feedback with no electrons in the trap and fire the field emission point at a low current until the self-excited response appears, indicating there is at least one electron in the trap. Then, the field emission point current is stopped and the electron is trapped.

We can take advantage of the magnetic bottle coupling to get more information about the axial motion by looking at the cyclotron spectrum. In Section 3.5.1, we calculate the cyclotron spectrum that results when the axial motion is driven and damped while the cyclotron spectrum is taken. The result is that there is a shift of the center of the cyclotron lineshape that depends on the axial amplitude, and a width that depends on the axial temperature.

Figure 6.2 shows the cyclotron spectrum when the axial motion is self-excited with unlimited direct feedback. The huge shift in the cyclotron frequency of over 85 MHz shows that the axial amplitude is 3.98 mm peak to peak, which is approximately half of the trap height! Even more surprisingly, the width gives an axial temperature measurement of 300 ± 50 mK. These measurements, however, are based on the magnetic bottle strength at the center of the trap. With such a large excursion, the effective magnetic bottle strength may be significantly different. Therefore, these measurements give only a weak estimate of the amplitude and temperature of the axial motion with such a large excitation.

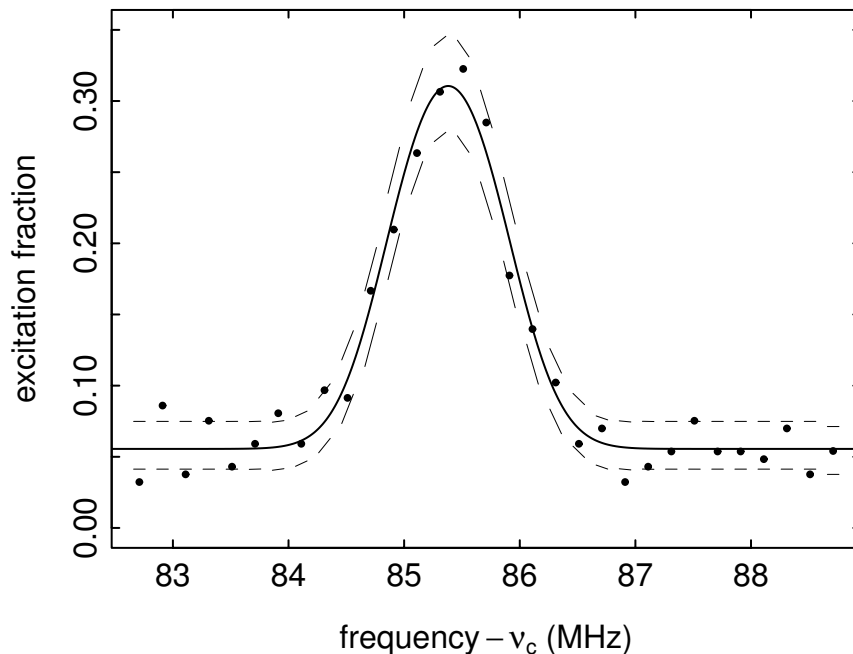


Figure 6.2: Cyclotron response with direct axial self-excitation. The large shift of ~ 85 MHz is due to the large axial amplitude. The dashed lines show the expected 68% confidence region for the data.

6.3 Limiting the Self-Excited Oscillator

Clearly, some mechanism is needed to decrease the gain or change the feedback phase as the amplitude increases. Even a small change in gain with amplitude could stabilize the excitation at a fixed amplitude. We should be able to tune the anharmonicity so that small fluctuations in the amplitude excitation do not cause changes in the frequency to first order. We tried several methods of controlling the amplitude.

6.3.1 Geometric Limiting

Dehmelt [84] suggests that the geometry of the trap can be used to limit the excitation amplitude. That is, as the amplitude increases it may interact more with

some electrodes and less with others. One of the major advantages of this method is that noise in the detection system does not change the amplitude regulation. In other words, it is not necessary to detect the amplitude at all; the regulation is completely internal to the trap.

Unfortunately, the geometric limiting as proposed by Dehmelt does not work because the effect is canceled out if a symmetric electrode is used for detection. For example, detecting on the top endcap and feeding back on the bottom endcap gives no gain dependence with amplitude because both the damping and the feedback drive amplitude change together. To have a geometric effect, a different electrode, such as a compensation electrode, must be used. It turns out that our trap does not have any single electrode with the right amplitude dependence (the interaction of the particle with the compensation and endcap electrodes increases with amplitude), so a pair of electrodes must be used with opposite phase drives going to each electrode. The electrode with a more rapidly increasing interaction then has a negative G , while the electrode with a more slowly increasing interaction has a positive $G > 1$. Calculations of the geometrical dependence of the fields from each electrode in our Penning trap were done by R. van Handel [35].

This uses up all of our drive lines, so the feedthrough cancellation scheme we have been using doesn't work. The solution is to use a split drive (5 MHz and $\nu_z - 5$ MHz) to eliminate the feedthrough. In the end, this was a very complicated arrangement that showed some amplitude control, but it was very difficult to adjust and did not give enough control to be useful. A major problem is that there is no easy way to experimentally be sure the phases of the two drives are opposite at the electrodes.

Also, there is generally still some feedthrough because the two drives mostly cancel each other out from the particle's point of view. While geometric limiting at first appears to be an attractive option, in practice it lacks the flexibility required to be suitable for detection in our trap.

6.3.2 Dither

Another idea to control the amplitude of the self-excited oscillator was to vary a parameter of the system periodically, often called dither. Dither has general applicability for controlling chaotic systems [87]. For the self-excited oscillator, the gain can be varied in order to make the amplitude grow then shrink back to zero and grow again. However, no usable excitation was ever obtained by this method.

A second way to use dither is to vary the gain and phase of the feedback simultaneously with some delay between the amplitude and phase modulation. It should be possible pick out an operating amplitude based on the direction of the anharmonicity at that amplitude. However, there is experimentally no easy way of evaluating whether the modulation phases and amplitudes are optimized. Little, if any, benefit was observed in the range of parameters tested.

6.3.3 Electronic Limiting

The most general means of limiting the amplitude is to simply analyze the detected signal and change the gain of the feedback loop electronically to regulate the amplitude of the excitation. There is, however, a potentially serious problem with this method. Noise added to the detected signal by the tuned circuit thermal noise and

the amplifiers almost completely bury the signal. So it seems that the problem may be circular: it is necessary to stabilize the amplitude before the frequency is stable enough for useful detection, but the signal must be detectable in order to stabilize the amplitude.

Ultimately, experimental results show that electronic limiting is feasible, even under the poor signal to noise ratio conditions which exist in our experiment. A mathematical analysis of the amplitude regulation is helpful in gaining an understanding of the system.

Since we will consider a broad range of devices and algorithms to control the amplitude of the excitation, it is useful to have some general theoretical framework for how the choice of algorithm affects the amplitude and frequency of the self-excited oscillator. Here, we follow a method similar to that shown by Lax [88] in his analysis of noise in oscillators. The goal is to develop a theoretical framework for comparing electronic limiting techniques.

We begin with the equation of motion for the self-excited harmonic oscillator with feedback phase $\phi = 0$ and gain G , Eq. (6.9),

$$\ddot{z} + \gamma_z \dot{z} + \omega_z^2 z = \gamma_z G \dot{z}. \quad (6.11)$$

We would like the gain to be adjusted around the self-excitation threshold based on the amplitude A of the oscillation, so it is convenient to write $G = 1 + \delta_G(A)$, where $\delta_G(A)$ is a function that describes the response of the electronic limiting system. We can put this description of the gain into Eq. (6.11) to get

$$\ddot{z} - \gamma_z \delta_G(A) \dot{z} + \omega_z^2 z = 0. \quad (6.12)$$

At this point we have already assumed that a slowly varying (relative to the axial frequency) amplitude A can be defined. Although Eq. (6.12) describes the response of the electronically limited oscillator, it is not yet usable since we have no means of connecting the amplitude A with the instantaneous displacement z . It is helpful to transform the equations to separate the rapid oscillation near ω_z from the slower amplitude and phase changes so we can identify the oscillation amplitude used by the electronic gain control. We define the complex variable $a(t)$ and its complex conjugate $a^*(t)$ such that

$$z(t) = \frac{1}{2} [a(t)e^{-i\omega_z t} + a^*(t)e^{i\omega_z t}] \quad (6.13)$$

$$\dot{z}(t) = \frac{1}{2} [\dot{a}(t)e^{-i\omega_z t} - i\omega_z a(t)e^{-i\omega_z t} + \dot{a}^*(t)e^{i\omega_z t} + i\omega_z a^*(t)e^{i\omega_z t}] \quad (6.14)$$

$$\begin{aligned} \ddot{z}(t) = \frac{1}{2} [\ddot{a}(t)e^{-i\omega_z t} - 2i\omega_z \dot{a}(t)e^{-i\omega_z t} - \omega_z^2 a(t)e^{-i\omega_z t} \\ + \ddot{a}^*(t)e^{i\omega_z t} + 2i\omega_z \dot{a}^*(t) - \omega_z^2 a^*(t)e^{i\omega_z t}]. \end{aligned} \quad (6.15)$$

Note that this transformation has maintained the position z as a real quantity. We do not simply use a complex form for z because the equations are nonlinear. Inserting this transformation into Eq. (6.12), taking the rotating wave approximation by keeping only terms with $e^{-i\omega_z t}$, and simplifying, we get a new differential equation for $a(t)$,

$$\ddot{a} - [2i\omega_z + \gamma_z \delta_G(A)] \dot{a} + i\omega_z \gamma_z \delta_G(A) a = 0. \quad (6.16)$$

Finally, we can write a in terms of the slowly varying real amplitude $A(t)$ and slowly

varying real phase $\phi(t)$,

$$a = A(t)e^{i\phi(t)} \quad (6.17)$$

$$\dot{a} = \dot{A}(t)e^{i\phi(t)} + i\dot{\phi}(t)A(t)e^{i\phi(t)} \quad (6.18)$$

$$\ddot{a} = \ddot{A}(t)e^{i\phi(t)} + 2i\dot{\phi}(t)\dot{A}(t)e^{i\phi(t)} + i\ddot{\phi}(t)A(t)e^{i\phi(t)} - \left[\dot{\phi}(t)\right]^2 A(t)e^{i\phi(t)}. \quad (6.19)$$

Inserting this change of variables into Eq. (6.16) gives a complex nonlinear differential equation in $A(t)$ and $\phi(t)$. Taking the imaginary part of the equation and simplifying gives

$$(\omega_z - \dot{\phi})\dot{A} = \frac{1}{2} \left[\gamma_z \delta_G(A) \omega_z - \gamma_z \delta_G(A) \dot{\phi} + \ddot{\phi} \right] A. \quad (6.20)$$

We can ignore $\ddot{\phi}$ compared to $\gamma_z \delta_g \omega_z$ unless $\delta_G \sim 10^{-7}$ or less, but then the system is very nearly in equilibrium, so we expect $\ddot{\phi}$ to be small anyway. With this approximation we get an elegant and natural result,

$$\dot{A} = \frac{1}{2} \gamma_z A \delta_G(A). \quad (6.21)$$

This result is important and quite general. In practice, the gain control system may average the signal for some length of time τ before determining A , but as long as $\tau \gg 1/\omega_z$ and $1/\tau$ is much larger than the resulting self-excited oscillator linewidth, Eq. (6.21) is still valid. This result gives us the means to calculate an effective amplitude dependent damping toward the equilibrium amplitude which is created by the gain control system.

6.4 Comparator Limited Self-Excitation

The simplest electronic limiting system is a comparator. If the detected signal is passed through a comparator, then the output signal amplitude is independent of the

input signal amplitude. Comparators have been studied as simple limiters that can often stabilize chaotic systems [89]. There is also significant precedent for the use of comparators in limiting self-excitation. The comparator limited self-excited oscillator is an important traditional system that has been studied extensively, including analysis of the phase noise [90, 91, 92].

We were inspired by the use of comparators to limit the amplitude of a self-excited oscillating beam [93]. However, our single electron system has a significant disadvantage: the signal to noise ratio is extremely low.

6.4.1 Noiseless Analysis

The amplitude of the drive out of the comparator A_c is constant and independent of the amplitude of the signal going into the comparator A . If we assume a noiseless system, then the input amplitude A is just proportional to the oscillation amplitude, so the gain of the loop is

$$G = \frac{A_c}{A}. \quad (6.22)$$

With this expression for G , we can easily represent the comparator in the electronic gain control framework which uses $\delta_G(A) = G - 1 = \frac{A_c}{A} - 1$. Plugging this expression for $\delta_G(A)$ into Eq. (6.21), we get

$$\dot{A} = \frac{1}{2}\gamma_z(A_c - A), \quad (6.23)$$

which simply shows that the amplitude exponentially damps toward the equilibrium amplitude A_c with the same time constant ($\frac{1}{2}\gamma_z$) as the damping of the oscillation toward zero amplitude in the absence of feedback. Thus, the simplest electronic

limiter, a noiseless comparator, results in exponential damping of deviations from equilibrium.

6.4.2 The Effects of Noise

In reality, the signal to noise ratio is very low, so noise should not be neglected when calculating the gain of the limiter. It has been calculated that the effect of the noise is to soften the limiter. That is, a hard limiter with noise is similar to a soft limiter. The signal power output S_o from the comparator with input power signal to noise ratio $(S/N)_i$ is [94]

$$S_o = A_c^2 \frac{\pi}{4} \frac{S_i}{N_i} {}_1F_1^2 \left[\frac{1}{2}; 2; -\frac{S_i}{N_i} \right], \quad (6.24)$$

where A_c is the output amplitude of the comparator and ${}_1F_1$ is a hypergeometric function. We can now use this to calculate the effective amplitude gain G of the limiter, changing to signal and noise amplitudes $A = \sqrt{S_i}$ and $A_N = \sqrt{N_i}$,

$$\begin{aligned} G &= \frac{\sqrt{S_o}}{A} \\ &= \frac{A_c}{A_N} \frac{\sqrt{\pi}}{2} {}_1F_1 \left[\frac{1}{2}; 2; -\frac{A^2}{A_N^2} \right]. \end{aligned} \quad (6.25)$$

Next, we replace the hypergeometric function with an equivalent representation in terms of the more familiar Bessel functions,

$$G = \frac{A_c}{A_N} \frac{\sqrt{\pi}}{2} e^{-\frac{1}{2} \frac{A^2}{A_N^2}} \left[I_0 \left(\frac{1}{2} \frac{A^2}{A_N^2} \right) + I_1 \left(\frac{1}{2} \frac{A^2}{A_N^2} \right) \right]. \quad (6.26)$$

A comparison of the amplitude response of the comparator in the noiseless and noise inclusive cases is shown in Figure 6.3. A comparison of the $\delta_G(A)$ for each case is shown in Figure 6.4. It is clear from these plots that the noise softens the

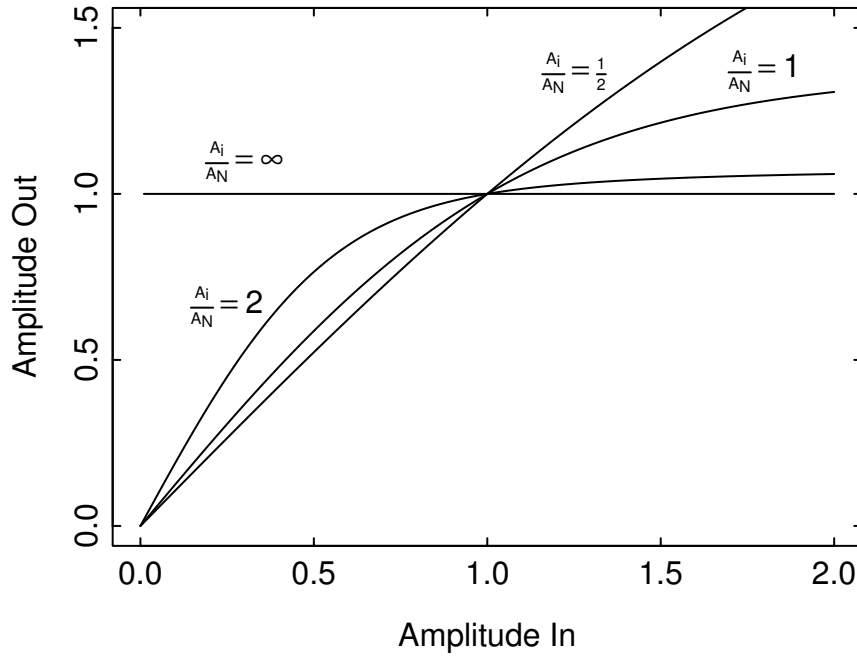


Figure 6.3: Comparator amplitude response for a signal without noise or combined with noise with the given signal to noise amplitude ratio.

response of the comparator, and that the variation in gain with amplitude $\delta_G(A)$ is significantly decreased even with a signal to noise ratio of one.

It is also useful to look at Eq. (6.26) in the weak signal limit, since it may give a more intuitively understandable result. For small x we can expand $I_0(x) + I_1(x) = 1 + x/2 + x^2/4 + \dots$. Retaining only the constant term, we can write the gain as

$$G = \frac{A_c}{A_N} \frac{\sqrt{\pi}}{2} e^{-\frac{1}{2} \frac{A^2}{A_N^2}}. \quad (6.27)$$

The effective drive strength coming out of the comparator is AG , which goes to zero with A rather than staying constant as in the noiseless comparator. Thus, we can see that the noise softens the response of the hard comparator.

This analysis has only been concerned with the amplitude (gain) changes associated with the noise. However, the noise actually also alters the phase of the drive

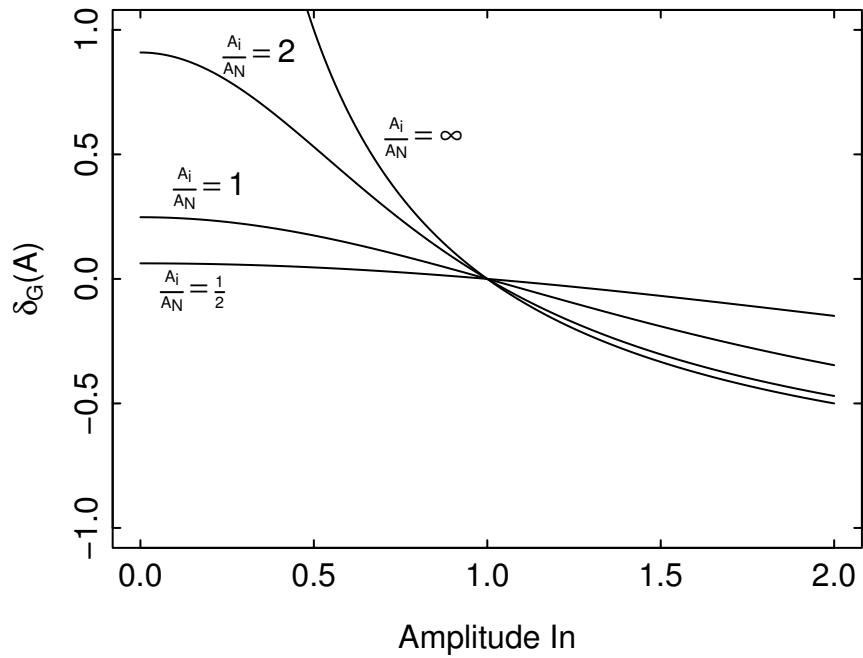


Figure 6.4: Change in gain $\delta_G(A)$ with a comparator for a signal without noise or combined with noise with the given signal to noise amplitude ratio.

signal. Further analysis on the effects of noise in narrow band limiters has been done by Jain [95] including the phase deviations of the signal caused by the noise. Taking advantage of the nonlinearity, it is possible to make the self-excited oscillator frequency independent of the feedback phase to first order around the operating point [93, 96], so the effects of the phase deviations can be minimized.

The comparator also removes all amplitude information from the noise going through it. Much of the fed back noise could actually cancel out noise that the particle experiences from the input of the first stage amplifier as with feedback cooling, but the comparator may interfere with this process. At the very least, the comparator mixes the signal and the many noise components, so each component may be scattered across many frequencies.

In order to avoid passing a signal completely buried in noise to the comparator, the signal must go through a very narrow filter first. In order to allow the use of a fixed frequency filter at an easily accessible frequency, the signal is amplified, filtered down to a bandwidth of a few MHz, and then mixed with a local oscillator down to 5 MHz. At 5 MHz, the signal is further amplified and filtered before going through a narrow active crystal filter.

The active crystal filter (see Figure 6.6) consists of a buffering amplifier on the

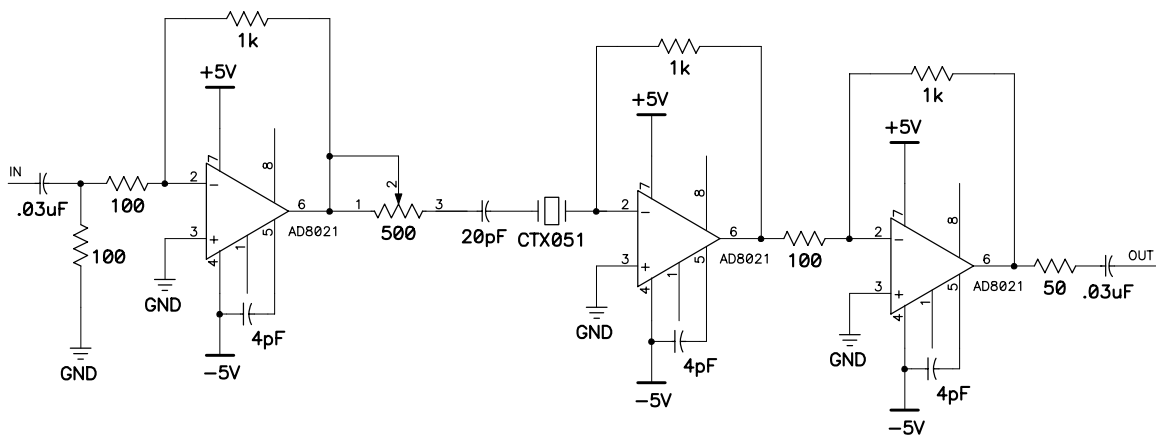


Figure 6.6: Schematic diagram of the active crystal filter used for comparator limited self-excitation.

input with a low impedance output (an AD8021 op-amp), a variable resistor to tune the filter width and a quartz crystal in series, and then an inverting amplifier with a low impedance input to buffer the output signal (another AD8021 op-amp). The input and output amplifiers provide gain and prevent the 50 Ω input and output transmission lines from adding resistance which would broaden the crystal resonance. In this arrangement, the filter can be made narrower than 50 Hz.

After passing through the narrow filter and comparator, the signal is again filtered to clean off higher harmonics output by the comparator, and is then used as a drive for

the electron. The local oscillator is passed through an electronic attenuator to adjust the amplitude, and then through an I & Q modulator which allows electronic variation of the phase. Finally, it is used as a second drive on the particle. The electron mixes the drives together while there is no measurable direct signal feedthrough to the amplifiers.

Example axial signal spectra are shown in Figure 6.7 with two different active

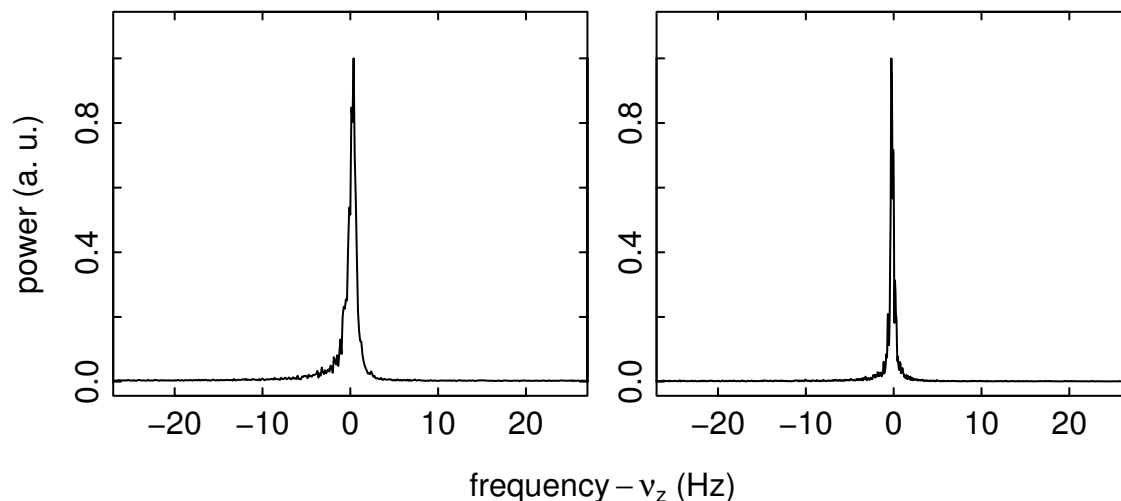


Figure 6.7: Hard limited self-excited oscillator response with a 150 Hz filter (left) and a 50 Hz filter (right), averaged over 80 s.

crystal filter widths. In each case, the phase and amplitude have been tuned to optimize the stability. Clearly, both peaks are narrower than the particle's driven linewidth, and the narrower filter gives a narrower linewidth. This is not surprising since there is less noise interfering with the performance of the comparator with a narrower filter. While the comparator is not the most gentle of limiters, the narrow filter and comparator can be easily integrated into the electronics of the experiment.

ARMA Analysis

Although it is very common to use a Fourier transform to generate a frequency domain representation of a signal (called a periodogram) such as in Figure 6.7, there are other methods. The goal of the analysis of signals from the self-excited oscillator is to determine the center frequency. While finding the peak of the Fourier transform is an excellent method for picking out a single sinusoidal signal from white noise, the Fourier transform of a stochastic process does not converge [97]. That is, if a signal is not coherent over the time scale of the sample, increasing the time length of the data may not improve the estimate of the frequency.

The problem is easily visible in Figure 6.8. On the left are spectra analyzed with a Fourier transform, with the system tuned to make a narrow lineshape or a broad lineshape. While the narrow lineshape gives a clear center frequency, the broad lineshape has many high maxima, and it is not clear which should be chosen as the true peak.

An alternative technique is the autoregressive moving average (ARMA) method. This is a method of fitting the data to a rational function model which can be chosen to match the expected features of the spectrum. In our case we choose an ARMA(2, 2) model, which is a peak of finite width plus background noise. We use a technique for determining the coefficients of the model (doing the fit) based on the method proposed by Cadzow [98, 99]. For details on the implementation of the ARMA algorithm, see [35]. The ARMA signal analysis of the same signals is shown on the right side of Figure 6.8. Clearly, there is a significant difference in the case of the incoherent signal, where we expect the ARMA method to outperform the Fourier transform

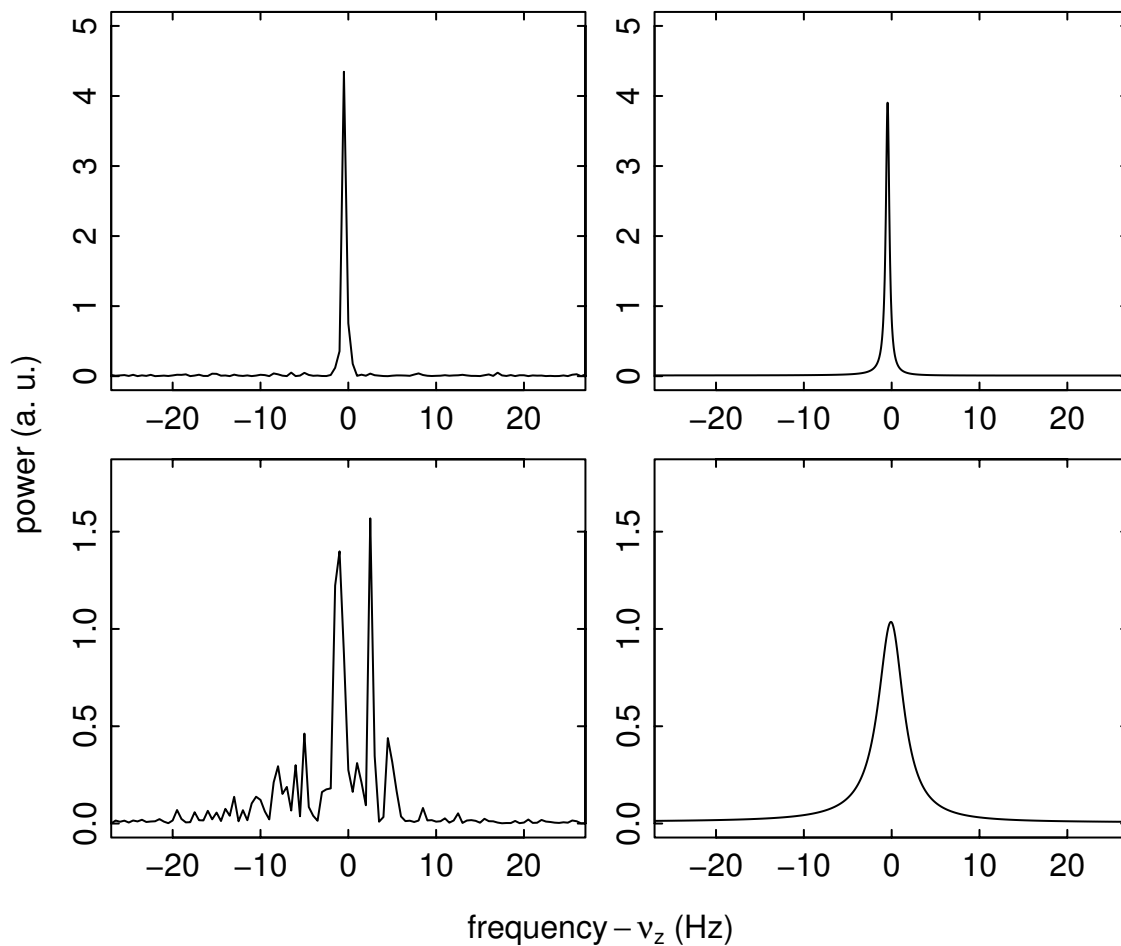


Figure 6.8: Comparison of periodogram (left) and ARMA (right) power spectrum estimation of the hard limited self-excited oscillator, taken near the harmonic amplitude (top) or in a highly anharmonic region (bottom).

method. Of course, we will normally operate the self-excited axial oscillator at the most coherent settings, but the incoherence may still be important over long time scales.

Absolute Amplitude Determination

We can once again take advantage of our ability to study the axial state by examining the cyclotron resonance. Figure 6.9 shows a series of cyclotron resonances

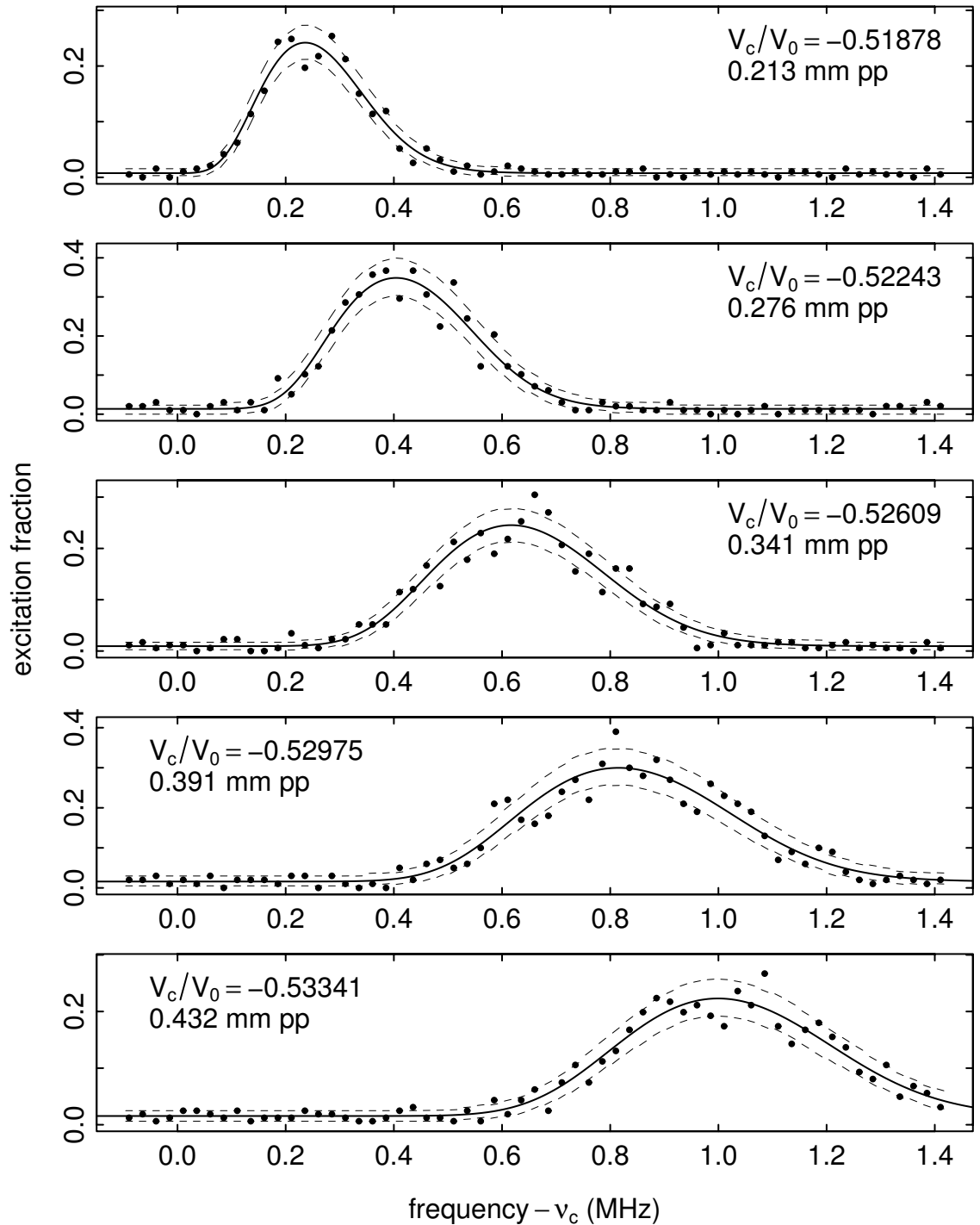


Figure 6.9: Cyclotron resonances at different feedback amplitudes and compensation potential settings. The dashed lines show the expected 68% confidence region for the data.

taken with comparator limited axial self-excitation at different amplitudes and compensation voltage settings. In each case the self-excitation amplitude is chosen to be at the most harmonic amplitude (narrowest response) for the given compensation voltage. The width of the cyclotron resonance is used to calculate the axial temperature. However, the width is different at the same temperature for different oscillation amplitudes (see section 3.5.1 for details). Saturation of the transition probability is also included in the fits.

While using the cyclotron spectra to determine the oscillation amplitude, the amplitude of the detected axial electrical signal is also recorded. The measured electrical and absolute amplitudes are plotted in Figure 6.10. A linear fit to that data yields a

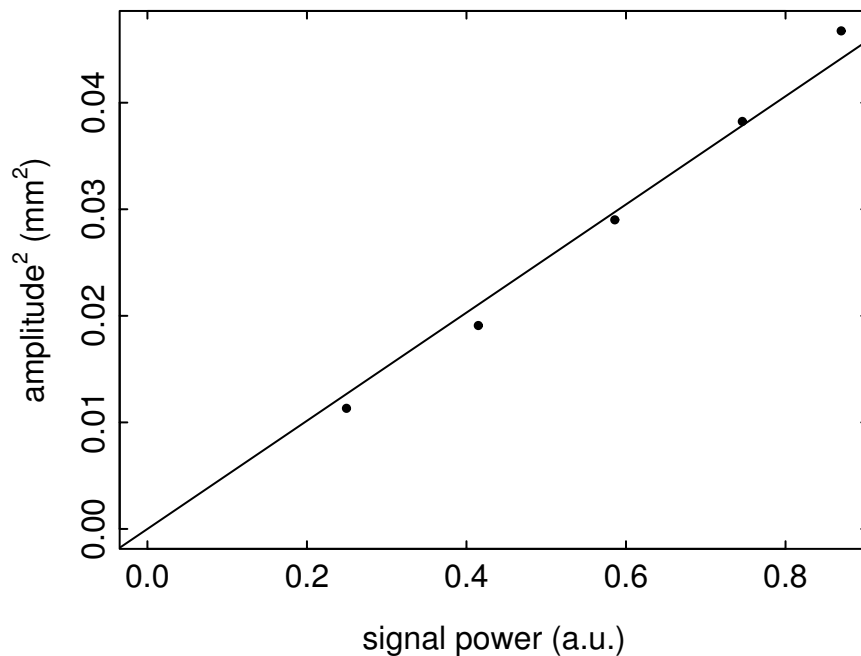


Figure 6.10: Absolute amplitude measured from a cyclotron spectrum plotted against the electrical signal measured. The fit gives an absolute calibration relating the signal size to the amplitude of the oscillation.

calibration for converting measured electric signal amplitudes into absolute oscillation

amplitudes.

Another result which comes from the cyclotron spectra in Figure 6.9 is the axial temperature. The axial temperature results for each amplitude are plotted in Figure 6.11. Surprisingly, the axial temperature is approximately independent of the

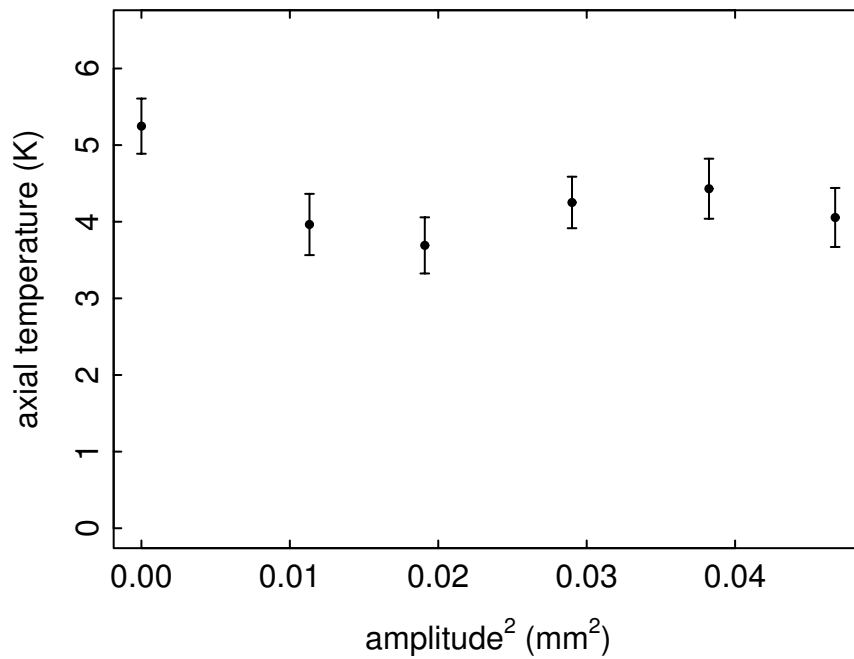


Figure 6.11: Axial temperature as measured from the cyclotron resonance at different axial amplitudes. The zero amplitude point had no feedback.

amplitude of the excitation and is about the same as the axial temperature without any feedback or drive and with the amplifiers on. Fortunately, this indicates that the comparator does not scramble the signal and noise so much that it heats up the particle.

Measuring the Axial Anharmonicity

With an absolute calibration of the axial amplitude compared to the electronic signal amplitude, it is fairly straightforward to map the axial anharmonicity. Figure 6.12 shows the axial frequency as the amplitude is varied at many compensation voltage settings. The procedure for each point is simple: set the attenuation of the drive to set the oscillation amplitude, measure the signal amplitude, and measure the peak frequency. In practice, there is one more complication. The response must be kept in the center of the active crystal filter passband before the comparator in order to avoid phase or amplitude distortion from the filter. This requires iterating the data acquisition procedure to shift the mixed down response frequency to the center frequency of the narrow filter.

The results show a variety of behaviors. When the compensation potential is low, there is no harmonic region. Instead, the frequency shifts down immediately with increasing amplitude. The slope of the frequency versus amplitude curve is infinite at a harmonic point. As the compensation voltage is increased, a harmonic point appears and moves to higher amplitudes. The harmonic point can be moved arbitrarily high in amplitude, but the region which is harmonic enough to be usable becomes fractionally smaller. For comparison, the harmonic region can only be shifted a few Hertz (less than a linewidth) from the zero amplitude frequency to be useful for driven detection. Thus, the amplitude for driven detection is limited.

The anharmonicity data in Figure 6.12 can be fit to polynomials to measure the $C_4^{(0)}$, $C_6^{(0)}$, D_4 , and D_6 parameters of the trap. Two other relevant trap parameters, $C_2^{(0)}$ and D_2 can be measured simply by tracking the axial frequency (from the

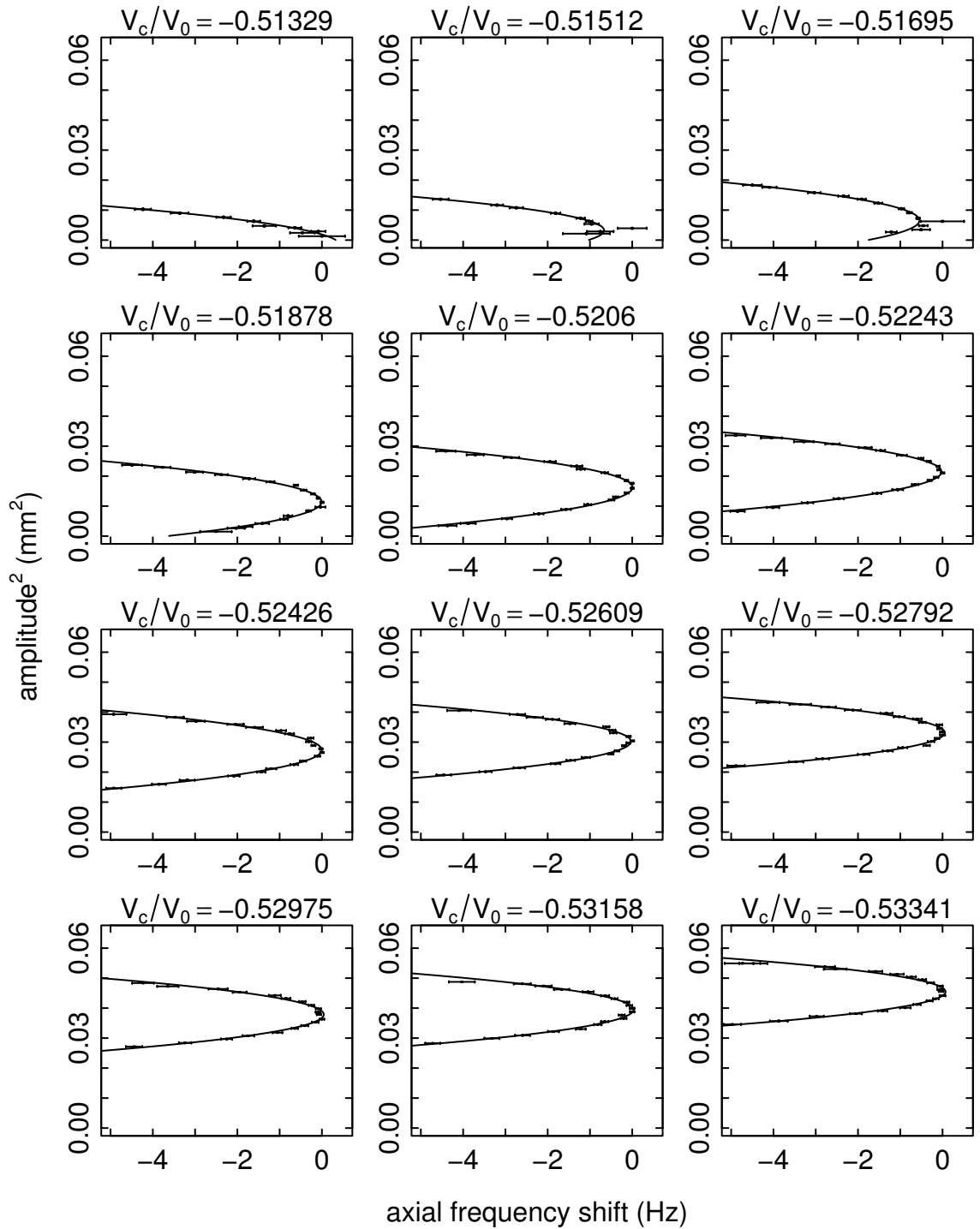


Figure 6.12: Axial frequency measured as a function of axial amplitude by varying the feedback gain while holding the feedback phase constant. This process is repeated at many compensation potential settings to map out the variation in anharmonicity.

center of the one-electron dip in the noise) as the ring and compensation voltages are changed. A complete discussion of the anharmonicity coefficients can be found in Chapter 2. All these results are plotted in Figure 6.13. As expected from the shape of the curves in Figure 6.12, the C_4 trap coefficient changes significantly in the range of compensation voltages used, while C_6 does not change very much. That is, the compensation potential setting is primarily shifting the parabola in A^2 , but not changing its curvature.

The results of the data analysis are shown in Table 6.1. As expected, $C_2^{(0)}$ and

coefficient	calculated	measured
$C_2^{(0)}$	0.1247(2)	0.1378(7)
$C_4^{(0)}$	-0.0148(38)	-0.028(1)
$C_6^{(0)}$	-0.0908(8)	1.2(2)
D_2	0.0011(9)	0.001424(1)
D_4	-0.0582(5)	-0.055(2)
D_6	0.0127(5)	2.5(3)
$\gamma = D_2/D_4$	-0.019(16)	-0.026(1)
V_{comp}/V_R for $C_4 = 0$	0.76(7)	1.01(3)
C_6 for $C_4 = 0$	-0.0875(19)	-0.065(10)

Table 6.1: Calculated and measured trap parameters. The uncertainties in the calculated values are estimated using 0.0005 inch variations in z_0 , ρ_0 , and Δz_c due to machining tolerance and thermal contraction.

D_2 measurements give precise results although there is some disagreement with the expected values. The first order anharmonicity coefficient measured with the self-excited oscillator is D_4 . The measurement gives a precise result which is close to the expected value. Although the C_6 values measured in the region tested were near the expected value, neither the slope (D_6) nor the intercept ($C_6^{(0)}$) were accurately determined. This is not surprising since C_6 varies little over the range of compensation potentials measured. The V_{comp}/V_R that gives $C_4 = 0$ is important since it is

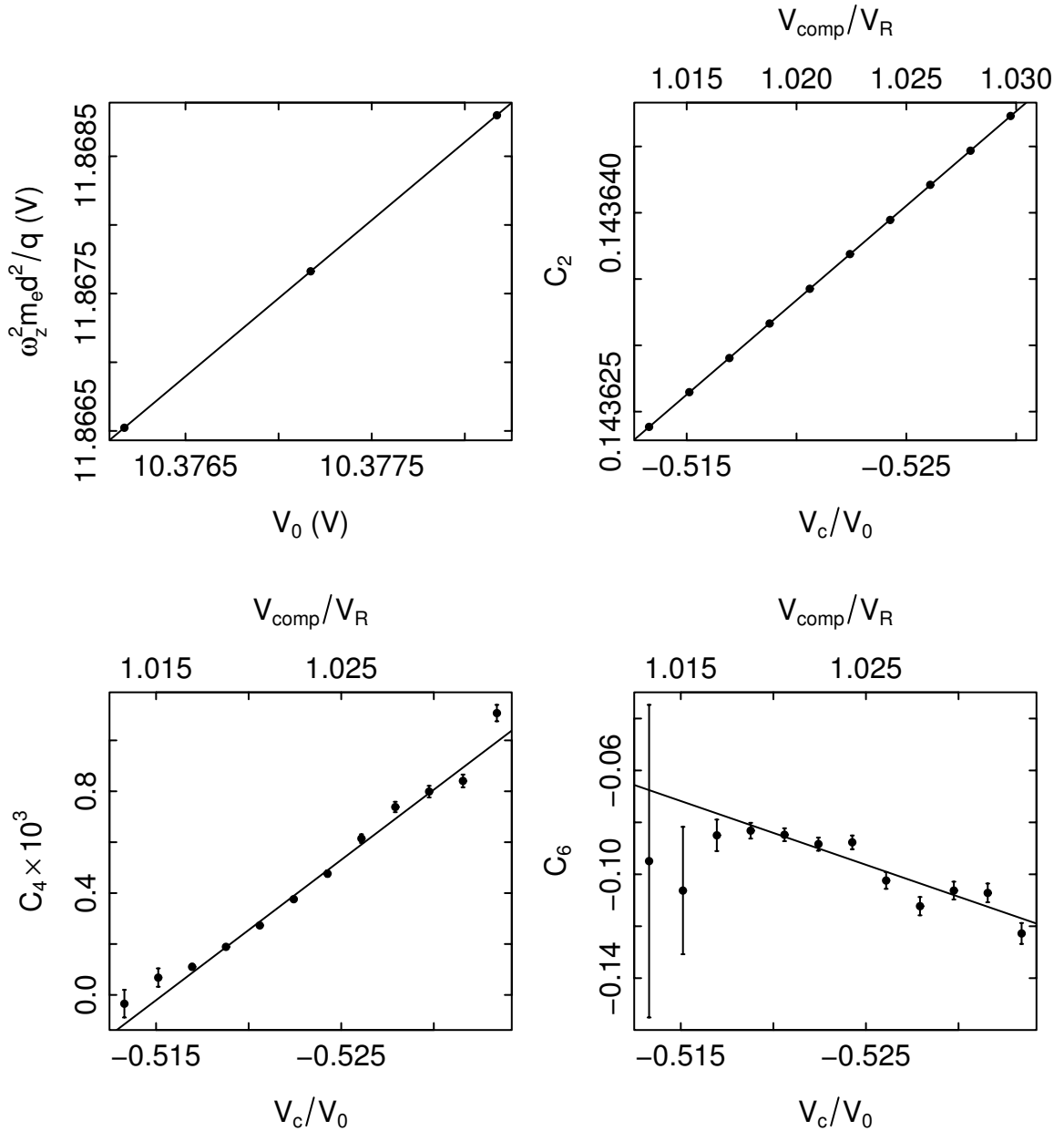


Figure 6.13: The change in axial frequency as the trapping potential is varied (upper left), used to find C_2 . The change in axial frequency as the compensation potential is varied (upper right), used to find D_2 . The variation in C_4 as measured from the anharmonic axial response at different compensation potential settings (lower left), gives a measure of D_4 . The variation in C_6 as measured from the anharmonic axial response at different compensation potential settings (lower right), gives a measure of D_6 .

the experimental starting point for compensation adjustments. We have seen that this value changes significantly depending on how the gaps between the electrodes are treated theoretically, so the disagreement between the calculation and measured values is not surprising.

A previous method of characterizing the trap anharmonicity used the parametric resonance shape to determine the anharmonicity coefficients [26]. However, those measurements did not use the cyclotron spectrum to obtain an absolute amplitude calibration, so a trap anharmonicity parameter had to be assumed to get an amplitude scale. The parametric method also requires a measurement of the parametric excitation threshold, so it is not as simple as using the self-excited oscillator method.

Amplitude and Phase Response Map

There are two parameters which control the operation of the comparator limited self-excited oscillator: the feedback amplitude A_c , and feedback phase ϕ . The amplitude of the feedback shifts the response frequency because of the anharmonicity of the axial motion. The feedback phase determines the frequency through Eq.(6.8). The response can be mapped out experimentally by recording the amplitude and frequency of the oscillation while varying the parameters, as in Figure 6.14. As with the anharmonicity measurements, the mixed down axial response must be in the middle of the narrow active crystal filter in order to avoid phase and gain distortion. Thus, the data acquisition process is iterated at each point. Many samples are taken in order to get an averaged amplitude, averaged frequency, averaged FWHM, and frequency standard deviation of the response.

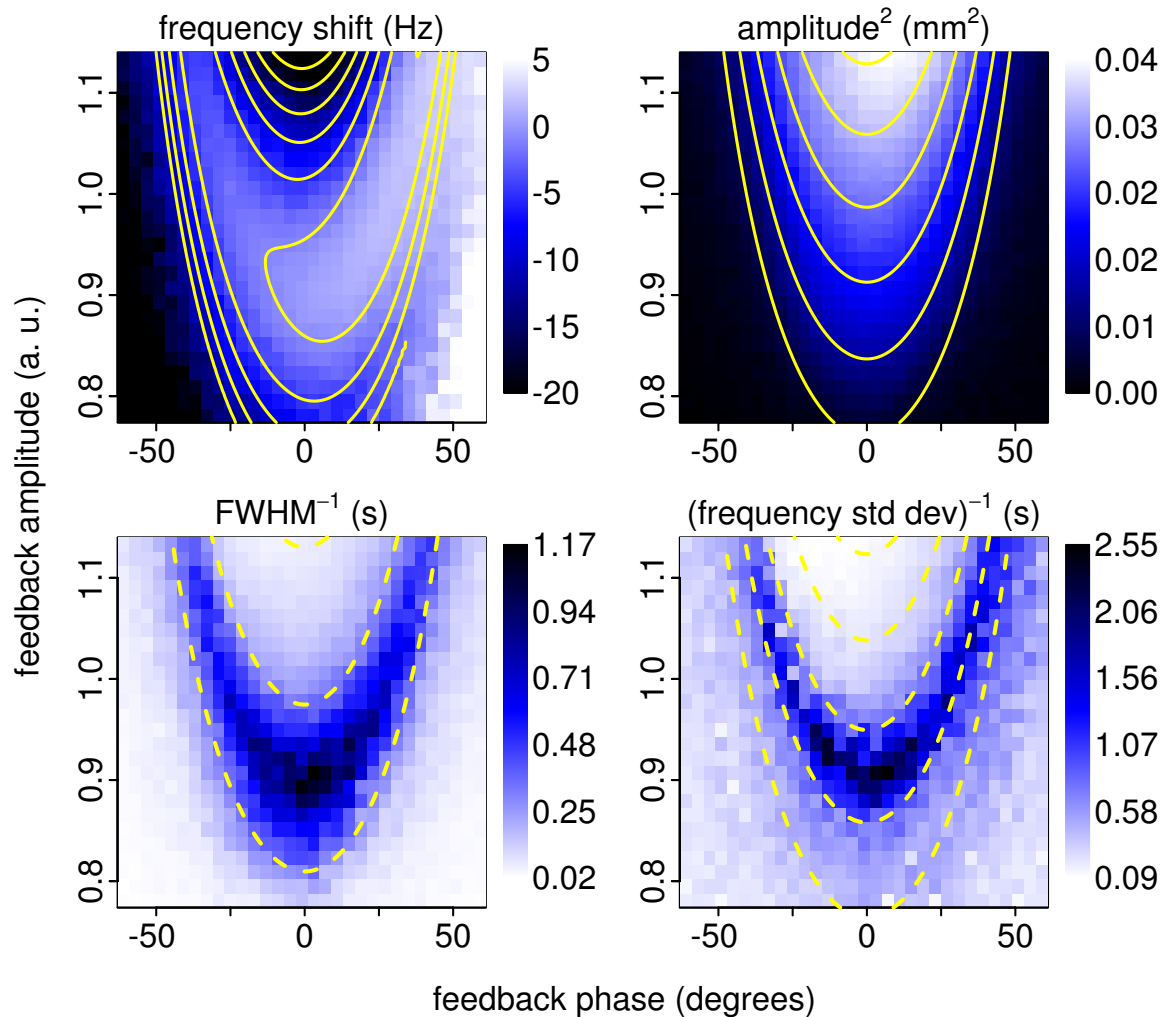


Figure 6.14: Maps of the hard limited self-excited oscillator response over different feedback phase and gain. The contours, calculated from the noiseless hard limited feedback theory, are at equal steps in frequency (upper left) or amplitude² (all others). In the frequency plot (upper left), the contours are only drawn in the region above the excitation threshold and the scale clips the extreme high and low frequencies of the region below threshold.

We can further understand the shape of the amplitude and phase response maps in Figure 6.14. At constant response amplitude, the frequency variation with phase can be found from Eq. (6.8) using the amplitude dependent frequency $\omega_z(A)$ already found from the anharmonicity analysis. Next, we need a way to determine the oscillation amplitude from the feedback gain.

In the absence of noise, we can combine Eq. (6.22) with Eq. (6.4) to get

$$A = A_c \cos \phi, \quad (6.28)$$

which gives a very simple expression for the oscillation amplitude A in terms of the feedback phase ϕ and the comparator output amplitude A_c .

Since noise cannot be neglected, we must include the effects of noise on the comparator behavior. So, we use Eq. (6.26), the noise softened limiter, and Eq. (6.4) to get

$$A_c \cos \phi = \left\{ \frac{1}{A_N} \frac{\sqrt{\pi}}{2} e^{-\frac{1}{2} \frac{A^2}{A_N^2}} \left[I_0 \left(\frac{1}{2} \frac{A^2}{A_N^2} \right) + I_1 \left(\frac{1}{2} \frac{A^2}{A_N^2} \right) \right] \right\}^{-1}. \quad (6.29)$$

It is important to notice that the noise does not modify the shape of the contours of constant A since at constant A the right side of Eq. (6.29) is constant and the relationship between A_c and ϕ is the same as for the noiseless case. The noise only changes the spacing between the contours. Although it is not very convenient, the right side of the equation is numerically invertible so this relation can give the amplitude of excitation A as a function of A_c and ϕ . This analysis is used for the contours in Figure 6.14.

In the very noisy limit, we can use Eq. (6.27) and again use Eq. (6.4) to solve for

the excitation amplitude,

$$A = \sqrt{2A_N^2 \log \left(\frac{A_c}{A_N} \frac{\sqrt{\pi}}{2} \cos \phi \right)}. \quad (6.30)$$

In this result, there is a clear threshold for oscillation, in contrast with the noiseless comparator. Choices of amplitude A_c or phase ϕ which give imaginary amplitudes are simply below the excitation threshold.

As expected, the parameters which give the most stable frequency (smallest FWHM or frequency standard deviation) are in the harmonic region of amplitude, as can be seen in Figure 6.14. It appears that the phase should just be centered on zero. However, if the amplitude noise were less significant, the most stable region would be at $\phi > 0$ where $\frac{d\nu_z}{d\phi} = 0$. This insensitivity to phase noise is the subject of the paper by Yurke [96] and actually relies on the anharmonicity of the oscillation. In a perfectly harmonic oscillator there are no parameter settings that make $\frac{d\nu_z}{d\phi} = 0$.

Rise Time

Frequency stability is not the only concern in detecting the axial motion. Quantum jump spectroscopy of the cyclotron and anomaly transitions requires shutting off all drives and even the axial amplifiers during the transition excitation in order to get narrow lineshapes. The axial detection is then turned back on and the particle state is checked. Thus, the rise time, the time it takes for the self-excited oscillator to start up, is important. If it takes too long for the axial motion to equilibrate for detection, the state may change before it can be detected. Figure 6.15 shows the transient amplitude response of the self-excited axial oscillator with several different narrow active crystal filter widths.

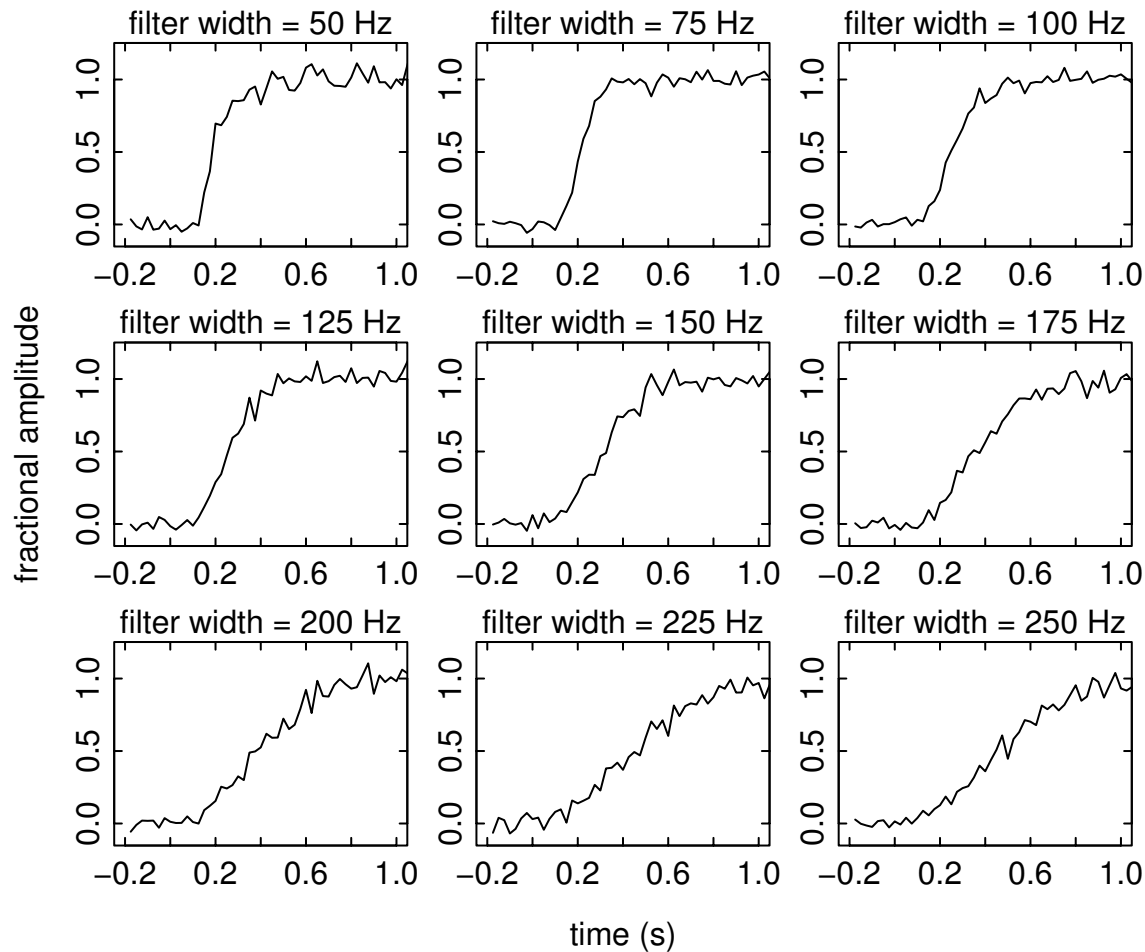


Figure 6.15: Transient response of the self-excited oscillator response at different pre-comparator filter widths. In each case the feedback was turned on at time = 0.

The results show that the wider the filter, the longer it takes for the self-excited oscillator to reach equilibrium. This may seem counter-intuitive because the delay going through a narrow filter is longer, so the response with a narrow filter should be slower to change. However, all of these rise times are long compared to the filter delay times, so the rise time is not limited by the delay of the filters..

The dominant effect is that the broader the filter, the lower the signal to noise ratio of the electrical signal going through the comparator. The lower signal to noise ratio

softens the limiter, decreasing the restoring feedback gain $\delta_G(A)$ at low amplitudes (see Figure 6.3). The result is that for a broader filter the rise time is longer, so the narrow filter improves both the rise time and the frequency stability, although it decreases the available bandwidth.

Ultimate Stability

Although we have seen how to optimize the amplitude and phase of the comparator limited self-excited oscillator to maximize the frequency stability, we have not looked for the optimal choice of compensation voltage setting. The standard deviation of the frequency after being optimized at each compensation voltage is plotted in Figure 6.16. It is clear that if the compensation voltage is too low, then there is either no harmonic amplitude or the harmonic amplitude is at so low an amplitude that the signal is not detectable. Therefore, it is reasonable that the frequency stability should be worse at low amplitudes. It is not obvious that the stability should get worse at high oscillation amplitudes. Further analysis of the optimal harmonic amplitude will be done in section 6.6.

With the compensation potential optimized, the attainable frequency stability for different averaging times can be measured. The stability may also depend on the signal analysis technique: periodogram (Fourier transform) or ARMA. The results are plotted in Figure 6.17. First, the results show that the narrower the filter, the better the stability, as expected. Second, the two analysis techniques give comparable results for short times where the signal looks like a sine wave buried in noise. However, the ARMA technique is superior for long averaging times where the incoherence of

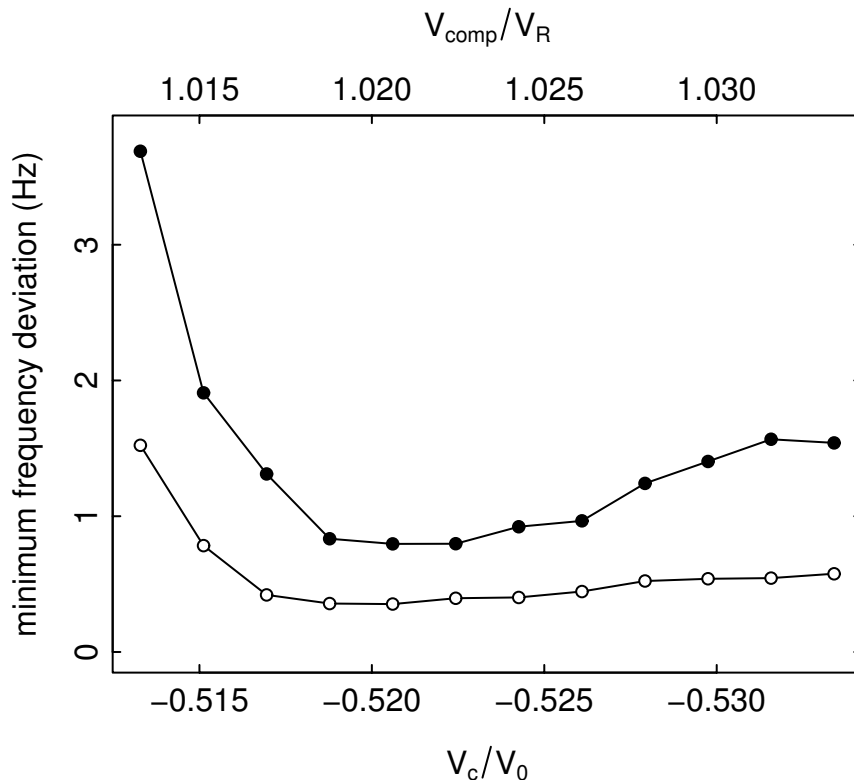


Figure 6.16: Frequency scatter measured at each compensation potential from the frequency standard deviation (open circles) or the FWHM of the ARMA peak (filled circles). These show what compensation voltage range should be chosen to get maximum axial frequency stability.

the signal can be resolved. For our typical averaging time of 1 s used for monitoring the cyclotron state, the choice of analysis technique is not important.

Ultimately, the purpose of the self-excited oscillator is to detect quantum jumps of the cyclotron or spin state. With all parameters optimized, Figure 6.18 shows the cyclotron state monitored over time with a 1 s averaging time at each point. The quantum jumps of approximately 12 Hz per cyclotron state are easily resolved. Despite this success, there is a visible problem. When the cyclotron state is excited there is more jitter of the axial frequency because the signal is no longer in the center

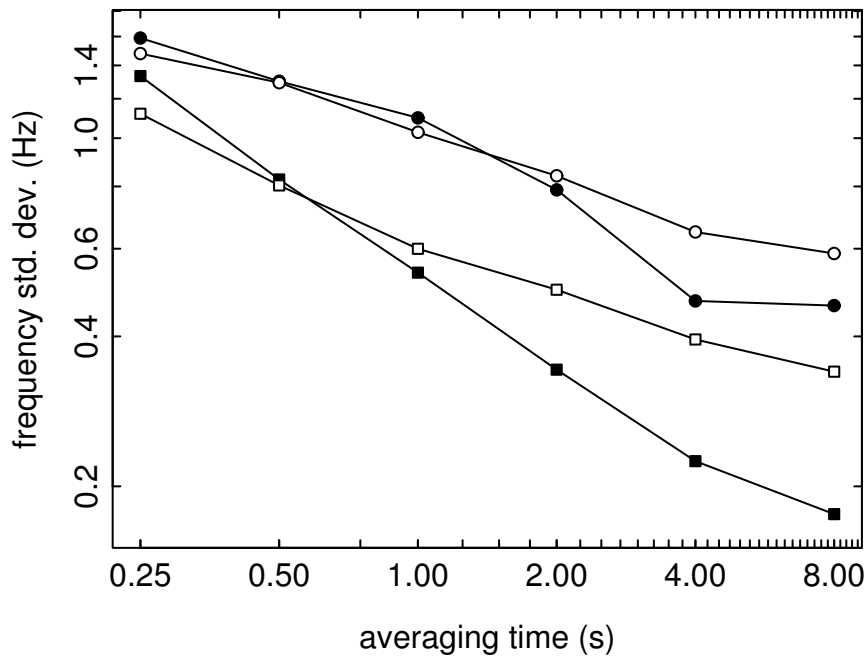


Figure 6.17: Frequency stability of self-excited axial oscillator based detection with a 150 Hz pre-comparator filter (circles) or 50 Hz pre-comparator filter (squares). In each case the frequencies are determined from the peak of the periodogram (open) or ARMA analysis (filled).

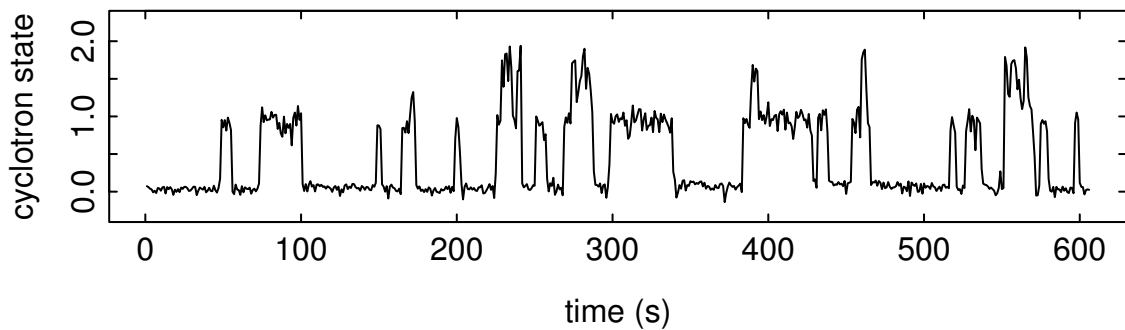


Figure 6.18: Quantum jumps of the cyclotron motion driven by a weak μ -wave drive as detected by monitoring the frequency of the hard limited self-excited axial oscillator.

of the active crystal filter. Thus, there is additional phase and amplitude distortion of the feedback which effectively changes the phase and amplitude parameters of the feedback to no longer be optimal. Although the frequency stability attained is

adequate for detecting these jumps, we would like to decrease the magnetic bottle strength significantly and thus decrease the jump size. It would be possible to make the filter narrower to improve the stability but there will likely be a trade off between stability and bandwidth. Fundamentally, there is no reason to have the bandwidth restriction. The solution is a more complex electronic limiter.

6.5 DSP Limited Self-Excitation

In order to increase the bandwidth of the electronically limited self-excited oscillator and possibly decrease the filter width in the limiter, we consider a more general limiter topology. Instead of forcing the feedback signal through the limiter, the signal is analyzed and an electronically variable attenuator is adjusted to change the gain going around the feedback loop. This topology is often called an automatic gain control (AGC) system.

Our initial attempts used our computer to analyze the signal and update the attenuation. This was not effective because the computer could not update the attenuation quickly enough to keep the self-excited oscillator under control. Therefore, we switched to using a dedicated digital signal processor (DSP) to analyze the signal and send out a correction signal to the voltage variable attenuator. A schematic diagram of the system is shown in Figure 6.19.

This system was implemented after we changed the axial frequency to 200 MHz, so all the results in this section were taken at this higher axial frequency. At the same time, the trap was replaced with a new trap with electrodes made of silver instead of copper. Finally, the DSP limited self-excited oscillator data was all taken with the

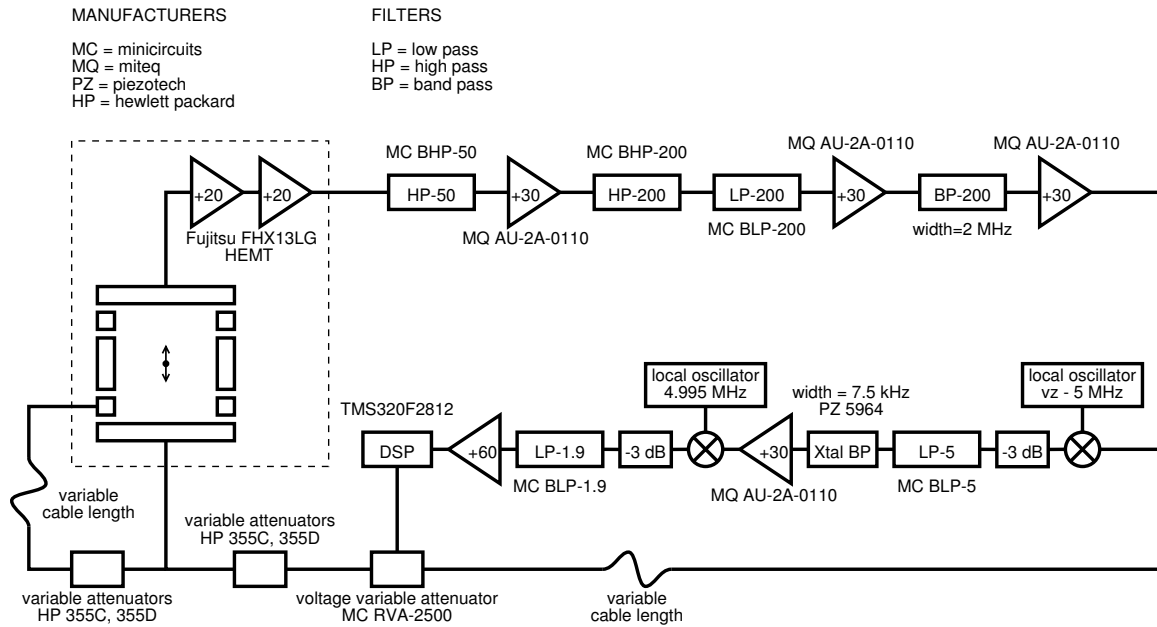


Figure 6.19: Schematic diagram for DSP limited self-excitation.

dilution refrigerator running and the first stage amplifier dissipating only $12 \mu\text{W}$.

We first pass the detected axial signal through a series of amplifiers and filters, with the narrowest filter being a homemade coaxial resonator filter with a bandwidth of under 2 MHz. Part of the signal is then split off and mixed down to 5 MHz where it goes through a narrow (7.5 kHz) bandwidth crystal filter and is further amplified. Finally, it is mixed down again to 5 kHz for analysis by the DSP. Note that the local oscillators used to mix the signal down are never used again to mix back up so the phase of the mixed down signal is arbitrary; the DSP only does amplitude analysis. The DSP analyzes the signal and outputs a slowly varying control signal to the voltage variable attenuator, which is placed in the feedback path which directly feeds the directed signal back into the experiment as a drive without any mixing stages.

In order to eliminate direct feedthrough of the drive to the amplifiers, the drive is applied on two electrodes with amplitudes and phases such that the coupling to the amplifier cancels, but the coupling to the electron does not. This method of feedthrough cancellation is superior for a wide bandwidth system because it does not require mixing the signal to an intermediate frequency (IF) and far less power is needed to drive the particle. With a large bandwidth and a lot of background noise, driving the particle with multiple frequencies for the particle to mix together might require prohibitively high total drive power for the dilution refrigerator to handle. The narrowest bandwidth element in this feedback loop is the first stage cryogenic amplifier, so the system can in principle utilize the full bandwidth available from the experiment.

6.5.1 DSP Algorithms

When the 5 kHz signal reaches the DSP, it is digitized by an analog to digital converter (ADC). Once digitized, almost arbitrary transformations can be performed in the digital domain. Finally, an analog control signal is produced by a digital to analog converter (DAC). What comes between the ADC and the DAC is the control algorithm, which is restricted only by the clock speed and memory of the DSP.

The starting point for the algorithms we have used is a discrete Fourier transform (DFT). The DFT calculates the Fourier integral for a set of fixed frequencies. The result of each integral is stored in a frequency bin, and the integral is weighted exponentially over time in each bin. This Fourier transform technique is used because an exponentially windowed DFT requires only a simple update to each frequency bin at

each time step without any additional information about the previous steps. A fast Fourier transform (FFT) is preferred for transforming a large data set at once, but it is not efficient for a continuously updated transform in terms of speed or memory consumption.

The exponential weighting time constant determines the frequency width of each frequency bin. The width of the frequency bin is analogous to the width of the narrow active crystal filter used in the comparator limited self-excited oscillator. Since the analysis is performed digitally in the DSP, there are no physical limitations, such as the quartz crystal Q , on the filter width. However, it is sensible to choose the frequency bin width to be larger than than the broadest linewidth of the self-excited oscillator. Otherwise, no frequency bin will contain the full particle signal and the response of the algorithm may be too slow to control the self-excitation. For the data presented here, the exponential time constant of the filtering is $\tau = 0.04$ seconds.

Since the exponentially weighted DFT creates Lorentzian shaped frequency bins in Fourier space, the bins are typically made to overlap significantly in order to smooth out the response variation between bins. In the end, the total bandwidth of the limiter is restricted by how many frequency bins the DSP can handle calculating given its finite clock speed and memory. In practice, this has been a total usable bandwidth of 50 to 100 Hz.

With the DFT of the signal available, the particle signal amplitude is identified as the magnitude of the frequency bin with the largest magnitude. Finally, this amplitude A is transformed by the programmed $\delta_G(A)$ function and is then output as the control signal for the voltage variable attenuator. For a detailed discussion of

the control algorithm and the DSP code, see Appendix C.

6.5.2 Analysis

In principle, the response function $\delta_G(A)$ programmed into the DSP can be any function desired. In practice, polynomials are by far the easiest functions to evaluate. Any other useful function can probably be adequately approximated with a polynomial. So far we have used a cubic polynomial,

$$\delta_G(A) = a_1(A_0 - A) + a_2(A_0 - A)^2 + a_3(A_0 - A)^3. \quad (6.31)$$

We can insert this $\delta_G(A)$ into Eq. 6.21 to find the differential equation for the amplitude response over time,

$$\dot{A} = \frac{1}{2}\gamma_z A [a_1(A_0 - A) + a_2(A_0 - A)^2 + a_3(A_0 - A)^3]. \quad (6.32)$$

We have so far only used $a_2 = a_3 = 0$, that is, a linear response function. For small displacements of A from A_0 , the amplitude exponentially damps back to A_0 . For large displacements, the behavior is more complex. Use of the nonlinear terms will likely be helpful for optimizing the rise time of the DSP limited self-excited oscillator in the future.

Since the effective filter width can be made much narrower (~ 10 Hz) with the DSP based limiter than with the comparator, the noise is significantly reduced. Also, since the background noise going through the variable attenuator is far less distorted than the noise going through the comparator, the noise feedback may have a cooling effect on the particle as with feedback cooling. Still, the noise causes the DSP to incorrectly estimate the signal size and excess noise introduced by the amplifier chain

has a heating effect. Put together, there is amplitude noise that may cause frequency noise due to the anharmonicity, and there is phase noise that is directly caused by the excess noise. For a thorough treatment of the effects of noise on self-excited oscillators, see Lax [88].

6.5.3 Experimental Results

After weeks of programming the DSP in assembly, the DSP limited self-excited oscillator was successful the first time it was tried. This immediate success is an indication of the robustness of the system. As with the comparator limited self-excited oscillator, the cleanest and most stable response is obtained when the amplitude of oscillation is tuned to be in the harmonic region. The axial signals detected with the DSP limited self-excited oscillator with the amplitude properly tuned or mistuned are shown in Figure 6.20. Clearly, the width of the response in the harmonic region is

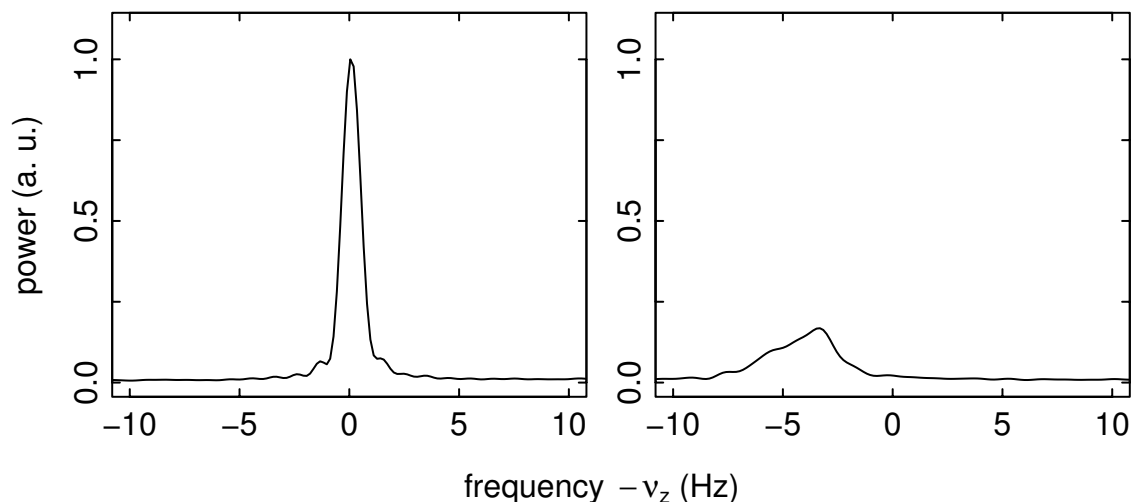


Figure 6.20: Comparison of the FFT of the detected self-excited oscillator signal with the amplitude tuned to the harmonic region (left) or with the amplitude mistuned (right). Each was taken with a 1 second square window with 100 spectra averaged.

limited by the Fourier transform resolution bandwidth with the 1 s sample length used in Figure 6.20. While taking much longer time samples adds additional problems, even with an 8 s sample, as in Figure 6.21, the true linewidth is not easily determined. It

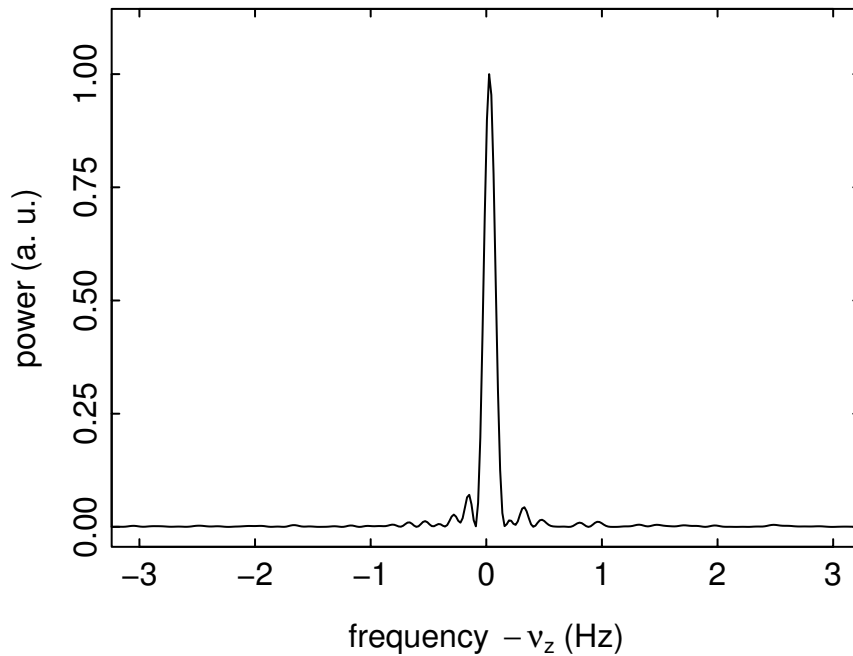


Figure 6.21: FFT of the detected self-excited oscillator axial signal with an 8 second square window.

appears that the stability of the DSP limited self-excited oscillator is not significantly limited by the typical instantaneous linewidth under reasonable conditions. This justifies the use of the FFT to find the peak of the response for tracking the axial frequency, which we use in all analysis of the DSP limited self-excited oscillator.

As with the unlimited and comparator limited self-excited oscillators, we can learn more about the DSP limited self-excited oscillator by analyzing the cyclotron spectrum during self-excitation. Cyclotron spectra at 3 different axial amplitudes and compensation voltages are plotted in Figure 6.22. In each case, the amplitude was

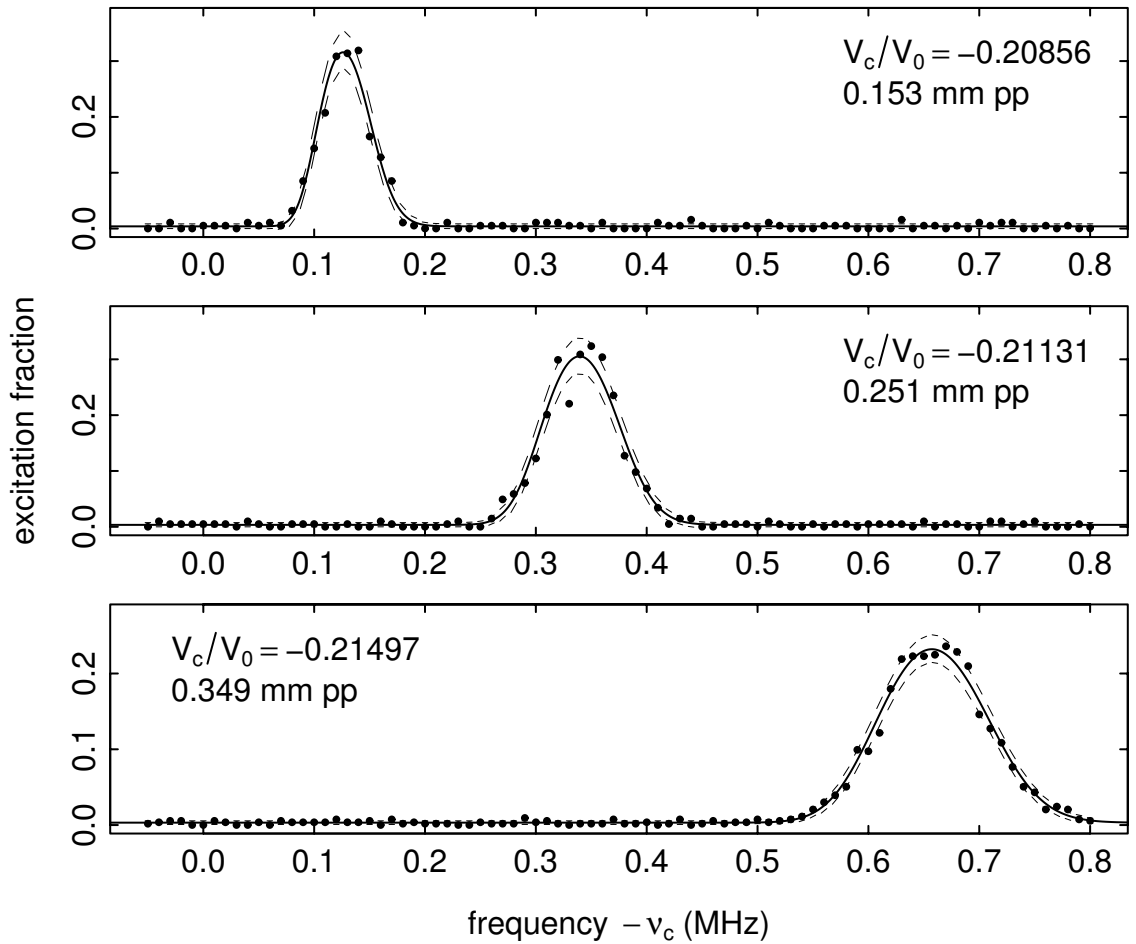


Figure 6.22: Cyclotron resonances at different feedback amplitudes and compensation potential settings with DSP limited self-excitation. The dashed lines show the expected 68% confidence region for the data.

centered in the harmonic amplitude region. When compared to Figure 6.9, it is clear that the width of the cyclotron peak is much narrower here. There are two reasons for the reduced width. First, the axial frequency is about 3 times higher, which makes the linewidths approximately 10 times narrower at the same axial temperature. Second, the axial temperature in all cases is somewhat lower. The axial temperatures for the three amplitudes are shown in Figure 6.23. Compare these to the axial temperatures for comparator limited self-excitation in Figure 6.11. The reduced axial temperature

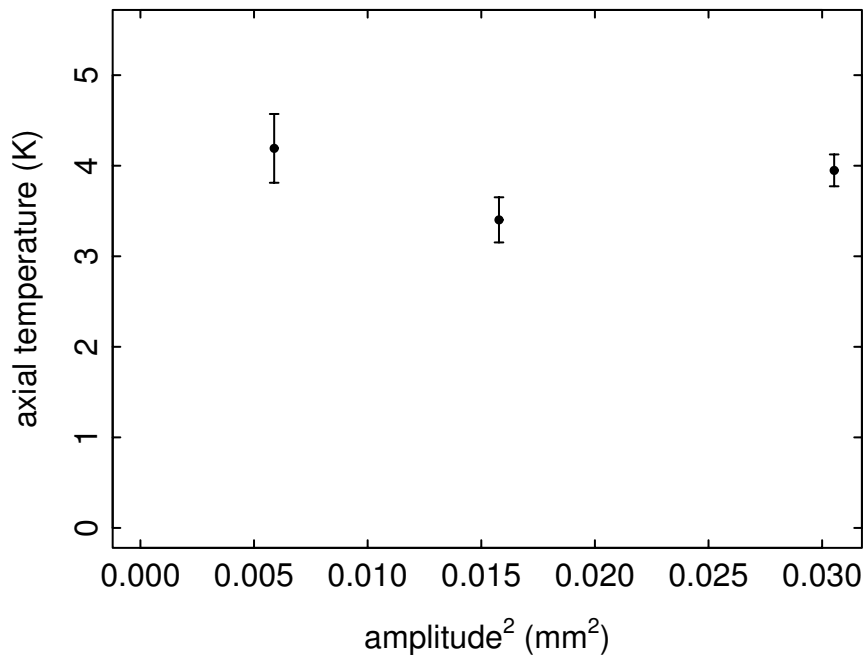


Figure 6.23: Axial temperatures measured from cyclotron spectra with different DSP limited self-excited oscillator amplitudes.

may be due to the cooling effect of the feedback which is obscured with the comparator because of the severe distortion of the noise that it causes. The axial amplitudes examined with DSP limited self-excitation are smaller than those with comparator limited self-excitation because the anharmonicity is more significant at this higher axial frequency.

The real test of the DSP limited self-excited oscillator is the frequency stability. Over a range of averaging times, the absolute frequency stability is better than that obtained with the comparator limited self-excited oscillator (see Figure 6.24). Although the fractional frequency is even better than an absolute comparison of the DSP and comparator limited self-excited oscillators indicates, there are many changes due to the increased axial frequency (see Section 2.3.3). It is not clear how much of

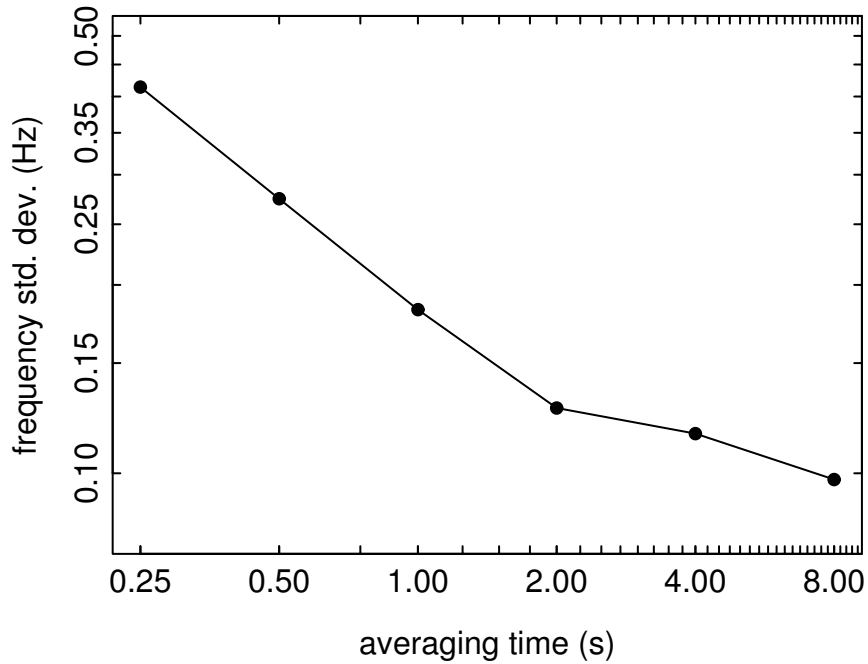


Figure 6.24: Frequency instability measured for different dwell times for the DSP limited self-excited oscillator.

the improvement is due to using the DSP instead of the comparator.

The purpose of monitoring the axial frequency is to detect quantum jumps of the cyclotron motion, as in Figure 6.25. There are very few points per jump in this data

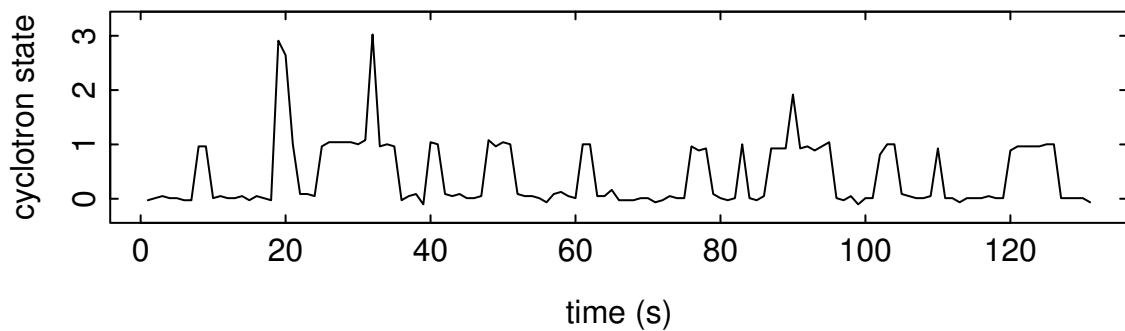


Figure 6.25: Quantum jumps as detected with the DSP limited self-excited oscillator.

because the cyclotron excited state lifetime was greatly reduced in the new trap used

in this run of the experiment. The frequency stability obtained is better than is needed to resolve the jumps, even though these jumps are 3 times smaller in frequency than those with $\nu_z = 64$ MHz. So, we are decreasing the magnetic bottle size by another factor of 3 which will further narrow the cyclotron and anomaly linewidths.

We have not yet systematically studied the rise time of the DSP limited self-excited oscillator, since it is sensitive to many parameters in the DSP algorithm. However, we have seen that it can be ~ 1 s even without much tuning, which is fast enough to be usable for quantum jump spectroscopy.

6.6 Frequency Stability with Limiting

With such clean fits to the cyclotron spectra of the self-excited electron, we found that the axial temperature appears to be approximately independent of the amplitude of oscillation. With this observation it is possible to estimate the frequency stability expected from self-excited oscillator based detection. The axial temperatures are used to estimate the amplitude variation which in turn causes frequency variation due to the axial anharmonicity.

We can with the probability distribution of axial energies with a driven, damped axial motion (see Section 3.5.1),

$$P_E(E_z) = \frac{1}{kT} e^{-\frac{E_z}{kT}} e^{-\frac{E_d}{kT}} I_0 \left(\frac{2}{kT} \sqrt{E_z - E_d} \right). \quad (6.33)$$

If the drive is strong, then $E_d \gg kT$ and if we only look near the peak, then $E_z \gg kT$ as well. We can then take the asymptotic limit $I_0(x) \sim \frac{1}{\sqrt{2\pi x}} e^x$ for $x \rightarrow \infty$. Combining

this expansion with Eq. (6.33) and simplifying, we get the asymptotic result

$$P_E(E_z) = \frac{1}{\sqrt{4\pi kT}(E_z E_d)^{\frac{1}{4}}} e^{-\frac{1}{kT}(\sqrt{E_z} - \sqrt{E_d})^2}, \quad (6.34)$$

for a driven amplitude much larger than the thermal amplitude. With the exception of the slowly varying $(E_z E_d)^{-\frac{1}{4}}$, this distribution is Gaussian in amplitude ($\propto \sqrt{E_z}$).

It is useful to compare the result in equation (6.34) to the standard expression for a normal distribution (Gaussian) $f(x)$ with center a and standard deviation σ ,

$$f(x) = \frac{1}{\sqrt{2\pi\sigma^2}} e^{-\frac{(x-a)^2}{2\sigma^2}}. \quad (6.35)$$

We can then see that the standard deviation for the Gaussian in $\sqrt{E_z}$ is $\sqrt{kT/2}$. So at one standard deviation from the center $\sqrt{E_z} = \sqrt{E_d} \pm \sigma$, or $E_z = (E_d + \sigma^2) \pm 2\sigma\sqrt{E_d}$. So the standard deviation for E_z is approximately $\sigma_E = \sqrt{2E_d kT}$. It is now convenient to switch to axial amplitude A instead of energy E . The relationship between them is simply $E_z = \frac{1}{2}m\omega_z^2 A_z^2$ and $E_d = \frac{1}{2}m\omega_z^2 A_d^2$. Thus, we can write the standard deviation of the axial amplitude,

$$\sigma_{A^2} = \sqrt{\frac{4A_d^2 kT}{m\omega_z^2}}. \quad (6.36)$$

To find the frequency standard deviation, we need to include the axial anharmonicity. Experimentally, the self-excitation is always centered at the amplitude where $\frac{d\omega_z}{d(A^2)} = 0$, and the amplitude which satisfies this condition can be tuned with the compensation electrode voltage. Thus, the A^4 or C_6 term dominates the anharmonicity. Since C_6 does not vary significantly over the range of compensation potential settings typically used, we will take it to be constant. We will also neglect higher order anharmonicities. Then, using equation (2.15), we can see that

$$\Delta\omega_z = \omega_z \frac{15C_6}{16(1 + C_2)d^4} (\Delta(A^2))^2. \quad (6.37)$$

So, the standard deviation of the axial frequency is

$$\sigma_{\omega_z} = \frac{15C_6 A_d^2 kT}{4(1 + C_2) d^4 m \omega_z}. \quad (6.38)$$

Recall that this result is only valid for strong drives. For a very weak drive, there is really still an axial energy variation $\sim kT$; it does not go to zero as these results state.

We are not simply interested in the absolute frequency stability of the oscillation; we need to detect the oscillation and pick out the peak frequency. How well the peak can be resolved depends on the signal to noise ratio of the total signal. The noise level is dominated by the thermal noise of the input tuned circuit, which is also at temperature T since it damps the particle. The thermal noise is just the Johnson noise for a resistor, $V_{noise} = \sqrt{4kTRB}$, where R is the resistance of the tuned circuit on resonance, B is the measurement bandwidth, and V_{noise} is the RMS noise voltage. The signal amplitude is from the current induced by the electron's motion through the tuned circuit resistance R . The RMS current from the electron's motion is $A\omega_z\sqrt{m\gamma_z/R}$ (see Chapter 2), so the RMS voltage is $V_{signal} = A\omega_z\sqrt{m\gamma_z R}$. Therefore, the detected signal to noise ratio is

$$\frac{V_{signal}}{V_{noise}} = A\sqrt{\frac{\omega_z^2 m \gamma_z}{4kTB}}. \quad (6.39)$$

So there is a trade off in the choice of amplitude for self-excitation. For very weak drives which result in oscillations smaller than the thermal amplitude, the frequency uncertainty is very large because the lineshape will not continue to narrow indefinitely as the amplitude is decreased, but the signal to noise drops to zero. At large driven amplitudes, the frequency jitter of the oscillation becomes larger with A^2 , which likely dominates over the signal to noise improvements as the amplitude is increased.

Experimentally, we observe that there is a broad sweet spot in the axial amplitude for optimal frequency detection. At low amplitudes it is difficult to determine the frequency at all because the noise is overwhelming. At higher amplitudes there is an optimum and then at high amplitudes the uncertainty increases slightly in the range accessible to experiments so far.

6.7 Other Observations with Self-Excitation

While taking data on the self-excited axial oscillator, we made several observations that do not contribute directly to the goal of monitoring the axial frequency, but are notable enough to include here. Further investigations into any of these could still be of interest in the future.

6.7.1 Self-Excitation of Multiple Electrons

At $\nu_z = 64$ MHz, we found a convenient and rapid way to load a single electron with direct unlimited self-excitation. First, the feedback phase, amplitude, and feedthrough cancellation are adjusted with an electron or electrons in the trap. Then, the trap is emptied by inverting the trapping potential. Finally, the field emission point is fired with a current that loads about 1 electron every 30 s while a spectrum analyzer is monitored. When an electron is loaded, a self-excitation response spike appears on the spectrum analyzer. If two electrons are loaded, a larger spike, with about twice the amplitude, appears (see Figure 6.26). More surprisingly, we have found that this huge response spike disappears if more than two electrons are loaded. It is instead replaced by an unstable washed out signal that is barely discernible.

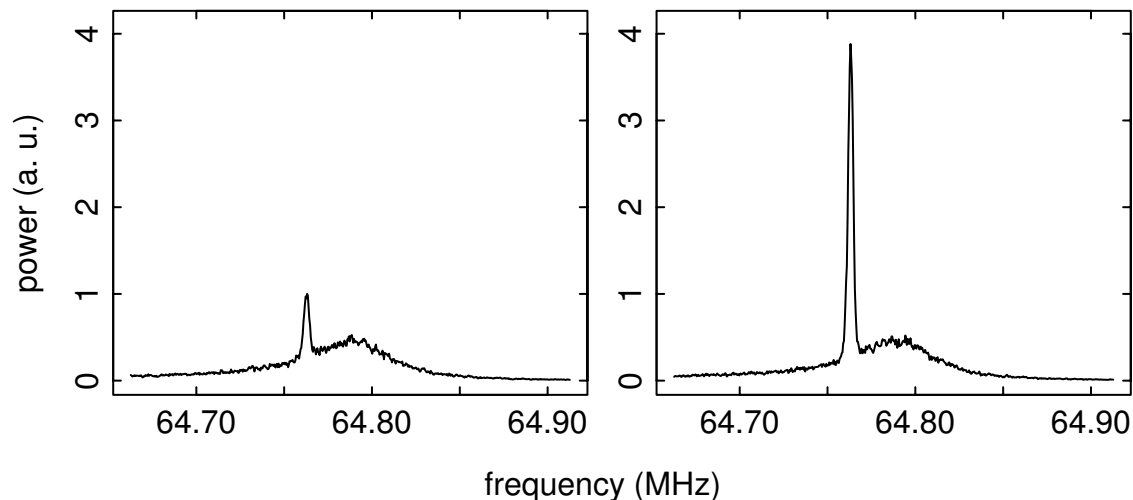


Figure 6.26: Large amplitude direct self-excitation of one electron (left) and two electrons (right).

We do not know what is special about the transition from two to three electrons, but one possibility is that with three or more electrons the internal degrees of freedom couple in more strongly and disrupt the large coherent oscillation that occurs with one or two electrons. The effects of magnetron cooling, axial temperature, excitation amplitude, and other conditions on this process have yet to be explored.

6.7.2 Magnetron Sideband Cooling and Self-Excitation

While using comparator limited self-excitation at $\nu_z = 64$ MHz, we observed an unusual interaction between self-excitation and magnetron sideband cooling. With a very strong cooling drive, a sustained axial response could be seen detuned from the axial frequency by the detuning of the cooling drive from the cooling resonance. The response at several cooling drive frequencies is shown in Figure 6.27. While a response from the cooling drive is not unusual, it normally fades in a few seconds

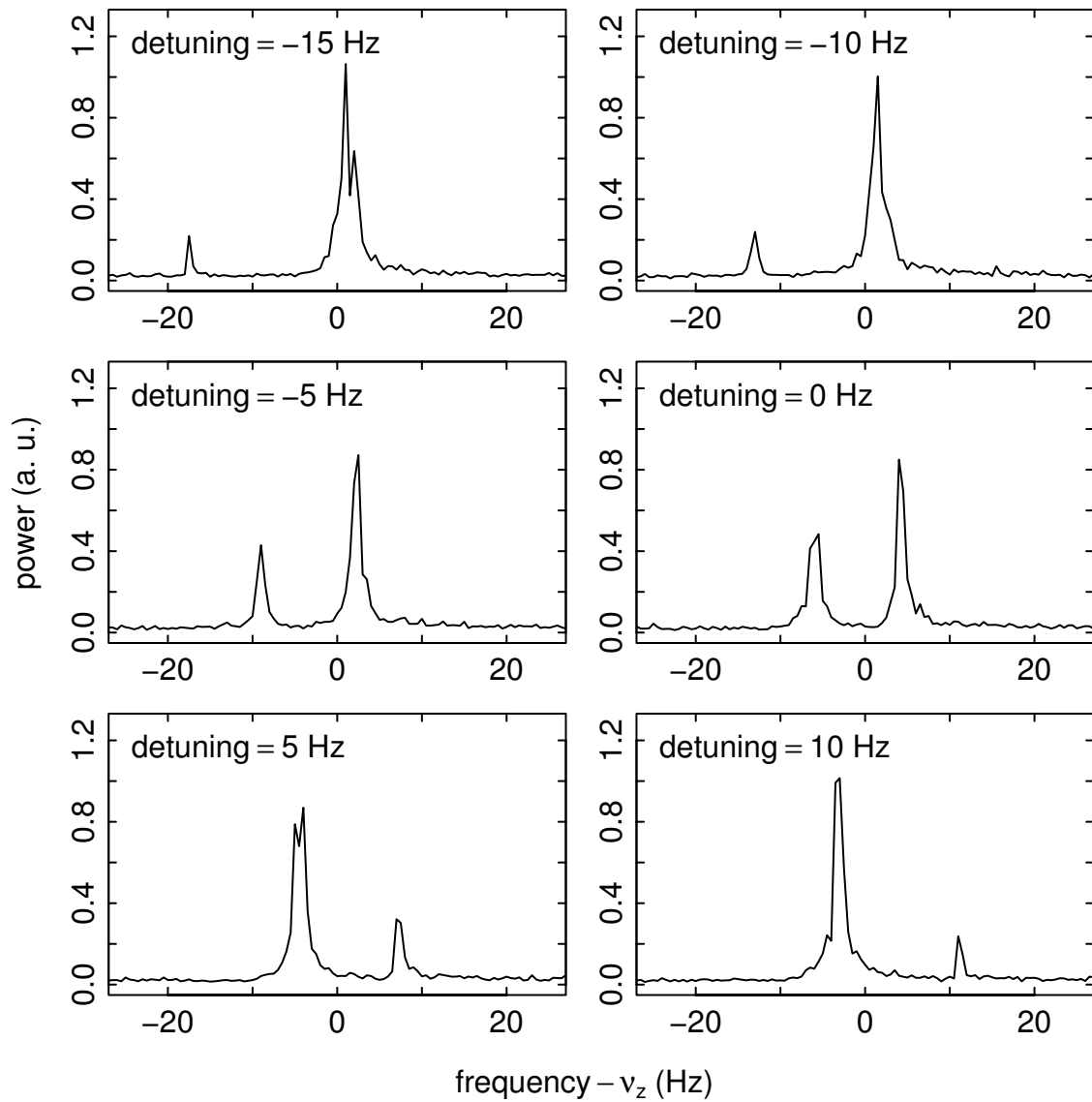


Figure 6.27: Self-excited axial oscillator response with a strong sideband cooling drive near resonance. In each plot, the detuning of the cooling drive from $\nu_z + \nu_m$ is indicated.

when cooling a single electron. The apparent repulsion visible in the figure between the cooling response and self-excitation response is also not understood. One possible application of this is the ability to continuously monitor the magnetron frequency by observing the axial response.

6.7.3 Parametrically Driven Self-Excitation

There has been interest in self-excited detection in the past, but experimental attempts centered around parametric feedback [26]. When our early tests with direct unlimited self-excitation failed to produce a useful response, we revisited parametric feedback, which requires doubling the detected signal before feeding it back.

Parametric feedback could solve the feedthrough problem trivially since the drive is not resonant with the amplifier. Also, the expected parametric self-excitation response does not have the amplitude control problems that direct resonant self-excitation has.

Unfortunately, we encountered two problems with parametric self-excitation which prevented a stable self-excited response. First, frequency doubling a signal always degrades the phase noise because all possible combinations of frequencies mix together in the process. When doubling a weak signal buried in noise, the already difficult to discern signal disappears in the noise, turning the feedback drive into a noise drive. The only solution is to filter the signal to as narrow a bandwidth as possible. With a narrow crystal filter in the signal path, we tried parametric self-excitation again. This time, the amplifier began to oscillate before the particle. Apparently the feedback loop and amplifiers formed a parametric down-converter with a lower threshold than the particle. With reduced drive coupling or a feedthrough cancellation drive, parametric self-excitation might still be successful, but such attempts would likely require more complexity than the already successful direct limited self-excitation technique.

Chapter 7

Towards $g - 2$

Although much progress has been made in cooling and detecting the axial motion, there are still technical obstacles to be overcome before the $g - 2$ measurement is completed. Furthermore, there are techniques which may allow continued improvement in the $g - 2$ measurement in the future.

7.1 Axial Sideband Cooling

It may be possible to reduce the axial temperature below the ambient temperature using a sideband cooling technique similar to the one used to cool the magnetron motion into the axial motion. By cooling the axial motion into the cyclotron motion, the limit on cooling is that the axial motion can get down to the same quantum state as the equilibrium cyclotron motion, which at 50 mK is the ground state.

Here we characterize two different axial-cyclotron sideband cooling techniques by the effective drive power available at the sideband as compared to the main cyclotron

peak. Since both methods rely on the spatial extent of the axial motion, it is useful to establish the length scale of the axial motion. The axial motion is a harmonic oscillator and so it has a classical turning point z . At this point the energy is classically $E_0 = \frac{k}{2}z^2$, where the axial frequency is $\omega_z = \sqrt{\frac{k}{m}}$. Since we are interested in cooling to the axial ground state, the smallest axial state we cool from has quantum number $n_z = 1$. If we equate the quantum mechanical energy $E_n = n_z \hbar \omega_z$ with the energy at the classical turning point we can get a distance scale z_n to associate with the quantum state,

$$n_z \hbar \omega_z = \frac{m \omega_z^2}{2} z_n^2 \quad \Rightarrow \quad z_n = \sqrt{\frac{2 n_z \hbar}{m \omega_z}}. \quad (7.1)$$

The relationship is useful in calculating the strength of sideband cooling processes.

7.1.1 Coupling by the Drive Geometry

Directly analogous to the method used to cool the magnetron motion, an axial-cyclotron cooling drive can be selected to have the appropriate geometry for sideband cooling. Since the cyclotron drive wavelength $\lambda_c \sim 2$ mm is smaller than the trap dimensions, λ_c sets the spatial scale for the drive. The cooling drive is most effective near a node, which effectively gives an amplitude modulated drive as the particle oscillates axially. This produces the appropriate sideband with power reduced by the square of the modulation depth,

$$\frac{P}{P_c} \sim \left(\frac{\pi z_n}{\lambda_z} \right)^2 = \frac{2 \pi^2 \hbar}{m \lambda^2 \omega_z} n_z. \quad (7.2)$$

Although no special care was taken to make the cyclotron frequency near the frequency of a cavity mode with appropriate geometry, we can see axial-cyclotron

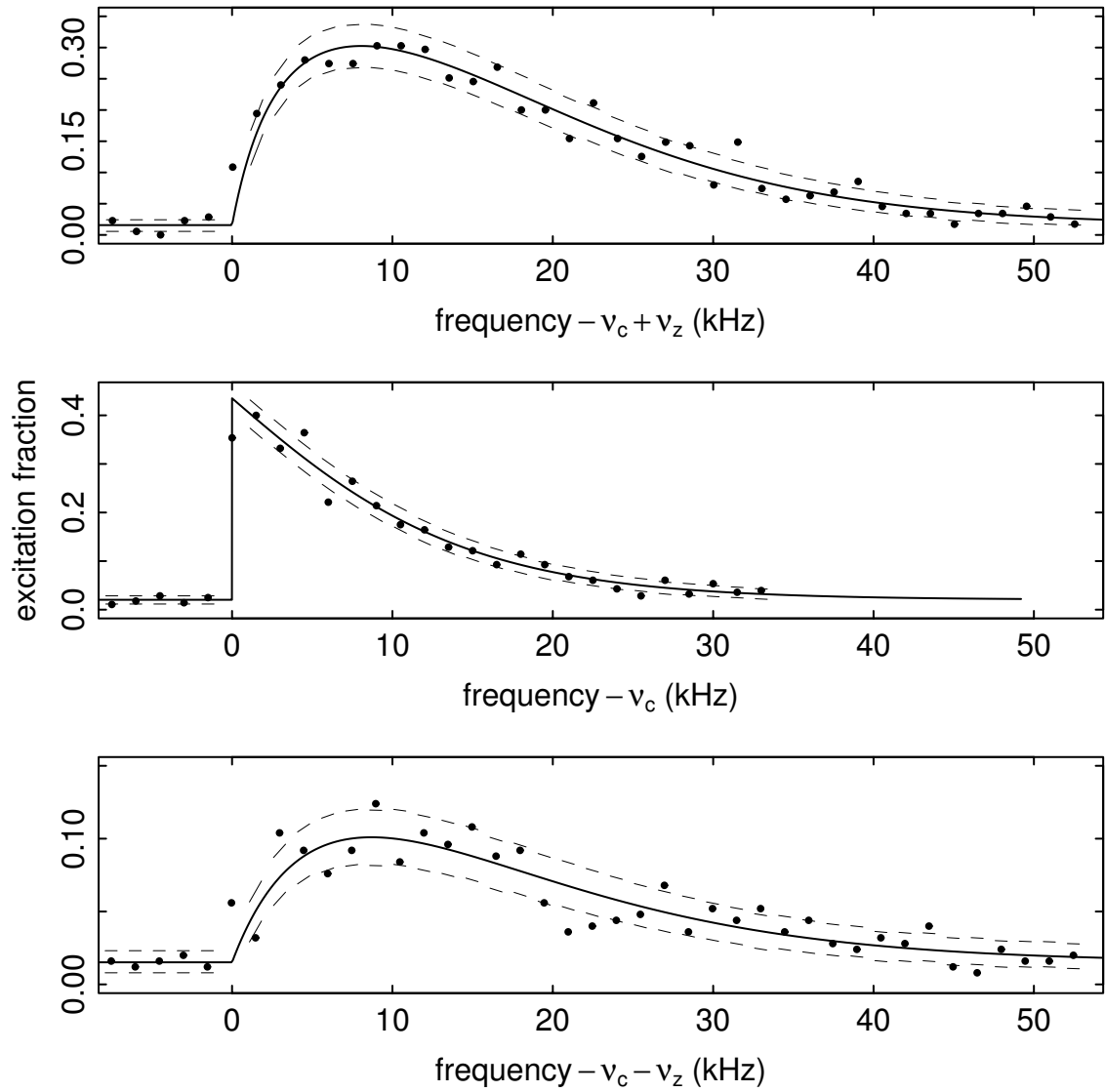


Figure 7.1: Axial-cyclotron sideband cooling (top) and heating (bottom) response. The direct cyclotron response is also shown (middle). The dashed lines show the expected 68% confidence region for the data.

sideband cooling and heating responses, as shown in Figure 7.1. The shapes of the cooling and heating responses are not identical to the resonant cyclotron response because the strength of the cooling and heating responses increase with increasing axial amplitude.

7.1.2 Coupling by the Magnetic Bottle

An alternative axial-cyclotron sideband cooling method utilizes the gradient in the magnetic field produced by the magnetic bottle used for detection. If the electron is moved off from the center of the trap, this produces a linear modulation of the cyclotron frequency with axial position with depth $\Delta\omega_z$. The effective reduction in the drive power for frequency modulation is $\sim \left(\frac{\Delta\omega_z}{\omega_z}\right)^2$.

The cyclotron frequency is generally given by $\omega_c = \frac{eB}{m}$. In a linear magnetic gradient of strength B_1 and uniform field B_0 , we have

$$\Delta\omega_z = \frac{B_1 z_n}{B_0} \omega_c = \frac{eB_1 z_n}{m}. \quad (7.3)$$

To finally get the power reduction,

$$\frac{P}{P_c} \sim \frac{2\hbar e^2 B_1^2}{m^3 \omega_z^3} n. \quad (7.4)$$

7.1.3 Comparison of Cooling Methods

By trying some sample parameters, we can get a direct comparison of these two axial-cyclotron sideband cooling methods. We will compare the effective drive strength for $n_z = 1$ and take the linear magnetic field gradient in the bottle sideband cooling case to be 1 T/m, which is easily obtainable with our magnetic bottle.

First we compare at axial frequency $\frac{\omega_z}{2\pi} = 65$ MHz, which is a typical frequency for detection of the axial motion. For the drive geometry method, $P \sim 1.4 \times 10^{-6}$; for bottle cooling, $P \sim 1.0 \times 10^{-7}$. Next, we compare at axial frequency $\frac{\omega_z}{2\pi} = 600$ kHz, which could be reached by lowering the trapping potential to ~ 1 mV. For the drive geometry method, $P \sim 1.5 \times 10^{-4}$; for bottle cooling: $P \sim 1.3 \times 10^{-1}$.

Clearly the bottle sideband cooling method has a strong advantage, but only when the axial frequency is very low. Both methods give stronger drives at lower axial frequencies because the axial states become more spatially extended. However, the bottle sideband cooling method improves more with a lower axial frequency because frequency modulation creates a stronger sideband when the modulation frequency is lower, even if the modulation depth is held constant.

7.2 $g - 2$ Measurement

Measuring $g - 2$ requires measuring the cyclotron, anomaly, and (for higher order corrections [12]) axial frequencies. While we have all the required components of the measurement, more progress is still needed to bring them all together.

7.2.1 Anomaly Transition

Although we have mostly focused on the cyclotron transition, we can also drive anomaly transitions. Experimentally, the detectable axial frequency shift due to an anomaly transition comes from the spin flip. The axial frequency shift due to a spin transition is indistinguishable from the one due to a cyclotron transition. However, an anomaly transition can either result in a jump down in axial frequency or a jump up in axial frequency that does not decay, depending on the direction of the transition. For anomaly spectra and further analysis, see [22].

7.2.2 Magnetic Field Stability

Since quantum jump spectroscopy is a relatively slow method for measuring the cyclotron and anomaly frequencies, it is important to have a stable magnetic field over at least a few hours. Although superconducting solenoid magnets are intrinsically very stable over time, other environmental effects may add significant magnetic field variations.

Stabilizing the Environment

Even with careful shimming, there is a practical limit to the uniformity of the magnetic field produced by our magnet. Therefore, small changes in the position of the trap in the magnetic field result in changes in the magnetic field. The position of the experiment may be affected by the external support structure temperature and the behavior of the cryogenics used to keep the experiment cool. In order to improve the stability of the field, we regulate the pressure in the cryogenic reservoirs and the air temperature around the experiment [22].

Copper Trap Difficulties

The copper used in our trap electrodes and base temperature structure has a highly temperature dependent magnetic susceptibility at dilution refrigerator temperatures which gave large fluctuations in the magnetic field with the base temperature [22]. In order to improve the field stability, we now primarily use materials such as silver, titanium, and molybdenum at the base temperature which have a much weaker temperature dependence in their magnetic susceptibilities at 100 mK.

7.3 Other Applications

In addition to precision measurements, there are other potential applications of one or more electrons in a Penning trap. The parametric response of the axial motion may be useful as a parametric amplifier or as a probe of the electromagnetic field at the cyclotron frequency [100]. The extreme sensitivity of the axial frequency to changes in the trapping potential could be used as a highly sensitive voltage to frequency converter, or it could be compared to a stable frequency synthesized to make a voltage reference. Another application of a trapped electron may be quantum computation.

7.3.1 Quantum Computing

The extremely long coherence times and proven record of precision measurements of a single electron in a Penning trap make it a natural candidate for quantum computing experiments [101, 102]. Present experiments with an electron in a Penning trap utilize conventionally machined electrodes with a size of around 1 cm, but this size could easily be decreased with simple microfabrication techniques. Smaller traps would exhibit increased coupling to the electron and decreased parasitic capacitance, making it possible to coherently couple electrons in an array of traps microfabricated on a surface. Information is stored in the lowest two states of the cyclotron and axial degrees of freedom. The axial motion is used for coupling between electrons, while the cyclotron states are used for setting the initial state, for the control bit in a controlled-not gate, and for reading out the result. The axial motion could be made intentionally anharmonic to assist in creating transitions between the lowest two states only.

There are several reasons for preferring an electronic system as a basis for quantum computing. Most importantly, the devices could easily be integrated with conventional electronics for control and interface purposes. Since it would ultimately be necessary to scale the system to a large number of qubits for useful computation, it is important that the support system for each qubit be compact and simple. The axial motions of individually trapped electrons could be coupled together by electrically connecting an electrode of one trap to an electrode of another trap. Operations on each electron or qubit involve applying the appropriate DC or RF drive signal to an electrode of a trap, so operations on many qubits can be performed simultaneously. Penning traps for quantum computing could be much simpler than the macroscopic traps used for precision measurements. The electrodes can be spread out over a flat surface and the field emission point can be eliminated. Instead of using a field emission point, electrons can be loaded by ejecting them from gold electrode surfaces with ultraviolet light.

While producing solid state devices with quantum dominated behavior requires challenging nanofabrication, the fundamental properties of a single electron in a Penning trap are not determined by the size of the trap. With only one electron in a trap, there is almost no intrinsic decoherence mechanism. The exception is the cyclotron motion, which is damped by synchrotron radiation. The cyclotron state lifetime is 0.1 seconds with a 5 Tesla magnetic field and 146 GHz cyclotron frequency and can be increased substantially by enclosing the trap with a cavity or by decreasing the magnetic field strength in order to lower the cyclotron frequency. The reason for shrinking the trap size is to speed up the computation by decreasing the parasitic capacitance

and increasing the coupling strength, not to change the fundamental properties of the system.

The primary disadvantage of using an electronic system is that if the oscillation frequencies are low enough to be experimentally convenient, the energy level spacings are so small that it is difficult to cool the particle to the quantum mechanical ground state. While it is experimentally easy to reach cryogenic temperatures around 4 K with modern pulse-tube refrigerators, it is still cumbersome to get much colder. Therefore, we propose cooling the electrons by coupling them electronically to an optically cooled, trapped ion [103]. In this manner, a simple laser setup could be used to cool a large number of electrons.

The advantage of a weakly coupled system is that the coherence time is long, but the difficulty it creates is that interactions may be slow. In order to maximize the electrical coupling to the trapped particle, it is desirable to choose a particle with a very high charge to mass ratio. This is the reason for choosing individually trapped electrons instead of ions or protons. The coupling between neighboring electrons can be turned on or off by bringing their axial frequencies close together or moving them far apart.

Implementation of the fundamental quantum logic gate, controlled-not, is straightforward with the addition of a magnetic bottle coupling as used for precision measurements in Penning traps. The required quadratic magnetic field gradient could be produced by external coils or by nickel under the trap electrodes. This coupling makes the axial frequency depend on the cyclotron state, so a drive applied to the axial motion can be conditionally coupled depending on the cyclotron state. Infor-

mation can be exchanged between the cyclotron and axial states with a drive of the appropriate geometry at the difference frequency. The same coupling that allows the implementation of the controlled-not gate can also be used to read out the final state of the cyclotron motion by measuring the axial frequency. Another trap with a larger number of electrons in it may serve as a parametric amplifier to boost the axial signal for detection.

7.4 Conclusions

Improved axial amplifiers at 64 MHz decreased the axial temperature and the cyclotron and anomaly linewidths by a factor of ~ 60 . Increasing the axial frequency and decreasing the strength of the magnetic bottle is expected to decrease the linewidth by another factor of 30, giving a total linewidth decrease of ~ 2000 . The increased axial frequency is made possible by new axial amplifiers and a flexible voltage source for the trapping potential. The decreased bottle size is practical because DSP limited self-excitation is a robust means of detecting small changes in the axial frequency. Although we do not plan to use it immediately, we have also seen that we can use feedback to decrease the axial temperature without a dilution refrigerator.

Compared to the 1987 $g - 2$ measurement [1], we have several advantages. With a higher axial frequency and reduced axial temperature, our expected cyclotron and anomaly linewidths are significantly narrower. The anomaly transition is easier to drive due to our lower axial temperature, higher axial frequency, and stronger magnetic bottle. This decreases the systematic error due to the high anomaly drive power. Finally, the cavity shifts in our cylindrical trap are easily understood compared to

those in a hyperbolic trap.

There is still the possibility of even further improvements in the $g - 2$ measurement. The correlated cyclotron and anomaly measurement technique could reduce the problems caused by magnetic field instabilities and decrease the effective transition linewidths. Axial-cyclotron sideband cooling could reduce the axial temperature further, perhaps reaching the ground axial state. It is plausible, with further improvements, that the accuracy of the $g - 2$ measurement could reach $\Delta a/a \sim 1 \times 10^{-10}$.

Improvements to $g - 2$ measurement techniques may also allow improvements in other measurements. Repeating the $g - 2$ measurement on a single trapped positron could give an improved test of CPT symmetry in leptons. By trapping a single proton and comparing its cyclotron frequency to that of a positron, the proton to electron mass ratio measurement could be improved. Finally, a single trapped electron may be useful for quantum computing.

Appendix A

Field Emission Point Etching

In 2001 our field emission point failed (probably due to a bad vacuum), and we had to make a replacement. Although these tips have been made for many years, we found no clearly written up procedure for etching them. After several attempts, we found the following procedure works consistently well.

Preparation:

- Materials: glass beaker, variac, copper pipe for outer electrode, and support for tungsten rod.
- Clean all materials to be involved in the etching carefully, especially the copper pipe (outer electrode). The materials and solution should be cleaned or replaced when they become discolored.
- Etching solution: 3 g NaOH dissolved in 150 mL distilled water.
- Etching: connect the variac across the tungsten rod and copper pipe immersed in the solution. Measure the etching current with a current meter in series.

Etching procedure:

1. The tungsten wire (welding rod) that we have is 0.020 in diameter. We need thinner than 0.018 in, so the excess must be etched away. Etch a 3.2 in length for 10 min at 1.0 A. The etched length can be cut in half into 2 pieces of 1.6 in length.
2. Each piece needs at least one cleanly cut end to be placed into the FEP holder. A rough end is cleaned up quickly by etching until the burrs are removed.
3. Dip the bottom ~ 0.05 in in silicone vacuum grease to prevent etching of the end of the tip.
4. Immerse the tungsten rod into the etching solution 0.2 in past the grease.
5. Etch with 350 mA for ~ 5 min or until tip is mostly etched.
6. Etch with 35 mA until the part of the tip with grease falls off (~ 4 min). Avoid letting excess bubbles accumulate on the grease as they may prematurely break off the tip.
7. Continue to etch with 35 mA for 20 s after the greased end falls off.
8. Carefully remove the tip from the etching solution vertically and allow to dry.

Field emission points can be etched without greasing part of the rod first. However, without the grease the tip must be watched very carefully during etching to stop at the right time.

Appendix B

High Frequency Feedthrough

We require a high frequency, low loss, coaxial feedthrough to carry the detected axial signal to the amplifier (see Chapter 4) as in Figure B.1. We use a glass to metal seal from Larson Electronic Glass with a copper tube as the outer conductor and a tungsten rod as the inner conductor. Since the glass is fragile and may be stressed by thermal gradients, care must be taken to avoid damaging it. We have found that the feedthroughs are robust, even when cycling to cryogenic temperatures. Since it is difficult to solder to the tungsten, some experimentation was required to find a procedure for assembling the feedthrough without damaging it.

Much higher temperature is required to solder to the tungsten than to silver, so some solder is attached to the tungsten first and the silver rod is attached later. The strategy for assembling the feedthrough assembly is to try to avoid thermal gradients across the glass that may cause excessive stress in the glass. Here is a procedure that we have found works well:

1. Clean the feedthrough carefully. The tungsten may be cleaned with sandpaper.

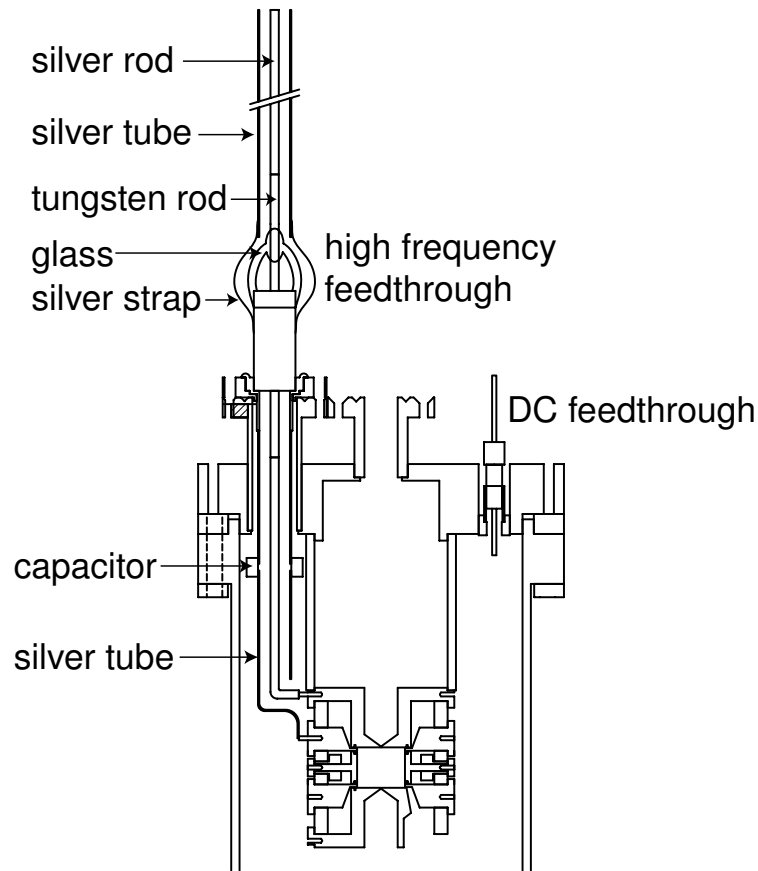


Figure B.1: Assembly of the high frequency amplifier feedthrough and trap.

2. With the feedthrough immersed in water to at least cover the glass, heat the tip of the tungsten rod with an oxygen-acetylene torch and attach a bead of CuAg eutectic solder with the aid of high temperature brazing flux. Repeat on the other end of the tungsten rod.
3. File and sand off excess solder from the tungsten rod tips so that there is a thin uniform layer of solder ~ 1 mm only on each tip.
4. With the glass portion of the feedthrough again under water, torch solder annealed silver rods to the tungsten rod ends with the same flux, minimal ad-

ditional solder, and minimal heat. Annealed silver rod is used to minimize mechanical stress on the feedthrough in later assembly.

5. Solder the feedthrough into the flange used to make an indium seal to the pinbase with PbSn solder paste. The paste should be applied all around the joint. Silver straps are also soldered to the sides of the feedthrough with more solder paste. The whole assembly is gradually heated to 225° C over 10 minutes and held there for 30 minutes in the air oven. The oven is then allowed to cool slowly.
6. Finally, clean off any excess solder flux, and the feedthrough is ready.

When soldering the silver rod to a trap electrode or the amplifier, care should be taken to avoid mechanically or thermally stressing the glass. No special care is required for cryogenic use, but it is advisable to cool down the feedthrough slowly and evenly.

Appendix C

DSP Program

The DSP limited self-excited oscillator experiments described in Chapter 6 use a Texas Instruments TMS320F2812 DSP to control the feedback gain in order to stabilize the amplitude of the oscillation. The DSP takes a Fourier transform of the input signal and determines the amplitude of the largest frequency component. First we describe the operation of the code mathematically, then we include the code.

Consider an input voltage signal over time $V_{in}(t)$ which the DSP digitizes with time step Δt . After some processing, it will create an analog output voltage $V_{out}(t)$, also with time step Δt . The output voltage $V_{out}(t)$ is used to control an electronic attenuator in the self-excitation feedback loop. Both the input and output are filtered such that the discretely sampled input and discretely updated output give a reasonable approximation of the continuous voltages. The clock speed of our DSP is 150 MHz, and the sampling rate used here is 25 kHz. This is much faster than the ~ 5 kHz input signal frequency or the frequency scale of the output voltage which is typically ~ 10 Hz.

The DSP takes a discrete Fourier transform (DFT), not a Fast Fourier Transform (FFT), so the Fourier integrals are explicitly calculated. Two sets of amplitude bins are calculated, $S_i(t)$ for the sine transform and $C_i(t)$ for the cosine transform where $i = 1, 2, 3, \dots, N$. That is, there are N frequency bins. In order to reduce the computation time, the phase $\phi_i(t)$ for each frequency bin is stored in an array and incremented by $\Delta\phi_i$ at each time step. It is $\Delta\phi_i$ that determines the frequency of each bin. Each $\phi_i(t)$ is allowed to wrap when it overflows the counter value. At each time step the frequency bins are updated as

$$\phi_i(t + \Delta t) = \phi_i(t) + \Delta\phi_i \quad (\text{C.1})$$

$$S_i(t + \Delta t) = (1 - \epsilon) S_i(t) + V_{in}(t + \Delta t) \sin[\phi_i(t + \Delta t)] \quad (\text{C.2})$$

$$C_i(t + \Delta t) = (1 - \epsilon) C_i(t) + V_{in}(t + \Delta t) \cos[\phi_i(t + \Delta t)]. \quad (\text{C.3})$$

The cosine and sine values are looked up in a table which is generated when the DSP is powered up. The positive constant $\epsilon \ll 1$ produces an exponential weighting in time, giving each frequency bin a finite bandwidth. The time constant τ for the exponential window in amplitude is

$$\tau = \frac{\Delta t}{\epsilon}. \quad (\text{C.4})$$

In the code presented here, $\alpha = 1 - \epsilon$ so $\epsilon = 9.76 \times 10^{-4}$ and $\tau = 0.04$ seconds. At this point the Fourier transform is complete.

The next calculation at each time step is to pick out the largest amplitude from the bins. Since square roots are computationally expensive, the maximum power $P_{max}(t)$ is found as

$$P_{max} = \max \{S_1^2 + C_1^2, S_2^2 + C_2^2, S_3^2 + C_3^2, \dots, S_N^2 + C_N^2\}. \quad (\text{C.5})$$

P_{max} is maintained as each frequency bin is calculated, so only memory for single value is required. Finally, the maximum amplitude $A_{max}(t)$ is calculated, requiring one square root per time step,

$$A_{max}(t) = \sqrt{P_{max}(t)}. \quad (\text{C.6})$$

Finally, the output voltage is a cubic polynomial transform of A_{max} ,

$$V_{out}(t) = P_0 + P_1 A_{max}(t) + P_2 [A_{max}(t)]^2 + P_3 [A_{max}(t)]^3. \quad (\text{C.7})$$

A cubic polynomial transform gives a lot of flexibility in adjusting the algorithm but is computationally easy.

In the actual code, some scaling is done to prevent numbers from overflowing or to make them properly saturate because all values are stored as integers (not floating point). The code itself is stored in flash memory on the DSP. The content of the flash memory survives when the DSP is powered down, but reading from the flash memory is slow. In order to speed up the code execution, the code copies a time critical portion of itself into the RAM, which can be accessed at the full speed of the DSP. The assembly code is included here for reference.

```
.global START
.c28_amode

;-----
; Operating parameters and constants
;-----

;settings
PWM_PERIOD      .set 0x1770      ;sampling period in clock cycles
                                   ; range 0x0001 to 0xFFFF
DPHASE0         .set 0x33333333 ;starting channel dphase (5 kHz)
DPHASE_STEP     .set 0x00029F16 ;dphase step between channels
```

```

; set to 1 Hz
N_FREQS      .set 64      ;number of frequency channels to use
; range: 1 to 64
; (cycle and program memory limited)
ALPHA        .set 0xFFC00000 ;exp weighting multiplier value
; about 8 Hz linewidth
ACC_SHIFT    .set 6      ;right shift to do
; before accumulating data
; puts output midpoint at 15% of input

;addresses and constants
DATA_TEMP    .set 0x000000 ;temporary data storage
SIN_TEMP     .set 0x000002 ;temporary sin data storage
COS_TEMP     .set 0x000004 ;temporary cos data storage
DATA_MAX     .set 0x000006 ;maximum value found address
ALPHA_A      .set 0x000008 ;exp weighting multiplier address
DPHASE0_A    .set 0x00000A ;starting channel dphase address
DPHASE_STEP_A .set 0x00000C ;dphase step between channels address
P0_A        .set 0x00000E ;transform constant*amp^0 address
P1_A        .set 0x000010 ;transform constant*amp^1 address
P2_A        .set 0x000012 ;transform constant*amp^2 address
P3_A        .set 0x000014 ;transform constant*amp^3 address
DATA_N       .set 0x000016 ;data^N storage for transform
DATA_OUT     .set 0x000018 ;final output accumulator
SD_ARRAY     .set 0x00001F ;sin data array start
; (32 bit data)
CD_ARRAY     .set (SD_ARRAY+2*N_FREQS) ;cos data array
; (32 bit data)
PHASE_ARRAY  .set (SD_ARRAY+4*N_FREQS) ;current phase array
; (32 bit data)
DPHASE_ARRAY .set (SD_ARRAY+6*N_FREQS) ;change in phase per step
; array (32 bit data)

;sin table constants
SIN_TABLE    .set 0x008000 ;starting address of sin table
N_SIN_TABLE  .set 0x2000 ;number of entries in sin table
SIN_TABLE_INCR .set (1 << 3) ;phase increment in sin table
COS_SHIFT    .set (0xFFFF/4) ;shift to evaluate cos with sin table

;-----
; Address constants
;-----

```

```
ADCCHSELSEQ1 .set 0x007103
ADCCHSELSEQ2 .set 0x007104
ADCCHSELSEQ3 .set 0x007105
ADCCHSELSEQ4 .set 0x007106
ADCINT       .set 0x000D4A ;PIE interrupt INT1.6
ADCMAXCONV   .set 0x007102
ADCRESULT0   .set 0x007108
ADCRESULT1   .set 0x007109
ADCRESULT2   .set 0x00710A
ADCRESULT3   .set 0x00710B
ADCRESULT4   .set 0x00710C
ADCRESULT5   .set 0x00710D
ADCRESULT6   .set 0x00710E
ADCRESULT7   .set 0x00710F
ADCRESULT8   .set 0x007110
ADCRESULT9   .set 0x007111
ADCRESULT10  .set 0x007112
ADCRESULT11  .set 0x007113
ADCRESULT12  .set 0x007114
ADCRESULT13  .set 0x007115
ADCRESULT14  .set 0x007116
ADCRESULT15  .set 0x007117
ADCST        .set 0x007119
ADCTRL1      .set 0x007100
ADCTRL2      .set 0x007101
ADCTRL3      .set 0x007118
EXTCONA      .set 0x007409
GPADIR       .set 0x0070C1
GPAMUX       .set 0x0070C0
GPFDIR       .set 0x0070D5
GPFMUX       .set 0x0070D4
GPFTOGGLE    .set 0x0070F7
GPTCONA      .set 0x007400
HISPCP       .set 0x00701A
PCLKCR       .set 0x00701C
PIEACK       .set 0x000CE1
PIECTRL      .set 0x000CE0
PIEIER1      .set 0x000CE2
PIEIFR1      .set 0x000CE3
PLLCR        .set 0x007021
T1CNT        .set 0x007401 ;GP Timer 1 Counter Register
```

```

T1CMPR      .set 0x007402 ;GP Timer 1 Compare Register
T1PR        .set 0x007403 ;GP Timer 1 Period Register
T1CON       .set 0x007404 ;GP Timer 1 Control Register
WDCR        .set 0x007029

```

```

;-----
; MAIN CODE - starts here
;-----

```

```

    .text

```

```

START:

```

```

    SETC OBJMODE          ;C28OBJ = 1 enable 28x object mode
    CLRC PAGE0           ;PAGE0 = 0 not relevant for 28x mode
    CLRC AMODE           ;AMODE = 0 disable C2xLP addressing
    CLRC SXM             ;SXM = 1 for C2xLP at reset,
                        ;SXM = 0 for 28x at reset
    CLRC C               ;Carry bit =1 for C2xLP at reset,
                        ;Carry bit = 0 for 28x at reset
    SPM 0               ;Set product shift mode zero

```

```

    EALLOW              ;allow emulation register access
    NOP
    NOP

```

```

;disable watchdog
    MOVW DP, #(WDCR >> 6)
    MOV @WDCR, #0x0068

```

```

;set PLL multiplier
    MOVW DP, #(PLLCR >> 6)
    MOV @PLLCR, #10
    MOV @AR0, #5000      ;delay to let PLL stabilize

```

```

LPLLD:      ;start delay loop
    NOP
    BANZ LPLLD, AR0--    ;end delay loop

```

```

;load fast code into RAM
    CLRC SXM            ;turn off sign
    MOVL XAR6, #fast_src
    MOVL XAR7, #FAST
    MOVL XAR5, #(fast_end - fast_src - 1)

```

```

LPMOVE:

```

```

PWRITE *XAR7, *XAR6++
ADDB XAR7, #1
BANZ LPMOVE, AR5--

;-----
; Initialize signal processing here

;store DPHASE0, DPHASE_STEP, ALPHA 32 bit values
MOV DP, #(DATA_TEMP >> 6)
MOV @DPHASE0_A, #DPHASE0
MOV @(DPHASE0_A+1), #(DPHASE0 >>16)
MOV @DPHASE_STEP_A, #DPHASE_STEP
MOV @(DPHASE_STEP_A+1), #(DPHASE_STEP >>16)
MOV @ALPHA_A, #ALPHA
MOV @(ALPHA_A+1), #(ALPHA >>16)

MOV @P0_A, #0x0000
MOV @P1_A, #0xE000
MOV @P2_A, #0x0000
MOV @P3_A, #0x0000

;initialize array pointers
MOVL XAR1, #SD_ARRAY      ;load starting address (22 bits)
MOVL XAR2, #CD_ARRAY      ;load starting address (22 bits)
MOVL XAR3, #PHASE_ARRAY   ;load starting address (22 bits)
MOVL XAR4, #DPHASE_ARRAY  ;load starting address (22 bits)
MOVL ACC, @DPHASE0_A      ;load ACC with initial dphase

;loop to initialize data
MOV @AR0, #(N_FREQS - 1)
LDINIT:                    ;data initialization loop
MOV *XAR1++, #0x0000      ;initialize to zero
MOV *XAR1++, #0x0000      ; set second 16 bits to zero
MOV *XAR2++, #0x0000      ;initialize to zero
MOV *XAR2++, #0x0000      ; set second 16 bits to zero
MOV *XAR3++, #0x0000      ;initialize to zero phase
MOV *XAR3++, #0x0000      ; set second 16 bits to zero
MOVL *XAR4++, ACC         ;copy new delta phase into DPHASE_ARRAY
ADDL ACC, @DPHASE_STEP_A  ;add delta dphase to ACC
BANZ LDINIT, AR0--        ;end data initialization loop

;build sin table

```

```

    MOVL XAR1, #SIN_TABLE      ;load starting address (22 bits)
    MOV AR2, #0x0000          ;initialize phase to zero
    MOV @ARO, #(N_SIN_TABLE - 1)
LBSIN:                          ;build sin table loop
    MOV ACC, AR2              ;load the phase into ACC
                                ; phase will now be treated as Q15
    LCR QSIN                  ;calculate sin
    MOV *XAR1++, ACC          ;store result (Q15)
    ADD AR2, #SIN_TABLE_INCR  ;increment the phase
    BANZ LBSIN, ARO--         ;end build sin table loop

;-----
; End of signal processing initialization

;setup interrupts
SETC VMAP                     ;set interrupt vector mapping
SETC INTM                     ;disable all maskable interrupts
MOVW DP, #(PIECTRL >> 6)
MOV @PIECTRL, #0x0001         ;set ENPIE -> use PIE vector
MOVW DP, #(ADCINT >> 6)
MOV @ADCINT, #ADCGET          ;set PIE vector for ADC interrupt
MOV @(ADCINT+1), #(ADCGET >> 16)
MOVW DP, #(PIEIER1 >> 6)
OR @PIEIER1, #0x0020          ;#0000 0000 0010 0000b
                                ; enable INT1.6 PIEIER
OR IER, #0x0001              ;enable INT1 IER
CLRC INTM                    ;enable maskable interrupts

;setup clocks
MOVW DP, #(PCLKCR >> 6)
OR @PCLKCR, #(1 << 0)        ;turn on EVA clock
OR @PCLKCR, #(1 << 3)        ;turn on ADC clock
MOVW DP, #(HISPCP >> 6)
AND @HISPCP, #0xFFF8         ;set high speed peripheral clock to x1

;ADC setup and power up
MOVW DP, #(ADCTRL1 >> 6)
MOV @ADCTRL1, #0x0090        ;setup ADC control register 1
                                ; #0000 0000 1001 0000
                                ; min acquisition window time (1 cycle)
                                ; divide HSPCLK by 2
                                ; cascaded mode

```

```

; start stop mode
MOVW DP, #(ADCTRL2 >> 6)
MOV @ADCTRL2, #0x4900 ;setup ADC control register 2
; #0100 1001 0000 0000b
; reset sequencer 1
; interrupt req INT FLAG SEQ1 enabled
; allow SEQ1/SEQ to start by EVA trigger
MOVW DP, #(ADCMAXCONV >> 6)
MOV @ADCMAXCONV, #0x000F ;take 16 samples
MOVW DP, #(ADCCHSELSEQ1 >> 6)
MOV @ADCCHSELSEQ1, #0x0000 ;set to sample ADCINA0
MOV @ADCCHSELSEQ2, #0x0000 ;set to sample ADCINA0
MOV @ADCCHSELSEQ3, #0x0000 ;set to sample ADCINA0
MOV @ADCCHSELSEQ4, #0x0000 ;set to sample ADCINA0
; results will be in ADCRESULT0-15
MOVW DP, #(ADCTRL3 >> 6)
MOV @ADCTRL3, #0x00C0 ;power up reference and bandgap circuits
; #0000 0000 1100 0000b
MOV @ARO, #0xFFFF ;wait > 5 ms
LADCD1:
RPT #0xFF
|| NOP
BANZ LADCD1, ARO--
MOV @ADCTRL3, #0x00EE ;setup ADC control register 3
; #0000 0000 1110 1110b
; power up the rest of the ADC
; set ADC clock to divide by 14
MOV @ARO, #0xFFFF ;wait > 20 us
LADCD2:
NOP
BANZ LADCD2, ARO--

;setup PWM
MOVW DP, #(GPAMUX >> 6)
OR @GPAMUX, #(1 << 6) ;set GPIOA6 MUX to PWM output
MOVW DP, #(EXTCONA >> 6)
MOV @EXTCONA, #0x0001 ;enable independent compare output mode
MOVW DP, #(T1CMPR >> 6)
MOV @T1CMPR, #0x01FF ;initialize timer compare register
; this sets initial duty cycle
MOVW DP, #(T1PR >> 6)
MOVW DP, #(GPTCONA >> 6)

```

```

MOV @GPTCONA, #0x0115      ;setup GP timer control register
                           ; set to #0000 0001 0001 0101b
                           ; output low when active
                           ; voltage increases with inc T1CMPR
                           ; period interrupt starts ADC
MOV @T1PR, #PWM_PERIOD    ; set period register
MOVW DP, #(T1CNT >> 6)
MOV @T1CNT, #0x0000       ;clear count register to 0
MOVW DP, #(T1CON >> 6)
MOV @T1CON, #0x1042       ;set continuous up count mode, enable
                           ; set to #0001 0000 0100 0010b
                           ; reload compare when counter is 0
                           ; update T1CMPR to change ouptut
                           ; duty cycle

;jump to the fast code
B FAST, UNC

;=====
; BEGIN CODE LOADED INTO RAM
;=====

.sect ".fast"
.label fast_src            ;load address of section
FAST:                      ;run address of section
NOP

END:
B END, UNC

;-----
; ISR - ADCGET
; Get new data point from ADC and update PWM
;-----

ADCGET:
CLRC OVM, SXM             ;turn off overflow saturation and sign

MOV DP, #(ADCRESULT0 >> 6) ;add up all the ADC measurements
MOVU ACC, @ADCRESULT0
ADDU ACC, @ADCRESULT1
ADDU ACC, @ADCRESULT2

```

```

ADDU ACC, @ADCRESLT3
ADDU ACC, @ADCRESLT4
ADDU ACC, @ADCRESLT5
ADDU ACC, @ADCRESLT6
ADDU ACC, @ADCRESLT7
ADDU ACC, @ADCRESLT8
ADDU ACC, @ADCRESLT9
ADDU ACC, @ADCRESLT10
ADDU ACC, @ADCRESLT11
ADDU ACC, @ADCRESLT12
ADDU ACC, @ADCRESLT13
ADDU ACC, @ADCRESLT14
ADDU ACC, @ADCRESLT15
SFR ACC, #4                ;divide sum of ADC measurements by 16

;-----
; ADC measurement is now in ACC
; range is 0x0000 to 0xFFFF (unsigned)
; begin signal processing code here

SPM 0                      ;set product shift mode to 0
SUB AL, #0x8000            ;convert to Q15
                          ; Q15 0x7FFF ~ 1
                          ; Q15 0x8000 = -1

MOV DP, #(DATA_TEMP >> 6)
MOVL @DATA_TEMP, ACC      ;load data into DATA_TEMP

ZAPA                      ;zero ACC, P, OVC
MOVL @DATA_MAX, ACC       ;zero DATA_MAX

;XAR0 reserved for looping
MOVL XAR1, #SD_ARRAY      ;load starting address (22 bits)
MOVL XAR2, #CD_ARRAY      ;load starting address (22 bits)
MOVL XAR3, #PHASE_ARRAY   ;load starting address (22 bits)
MOVL XAR4, #DPHASE_ARRAY  ;load starting address (22 bits)
;XAR5 used for looking up sin values

.loop N_FREQS
;look up sin
MOVL ACC, *XAR3           ;load ACC with current phase
SFR ACC, #16             ;shift to get upper 16 bits

```

```

SFR ACC, #3                ;shift for memory offset for sin lookup
ADD ACC, #SIN_TABLE        ;add sin table starting address
MOVL XAR5, ACC
MOVU ACC, *XAR5            ;copy the sin table value into ACC
MOVL @SIN_TEMP, ACC       ;load sin into SIN_TEMP

;look up cos
MOVL ACC, *XAR3           ;load ACC with current phase
SFR ACC, #16             ;shift to get upper 16 bits
ADD AL, #COS_SHIFT       ;phase offset to get cos instead of sin
                           ; let it wrap if neccessary

SFR ACC, #3                ;shift for memory offset for sin lookup
ADD ACC, #SIN_TABLE        ;add sin table starting address
MOVL XAR5, ACC
MOVU ACC, *XAR5            ;copy the sin table value into ACC
MOVL @COS_TEMP, ACC       ;load cos into COS_TEMP

SETC SXM, OVM             ;set sign bit, saturate on overflow

;sin calculation
MOVL XT, *XAR1
QMPYXUL P, XT, @ALPHA_A   ;P=sindata(old)*alpha
MOV T, @SIN_TEMP
MPY ACC, T, @DATA_TEMP    ;ACC=sin*data
SFR ACC, #ACC_SHIFT      ;shift result to give room to accumulate
ADDL ACC, P               ;ACC=sin*data+sindata(old)*alpha
MOVL *XAR1, ACC           ;store the new transform data
MOVL XT, ACC
QMPYL ACC, XT, *XAR1++    ;ACC=sindata^2
MOVL @SIN_TEMP, ACC

;cos calculation
MOVL XT, *XAR2
QMPYXUL P, XT, @ALPHA_A   ;P=cosdata(old)*alpha
MOV T, @COS_TEMP
MPY ACC, T, @DATA_TEMP    ;ACC=cos*data
SFR ACC, #ACC_SHIFT      ;shift result to give room to accumulate
ADDL ACC, P               ;ACC=cos*data+cosdata(old)*alpha
MOVL *XAR2, ACC           ;store the new transform data
MOVL XT, ACC
QMPYL ACC, XT, *XAR2++    ;ACC=cosdata^2

```

```

CLRC SXM, OVM                ;clear sign bit
                               ; don't saturate on overflow

MOVL P, @SIN_TEMP
ADDL ACC, P                   ;ACC=sindata^2+sindata^2

MAXL ACC, @DATA_MAX           ;ACC=max(DATA_MAX, ACC)
MOVL @DATA_MAX, ACC          ;store new max in DATA_MAX

MOVL ACC, *XAR3               ;load phase into ACC
ADDL ACC, *XAR4++             ;add delta phase to phase and increment
MOVL *XAR3++, ACC            ;store updated phase and increment
.endloop

;max value is in DATA_MAX
MOVL ACC, @DATA_MAX
SETC OVM
ADDL ACC, ACC                 ;double and saturate up to sign bit
LSL ACC, #1                   ;shift left to use sign bit
LCR QSQRT                     ;take the sqrt of the data
                               ; data in AL, range 0 to #FFFF

;polynomial transformation of amplitude
CLRC OVM
SUB AL, #0x8000               ;transform to Q15

SETC SXM, OVM                 ;set sign bit and saturation
SUB AL, @PO_A                 ;data offset
MOV AH, AL                    ;move AL into AH so
                               ; overflow is for signed

MOV AL, #0
; ADDL ACC, ACC                ;repeat to scale output
MOV @DATA_MAX, AH
CLRC OVM                       ;don't saturate
CLRC OVC                       ;clear overflow counter

MOV T, @P1_A
MPY ACC, T, @DATA_MAX         ;ACC=P1*data
MOVL @DATA_OUT, ACC           ;start accumulating result in DATA_OUT

MOV T, @DATA_MAX              ;move data into T
MPY ACC, T, @DATA_MAX
SFR ACC, #15                  ;shift to use full range

```

```

MOVL @DATA_N, ACC          ;store data^2
MOV T, @P2_A
MPY ACC, T, @DATA_N        ;ACC=P2*data^2
ADDL @DATA_OUT, ACC        ;accumulate term in DATA_OUT

MOV T, @DATA_MAX           ;move data into T
MPY ACC, T, @DATA_N        ;ACC=P2*data^2
SFR ACC, #15               ;shift to use full range
MOVL @DATA_N, ACC         ;store data^3
MOV T, @P3_A
MPY ACC, T, @DATA_N        ;ACC=P3*data^3
ADDL ACC, @DATA_OUT        ;final accumulate in ACC

ADDL ACC, ACC              ;double ACC with saturation
ADDL ACC, ACC              ;double ACC with saturation
SAT ACC                    ;saturate ACC based on OVC

SFR ACC, #16               ;shift
ADD AL, #0x8000            ;convert to unsigned

;-----
; Output value taken from AL here
; range is 0x0000 to 0xFFFF (unsigned)
; end of signal processing code

CLRC SXM                   ;clear sign bit
MOV T, AL
MOV @ARO, #PWM_PERIOD
MPYU ACC, T, @ARO          ;scale to PWM period

;update PWM output
MOVW DP, #(T1CMPR >> 6)
MOVH @T1CMPR, ACC

;get ready for next interrupt
MOVW DP, #(ADCTRL2 >> 6)
MOV @ADCTRL2, #0x4900      ;identical to line in ADC setup
                           ; reset ADC sequencer 1

MOVW DP, #(ADCST >> 6)
MOV @ADCST, #0x0010        ;clear ADC SEQ1 interrupt
MOVW DP, #(PIEACK >> 6)
MOV @PIEACK, #0x0001       ;acknowledge INTx.6

```

```

    CLRC INTM          ;re-enable interrupts
    IRET              ;return from interrupt

;-----
; File Name       : qsqrt.asm
;
; Originator      : Advanced Embeeded Control (AEC)
;                  Texas Instruments Inc.
;
; Description     : This file contain source code for fixed point SQRT
;                  function implemented using Tylor series
;-----
; Tylor Series Approximation of SQRT:
; Algorithm       :
; The following equation approximates the sqrt(x), where 0.5<= x <=1.0
; 0.5*sqrt(x)= 0.7274475*x-0.672455*x^2+0.553406*x^3-0.2682495*x^4
;                +0.0560605*x^5+0.1037903
;
; To determine the sqrt of an input value outside the range [0.5, 1.0]
; the input should be scaled to a number within the range.
;-----

a0      .set      06a48h      ; 0.1037903 scaled by 2^18
a1      .set      05d1dh      ; 0.7274475 scaled by 2^15
a2      .set      0a9edh      ; -0.672455 scaled by 2^15
a3      .set      046d6h      ; 0.553406 scaled by 2^15
a4      .set      0bb54h      ; -0.2682495 scaled by 2^16
a5      .set      00e5ah      ; 0.0560605 scaled by 2^16

SQRT2   .set      05a82h      ;(1/sqrt(2)) in Q15 format
                          ; Also sqrt(2) in Q14 format

QSQRT:
                          ; ACC=X in Q16 format
    SETC SXM              ; Set the sign ext. mode
    MPY P,T,#0            ; P=0
    LSR64 ACC:P,#1        ; X=X/2

    CSB ACC                ; Count sign bits, T=E
    LSL64 ACC:P,T          ; ACC=x=X/(2^(E-15)) in Q31 format

    TBIT @T,#0            ; TC=odd/even shift indicator

```

```

MOV AR4,T           ; AH=n
MOVL XT,ACC         ; T=x in Q31
MOV AH,AR4          ; AH=n
LSR AH,#1           ; AH=n/2
MOV AR4,AH          ; AR4=n/2

MPY ACC,T,#a5       ; ACC=x*a5 in Q31
ADD ACC,#a4<<15     ; ACC=a4+x*a5 in Q31

QMPYL ACC,XT,@ACC   ; ACC=x*(a4+x*a5) in Q30
ADD ACC,#a3<<15     ; ACC=a3+x*(a4+x*a5) in Q30

QMPYL ACC,XT,@ACC   ; ACC=x*(a3+(a4+x*a5)) in Q29
ADD ACC,#a2<<14     ; ACC=a2+x*(a3+(a4+x*a5)) in Q29

QMPYL ACC,XT,@ACC   ; ACC=x*(a2+x*(a3+(a4+x*a5))) in Q28
ADD ACC,#a1<<13     ; ACC=a1+x*(a2+x*(a3+(a4+x*a5))) in Q28

QMPYL ACC,XT,@ACC   ; ACC=x*(a1+x*(a2+x*(a3+(a4+x*a5)))) in Q27
ADD ACC,#a0<<9      ; ACC=a0+x*(a1+x*(a2+x*(a3+(a4+x*a5)))) in Q27
                    ; ACC=0.5sqrt(s*x) in Q27
                    ; ACC=sqrt(s*x) in Q26

;----- De-normalise the result -----

MOVH T,ACC<<5       ; ACC=sqrt(s*x) in Q15
MPY P,T,#SQRT2     ; P=sqrt(s*x)*(1/sqrt(2)) in Q30 format

LSL ACC,#4          ; ACC=sqrt(s*x) in Q30
MOVL P,ACC,NTC     ; P=sqrt(s*x) in Q30, if n is odd
MOVL ACC,P

MOV T,AR4
LSRL ACC,T          ; ACC=sqrt(x) in Q30
MOVH AL,ACC<<2     ; AL=sqrt(x)
LRETR

.label fast_end    ;load address of section end

;=====
; END CODE LOADED INTO RAM
;=====

```

```

.text

;-----
; File Name      : qsin.asm
;
; Originator     : Advanced Embeeded Control (AEC)
;                 Texas Instruments Inc.
;
; Description    : This file contain source code for fixed point SIN
;                 function implemented using Tylor series
;
; Date           : 21/1/2002
;-----
; Tylor Series Approximation in the first quardrant:
;
;  $\sin(x) = 3.1406625*x + 0.02026367*x^2 - 5.325196*x^3 + 0.5446778*x^4$ 
;  $+ 1.800293*x^5$ , where 'x' is the normalized radians
;-----

K5      .set 0x6480          ; Scaled to Q13
K4      .set 0x52FF          ; Scaled to Q20
K3      .set 0xAACC          ; Scaled to Q12
K2      .set 0x45B8          ; Scaled to Q15
K1      .set 0x7338          ; Scaled to Q14

QSIN:
    SETC SXM,OVM            ; ACC=x
    MOV ACC,AL<<16          ; AH='x', AL=0
    CLRC TC
    ABSTC ACC                ; TC= sign(x), AH=abs(x)

    LSL ACC,#1              ; Convert to first quadrant (0 to pi/2)
    ABS ACC
    SFR ACC,#1

    MOVL XT,ACC             ; XT=x in Q31 and in first quardrant

; Comment Next 2-instructions, if this works
    MPY ACC,T,#K1

```

```

; MOV AR5,#K1          ; AR5=K1
; MPY ACC,T,AR5        ; ACC=K1*x in Q29

ADD ACC,#K2<<14        ; ACC=K1*x+K2 in Q29

QMPYL ACC,XT,ACC       ; ACC=(K1*x+K2)*x in Q28
ADD AH,#K3             ; ACC=(K1*x+K2)*x+K3 in Q28

QMPYL ACC,XT,ACC       ; ACC=((K1*x+K2)*x+K3)*x in Q27
ADD ACC,#K4<<7         ; ACC=((K1*x+K2)*x+K3)*x+K4 in Q27

QMPYL ACC,XT,ACC       ; ACC((((K1*x+K2)*x+K3)*x+K4)*x in Q26
ADD ACC,#K5<<13        ; ACC((((K1*x+K2)*x+K3)*x+K4)*x+K5 in Q26
QMPYL ACC,XT,ACC       ; ACC((((((K1*x+K2)*x+K3)*x+K4)*x+K5)*x in Q25

LSL ACC,#6            ; in Q31
ABS ACC               ; Saturate to 0x7fff
NEGTC ACC             ; ACC=-sin(x), if TC=1
MOV AL,AH
LRETR

;=====
; RESET INSTRUCTION
;=====

.sect ".reset"

B START, UNC          ;jump to starting point

.end

```

Bibliography

- [1] R. S. Van Dyck Jr., P. B. Schwinberg, and H. G. Dehmelt, *Phys. Rev. Lett.* **59**, 26 (1987).
- [2] W. V. Hughes and T. Kinoshita, *Rev. Mod. Phys.* **71**, S133 (1999).
- [3] T. Kinoshita and M. Nio, *Phys. Rev. Lett.* **90**, 021803 (2003).
- [4] T. Kinoshita, *IEEE Trans. on Instrumentation and Measurement* **50**, 568 (2001).
- [5] M. C. George, L. D. Lombardi, and E. A. Hessels, *Phys. Rev. Lett.* **87**, 173002 (2001).
- [6] K. Pachucki and J. Sapirstein, *J. Phys. B* **35**, 1783 (2002).
- [7] A. Wicht, J. M. Hensley, E. Sarajlic, and S. Chu, in *Proc. 6th Int. Symposium on Frequency Standards*, edited by P. Gill (World Scientific, Singapore, 2002).
- [8] W. Liu *et al.*, *Phys. Rev. Lett.* **82**, 711 (1999).
- [9] E. Krüger, W. Nistler, and W. Weirauch, *Metrologia* **36**, 147 (1999).
- [10] P. J. Mohr and B. N. Taylor, *Rev. Mod. Phys.* **72**, 351 (2000).
- [11] A. M. Jeffery, R. E. Elmquist, L. H. Lee, J. Q. Shields, and R. F. Dziuba, *IEEE Trans. on Instrumentation and Measurement* **46**, 264 (1997).
- [12] L. Brown and G. Gabrielse, *Rev. Mod. Phys.* **58**, 233 (1986).
- [13] H. Dehmelt, *Am. J. Phys.* **58**, 17 (1990).
- [14] S. Peil and G. Gabrielse, *Phys. Rev. Lett.* **83**, 1287 (1999).
- [15] S. Peil, Ph.D. thesis, Harvard University, 1999.
- [16] L. S. Brown, G. Gabrielse, K. Helmerson, and J. Tan, *Phys. Rev. Lett.* **55**, 44 (1985).

-
- [17] L. S. Brown and G. Gabrielse, Phys. Rev. A **32**, 3204 (1985).
- [18] G. Gabrielse, X. Fei, L. Orozco, R. Tjoelker, J. Haas, H. Kalinowsky, T. Trainor, and W. Kells, Phys. Rev. Lett. **65**, 1317 (1990).
- [19] D. Wineland, P. Ekstrom, and H. Dehmelt, Phys. Rev. Lett. **31**, 1279 (1973).
- [20] G. Gabrielse and F. C. Mackintosh, International Journal of Mass Spectrometry and Ion Processes **57**, 1 (1984).
- [21] G. Gabrielse and H. Dehmelt, Phys. Rev. Lett. **55**, 67 (1985).
- [22] B. Odom, Ph.D. thesis, Harvard University, Unfinished.
- [23] L. S. Brown, G. Gabrielse, J. Tan, and K. C. D. Chan, Phys. Rev. A **37**, 4163 (1988).
- [24] H. Dehmelt, Proc. Natl. Acad. Sci. USA **83**, 2291 (1986).
- [25] H. Dehmelt, Proc. Natl. Acad. Sci. USA **83**, 3074 (1986).
- [26] Ching-Hua Tseng, Ph.D. thesis, Harvard University, 1995.
- [27] R. S. Van Dyck Jr., D. J. Wineland, P. A. Ekstrom, and H. G. Dehmelt, App. Phys. Lett. **28**, 446 (1976).
- [28] D. Wineland, , and H. G. Dehmelt, J. App. Phys. **46**, 919 (1975).
- [29] C. H. Tseng, D. Enzer, and G. Gabrielse, Phys. Rev. Lett. **59**, 2094 (1999).
- [30] K. Thorne, R. Drever, and C. Caves, Phys. Rev. Lett. **40**, 667 (1978).
- [31] L. Brown, Ann. Phys. **159**, 62 (1985).
- [32] T. Steimle and G. Alber, Phys. Rev. A **53**, 1982 (1996).
- [33] M. Scully and M. Zubairy, *Quantum Optics* (Cambridge University Press, New York, 1997).
- [34] R. Loudon, *The Quantum Theory of Light* (Oxford University Press, New York, 1983).
- [35] Ramon van Handel, Master's thesis, Vrije Universiteit, 2002.
- [36] M. W. Pospieszalski, S. Weinreb, R. D. Norrod, and R. Harris, IEEE Trans. on Microwave Theory and Techniques **36**, 552 (1988).
- [37] M. W. Pospieszalski, IEEE Trans. on Microwave Theory and Techniques **37**, 1340 (1989).

-
- [38] E. E. M. Woestenburg and L. Nieuwenhuis, Technical Report No. 205, Netherlands Foundation for Research in Astronomy, (unpublished), internal technical report.
- [39] E. E. M. Woestenburg and L. Nieuwenhuis, *Elect. Lett.* **30**, 524 (1994).
- [40] C. Hagmann, P. Sikivie, N. S. Sullivan, and D. B. Tanner, *Phys. Rev. D* **42**, 1297 (1990).
- [41] S. L. Pohlen, R. J. Fitzgerald, J. M. Hergenrother, and M. Tinkham, *App. Phys. Lett.* **74**, 2884 (1999).
- [42] G. Gabrielse, A. Khabbaz, and D. S. Hall, *Phys. Rev. Lett.* **82**, 3198 (1999).
- [43] J. D. Cressler, *IEEE Trans. on Microwave Theory and Techniques* **46**, 572 (1998).
- [44] T. Mimura, *IEEE Trans. on Microwave Theory and Techniques* **50**, 780 (2002).
- [45] S. Urazhdin and S. H. Tessmer, *Rev. Sci. Inst.* **73**, 310 (2002).
- [46] L. X. He, K. P. Martin, R. J. Higgins, J. S. Brooks, P. R. Jay, and P. Delescluse, *Solid State Commun.* **59**, 691 (1986).
- [47] W. W. Macalpine and R. O. Schildknecht, *Proc. of the IRE* **47**, 2099 (1959).
- [48] C. Caves, *Phys. Rev. D* **26**, 1817 (1982).
- [49] B. R. Mollow and R. J. Glauber, *Phys. Rev.* **160**, 1076 (1967).
- [50] B. R. Mollow and R. J. Glauber, *Phys. Rev.* **160**, 1097 (1967).
- [51] J. Tan, Ph.D. thesis, Harvard University, 1992.
- [52] B. D'Urso, B. Odom, and G. Gabrielse, *Phys. Rev. Lett.* **90**, 043001 (2003).
- [53] J. B. Johnson, *Phys. Rev.* **32**, 97 (1928).
- [54] H. Nyquist, *Phys. Rev.* **32**, 110 (1928).
- [55] M. J. O. Strutt and A. Van Der Ziel, *Physica* **9**, 513 (1942).
- [56] A. Van Der Ziel and M. J. O. Strutt, *Physica* **9**, 528 (1942).
- [57] C. Kittel, *Elementary Statistical Physics* (John Wiley & Sons, Inc., New York, 1958).
- [58] J. M. W. Milatz, J. J. Van Zolingen, and B. B. Van Iperen, *Physica* **19**, 195 (1953).

- [59] P. G. Roll, R. Krotkov, and R. H. Dicke, *Ann. Phys.* **26**, 442 (1964).
- [60] R. L. Forward, *J. App. Phys.* **50**, 1 (1979).
- [61] B. E. Bernard and R. C. Ritter, *J. App. Phys.* **64**, 2833 (1988).
- [62] P. F. Cohadon, A. Heidmann, and M. Pinard, *Phys. Rev. Lett.* **83**, 3174 (1999).
- [63] M. Pinard, P. F. Cohadon, T. Briant, and A. Heidmann, *Phys. Rev. A* **63**, 013808 (2001).
- [64] D. Vitali, S. Mancini, and P. Tombesi, *Phys. Rev. A* **64**, 051401 (2001), rapid communication.
- [65] N. Beverini, V. Lagomarsino, G. Manuzio, F. Scuri, G. Testera, and G. Torelli, *Phys. Rev. A* **38**, 107 (1988).
- [66] S. L. Rolston and G. Gabrielse, *Hyperfine Interactions* **44**, 233 (1988).
- [67] T. P. Heavner, M. Zuo, P. Hayes, and G. H. Dunn, *Physica Scripta* **T59**, 414 (1995).
- [68] V. Lagomarsino, G. Manuzio, and G. Testera, *Phys. Rev. A* **44**, 5173 (1991).
- [69] G. Zhang, J. Shen, and J. Dai, *Phys. Rev. A* **60**, 704 (1999).
- [70] S. van der Meer, *Rev. Mod. Phys.* **57**, 689 (1985).
- [71] S. Rainville, M. P. Bradley, J. V. Porto, and J. K. Thompson, *Hyperfine Interactions* **0**, 1 (2001).
- [72] J. Eschner, B. Appasamy, and P. E. Toschek, *Phys. Rev. Lett.* **74**, 2435 (1995).
- [73] M. G. Raizen, J. Koga, B. Sundaram, Y. Kishimoto, H. Takuma, and T. Tajima, *Phys. Rev. A* **58**, 4757 (1998).
- [74] D. Rugar and P. Grütter, *Phys. Rev. Lett.* **67**, 699 (1991).
- [75] F. DiFilippo, V. Natarajan, K. R. Boyce, and D. E. Pritchard, *Phys. Rev. Lett.* **68**, 2859 (1992).
- [76] V. Natarajan, F. DiFilippo, and D. E. Pritchard, *Phys. Rev. Lett.* **74**, 2855 (1995).
- [77] K. Oide, Y. Ogawa, and H. Hirakawa, *Jap. J. App. Phys.* **17**, 429 (1978).
- [78] J. C. Price, *Phys. Lett. A* **134**, 380 (1989).

-
- [79] F. Reif, *Fundamentals of Statistical and Thermal Physics* (McGraw-Hill, Inc., New York, 1965).
- [80] M. J. Buckingham, *Noise in Electronic Devices and Systems* (John Wiley & Sons, Inc., New York, 1983).
- [81] J. Courty, A. Heidmann, and M. Pinard, arXiv:quant-ph/0107138 (unpublished).
- [82] F. Grassia, J. Courty, S. Reynaud, and P. Touboul, arXiv:quant-ph/9904073 (unpublished).
- [83] J. Courty, F. Grassia, and S. Reynaud, arXiv:quant-ph/0110021 (unpublished).
- [84] H. Dehmelt, W. Nagourney, and J. Sandberg, Proc. Natl. Acad. Sci. USA **83**, 5761 (1986).
- [85] T. R. Albrecht, P. Grütter, D. Horne, and D. Rugar, J. App. Phys. **69**, 668 (1991).
- [86] A. N. Cleland and M. L. Roukes, Nature **392**, 160 (1998).
- [87] E. Ott, C. Grebogi, and J. A. Yorke, Phys. Rev. Lett. **64**, 1196 (1990).
- [88] M. Lax, Phys. Rev. **160**, 290 (1967).
- [89] N. J. Corron, S. D. Pethel, and B. A. Hopper, Phys. Rev. Lett. **84**, 3835 (2000).
- [90] A. Dec, L. Tóth, and K. Suyama, IEEE Trans. on Circuits and Systems - II: Analog and Digital Signal Processing **45**, 757 (1998).
- [91] S. Pavan and Y. P. Tsividis, IEEE Trans. on Circuits and Systems - I: Fundamental Theory and Applications **45**, 547 (1998).
- [92] A. Demir, A. Mehrotra, and J. Roychowdhury, IEEE Trans. on Circuits and Systems - I: Fundamental Theory and Applications **47**, 655 (2000).
- [93] D. S. Greywall, B. Yurke, P. A. Busch, A. N. Pargellis, and R. L. Willett, Phys. Rev. Lett. **72**, 2992 (1994).
- [94] W. R. Davenport Jr., J. App. Phys. **24**, 720 (1953).
- [95] P. C. Jain, IEEE Trans. on Information Theory **18**, 332 (1972).
- [96] B. Yurke, D. S. Greywall, A. N. Pargellis, and P. A. Busch, Phys. Rev. A **51**, 4211 (1995).

- [97] P. M. T. Broersen, *IEEE Trans. on Instrumentation and Measurement* **49**, 766 (2000).
- [98] J. A. Cadzow, *IEEE Trans. on Acoustics, Speech, and Signal Processing* **28**, 524 (1980).
- [99] J. A. Cadzow, *Proc. of the IEEE* **70**, 907 (1982).
- [100] J. Tan and G. Gabrielse, *Phys. Rev. A* **48**, 3105 (1993).
- [101] S. Mancini, A. Martins, and P. Tombesi, *Phys. Rev. A* **61**, 012303 (1999).
- [102] G. Ciaramicoli, I. Marzoli, and P. Tombesi, *Phys. Rev. A* **63**, 052307 (2001).
- [103] D. J. Heinzen and D. J. Wineland, *Phys. Rev. A* **42**, 2977 (1990).